Dissertation

submitted to the

Combined Faculties of the Natural Sciences and Mathematics

of the Ruperto-Carola-University of Heidelberg, Germany

for the degree of

Doctor of Natural Sciences

Put forward by

Claire Antel

born in Johannesburg

Oral examination on February 4th, 2019

Enhancing low mass dark matter mediator resonance searches with improved triggering in the ATLAS detector

Referees:
Prof. Dr. Monica Dunford
Prof. Dr. Stephanie Hansmann-Menzemer

Zusammenfassung

Dunkle Materie ist ein wesentlicher Bestandteil unseres Universums, jedoch ist ihre Eigenschaft bisher den Teilchendetektoren entgangen. Dunkle Materie kann in Protonenkollisionen am Large Hadron Collider durch die Herstellung und den anschließenden Zerfall eines Mediators erzeugt werden, der das Standardmodell mit dem dunklen Sektor koppelt. Neue Suchstrategien zielen darauf ab, den schwer zugänglichen Phasenraum bei geringen Massen zu erschließen, bei dem die beschränkte Triggerbandbreite die Sensitivität aufgrund der vielen niederenergetischen Interaktionen in Protonkollisionen stark einschränkt. Eine dieser Suchstrategien ist die Trigger-Objekt-Level-Analyse. In dieser wird die Bandbreitenbeschränkung umgangen, indem Objekte auf Triggerebene gespeichert werden, die ausschließlich aus einem Teil der vollen Ereignisinformation rekonstruiert wurden. Die Analyse ist daher eng mit den Fähigkeiten des Triggersystems verknüpft. Die vorliegende Arbeit umfasst verschiedene Verbesserungen der Triggerfunktionen des ATLAS-Detektors, um die Sensitivität gegenüber neuer Physik zu steigern. Ein neuer Algorithmus zur Identifikation der Protonenkreuzung für hochgesättigte Impulse wurde entwickelt, der den zum Auslösen erforderlichen Energiebereich des First-Level-Triggers auf die neuen hohen Energien des LHC Run 2 erweitert. Der Algorithmus wurde erfolgreich beauftragt und für Run 2 dauerhaft aktiviert. Die Leistung des High-Level-Jet-Triggers wird erweitert, um die Spurrekonstruktion auf Triggerebene als Eingabe eines neuen Trigger-Upgrades zu verwenden. Es wird demonstriert, wie dies die Sensitivität gegenüber niederenergetischer Resonanzen der Dunkle Materie in der Trigger-Objekt-Level-Analyse in zukünftigen Datenerfassungen des LHC verbessern wird.

Abstract

Dark matter comprises a significant component of our universe, but its particle nature has evaded particle detectors thus far. Dark matter may be produced in proton collisions at the Large Hadron Collider through the production of a mediator that couples the Standard Model to the dark sector. With no hint of new particles in the most accessible mass range, new search strategies aim to access the challenging phase space that lies at low masses, where current trigger bandwidth limitations have strongly constrained the sensitivity owing to the many low energy interactions that occur within proton collisions. One particular search strategy is the Trigger-object Level Analysis, which circumvents bandwidth limitations by recording only objects reconstructed from partial event information at trigger-level and is therefore intimately linked to the capabilities of the trigger system. The body of work herein encompasses various improvements of the triggering capabilities of the ATLAS detector in order to retain and enhance the sensitivity to new physics. A new bunch-crossing identification algorithm is commissioned for highly saturated pulses, extending the triggerable energy range of the first-level trigger to the new high energies of the LHC Run 2. The algorithm is successfully commissioned and permanently activated for Run 2 data taking. The capability of the high-level jet trigger is expanded in order to utilise trigger-level track reconstruction from the input of a new trigger upgrade. It is demonstrated how this will improve the sensitivity to low mass dark matter resonances in the Trigger-object Level Analysis in future data taking runs of the LHC.

Acknowledgements

I am grateful for having received the opportunity to conduct science at the world's most powerful particle collider. For this I owe a great debt of gratitude to my supervisor, Monica Dunford and the people of the Heidelberg research training group who funded my years as a doctorate student. My introduction to ATLAS and the Heidelberg group would not have happened without my previous supervisor, Andrew Hamilton. Thanks, Andrew.
I wish to thank Monica further for her guidance that lead me to the exciting work that I became involved in. I appreciated her creative ideas, inspirational stories and especially her words of encouragement during the past couple of months. Not once did I leave her office without feeling more motivated or more self-confident.
I would like to give thanks to Prof. Dr. Stephanie Hansmann-Menzemer for agreeing to co-review my thesis.
The comforts we enjoy within the ATLAS group at the KIP institute are owed to Prof. Hans-Christian Schultz-Coulon, and for this I would like to thank him and express my respect. I would also like to express my appreciation for Petra for dealing with all our badly filled-out paper work as secretary and still being nice about it.
I would like to thank Pavel and Martin for the large amount of time they dedicated to reviewing my thesis, as well as Jan, Silvia, Hanno, Martin Klassen, Falk, Philipp and Dan for acting as reviewers for parts of my thesis.
I want to thank the L1Calo group at CERN, especially Bruce, who always cared for my well-being, and crazy Eduard, whose words of encouragement meant a great deal to me. Jan and Silvia, thanks for making me laugh. Martin, thank you again for guiding me as technical supervisor through my L1Calo work.
I would like to express my appreciation for the TLA team for creating a stimulating working environment and providing feedback on my TLA work.
My friends and family were a great source of emotional support during my time here. Merve and Hanno, I really appreciated your friendship, support and day-dreamings of the future. Hanno, I hope one day you will offer me a ride in your fancy RV. Stanislav, you were an insufferable office mate, but otherwise a great friend when no open office windows in the dead of winter were involved.
I cannot express enough how grateful I am for my CERN friends and our Alpine adventures. Danny, thanks for being my adventure buddy in snowboarding, mountain biking and countless hiking expeditions. I hope we haven't shared our last sandwich blog post yet. Sam, no one could want for a more life-loving friend to conquer prominent mountains with. Dan, I look forward to being your climbing partner again. Thank you for being infinitely patient with me this year.
Finally, I would like to express my deepest gratitude to my parents and my brother. Without their unwavering support, my time as PhD student would have been a lot harder. I hope to hang out with you guys more frequently in the future.

Contents

1 Introduction **1**

2 The Standard Model of Particle Physics **5**

2.1 Introduction 5

2.2 Mathematical framework of the Standard Model 7

2.2.1 Electroweak symmetry breaking and the Higgs field 8

2.2.2 Electroweak interactions 9

2.2.3 Strong interactions 10

2.3 Beyond the Standard Model 13

3 Dark Matter **15**

3.1 History and observations 15

3.2 Experimental searches for dark matter particles 16

3.2.1 Empirical knowledge on dark matter 16

3.2.2 Theoretical and practical constraints 17

3.2.3 Weakly interacting massive particles 18

3.2.4 Detection methods 19

4 The Large Hadron Collider **27**

4.1 Introduction 27

4.2 The injector chain 27

4.3 LHC design 28

4.4 Towards High Luminosity LHC 30

5 The ATLAS experiment **31**

5.1 The detector . . . 31

5.1.1 The inner detector . . . 33

5.1.2 The calorimeter . . . 34

5.1.3 The muon spectrometer . . . 36

5.2 ATLAS Computing . . . 36

5.2.1 Data reconstruction . . . 36

5.2.2 Simulation . . . 36

5.3 Data object definitions . . . 37

5.3.1 Primary tracks and vertices . . . 38

5.3.2 Jets . . . 39

5.3.3 Pile-up jets . . . 43

6 The ATLAS trigger system **47**

6.1 The Level-1 trigger . . . 47

6.1.1 The Level-1 Muon Trigger . . . 48

6.1.2 The Level-1 Calorimeter Trigger . . . 49

6.2 The High-Level Trigger . . . 51

6.2.1 Online tracking . . . 51

6.2.2 Online jet reconstruction . . . 52

6.3 Data transfer . . . 52

6.4 The trigger menu . . . 53

6.5 Data recording streams . . . 53

6.6 Trigger rates . . . 54

7 A new Level-1 calorimeter algorithm for enhanced bunch crossing identification **57**

7.1 Trigger tower pulse preprocessing . . . 57

7.1.1 Analogue to digital conversion . . . 59

7.1.2 Pedestal correction and filtering . . . 59

7.1.3 Bunch crossing identification . . . 61
7.1.4 ADC to energy conversion . . . 62
7.2 Run 2 mistiming problem . . . 62
7.3 The Sat80 algorithm logic . . . 64
7.4 Calibration of algorithm thresholds . . . 67
7.5 Validation and performance . . . 72
7.5.1 Spy mode . . . 73
7.5.2 Activation . . . 74
7.6 Final Run 2 performance . . . 75

8 Dijet resonance searches: An overview 79
8.1 Dijet exclusion limits on Z' after LHC Run 1 . . . 79
8.2 New dijet search strategies in LHC Run 2 . . . 81
8.3 ATLAS dijet exclusion limits on Z' in LHC Run 2 . . . 81

9 The Trigger-object Level Analysis 83
9.1 Introduction . . . 83
9.2 The data scouting stream . . . 85
9.3 Trigger-level jet calibration . . . 86
9.4 Pile-up effects in dijets . . . 88
9.5 Future developments for TLA . . . 88
9.5.1 Future searches . . . 88
9.5.2 Search feasibilities in the presence of pile-up . . . 91
9.5.3 Tracks in TLA . . . 95

10 The new Fast-Tracker: online tracking 97
10.1 Physics Motivation . . . 97
10.2 Fast tracker system and track reconstruction . . . 99
10.3 FTK-HLT jet trigger integration . . . 102

11 FTK jet pile-up rejection studies **105**

11.1 Event selection and object definition . . . 105

11.2 Vertex reconstruction efficiency . . . 106

11.3 Computation of JVT . . . 107

11.4 Rejection variable performance . . . 108

11.4.1 Changes with pile-up . . . 108

11.4.2 Changes with jet kinematics . . . 110

11.5 Comparison to offline performance . . . 111

11.6 Pile-up rejection for a dijet + ISR jet signal . . . 112

11.7 Pile-up rejection for a $t\bar{t}$ signal . . . 113

11.8 Summary and final remarks . . . 116

12 Conclusion **119**

A Appendix **123**

A.1 The history of hadron colliders . . . 123

A.2 ATLAS 2017 Trigger Menu . . . 125

A.3 HLT Jet Trigger with integrated FTK tracks . . . 126

A.4 JVT p_T and η-binned acceptance efficiency . . . 128

A.5 Pile-up rejection in $t\bar{t}$ signal . . . 128

A.5.1 The crystal ball function . . . 128

A.5.2 Variable distributions . . . 129

A.5.3 Cutflows . . . 129

A.5.4 Non-normalised W and top mass distributions . . . 130

Chapter 1

Introduction

Looking at the large-scale structure of the universe, it is evident that there is a "dark" component that has a gravitational influence on the matter that is visible to us. It is termed dark matter and measurements suggest that it makes up 63% of all matter in the universe. One of the greatest questions in modern physics is to figure out what dark matter is made up of. The leading theory is that it is a type of new particle not encapsulated in the current Standard Model of fundamental particles.
But it has already been almost 100 years since scientists first started growing suspicious of its presence. Thus, the question on the nature of dark matter grows ever more puzzling and intriguing, as it succeeds to remain elusive.
The challenge of finding a suitable dark matter particle candidate has pushed experiments to develop novel ideas and techniques to search for any type of new signal. One avenue for the search for dark matter is in colliders: Dark matter particles might be produced at the Large Hadron Collider (LHC). The unprecedented amount of data and beam energies generated by the most powerful particle collider to date may uncover a signal that will prove to be a link to the dark matter sector.
A particularly challenging aspect of a collider experiment is that the data that is collected must be decided a priori by the collaboration, as only 0.005% of collisions can be recorded to permanent storage and further scrutinised. The fraction that is kept is decided by the detector's trigger system: It relies on a trigger menu of signatures that determine which events to record. Since the nature of dark matter is unknown, searches for it cover a vast amount of possible signatures.

One strategy is to aim to be inclusive as possible. This strategy is adopted by the so-called Trigger-object Level Analysis (TLA). The TLA makes use only of data that has been reconstructed at the High-Level Trigger (HLT) instead of complete event information from the full detector read-out. The reduced event size allows it to circumvent trigger bandwidth constraints and collect data below conventional trigger thresholds. The TLA relies on the fact that HLT algorithms strive to be as similar as possible to those used in offline reconstruction within the CPU constraints of the trigger.

This thesis describes a body of work dedicated to improving upon and expanding the capabilities of the trigger of the ATLAS detector in Run 2 of the LHC and beyond. The results of the work herein ultimately achieved two objectives.
The first is the commissioning of a new proton bunch crossing identification algorithm that is executed in firmware of the first-level trigger, enabling the system to reliably trig-

ger at the new beam energies of LHC Run 2.
The second is the integration of the input from a newly installed hardware component designed to perform real-time track reconstruction in the software-based trigger system. The physics motivations driving this work is the future improvement of dark matter mediator searches as well as more complicated multijet topologies at low resonance masses within the framework of the TLA.

The thesis begins with an overview of the Standard Model in Chapter 2. The chapter concludes with an outline of why it is expected that physics beyond the Standard Model exists. In Chapter 3 one avenue of new physics is motivated in particular: dark matter. Reasons are provided as to why it is believed that dark matter should be a new particle and the many detection methods that are employed in particle physics to search for dark matter signals are described. The complementarity between each detection method and the current status of scientific results are highlighted.
Chapters 4 and 5 provide a description of the Large Hadron Collider and the ATLAS detector, respectively. Since the work intimately deals with the ATLAS trigger system, it is described in detail in a separate Chapter 6. In Chapter 7, the process of commissioning of the new bunch crossing identification algorithm for the detector's first-level trigger system is described, ending with its official activation in physics data taking. Thereafter, the focus turns to the implementation of new algorithms in the detector's higher level jet trigger to incorporate online tracks reconstructed by the Fast Tracker (FTK), a new trigger component. The baseline motivation are low mass resonance searches from the production of dark matter mediators. Whilst in Chapter 8 a short overview is given of all current search strategies for low mass mediator resonances in dijets, the Trigger-object Level Analysis technique is explored in detail in Chapter 9. FTK is introduced and the benefits it will provide to the TLA by providing reconstructed tracks at trigger-level, are motivated. The FTK system is described in full in Chapter 10, including the implementation of FTK tracks in the higher level jet trigger. In Chapter 11 the first studies on the utilisation of FTK tracks in jets are conducted. The ability to use FTK tracks in order to reject background events that become prevalent at low masses are tested and compared to tracks that are reconstructed using full-resolution tracking information and more sophisticated algorithms. Although the full installation of the FTK hardware did not come to pass before the conclusion of the LHC data taking period of Run 2, the studies offer an outlook on the improved sensitivity to new low mass particles that can be accomplished with the successful installation of the upgrade at the commencement of Run 3 of the LHC.

Author's contribution

The ATLAS experiment requires a large team of scientists not only to produce final physics results, but also to extensively validate recorded data and ensure the constant functioning of the detector hardware and software. This is something I came to deeply appreciate by working on numerous levels of the experiment.
The start of my doctorate studies coincided with the start-up of the Large Hadron Collider for Run 2. I was fortunate to be one of the first people to analyse 6.5 TeV beam data, although in raw digital form. My initial task was to verify the analogue timing of the Level-1 calorimeter trigger towers during beam 'splashes': A circulating beam is made to collide with collimators upstream of the detector, thereby creating a shower of secondary

particles that stream through the detector from one side. Many of the detector channels are thereby 'lit-up' simultaneously.
During the first year of data taking, I worked on the fine-timing of the Level-1 calorimeter trigger towers, which involved the tuning of the pulse delay of 1 nanosecond steps to ensure that the peak of the underlying analogue pulse is sampled during pulse digitisation. I improved the fine-timing by making use of special data that contained 80 MHz digitised trigger tower pulses, taking advantage of the high resolution measurement of the pulse shape. Based on the same data, I could further obtain a better estimate of the fit parameters for each tower. These were used in the fine-timing of trigger towers digitised at 40 MHz in subsequent years.
The special 80 MHz trigger tower data was collected in order to commission a new bunch crossing identification (BCID) algorithm for saturated pulses. Whilst the algorithm concept had been developed before my time, and the necessary FPGA implementations were performed by a work colleague, I performed the analysis to derive the algorithm parameters and extensive validation studies of its performance.
Later I joined the Trigger-object Level Analysis (TLA). The analysis is closely involved in the ATLAS High-Level Trigger (HLT) as it analyses jets that have been reconstructed in the HLT. During my time with the analysis team I helped in the commissioning of a new jet trigger, and in measuring pile-up effects in the TLA dijet search.
My major contribution to the TLA, however, is the software integration of the Fast Tracker output into the HLT jet trigger. The task proved to be a tremendous undertaking, resulting in changes of various software packages, modifications to the software of core classes and extensive testing. The jet trigger software is now prepared to run with FTK input at the activation of FTK jet triggers in the trigger menu.
The FTK system upgrade was expected to be complete by the last data taking year of Run 2. Unfortunately, the project incurred several technical delays that resulted in its commissioning being incomplete by the end of Run 2. It instead went under heavy review with the consideration of cancelling the project if faith and funding could not be restored. A campaign within the collaboration was organised in order to once again show case how the FTK system will serve to improve the physics at ATLAS. I became involved in conducting the first studies on the performance of FTK jets in order to demonstrate not only their usefulness in the trigger but also for the physics conducted by the Trigger-object Level Analysis.

Chapter 2

The Standard Model of Particle Physics

2.1 Introduction

The Standard Model of particle physics describes all particles and their interactions that we know of and that we believe to be fundamental. It unifies the strong, weak and electromagnetic force in a single framework based on internal gauge symmetries of the unitary product group $SU(3) \times SU(2) \times U(1)$, where $SU(3)$ is responsible for the strong force and $SU(2) \times U(1)$ together generate the electroweak force. The following description of the Standard Model is by no means intended to be an exhaustive discussion of its theory. The information in this chapter is based on several sources [1–4] that the reader may refer to for a more comprehensive picture of the Standard Model.

Figure 2.1 presents the Standard Model "family portrait". The two major types of fundamental particles are differentiated by spin: fermions, of spin quantum number 1/2, and bosons, of integer spin quantum numbers. This results in fundamentally different behaviour as spin-1/2 particles obey Fermi-Dirac statistics whilst integer spin particles obey Bose-Einstein statistics. Fermi-Dirac particles are forbidden to occupy identical quantum states, so that fermions lead to the formation of structures of matter from protons to atoms to stars. Bosons are free to occupy any quantum state and the exchange of two bosons with the same quantum numbers will leave the quantum state of the system unchanged. When a force acts out between fermions, it is because bosons are being interchanged between them.

Fermions are further categorised into quarks and leptons, each consisting of 3 generations. Quarks, in addition to electric charge, carry a colour charge - red, blue or green.
Each lepton generation consists of a charged lepton and its (neutral) neutrino partner: the electron and electron neutrino, the muon and muon neutrino, and the tau and tau neutrino. Each quark generation consists of an "up-type" and "down-type" quark: (the lighter) up and down, strange and charm, and (the heavier) bottom and top quarks (u , d , s , c , b , and t).

The photon, gluon, $W^{\pm}$ and Z are the force carriers of the electromagnetic, strong,

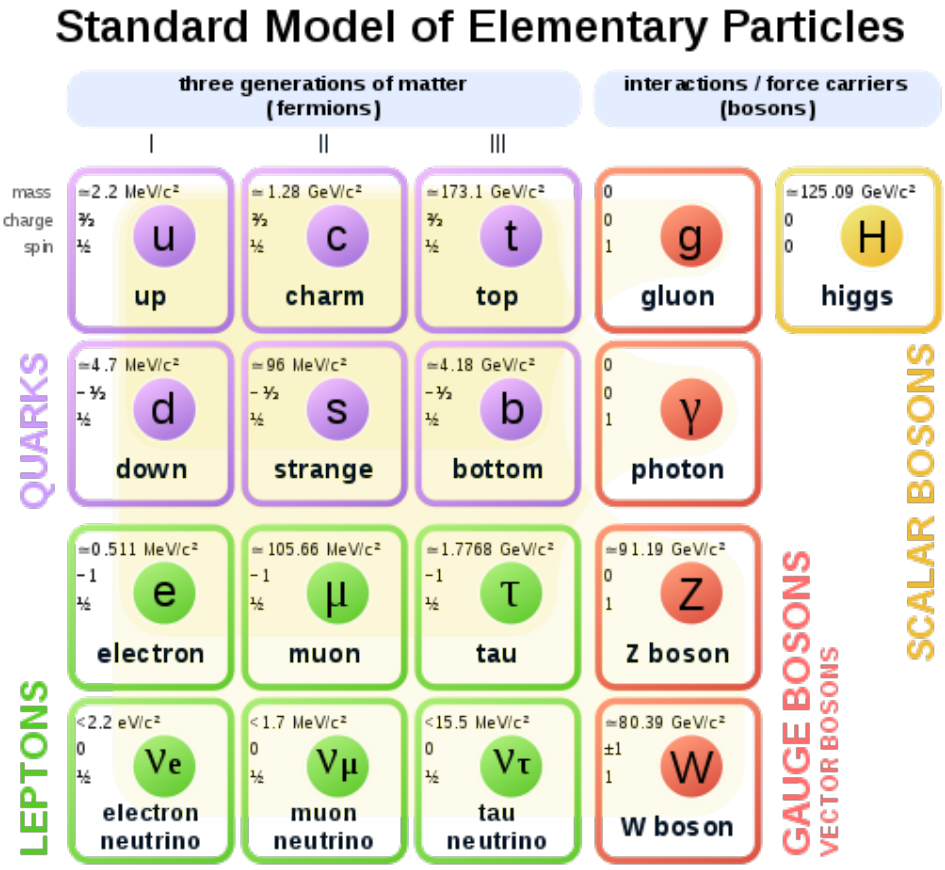

Figure 2.1: The fundamental particles of the Standard Model can be sorted into categories as schematically represented here. Shown are 12 types of fermions further categorised into three generations of quarks and three generations of leptons, and five types of bosons. Four bosons are associated to the three fundamental forces: The gluon to the strong force, the photon to the electromagnetic force and the $W^{\pm}/Z$ bosons to the weak force. The scalar Higgs boson arising from electro-weak symmetry breaking is the fifth boson. The theoretical graviton, associated to the gravitational force, lies outside of the description of the Standard Model theory. Taken from [5].

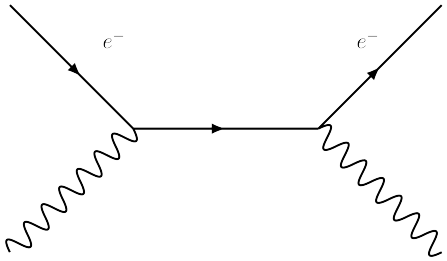

Figure 2.2: *Compton scattering*: A photon scatters off an electron, imparting some of its energy to the recoiling electron. It is a prominent process in radiation therapy, in which incident photons serve to ionise loosely bound electrons to break up malignent cells.

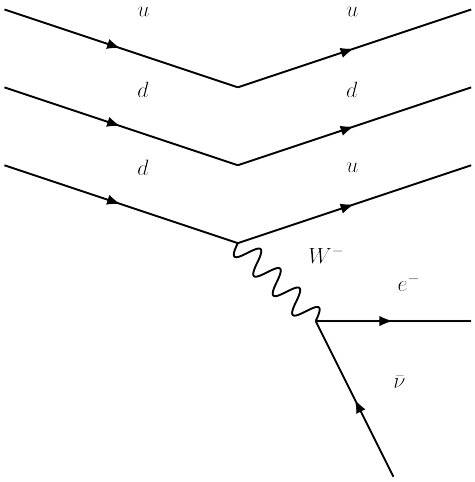

Figure 2.3: *Radioactive decay*: The weak force is responsible for radioactive decay, as $W^{\pm}$ boson exchange is the only interaction through which particles are able to change their flavours. A neutron, comprised of (udd) quarks may in this way change into a proton, comprised of (uud) quarks, thereby changing an atom into a different more stable type of nuclide.

charged weak and neutral weak force respectively[1]. Examples of Standard Model processes are depicted in Figures 2.2 and 2.3.

All matter we commonly encounter consists of the *lightest* fundamental particles: Protons and neutrons consist of up and down quarks and atoms are made up of protons, neutrons and electrons. Due to their larger mass, energy is required to create other types of particles. During the very early universe, high enough temperatures existed to thermally produce all particle types. The most energetic naturally produced particles that we encounter are cosmic rays which interact with the Earth's atmopshere, providing energy to briefly create heavier particles, such as pions and muons[2]. We create energy for conversion into mass in particle accelerators by accelerating particles to speeds close to the speed of light, thereby producing and discovering new particles.

2.2 Mathematical framework of the Standard Model

The mathematical framework of the Standard Model (SM) relies on quantum field theory (QFT). Further dynamics of the system are described by a Lagrangian.
In QFT, particles are treated as excitations of continuous fields rather than discrete points with defined positions in space. Thus, it is more common to work with the Lagrangian

[1]The graviton, carrier of the gravitational force, is only theorised. In [6] it is roughly estimated that a detector of a maximum mass of Jupiter and neutrino shielding of a couple of light years in depth for materials of ordinary density, is required to detect gravitons.

[2]The cosmic ray energy spectrum peaks between 10 and 100 GeV. However, ultrahigh cosmic rays can occur, which have energies on the order of > 60 EeV [7]. The most energetic cosmic ray measured to date had an energy of 300 EeV, which is 45 million times greater than the proton energies in the LHC.

density, $\mathcal{L}$ defined as

$$L = \int \mathcal{L} d^3x \tag{2.1}$$

The Lagrangian density is a function of the field and its local spatial and time derivatives. Assuming the *principle of least action* (particles move along a path of least resistance), any action would involve finding the minimal path integral. The solution to this minimising function is the Euler-Lagrange equation, which for a field, $\Phi(x^\mu)$, is

$$\partial_\mu \left(\frac{\partial L}{\partial(\partial_\mu \Phi(x^\mu)_i)}) \right) = \frac{\partial L}{\partial \Phi(x^\mu)_i} \tag{2.2}$$

A Lagrangian, $\mathcal{L}$, must fulfill the above solution. The Standard Model is in particular a *gauge* quantum field theory. A gauge quantum field theory enforces the Lagrangian to be locally gauge invariant - the measured physical state should be unaffected by any local group transformations. This constraint gives rise to gauge fields, the quanta of which describe spin-1 (gauge) bosons. The photon, gluons and weak bosons are gauge bosons. Generated gauge bosons leave the theory no longer gauge invariant if they have mass, which is in contradiction to the existence of the massive W and Z bosons. The electroweak symmetry breaking mechanism is required to generate the mass terms for massive gauge bosons.

2.2.1 Electroweak symmetry breaking and the Higgs field

Mass terms for gauge bosons and fermions arise in the interactions with the Higgs field, which acquires a non-zero expectation value, v, via the so-called *electroweak symmetry breaking* mechanism. The Higgs field is described as a scalar field doublet of the form

$$\Phi = \begin{pmatrix} 0 \\ \Phi_0 + \frac{h(x)}{\sqrt{2}} \end{pmatrix}$$

where h(x) represents the field of the scalar Higgs boson. The potential term for the scalar field is

$$V(\Phi) = \mu^2 \Phi^\dagger \Phi + \frac{\lambda^2}{2} (\Phi^\dagger \Phi)^2. \tag{2.4}$$

If $\lambda > 0$ and $\mu^2 < 0$, the potential is non-zero and has an infinite set of minima at $\frac{\mu^2}{\lambda} = v^2$, where one arbitrarily chosen value corresponds to the true physical state. Nature's choice in value is known as *spontaneous symmetry breaking*. Expanding the field around the vacuum state, v, results in the description of a massive scalar field and an excitation field of a massless scalar boson, a Goldstone boson.
Imposing local gauge invariance on the Lagrangian for a scalar doublet generates a gauge boson that is necessarily massless. However through the interactions with the Goldstone boson, a new gauge boson emerges with an acquired mass term. The additional degree of freedom for the longitudinal polarisation of the massive particle is acquired from the transverse polarisation degrees of freedom of the massless Goldstone vector field, which subsequently disappears.
The requirement of local gauge invariance in the local gauge symmetry group of the electroweak sector results in three goldstone bosons. Each provide a longitudinal polarisation that are manifested by the massive physical states of the W^+, W^- and Z bosons.

2.2.2 Electroweak interactions

Charged weak interactions couple only left-handed fermions and right-handed anti-fermions. Left-handed lepton and quark fields transform as the following doublets under SU(2), respectively [1],

$$\Psi_i = \begin{pmatrix} \bar{\nu_i} \\ \ell_i \end{pmatrix}$$

,

and

$$\Psi_i = \begin{pmatrix} u_i \\ d'_i \end{pmatrix}$$

,

where d'_i are the doublet partners of up-type quarks that take part in the charged-current weak interaction. These are mixed states of down-type quark mass eigenstates, d_j, defined by $d'_i = \sum_j V_{ij} d_j$. The quark mixing matrix, V_{ij}, is known as the *Cabibbo-Kobayashi-Maskawa* (CKM) matrix. It includes three mixing angles and a CP-violating phase, δ, that results in different transformations for particles and anti-particles.
Left-handed and right-handed fermion fields are differentiated by their weak isospins T. Weak interactions conserve the quantum quantity, T_3, the third component of T. Fermion doublet fields have weak isospin quantum number, $T_3 = \pm 1/2$. W bosons carry weak isospin $T = 1$. Right-handed fermions form singlets with weak isospin $T = 0$. They therefore do not undergo charged-current weak interactions.

The gauge bosons of the $SU(2) \times U(1)$ gauge group are B_μ and W^i_μ, where $i = 1, .., 3$, respectively, with corresponding gauge coupling constants, g and g'. The weak angle is defined as $\theta_W = \tan^{-1}(g'/g)$. The mixed state of B_μ and W^i_μ, $B\cos\theta_W + W^3 \sin\theta_W$ results in the physical field manifested by the photon, A. The weak fields manifested by the W and Z bosons are $W^\pm = (W^1 \mp iW^2)/\sqrt{2}$ and $Z = -B\sin\theta_W + W^3\cos\theta_W$.

The Lagrangian of the fermionic fields after electroweak symmetry breaking is

$$\begin{aligned} \mathcal{L}_\mathcal{F} = & \sum_i \bar{\psi}_i (i\partial\!\!\!/ - m_i - y_i H)\psi_i \\ & - \frac{g}{2\sqrt{2}} \sum_i \bar{\psi}_i \gamma^\mu (1-\gamma^5)(T^+ W^+_\mu + T^- W^-_\mu)\psi_i \\ & - e \sum_i Q_i \bar{\psi}_i \gamma^\mu \psi_i A_\mu \\ & - \frac{g}{2\cos\theta_W} \sum_i \bar{\psi}_i \gamma^\mu (g^i_V - g^i_A \gamma^5)\psi_i Z_\mu. \end{aligned} \tag{2.7}$$

The first term in the Lagrangian contains the Yukawa couplings $y_i = \frac{m_i}{v}$ - the coupling of the fermion fields to the Higgs field. The second, third and fourth terms describe the weak charged-current interactions, the electromagnetic and the weak neutral-current interactions.
T^+ and T^- are weak isospin operators for the fermion doublet transformations in weak-charged current interactions, in which $T_3 = -1/2 \to T_3 = +1/2$ and $T_3 = +1/2 \to T_3 =$

$-1/2$, respectively.

For the last term, g_V^i and g_A^i are the vector and axial-vector couplings defined as

$$g_V^i = T_{3L}^i - 2Q_i \sin^2 \theta_W \tag{2.8}$$

and

$$g_A^i = T_{3L}^i. \tag{2.9}$$

Here, T_{3L}^i is the weak isospin of left-handed fermion i, and Q_i is the charge of the fermionic field in units of e.

2.2.3 Strong interactions

The SU(3) component of the Standard Model describes the interaction of gluons and quarks, the dynamics of which is broadly termed *Quantum Chromodynamics* (QCD). It is encapsulated in the following Lagrangian,

$$\mathcal{L}_{\mathcal{QCD}} = \sum_{a,b} \bar{\psi}_{q,a}(i\gamma^\mu \partial_\mu \delta_{ab} - g_s \gamma^\mu t_{ab}^C G_\mu^C - m_q \delta_{ab})\psi_{q,b} - \frac{1}{4} F_{\mu\nu}^A F^{A\mu\nu}, \tag{2.10}$$

where γ^μ are the Dirac γ-matrices, $\psi_{q,a}$ are quark-field spinors with colour charge index $a = 1, .., 3$, for a quark of flavour q and mass m_q. G_μ^C represents the gluon fields, where $C = 1, .., 8$, is the index of each gluon. The term t_{ab}^C represents the eight 3×3 matrices that are the generators of the SU(3) group, and g_s is the coupling constant for the strong interaction. $F_{\mu\nu}^A$ is the field tensor, which can be expanded as

$$F_{\mu\nu}^A = \partial_\mu G_\nu^A - \partial_\nu G_\mu^A - g_s f_{ABC} G_\mu^B G_\nu^C. \tag{2.11}$$

The f_{ABC} term represents the structure constants of the SU(3) group.

2.2.3.1 Running coupling

A feature of QCD is the fact that the strong coupling constant has a logarithmic dependence on the momentum transfer of a process that becomes weaker at high energy scales. The measured dependence of the coupling constant in terms of $\alpha_s = g_s^2/4\pi$ on the energy scale, Q, is shown in Figure 2.4. For energy scales in the range of 100 GeV to a few TeV, $\alpha_s \sim 0.1$ but becomes on the order of unity for energy scales below 1 GeV. For cases where $Q^2 \gg \mu^2$ where μ^2 is a chosen reference energy scale, the running coupling is

$$\alpha_s(Q^2) = \frac{\alpha_s(\mu^2)}{1 + \beta_0 \alpha_s(\mu^2) \ln(|Q^2|/\mu^2)} \tag{2.12}$$

where $\beta_0 = (11N_C - 2N_f)/12\pi$, in which N_c and N_f are the number of colour charges and flavours, respectively.
The coupling constant can be evaluated using the following perturbative expansion in powers of α_s,

$$\mu_R^2 \frac{d\alpha_s(Q^2)}{d\mu_R^2} = \beta(\alpha_s) = -(\beta_0 \alpha_s + \beta_1 \alpha_s^2 + \beta_2 \alpha_s^3 + \mathcal{O}(\alpha_s^4)). \tag{2.13}$$

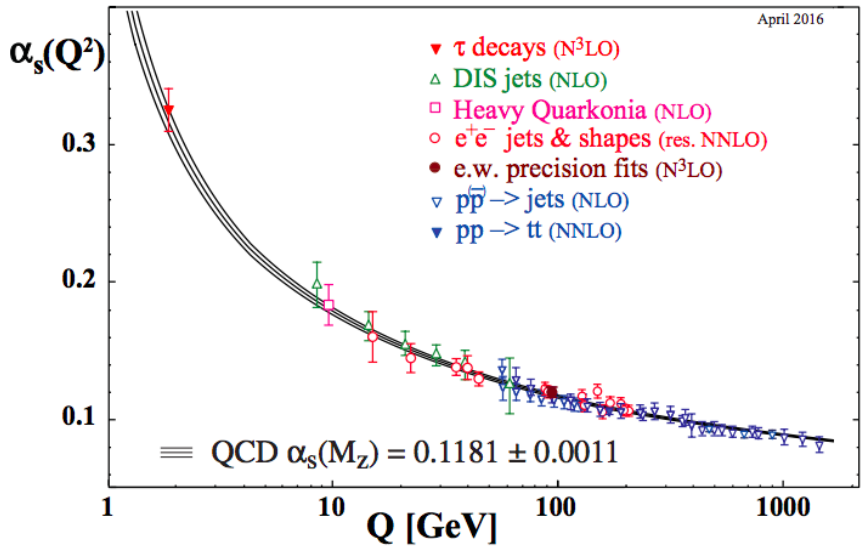

Figure 2.4: Combined measurements of α_s as a function of the energy scale, Q. Taken from [1].

Therefore, for $Q^2 \gg \mu^2$, *perturbative QCD* calculations can be used and rely on the evaluation of the coefficients in the expansion to predict observables in QCD.

The dependence of the strong coupling on Q^2 has two consequences: *colour confinement* and *asymptotic freedom*.
Colour confinement is a result of the very large coupling at large distances (small momentum transfers). As quarks are forced apart, connecting colour fields in the space between narrow into flux-tubes of constant width. At a certain distance the field energy greatly exceeds the rest energy of a quark-antiquark ($q\bar{q}$) pair and the tube breaks in two as a new $q\bar{q}$ pair is created with each quark terminating one end of the new tubes. As a result quarks are never found in isolation. The process is known as *hadronisation* and cannot be treated perturbatively.
Asymptotic freedom holds in instances of small couplings at large momentum transfers - or small distances - in which, as a result, QCD processes *can* be treated perturbatively. In the case of a proton-proton interaction in which a large amount of energy is transferred, asymptotic freedom allows one to evaluate the resulting "hard scattering process" up until the onset of hadronisation.

2.2.3.2 QCD processes in proton collisions

The Feynman diagrams depicted in Figure 2.5a illustrate hard scatter processes in proton collisions that result in the production of either quarks or gluons, collectively referred to as partons. They are shown at first order in perturbative QCD. In reality, *higher order* effects come into play, such as gluon radiation, $q \to qg$, and loop corrections, examples of which are depicted in Figure 2.5b. Each additional higher-order process introduces a new vertex with an extra term containing α_s. Due to the relatively large value of g_s and gluon self-interaction, partons result in a *parton shower* in which there is prolific radiation emission and self interaction. This is true for both the incoming and outgoing partons, for which radiation emission is commonly referred to as *initial* and *final state radiation*, respectively.

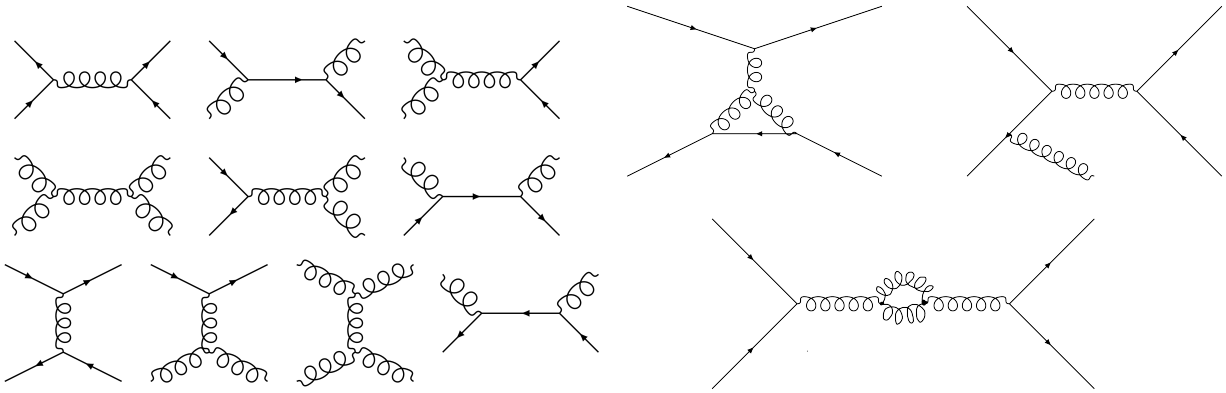

(a) to first order (b) higher order terms

Figure 2.5: Feynman diagrams that result in two partons in the final state from quark and gluon interactions in proton collisions.

The evolution of a parton shower becomes more complicated owing to colour confinement. A parton shower will continuously evolve until all particles in the shower have decayed into and formed colour-neutral stable states.

Further levels of complication arise when considering the interactions of partons within the complete proton collision. The resulting kinematics are dictated by the protons' parton distributions. The cross-section of proton interaction is given by

$$\sigma_{ij\to k} = \int dx_1 \int dx_2 f_i^1(x_1) f_j^2(x_2) \hat{\sigma}_{ij\to k} \tag{2.14}$$

where $\hat{\sigma}$ is the cross section of the hard process described by the quantum mechanical transition matrix element, and $f_i^a(x)$ is the *parton distribution function* describing the probability of finding a parton i in proton a with momentum fraction x of the proton's total momentum. The function additionally depends on the energy scale Q^2 and it is in practice unknown how to derive the function. It is therefore parameterised based on experimental data and the DGLAP[3] evolution equations which evolve the function to the required Q^2. In addition, reality includes the underlying event: the colour-charged partons within the protons that did not participate in the hard interaction but nevertheless contribute to the evolution towards a final colourless state.

A detector at a hadron collider measures the parton shower, the underlying event and initial and final state radiation. For experiments, this means quarks of the hard process need to be recovered by reverse-engineering the showering processes. This is done through the use of algorithms that collect the collimation of particles in a parton shower and let the collection as a whole define the direction and momentum of the initial quark. The resulting collection is known as a jet.

[3]Dokshitzer-Gribov-Lipatov-Altarelli-Parisi - named after the authors who independently published the formulation of equations that dictate the rate of change of parton densities in a proton with varying energy scales.

2.3 Beyond the Standard Model

Whilst the Standard Model has been successful in describing all known fundamental particles and their interactions, there are several indications that the framework is incomplete and that particles beyond the Standard Model must exist.

For example, new physics is postulated to exist at the point where the couplings of the three fundamental forces of the SM unify. The theory of the gauge symmetry that unifies all particles under one coupling is termed the *Grand Unified Theory* (GUT). The scale is determined by the intersection of the running couplings, which sets $\Lambda_{GUT} \sim 10^{16}$ GeV. The unification of all four forces, including gravity, represents another point at which new particle mediators are postulated and encapsulated in the *Theory of Everything*. This is expected at scales of $\sim 10^{19}$ GeV.

Related to this is the concern of the *naturalness* of the Standard Model. It is expected that any dimensionless free parameters in the Standard Model should be on the order of unity. However, there exist free parameters that seem remarkably *fine-tuned*. One such example relates to the fine-tuning of the Higgs mass, which arises from the large discrepancy that is observed between the strength of the weak force and a new force at GUT scale or the gravitational force. The Higgs mass depends on the parameter μ in the potential term of the Higgs field and quadratically divergent radiative corrections,

$$m_H^2 = 2\mu^2 + \delta m_H^2. \tag{2.15}$$

Yukawa couplings of fermion fields, λ_f contribute to the radiative term with corrections of the form

$$\Delta m_H^2 = -\frac{|\lambda_f|^2}{8\pi^2}[\Lambda_{UV}^2 + ...] \tag{2.16}$$

where Λ_{UV} is the cut-off scale of the SM theory. The radiative contributions can be regulated by tuning μ in such a way as to result in the measured Higgs mass. However, the issue becomes greater if one expects new particles at higher energy scales. Any new particle beyond the SM will add to the correction term, such as in the case of a new scalar particle,

$$\Delta m_H^2 = \frac{|\lambda_f|^2}{16\pi^2}[\Lambda_{UV}^2 - 2m_s^2 \ln(\Lambda_{UV}/m_s) + ...]. \tag{2.17}$$

Since the correction grows larger for more massive particles and new particles are expected at the very least at the GUT scale, the comparably small measured mass of the Higgs indicates a source of extreme fine-tuning. The theory of *Supersymmetry* [8, 9] offers an elegant solution, by introducing a supersymmetric bosonic partner for every fermionic particle, and vice versa. Thus particles and their superpartners differ only in their spin. The outcome is that supersymmetric particles contribute corrections to the Higgs mass that exactly cancel that of the particle counterpart. This offers a simple explanation of the smallness of the observed Higgs mass. The mass difference between ordinary SM particles and the superset would occur through a mechanism of spontaneous symmetry breaking and requires to be soft enough for radiative cancellations to remain effective. This results in supersymmetric particle masses of no more than a few TeV and had lent exciting prospects of discovery at hadron colliders. The non-discoveries of new particles at the Large Hardon Collider has largely discredited a minimal supersymmetric standard

model that would serve to stabilise the weak scale [10, 11].

Another fine-tuning problem is the CP-violating angle in the strong sector, so far measured to be consistent with zero (analogous to the CP-violating phase in the CKM matrix in weak couplings), but there is no reason for it to be so, and suggests a new process that suppresses strong CP-violation. This is known as the strong CP problem.

The Standard Model does not offer explanations for several observations, examples of which are neutrino masses, matter-antimatter asymmetry and dark matter.
Neutrino masses have been established to be extremely small but non-zero from measurements of neutrino oscillations, a phenomena in which neutrinos are observed to change their flavours when propagating over large distances and which is only possible if neutrinos have mass. The mechanism that generates their mass has not been proven in the SM, however. Other lepton masses are generated via the Yukawa coupling of right- and left-handed states. But experimentally only left-handed neutrinos and right-handed anti-neutrinos have been observed, making it unclear that neutrinos are Dirac particles with a Yukawa coupling.
In order to explain the matter-anti matter asymmetry in the universe, a CP-violating process is required that causes an imbalance in the number of particles and anti-particles in the early universe. CP-violation in weak interactions is insufficient to account for the matter-antimatter asymmetry, which calls for other sources of CP-violation.
Finally, the Standard Model offers no candidate particle for dark matter, a type of weakly-interacting particle that makes up the dominant matter component of our universe. Motivations for the existence of dark matter and its particle nature are provided in the next chapter.

Chapter 3

Dark Matter

3.1 History and observations

There is irrefutable evidence of the existence of a type of matter other than ordinary baryonic matter of the Standard Model. It has thus far been inferred to exist only through the observation of gravitational effects on ordinary matter in outerspace, however it does not appear to interact electromagnetically. We therefore refer to it as "dark matter". The observations tell us it is the dominant component of all matter in our universe, making up 63% of it [12].
The first speculations on dark matter were made in 1922 by Dutch scientist Jacobus Kapteyn, who studied stellar rotation curves of the Milky Way. He noted, "The most striking feature brought out by these numbers is undoubtedly the fact that at distances from the axis exceeding 2000 parsecs the linear velocity of the stars is nearly constant" [13], implying that the mass density did not drop off along with our galaxy's luminous mass. Several decades later, Rubin et al.'s investigations of 21 spiral galaxies [14], all demonstrating flattening velocity curves at large radii, was robust proof that the universe was largely composed of dark matter. Since then numerous observations from other astrophysical sources have contributed to the growing case of the Existence of Dark Matter. For example, measurements of Supernovae Type Ia distances [15], the Cosmic Microwave Background [12, 16] and Lyman-α Forest absorption lines in distant galaxies [17] are used to study density fluctuations in the universe for different periods in time, thereby deriving cosmological parameters - one of these being the dark matter density component, consistently measured at $\sim 23\%$ of the total energy density of the universe. Radial velocities, X-ray measurements of hot gas distribution [18], strong gravitational lensing of clusters of galaxies [19] and massive N-body simulations of structure formation [20] have illustrated the presence of dark matter via its gravitational effects. Whilst it was previously thought that dark matter was likely composed of solid objects such as dead stars or black holes, over the years, not enough of such solid dark floating objects were detected. Instead the hypothesis that dark matter is a new type of particle grew popular, giving rise to a first-time collaboration between astrophysicists and particle physicists. The collisions of galaxy clusters have been found to be strong evidence of such a nature. The most famous example is the Bullet Cluster, which has undergone a collision through a larger galaxy cluster. The gas within the cluster makes up most the baryonic (luminous) matter of the cluster. It is evident that the gas distribution mapped by x-ray emissions is clearly separated from and lags behind a dark matter distribution detectable via weak gravitational lensing. Dark matter thus appears as an entity of its own [21]. Recently, a

possibly first hint of dark matter exhibiting a particle nature was reported in studies of Hydrogen absorption lines from the light of early stars [22]. It had been predicted that the ultraviolet light emerging after the formation of the earliest stars would penetrate the primordial hydrogen gas and alter excitation energies. In particular, the 21 cm hyperfine splitting absorption line would have a lowered frequency. The Edges (Experiment to Detect the Global Epoch of reionisation Signature) are low-band instruments that detected this signal at 78 MHz. The shape of the absorption line, however, suggested a gas that is cooler than predicted. Interactions between a 'cold' dark matter and baryonic matter is a possible cooling mechanism during this time.

3.2 Experimental searches for dark matter particles

A large effort in the field of particle physics is directed at searches for dark matter particle candidates. The empirical knowledge on dark matter to date is used to derive dark matter particle models and guide searches.
The next three sections summarise: What we can infer from the empirical knowledge we have, general guidelines motivated by theoretical and practical constraints, and the popular dark matter particle model of weakly interacting massive particles (WIMPs).
Due to its elusive nature, technology and experimental techniques play a big role in the search for a dark matter candidate. The final section gives an overview of the types of dark matter detection methods - with a focus on collider experiments - and the current experimental exclusion limits achieved today.

3.2.1 Empirical knowledge on dark matter

The most accurate encapsulation of all of astrophysical measurements of dark matter is the ΛCDM model [16, 23], a cosmological model that describes the evolution of our universe assuming a "Big Bang" origin. It is largely based on empirical data. One of the parameterisations is Λ, a dark energy density component that accounts for the accelerating expansion counteracting gravitational collapse. The other feature is a cold dark matter (CDM) component that serves as a seed to large scale structure formation of baryonic matter as we observe it today.

The following is what is inferred for dark matter assuming the ΛCDM model:

- Dark matter is cold: It moves non-relativistically at the time of galaxy formation. This is supported by simulations of large scale structure formation that favour the *bottom-up approach*, rather than the *top-down approach*. In the former, larger structure is created starting from small structures that coalesce. In the latter, large structure form first that subsequently fragment into smaller components. Due to its non-relativistic speeds, cold dark matter tends to 'clump' under mutual gravitational attraction, seeded by early small-scale density fluctuations. This draws baryonic matter together under the growing gravitational influence of concentrated dark matter regions, presenting the opportunity for the formation of gas molecules and eventually galaxies. Relativistic dark matter, in contrast, would have enough energy to overcome the gravitational pull to early seeds, leading to a more diffused large scale structure.

- $\Omega_\chi \approx 0.24$ [12, 16], where Ω_χ is the cosmological density parameter for dark matter. It measures the ratio of the energy/matter density of the present-day universe that

is comprised of dark matter, ρ_χ, and the critical density, ρ_c, which is the total energy/matter density of a universe assumed to be perfectly flat:

$$\Omega_\chi = \frac{\rho_\chi}{\rho_c} \tag{3.1}$$

- It interacts with 'our' world, at least gravitationally. Observations of gravitational interactions are purely astrophysical. The results from the Edges experiment [24] is the first observed hint of what may possibly be another type of interaction between dark matter and SM particles.

3.2.2 Theoretical and practical constraints

There are several assumptions made in dark matter searches that can be drawn from theoretical as well as practical constrains. These are:

- Dark matter must be a stable particle on cosmological time scales. It would otherwise have decayed away by this point.
- The production of dark matter in the early Universe cannot exceed the inferred dark matter density (Ω) measured today. This sets bounds on the allowed mass-coupling phase space for dark matter candidates in hypothesised models. The alternative to this assumption is assuming an alternative theory to the ΛCDM model.
- Nor can it lead to an underproduction of DM. This assumption can be relaxed if one assumes the sought dark matter particle only constitutes a subcomponent of the dark matter sector.
- Dark matter interacts with Standard Model particles other than only gravitationally, albeit very weakly. This is a *necessary* assumption because if no other type of interaction exists, then particle detectors cannot hope to detect signals from dark matter. It is also theoretically favoured, as dark matter production and observed abundance can be most simply described by the idea of thermal freeze-out. The idea is based on the assumption that dark matter interacts with ordinary matter strongly enough for both to have existed in thermal equilibrium in the early universe. The dark matter abundance can be relatively easily determined by the point at which all DM interactions with the SM keeping it in thermal equilibrium have ceased owing to the expansion of the Universe.

Popular examples of dark matter particle models are sterile neutrinos, QCD axions and weakly interacting dark matter particles (WIMPs).
Neutrino-type particles are popular dark matter candidates as they are a known type of particle and only interact weakly. SM neutrinos (active neutrinos) alone cannot constitute the whole dark matter component [1], however, as they do not have enough mass to explain the observed relic dark matter abundance. A sterile neutrino [25] is a hypothetical right-handed neutrino that via a *mixing* of sterile and active neutrino states can couple weakly to the Standard Model sector. Sterile neutrinos in the mass range of several keV are viable candidates [25].
A QCD axion [26] is a hypothetical particle that is a solution to the strong CP problem in SM. The solution is a new global symmetry (known as the Peccei-Quinn symmetry) in which the CP-violating angle is replaced by a dynamical field. The axion emerges as the

Goldstone boson after a spontaneous symmetry breaking after which the field relaxes to an expectation value of zero. The QCD axion is postulated to be very light: The favoured mass range is between 1-100 μeV. Axions can be detected when they are converted to photons in a strong magnetic field. Presently only one experiment exists that is sensitive enough to detect a QCD axion signal, the Axion Dark Matter eXperiment (ADMX) [27]. The WIMP model is the leading motivation across a large portion of experiments, and specifically so at collider experiments. It is therefore described fully in the following section.

3.2.3 Weakly interacting massive particles

The model of weakly interacting massive particles is based on a general description of a dark matter candidate that fullfills minimum criteria: It interacts weakly, it is massive enough to be non-relativistic at the time of early galaxy formation and it is produced thermally in the early universe. Thermally produced means that dark matter particles are pair-produced out of the thermal bath (process (a)) in the early hot universe and kept in thermal equilibrium via the production, scattering and annihilation type interaction processes (processes (a)-(c)) with fermionic matter:

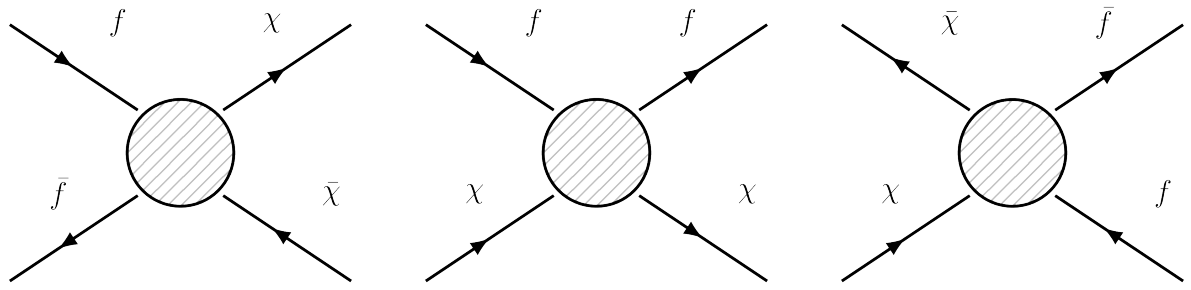

(a) dark matter pair production (b) dark matter-fermion scattering (c) dark matter annihilation

Two things affect the number density of dark matter as the universe cools. Firstly, roughly when $T < m_\chi$, there is insufficient energy for the pair production of dark matter particles out of the thermal bath, meaning production processes cease. At this point the number density becomes exponentially suppressed as annihilation processes continue. The second effect is the Hubble expansion, H(t), through which the mean distance of particles grows. At some point, this distance becomes large enough for interaction processes to cease. This happens approximately when the interaction rate becomes smaller than the Hubble expansion:

$$\Gamma(T) = \langle \sigma_A v \rangle n < \mathrm{H(T)} \tag{3.2}$$

where σ_A is the annihilation cross-section to SM fermions, v is the particles' relative velocities, n is the number density and H is the expansion rate. The temperature at which the co-moving number density remains constant, T_F, is termed the point of *freeze out*. Annihilation and production processes no longer take place and the dark matter number density at the time of freeze-out now only scales with the expansion of the universe. The point of freeze out can be linked to the relic dark matter density measured today.

Through the evolution of Boltzmann statistics it turns out that for a non-relativistic

particle , the relic density is [1]

$$\Omega_\chi h^2 \approx 0.12 \frac{2 \times 10^{-26} \mathrm{cm}^3 \mathrm{s}^{-1}}{\langle \sigma_A v \rangle}, \tag{3.3}$$

If one were to assume a weakly interacting particle and $\alpha \approx 0.01$, then the annihilation cross-section is approximately $\langle \sigma_A v \rangle \approx \alpha^2/((100\,\mathrm{GeV})^2) \approx 10^{-25} \mathrm{cm}^3 \mathrm{s}^{-1}$, which is close to what is needed to account for the dark matter abundance today [28]. The fact that the relevant scales of the WIMP model are comparable to the SM weak scale, is termed the 'WIMP miracle'. It became the leading model for dark matter particle physics, particularly as these energies are immediately accessible to modern colliders.
The theory of Supersymmetry, which was introduced in Chapter 2, naturally offers a WIMP candidate. The lightest supersymmetric particle (LSP) is a stable particle, as decays to Standard Model particles are forbidden under *R-Parity conservation*. Since all Standard Model particles have an R-parity of 1 and all supersymmetric particles have an R-parity of -1, conservation of R-parity[1] implies that any decay of a supersymmetric particle must include a lighter supersymmetric particle in the final state. A favoured candidate is the heavy neutralino as the LSP [29, 30].

Since WIMP candidates are expected at the weak scale, the WIMP model is the leading model in dark matter searches at the LHC.

3.2.4 Detection methods

Detection methods can be broadly categorised into: Direct detection (DD), indirect detection (ID) and collider experiments.
In *indirect detection experiments* one hopes to infer the presence of intergalactic dark matter by detecting gamma-rays, Z bosons or antimatter from dark matter annihilation. To escape the high background noise on Earth, such experiments are ideally placed in space. A challenge in indirect detection experiments is the large uncertainty on the astrophysical background and its interaction with the detected particles as they travel through space, such as scattering, absorption, magnetic acceleration or deflection.
In *direct detection experiments* one looks for signs of dark matter particles interacting with the detector material. As the interaction is assumed to be rare, direct detection experiments gain by having a very large volume and being situated deep under ground, water or ice where they are shielded from cosmic ray interactions.
Finally, *collider experiments* aim to analyse possible dark matter production in collisions, the strategies for which are covered in detail in the final section.

In order to facilitate comparisons between the three different detection methods it is helpful to assume a common theoretical model in which to cast the results from all types of experiments. A simple model is the assumption of an additional mediator, R, that acts as communicator between the dark matter sector and the Standard Model sector. Only the essential parameters are postulated within the model such as the mediator couplings to quarks and dark matter, the mediator and dark matter mass as well as the form of interaction. This is termed a *simplified dark matter model* [31]. Currently, experiments

[1] In the theory of Supersymmetry, baryon and lepton numbers are not mathematically conserved. To account for the experimentally measured conservation of lepton and baryon numbers, an R-parity symmetry is defined, $P_R = (-1)^{3(B-L)+2s}$, where s, B and L are the spin, lepton and baryon number [29].

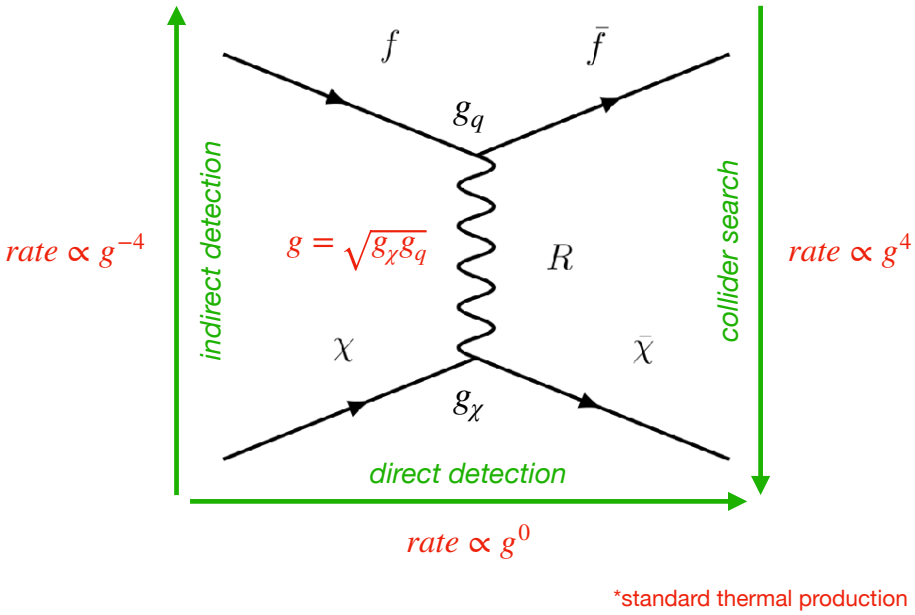

Figure 3.1: Schematic representation of the different detection methods that are used in the search for dark matter particles. Indirect detection is the search for the annihilation products of a dark matter particle-anti-particle pair, direct detection is the search for dark matter-fermionic scattering and a collider search is the search for dark matter produced in collisions. Each type of detection depends on the effective coupling strength, $g = \sqrt{g_q g_\chi}$, in a different way (assuming standard thermal production). The dependence is calculated from the coupling strength at each vertex interaction and the dark matter density, ρ, explained more fully in the text.

are sensitive to a range of mediator couplings that would have led to sizeable dark matter annihilation rates in the early Universe such that overproduction of dark matter is avoided. For this reason, the model has become a benchmark model for present dark matter searches [32]. Figure 3.1 is a graphical representation of the mediator model and of the processes the different detection methods probe. It furthermore qualitatively shows the complimentarity of the different methods, which is explained in the following.
In the graphic, g is defined as the effective combined Dark Sector coupling to SM quarks and to DM particles, $g = \sqrt{g_q g_\chi}$. Due to the two vertex interactions, the relationship of g to the cross-section will scale as $\sigma \propto g^4$. Additionally, indirect and direct detection depend on the dark matter density. For standard thermal production of dark matter, the DM density scales inversely with the annihilation cross-section so that $\rho \propto g^{-4}$. Direct detection is directly proportional to ρ and indirect detection to ρ^2. Therefore, the event rate for collider searches scales as $\sigma \propto g^4$, for direct detection as $\sigma \times \rho \propto g^{4-4} = g^0$ and indirect detection as $\sigma \times \rho^2 \propto g^{4-4\times 2} = g^{-4}$. As a result, indirect searches have increased sensitivities to small couplings and collider searches have an increased sensitivity to large couplings. Due to the interplay of coupling strength and dark matter abundance, direct detection searches have minimal dependence on coupling.

The assumed form of the dark matter particle, R, that acts as mediator between the dark sector and the Standard Model sector makes a difference on the strength of constraints set by various experimental results. Here, the dark matter mediator is assumed

to be a vector, from now on referred to as Z'. The Lagrangian for interactions with a Dirac dark matter fermion and SM quarks has the form

$$\mathcal{L} = Z'\bar{\chi}\gamma^{\mu}(g_{\chi}^{V} - g_{\chi}^{A}\gamma^{5})\chi + \Sigma_{f=q,l}Z'\bar{f}\gamma^{\mu}(g_{f}^{V} - g_{f}^{A}\gamma^{5})f, \tag{3.4}$$

where χ is assumed to be a Dirac dark matter fermion, and q and ℓ denote SM quarks and leptons, respectively. g_{χ}^{V} and g_{f}^{V} are vector couplings and g_{χ}^{A} and g_{f}^{A} are axial-vector couplings. The interpretation of experimental results changes depending on whether vector or axial-vector coupling terms are chosen to dominate. If vector couplings are present then the scattering of dark matter particles off nuclei is *spin-independent*. If axial-couplings prevail, then scattering interactions are *spin-dependent*. The terms for the spin-dependent and spin-independent scattering cross-sections are [33]

$$\sigma_{N}^{SD} = a_{N}^{2}\frac{3\mu_{N_{\chi}}^{2}}{\pi M_{R}^{4}} \tag{3.5}$$

$$\sigma_{N}^{SI} = f_{N}^{2}\frac{\mu_{N_{\chi}}^{2}}{\pi M_{R}^{4}}, \tag{3.6}$$

respectively. N denotes either a proton p or neutron n and $\mu_{N_{\chi}}^{2} = \frac{m_{\chi}m_{N}}{m_{\chi}+m_{N}}$. For SD interactions, $a_{N} = g_{\chi}^{A}\sum_{q=u,d,s}\Delta q^{N}g_{q}^{A}$ where Δq^{N} quantifies the contribution of light quarks to the nucleon spin. In the case of SI interactions, $f_{p} = g_{\chi}^{V}(g_{\mu}^{V} + 2g_{d}^{V})$ and $f_{n} = g_{\chi}^{V}(2g_{\mu}^{V} + g_{d}^{V})$ are the effective couplings in the case of proton and neutron scattering respectively. The effect of equation 3.6 is that spin-independent scattering receives a coherent enhancement proportional to the square of the nucleus mass. Due to the enhancement, current direct detection constraints are very strong. If vector coupling terms are suppressed, however, the enhancement no longer exists. In this case, direct detection limits are weakened, and collider search limits grow stronger in relation.

The interplay between searches in different detection methods are demonstrated in the ATLAS plots in Figures 3.2a and 3.2b in the case of spin-independent and spin-dependent scattering, respectively. ATLAS results have been recast into bounds on the nucleon scattering cross-section via equations 3.5 and 3.6 for comparison purposes. XENON1T [34], LUX [35], PandaX [36], CRESST-III [37] and DarkSide [38] are direct detection experiments. The first four experiments are liquid xenon time projection chambers (TPCs) housed in deep underground laboratories. CRESST-III [37], a cryogenic detector, and DarkSide [38], a liquid argon TPC using specially sourced argon of very little radioactivity, are extremely sensitive experiments that target low mass particles. 'Dijet' and '$E_{\mathrm{T}}^{\mathrm{miss}}$' represent two different dark matter search strategies at ATLAS.
In the case of spin-independent scattering, the strongest constraints for WIMP masses above 6 GeV is set by direct detection experiments. However, when vector-couplings are suppressed, ATLAS constraints surpass all direct detection constraints.

3.2.4.1 Collider experiments

In *collider experiments* one hopes to create the dark matter particle itself in a collision. The colliding energy needed for dark matter production depends on the unknown mass of the DM particle as well as the mass of the boson mediating the interaction between the

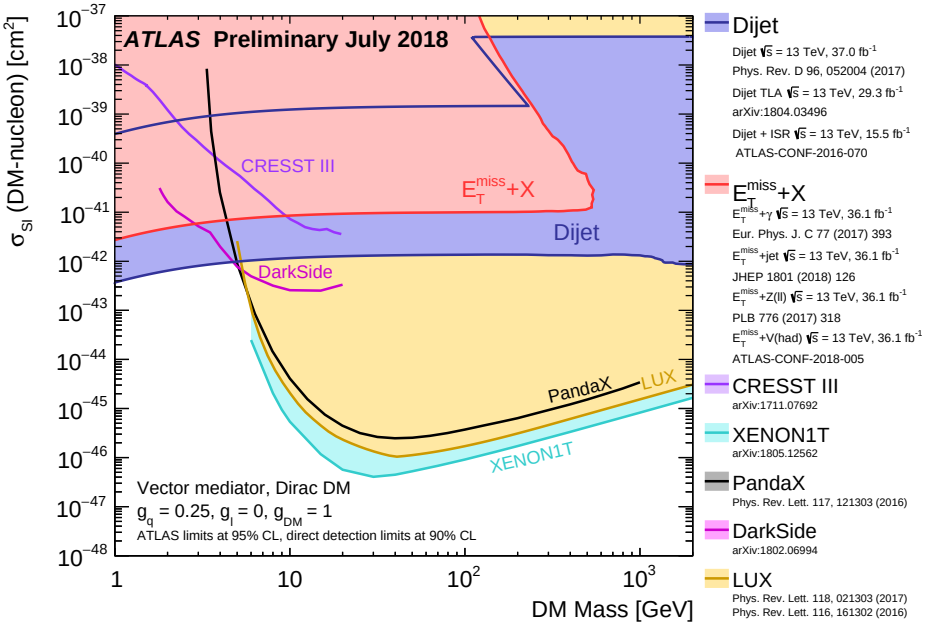

(a) Vector mediator

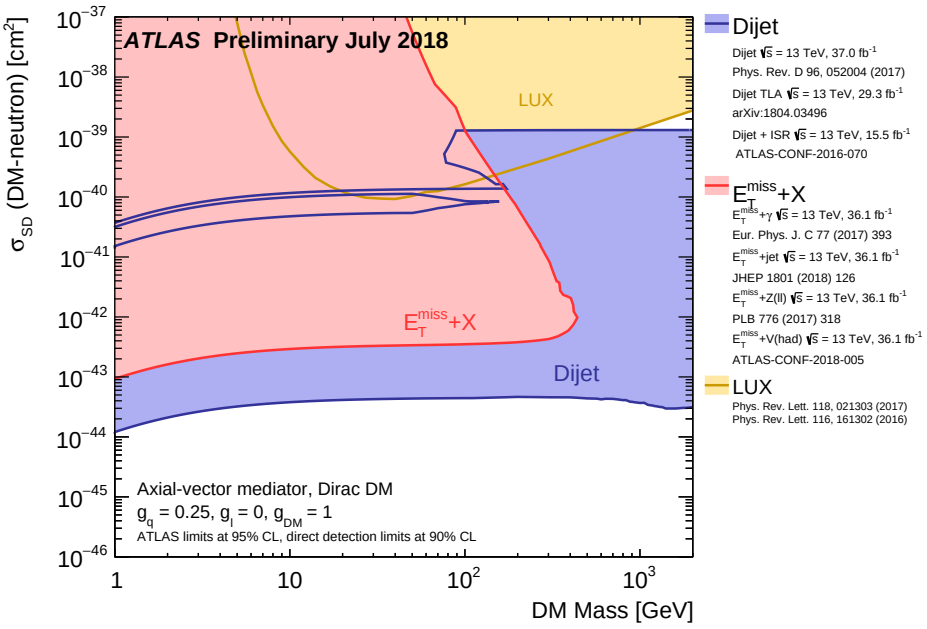

(b) Axial-vector mediator

Figure 3.2: 3.2a: Limits on the *spin-independent* dark matter-proton scattering cross-section, $\sigma^{SI}_{DM-nucleon}$, are shown as a function of dark matter mass from DD and collider searches, assuming $g_q = 0.25$ and $g_{DM} = 0.1$. The '$E_{\mathrm{T}}^{\mathrm{miss}}$' and 'Dijet' bounds represent ATLAS results from two different dark matter search channels. XENON1T, LUX, PandaX, DarkSide and CRESST-III represent direct detection experiments. The two latter experiments focus on low WIMP masses. 3.2b: This time, limits are shown on the *spin-dependent* dark matter-proton scattering cross-section, $\sigma^{SD}_{DM-nucleon}$, as a function of dark matter mass for the same coupling values as in Figure 3.2a. The results of the same ATLAS analyses are recast here. Only the LUX limits are shown for comparison. To note is the stronger constraint on low scattering cross-section in the ATLAS result relative to the DD search if spin-dependent - i.e. axial-vector mediator - couplings are assumed. Taken from [39].

SM particles in the collision and the dark matter particles. Since dark matter interacts very weakly, dark matter is expected to leave no trace in a collider detector. That is why searches focus on a signature that exhibits an energy imbalance in the transverse plane of the detector. An example signature is illustrated in Figure 3.3, in which dark matter particles are pair produced, along with an initial state radiation gluon (a mono-jet) from one of the incoming quarks. The interaction is assumed to be mediated by an axial-vector boson, Z'_A. It is necessary for a dark matter particle to be produced *in association* with a Standard Model particle that deposits its energy in the detector calorimeter, else there is no signal to initiate the recording of the event and also an energy imbalance cannot be measured. The dark matter particle is identified by the missing transverse energy, $E_{\mathrm{T}}^{\mathrm{miss}}$, that is supposed to balance the observed transverse energy. The measurement of

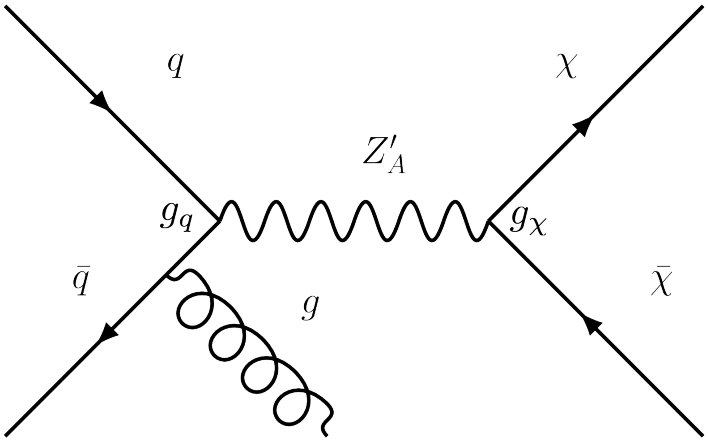

Figure 3.3: An example signature for $E_{\mathrm{T}}^{\mathrm{miss}}$+associated SM particle searches conducted at colliders, in which dark matter particles are pair-produced along with an initial state radiation gluon. The particle mediating the interaction is assumed to be an axial-vector boson, Z'_A. The dark matter particles are expected to leave no measurable trace in the detector. The process can however be identified by the missing transverse energy, $E_{\mathrm{T}}^{\mathrm{miss}}$, counteracting the transverse energy of the associated jet.

$E_{\mathrm{T}}^{\mathrm{miss}}$ with no observed excess over background allows limits to be set on the dark matter mass, the mediator boson mass and couplings, g_q and g_χ, of the mediator boson to the SM quarks and the dark matter particles, respectively.

Another avenue of collider searches is the search for the mediator particle itself, since if the coupling, g_q in Figure 3.3 exists, then the mediator particle is also able to decay to SM particles through the same coupling. An example signature is shown in Figure 3.4, in which the mediator is produced from and decays back to a quark-anti-quark pair. The advantage is that the signature is a visible decay in the form of deposited energy in the detector calorimeter. Since the process, as shown in Figure 3.4, is an s-channel production of the new particle, the invariant mass of the decay products will form a resonance at the mediator mass. The analysis strategy is thus a search for an excess in the mass spectrum of the decay products.

In the following, it is shown how the two different search strategies, dijet and $E_{\mathrm{T}}^{\mathrm{miss}}$ searches, are complimentary in the phase space that they probe.
Figure 3.5 presents combined exclusion limits on the dark matter versus mediator mass plane from several different experiments, assuming a simplified dark matter model with an axial vector mediator. Direct detection limits are based on LUX results from 2013 [35]

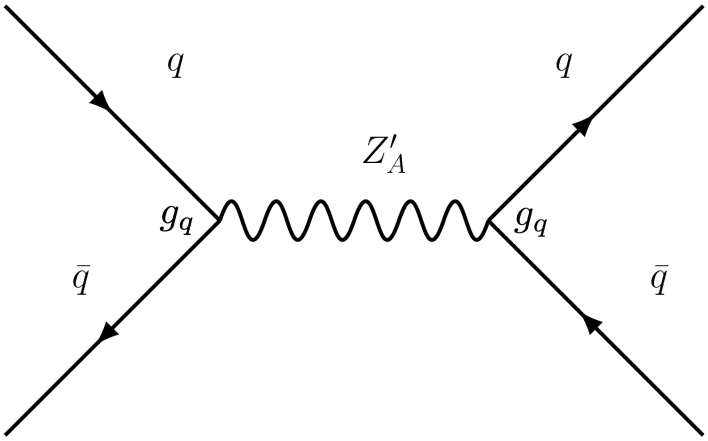

Figure 3.4: An example signature for a direct dark matter mediator search conducted at colliders, in which a dark matter mediator is produced from and decays back into a quark-anti-quark pair. The particle mediating the interaction is assumed to be an axial-vector boson, Z'_A. The production is an s-channel process, thus a new mediator can be identified by a resonance in the invariant mass spectrum of the decay products.

and collider limits are based on results from current and past hadron collider experiments: ATLAS [40] and CMS [41, 42] from the 2012 dataset at the LHC, UA2 [] at the $Sp\bar{p}S$ and CDFII [43] at the Tevatron. The chosen coupling values in this case are $g_q^A = g_\chi^A = 1$, so that the coupling ratio $g_\chi^A/g_q^A = 1$.
The $E_{\mathrm{T}}^{\mathrm{miss}}$ search region (green dashed line) is most sensitive to the region below the $m_\chi = m_R/2$ line, as indicated. For higher dark matter masses, the decay of the mediator to $\chi\bar{\chi}$ is kinematically disallowed, which is why the sensitivity of the search falls off.
In contrast, dijet searches (blue dashed line) are able to probe freely large values of m_χ as they are not limited to kinematically allowed mediator decays to the fermionic DM. $E_{\mathrm{T}}^{\mathrm{miss}}$ exclusion limits fall off sooner along the $m_{Z'}^A$ axis since sufficient energy is required not only to produce the massive mediator but also the radiated jet against which the mediator is required to recoil. Dijet searches horizontally sweep much of the intermediate region, whilst $E_{\mathrm{T}}^{\mathrm{miss}}$ and direct detection searches cover the low mass corner.
It is apparent that the region where dark matter production corresponds to exactly the dark matter relic density indicated by the red line has mostly been excluded. One exception is a narrow region at high mediator masses along the $m_\chi = m_R/2$ line. This feature stems from the fact that once $m_\chi > m_R$ direct annihilation to the dark matter mediator becomes possible. The additional annihilation channel induces a turn-around in the dark matter relic density contour.
Unexcluded phase space that does not result in dark matter overproduction (it lies below the red line) opens up at low mediator masses for dark matter masses above roughly 100 GeV. Bordering this region from above are the dijet collider searches.
It is now worth considering how the exclusion regions shift when different sets of coupling value are assumed. In Figure 3.6 exclusion limits are shown for coupling values $g_q^A = 0.25$ and $g_\chi^A = 1$ so that the coupling ratio $g_\chi^A/g_q^A = 4$. Both the $E_{\mathrm{T}}^{\mathrm{miss}}$ and dijet exclusion limits have weakened due to the weaker coupling to quarks and the subsequent reduced production of the dark matter mediator. The dijet limits fall off at dark matter masses to the left of the $m_\chi = m_R/2$ line, because of an enhanced (reduced) branching ratio to dark matter particles (quarks) relative to Figure 3.5. The dijet exclusion region that remains at low m_χ represents the region that was covered by ATLAS and CMS searches

using data collected in 2012 of an integrated luminosity of 20.3 fb^{-1}. The challenge for Run 2 of the LHC has been to fill the gap at lower mediator masses for low coupling values where limits from previous experiments have weakened.

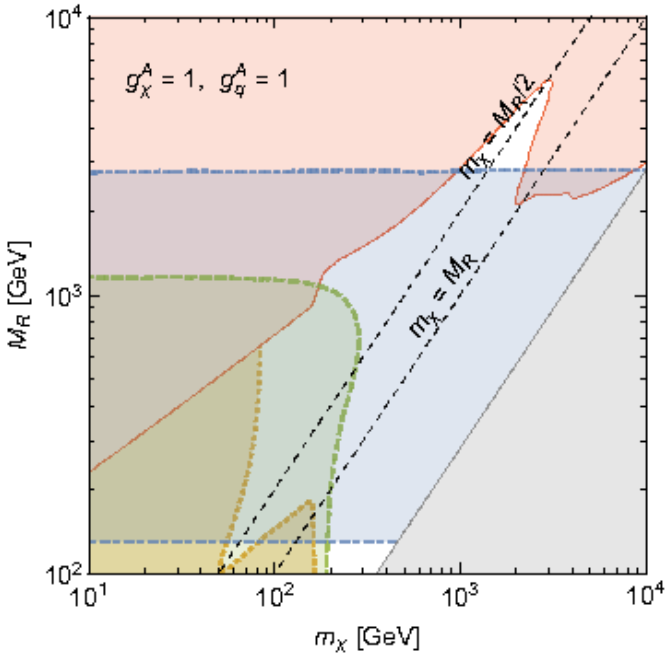

Figure 3.5: Combined exclusion limits (at 95% C.L.) for direct detection (orange dotted line) and collider searches for $E_{\mathrm{T}}^{\mathrm{miss}}$ + jet (green dashed line) and dijet (blue dashed line) final states are shown for a simplified dark matter model with an axial vector mediator and coupling values $g_q = g_\chi = 1$. The red line indicates the contour for the measured dark matter relic density, so that the red region is the excluded region due to dark matter overproduction. The grey area marks the region in which perturbative calculations become invalid. The limits represent the status of experimental constraints in 2015. Taken from [33].

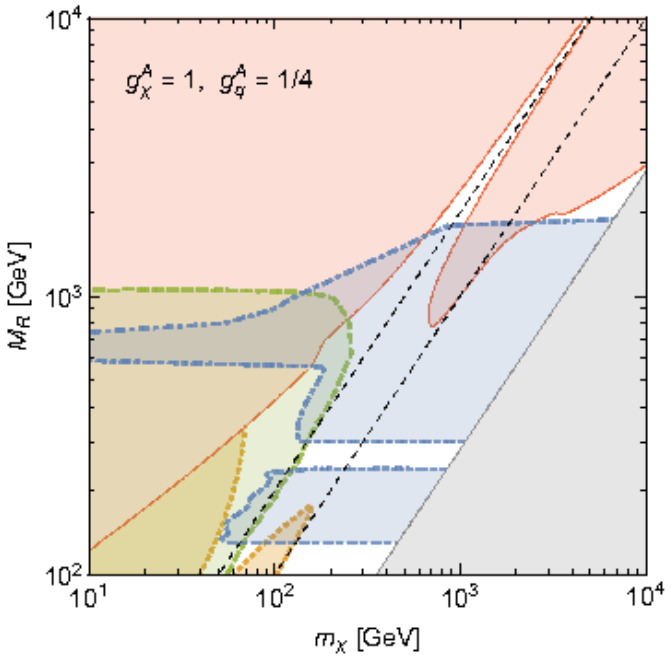

Figure 3.6: Same as in 3.5, but now for coupling values $g_q = 0.25$ and $g_\chi = 1$. Taken from [33].

Chapter 4

The Large Hadron Collider

4.1 Introduction

The construction of the LHC was approved by the CERN council in 1994 and became CERN's operating flagship collider, the highest energy collider in the world, in 2008. It makes use of a tunnel that stretches 100 meters below ground and 27 km in circumference across the border of France and Switzerland [44].

The physics motivations for the construction of the LHC are represented by the experiments located at four points at which the circulating proton beams intersect: ATLAS, ALICE, CMS and LHCb. The two general purpose detectors, ATLAS and CMS, share the same goals, the major ones being: the search for a Higgs Boson candidate and subsequent measurements of its properties for deviations from the predicted particle, precision measurements of the Standard Model, and the search for new particles, from supersymmetric partners to dark matter candidates.
The LHCb (b is for beauty) experiment is a single-arm spectrometer that measures particle collisions in one hemisphere only. The experiment is specialised in studying the fundamental question of the Universe's matter-antimatter asymmetry by studying CP violation in particle processes involving hadrons comprised of b and c quarks. The ALICE (A Large Ion Collider Experiment) detector is designed to study quark-gluon plasma from the collisions of ion particles[1]. The conditions within which the quark-gluon plasma is formed is akin to the state of the universe several milliseconds after the Big Bang.

4.2 The injector chain

In order to achieve the acceleration needed to circulate beams to up to 7 TeV, an injector chain of accelerators is used, a schematic of which is depicted in Figure 4.1. The proton source is a hydrogen tank located at the start of a linear accelarator (LINAC 2). The hydrogen is passed through an electric field so that the electrons are stripped. Radio-frequency cavities are used to accelerate the protons to 50 MeV, which are then filled into the Proton Synchrotron Booster (PSB). Its role is to boost the protons to an

[1] Plasma is a fourth state of matter in which an additional degree of freedom is obtained from the loss of rigidity within the matter. In the case of a quark-gluon plasma, quarks and gluons are asymptotically free, no longer confined in hadrons

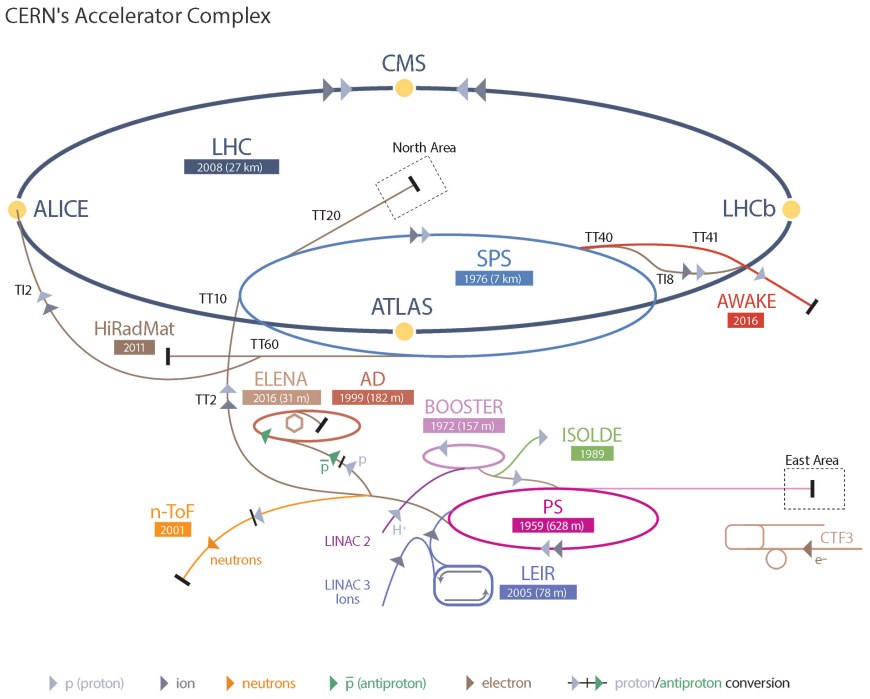

Figure 4.1: The accelerator complex at CERN. The proton beam source for LHC is at LINAC 2. The protons are injected into the PSB, PS and the SPS before they are ramped up to colliding energies in the LHC. Taken from [44].

energy of 1.4 GeV before they are injected into the Proton Synchrotron (PS). The PS ramps the energy up to 25 GeV before injecting the proton beam into the Super Proton Synchrotron. The PS is also the provider of ion beams to fixed target ion experiments. The SPS is used to ramp up the beam energy to 450 GeV for injection into the LHC. It is also the supplier of particle beams to a line of fixed-target clients.

4.3 LHC design

The LHC relies on superconducting magnets, using in total 1232 dipole magnets and 392 quadrupole magnets, which are cooled to a temperature of a couple of Kelvin using superfluid helium. Dipole magnets are used to guide the particles in their circular path and quadrupole magnets focus the beams. In addition there are 16 radio frequency (RF) cavities - chambers that generate a resonating oscillating electromagnetic field to push particles along. Operating at a rate of 400 MHz, they serve to accelerate the beams from injection to collision energies.
The proton beam is not continuous: it is divided into so-called proton bunches with 25 nanosecond spacing. When protons are made to collide at the centre of a detector it is referred to as a bunch crossing.

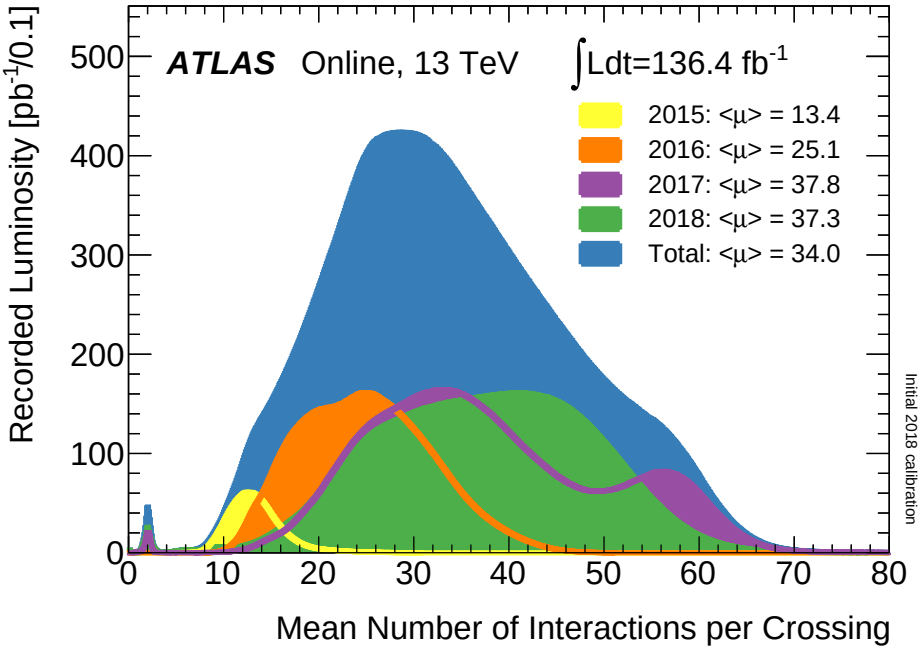

Figure 4.2: The profile of the average number of interactions per bunch crossing at ATLAS is shown for each year of LHC Run 2. Taken from [45].

The LHC design parameters are

- Instantaneous luminosity : 1×10^{34} cm^{-2}s^{-1}
- Number of protons per bunch: 1.1×10^{11}
- Number of proton bunches per beam: 2808
- Proton bunch spacing: 25 ns.

During Run 2 operations the LHC has surpassed its design luminosity and achieved a maximum instantaneous luminosity of 2.06×10^{34}cm^{-2}s^{-1}. This was achieved by honing the parameters that appear in the equation for machine luminosity as follows [44]:

$$L = \frac{N_b n_b f_{rev} \gamma_r}{4\pi \epsilon_n \beta^*} F. \tag{4.1}$$

Here, f_{ref} is the revolution frequency and $\gamma_r = \frac{1}{\sqrt{1-v^2/c^2}}$ the relativistic γ factor of the beam system, and are fixed for the LHC. N_b and n_b refer to the number of protons per bunch and the number of bunches per beam, respectively.
During Run 2, the LHC was operated with the minimum allowable bunch spacing of 25 ns. Collisions occurred at a rate of 40 MHz with the maximum possible number of bunches in the ring. The LHC proceeded to go beyond the design parameters by sharpening the remaining parameters. The normalised transverse emittance, ϵ_n and the beta function, β^*, are both a measure of the beam size. Whilst ϵ quantifies the general transverse beam size, β^* is a measure of the beam 'squeeze' at the interaction point. The final emittance already depends on what occurs in the injector chain. A 'multi-turn injection' into the PSB, whereby protons are 'overlaid' onto a circulating beam at injection, is one of the largest sources of emittance blow-up in the injector chain [46]. A new filling scheme was

commissioned and put in operation in 2017 that effectively reduced the number of turns during the PSB injection, along with the emittance. The β^* was reduced through an improved scheme of the quadrupole magnet configurations [47]. The final parameter, F, is the geometric luminosity reduction factor. It depends on the proton bunch length, the transverse beam size at the interaction point, and the crossing angle between the two beams. With improved knowledge of the beam dynamics, the crossing angle was reduced so that the elongated bunches collide in a closer to head-on manner.

The increased luminosity means there is a higher probability of an interesting event occurring at the centre of a detector. At peak luminosity achieved in Run 2, a peak of ~70 proton collisions occurred per bunch crossing. For experiments this increases the data output per year. At the same time, it poses a significant challenge. The flow of energy from additional interactions(referred to as pile-up) is overlaid on the interaction of interest - the hard scatter - upping the stochastic noise levels. Furthermore, particles from other collisions become a source of background in the attempt to select particles from the hard scatter in data.
Figure 4.2 displays the profile of the mean number of interactions per bunch crossing, or μ, that each year of the LHC Run 2 amounted to. The value for the mean μ is the mean of the poisson distribution of μ for each bunch. The value for μ is calculated from the measured per bunch luminosity,

$$\mu = \frac{\mathcal{L}_{bunch}\sigma_{inelastic}}{f_{rev}}, \tag{4.2}$$

where $\sigma_{inelastic}$ is the total inelastic cross-section for proton-proton collisions, taken as 80 millibarns at 13 TeV, and f_{rev} is the LHC revolution frequency. For the data in Figure 4.2, the per bunch luminosity, $\mathcal{L}_{bunch}$, is measured using luminosity monitors installed upstream from the ATLAS detector.

4.4 Towards High Luminosity LHC

For the next two decades, a series of upgrades aim to exploit the LHC machine fully [48]. The machine will come into operation again at the maximum possible centre-of-mass energy of 14 TeV in 2021. It is foreseen that the instantaneous luminosity will be pushed to its limit in two phases whilst keeping the beam energies constant. The first phase or Run 3 of the LHC to commence in 2021 will have an instantaneous luminosity of 3.0×10^{34} cm^{-2}s^{-1}. The number of collisions per beam crossing will average at 60 and experiments will collect data amounting to approximately 300 fb^{-1}. In the second phase, planned for 2026, the luminosity will be ramped up to $5 - 7.0 \times 10^{34}$ cm^{-2}s^{-1} to produce on the order of 3000 fb^{-1}. Around 200 proton collisions per bunch crossing is expected. This requires a series of upgrades to detector hardware and trigger system in order to cope with the intensifying collision environment.

Chapter 5

The ATLAS experiment

The ATLAS detector [49] is a general-purpose detector located at one of the interaction points on the LHC ring, 100 metres below ground. The physics goals of the experiment include the search for the Higgs Boson and measurement of its properties, precision measurements of the Standard Model and searches for undiscovered particles in the new energy regime of the LHC or in rare processes. The ATLAS experiment is a large collaboration of over 3000 scientists who together represent 38 different countries [50].

5.1 The detector

The ATLAS detector follows the typical hermetic detector design: it is composed in a layered manner of several different types of sub-detectors, namely a tracker, calorimeter and muon spectrometer, each making use of a different technology to measure particle properties.

A cut-away view of the ATLAS detector is shown in Figure 5.1. Its general shape is that of a barrel, 44 m in length, with two end-caps on either end, 25 m in diameter. The beam pipe runs along the z-axis of the cylindrical geometry. The various sub-detectors are labelled in the figure. Starting at a radius of 33 mm around the beam axis lies the Inner Detector (ID). This component is used for the measurement of charged particle tracks within $|\eta| < 2.5$ with high precision as the particles pass through. The magnetic field of a superconducting solenoid is used to bend the particle trajectories. Outside of the solenoid lie the calorimetry components. This is a 'destructive' detector component as it absorbs outgoing particles in order to measure their energies. The calorimetry system covers a wide η range, up to $|\eta| < 4.9$ and is therefore also sensitive to forward radiation. The interaction rate of muons and neutrinos is small enough for these two particle types to pass through the calorimeters unhindered. The muon spectrometer comprises the final layer, measuring charged particles that are not absorbed in the calorimeters, namely muons. A part of the muon detection system are three large superconducting toroids. There is a large space between the magnets and the muon spectrometer within which the paths of muons are greatly bent by the toroidal magnetic field. Both the calorimeter and muon system have coarse-granularity components for triggering.

The following detector coordinate directions are applied: the z–axis points along the beam axis; x- and y-axes define a plane perpendicular to it, where the positive x direction

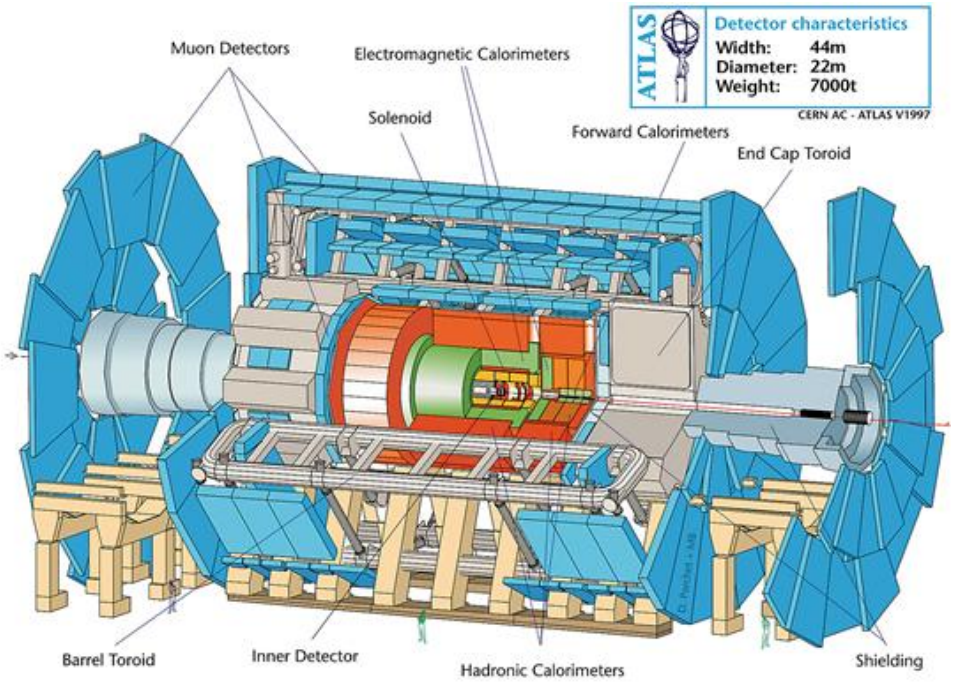

Figure 5.1: A cut-away view of the ATLAS detector is shown. The detector follows the modern general-purpose detector design. It consists of several subcomponents which form concentric rings or end-caps centred at the interaction point: a tracking system, a magnetic solenoid, electromagnetic and hadronic calorimeter system, a muon spectrometer and magnetic toroids. The close-to 4π detector coverage makes the measurement of non-interacting particles possible through the measurement of an energy imbalance.

is defined as from the interaction point to the centre of the ring and the positive y direction as upwards; ϕ and θ are the azimuthal and polar angle from the x–axis and positive z–axis, respectively. It is more common for the angle in θ to be expressed in terms of pseudorapidity, $\eta = -\ln[\tan(\theta/2)]$. This is a useful spatial coordinate as it approximates to a particle's rapidity, y, for light particles. The rapidity difference between two particles is Lorentz invariant under transformations along the longitudinal axis. For low masses, a Taylor expansion for rapidity results in the following relation

$$y = \eta - \frac{\cos\theta}{2}\left(\frac{m}{p_T}\right)^2 \tag{5.1}$$

For particles where $p_T >> m$ then, the measurement of $\Delta\eta$ for two light particles is approximately Δy and so independent of any initial longitudinal boost. The value for η ranges from 0, perpendicular to the beam axis, to $\pm\infty$ along the beam axis. Detection of particles extends down to roughly $\eta = \pm 4.9$. The close-to full 4π coverage is an important feature of a general-purpose detector as it makes the identification of particles such as neutrinos that do not interact with the detector itself possible by measuring the energy imbalance between the detector hemispheres.
A commonly used measurement of distance is ΔR, the distance in the $\eta - \phi$ plane defined as $\sqrt{\Delta\eta^2 + \Delta\phi^2}$. Another oft-measured quantity is a particle's transverse momentum. This is because most collisions will result in proton-proton diffractive scattering, the outgoing particles travelling at small angles to the beam axis. Generally events of interest result from the head-on collision of two partons within the colliding protons, interacting on average at rest in the lab frame. The colliding energy is transformed into new particles which can carry momenta perpendicular to the beam. Events of interest are thus char-

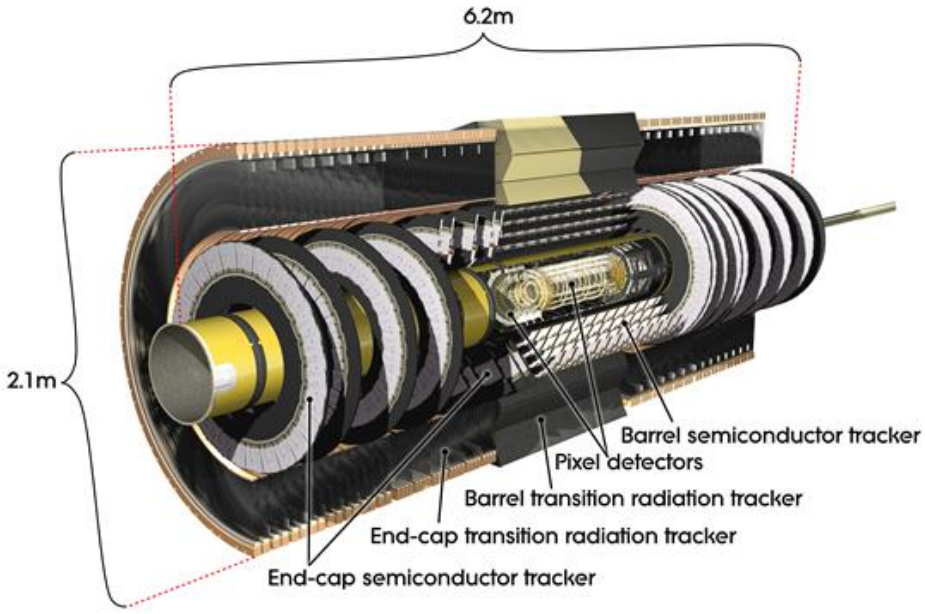

Figure 5.2: The ATLAS inner detector is a tracking system that makes use of pixel and silicon microstrip trackers and straw tubes of a transition radiation tracker in order to measure momenta and vertices of charged particle tracks with high precision. Taken from [49].

acterised by a large amount of transverse momentum rather than the total momentum. Due to conservation of energy, energy is expected to be balanced in the transverse plane. *Missing transverse energy*, denoted $E_{\mathrm{T}}^{\mathrm{miss}}$ and defined as the negative sum of p_T of all particles in the event, is used as a measurement for invisible particles.

5.1.1 The inner detector

The Inner Detector (ID), a 1.1 m in radius and 6.2 m in length sub-detector, is dedicated to reconstructing charged particle tracks with $p_T > 400$ MeV up to $|\eta| = 2.5$. The different components that make up the ID are shown in Figure 5.2. It employs a pixel detector for the very inner layer, a silicon microstrip tracker (SCT) at larger radii, and gaseous straw tubes in a transition gap radiation tracker (TRT) in the outermost ID layer. The ID is surrounded by a 2 Tesla superconducting magnetic solenoid in which charged particle trajectories are made to bend, so that the particles charge and momentum can be extracted from the degree and direction of curvature.
The pixel detector is comprised of three layers of high-granularity superconducting silicon pixels and constructed as close as possible around the beam axis. The high granularity and close proximity is required in order to be able to extrapolate to the collision vertex with as little ambiguity as possible. Additionally it is required for the measurement of secondary vertices of heavy (bottom or charm) flavoured hadrons which have longer lifetimes relative to the lighter quark flavours and so are expected to decay with a delay in the very inner region of the ID. The presence of a large amount of pile-up vertices impinges on the performance of the ID to precisely separate vertices. Therefore before the start of Run 2, a new first pixel layer was inserted, the *insertable B-layer* (IBL), with a mean radius of 33 mm.
The SCT is comprised of four layers of silicon microstrips. Both components consist

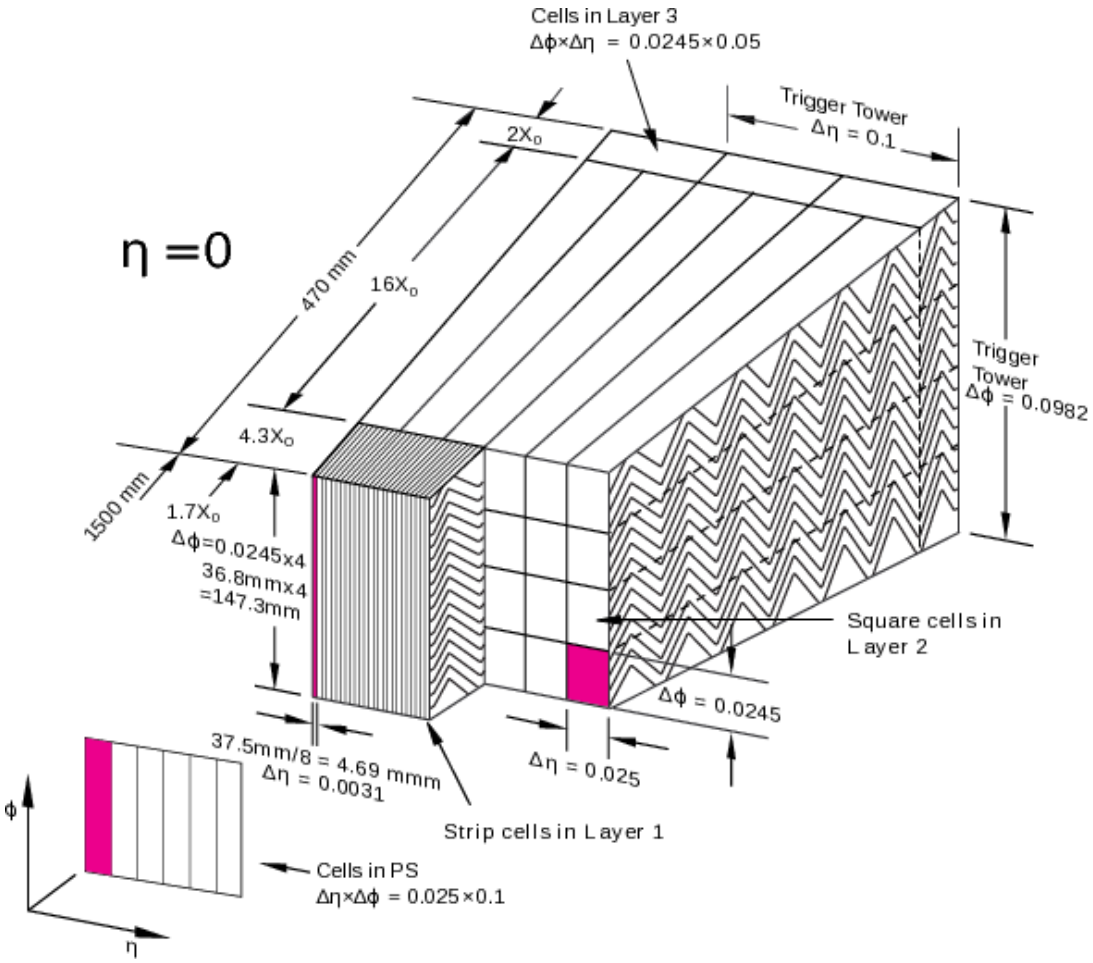

Figure 5.3: A schematic of the sampling layers in the EM barrel calorimeter at $\eta = 0$, displaying the accordion structure and granularity. The first sampling layer has a granularity of $\Delta\eta \times \Delta\phi = 0.0031 \times 0.1$. The second sampling layer is where most of the energy is deposited and therefore has a fine granularity of $\Delta\eta \times \Delta\phi = 0.025 \times 0.025$, while the third sampling layer has a slightly reduced granularity. Trigger towers are used to sample calorimeter signals during first-stage triggering with a coarse granularity of $\Delta\eta \times \Delta\phi = 0.1 \times 0.1$. Taken from [49].

of a barrel made up of concentric cylinders and rings in the end-cap region, orientated perpendicular to the beam axis.
The TRT makes use of 4 mm in diameter straw tubes. These are arranged parallel to the beam axis in the barrel region (in roughly 36 layers) and radially in wheels in the end-cap region which extends down to $|\eta| = 2$. The measurements performed by the TRT are of lower precision and only provide information in the radial and azimuthal direction. However, due to the greater number of layers, it receives more hits than the inner region, offering a more continuous track measurement and enhances the identification of electrons and positrons.

5.1.2 The calorimeter

ATLAS makes use of sampling calorimetry, in which absorber material initiates a particle shower for incident particles, and active material generates light or charge signals from the shower and sends as output an electronic signal proportional to the incident energy. An electromagnetic (EM) calorimeter is used to capture electromagnetic showers initi-

ated by incident electrons and photons. A hadronic calorimeter is used to fully capture hadronic showers initiated by strongly-interacting particles such as fragmenting quarks and pions. It is located behind the EM calorimeter, as such showers are typically initiated in the EM layers before penetrating beyond the depth of the EM calorimeter.
Hadronic showers have an electromagnetic and non-electromagnetic component, where the latter does not contribute all of its energy to the signal. The invisible energy mainly consists of the released binding energies of nucleons. As a result, the calorimeter response differs between electromagnetic and hadronic shower components. The measured energy of hadronic showers fluctuates depending on the fractional contribution of each component and falls short of the true energy owing to the invisible energy component. The non-compensation is corrected for in the calibration of hadronic jets.

The calorimeter system is located between the inner detector and the muon detector and makes use of two types of calorimeters, a liquid argon and a tile calorimeter, that together cover the region $\eta < 4.9$. It has in total approximately 100 000 cells.

The inner barrel region covering $|\eta| < 1.4$ and an end-cap region extending further to $1.3 < |\eta| < 3.2$ is covered by the liquid argon (LAr) electromagnetic calorimeter, which makes use of liquid argon as the active material and lead as the absorbing material. It is finely segmented for precise measurements of electron and photon energies.
Its construction makes use of an accordion design in which the electrodes and absorber material are arranged in an accordion ("zig-zag") shape, resulting in an unbroken surface all the way along the azimuthal direction.This can be seen in Figure 5.3.
The central region is barrel-shaped but split into two identical half-barrels, leaving a gap of a few millimetres between them. An EM wheel in the end-cap consists of a bigger and smaller wheel, which cover the region in $1.4 < |\eta| < 2.5$ and $2.5 < |\eta| < 3.2$, respectively. The barrel and the larger EM wheel each have three sampling layers, whilst the small EM wheel has been limited to two. A schematic of the three sampling layers of the EM barrel calorimeter at $\eta = 0$ is displayed in Figure 5.3. The sampling layers are of varying granularity and are finest in the central η region. The finest granularity is $\Delta\eta \times \Delta\phi = 0.025 \times 0.025$ in the middle calorimeter layer at $|\eta| < 1.8$, where most of the energy is deposited.
Due to the amount of material in front of the barrel - such as the solenoid - a presampling layer is placed in front of the inner surface of the calorimeter in order to correct for the energy that is absorbed before it reaches the barrel. The granularity of the triggering system of the calorimeter is also indicated in Figure 5.3. One trigger channel is known as a trigger tower. It has a minimum granularity of $\Delta\eta \times \Delta\phi = 0.1 \times 0.1$ in the central region.

The tile calorimeter covers the outer barrel ($|\eta| < 1.0$) and extended barrel region ($0.8 < |\eta| < 1.7$). It measures hadronic energy using the emitted light from scintillation tiles and uses steel as the absorbing material. Its role is to measure the energies of more centrally placed hadronic jets with a minimum granularity of 0.1×0.1 in $\Delta\eta \times \Delta\phi$.

LAr calorimetry is further utlised for hadronic measurements in the outer end-cap and forward regions. The hadronic LAr calorimeter consists of one wheel in each end-cap, comprised of parallel copper plates and together covering the region $1.4 < |\eta| < 3$. Since hadronic shower shapes are wider, the hadronic component has a coarser granularity than the LAr EM component, the finest being 0.1×0.1. Finally, there is the forward

calorimeter that covers the very forward and highest-radiation region $3 < |\eta| < 4.8$. The absorber mediums are copper and tungsten. Tungsten was chosen for its high density as it limits the size of showers and reduces leakage into surrounding calorimeter components.

5.1.3 The muon spectrometer

The muon spectrometer measures coincident hits from particles that are curved within the field of the toroidal magnet. The spectrometer consists of a barrel that extends to $|\eta| = 1.05$ and two end-caps that cover the range $1.05 < |\eta| < 2.7$. Muon momenta are measured with precision in three layers of monitored drift tubes (MDT). Additionally an inner layer exists that is equipped with cathode strip chambers (CSC), which each consist of four sensitive layers. Three doublet layers of resistive plate chambers (RPC) covering $|\eta| < 1.05$ together with one triplet layer and two doublet layers of thin gap chambers (TPC) covering $1.05 < |\eta| < 2.4$ are used for triggering and the measurement of η and ϕ coordinates.

5.2 ATLAS Computing

5.2.1 Data reconstruction

ATLAS data reconstruction and data analysis relies on a set of high energy physics-specific tools and object classes defined within the Athena [51] software framework[1]. The Athena framework is common to all stages of data reconstruction, namely: in simulated reconstruction, offline reconstruction as well as the reconstruction of online data in the software-based High-Level Trigger of the ATLAS detector.

The reconstruction of data occurs on the LHC computing grid [53]. The grid infrastructure consists of several *tiers*. Data recorded by the ATLAS detector is first streamed to *Tier0*, the computing centre at CERN. The raw data undergoes first-pass processing to produce analysable data and is also stored on magnetic tape. Duplicated raw and processed data is distributed to several[2] *Tier1* sites around the world, that offer the facilities to store and reprocess all data for recalibration. *Tier2* sites are universities or other scientific institutes that provide computing power for tasks such as data analysis, analysis-specific production of datasets of reduced size, and production of simulated data.

5.2.2 Simulation

ATLAS physics analyses rely heavily on simulation in order to model well-known Standard Model signals as well as hypothetical new physics processes to be used in data calibration and optimisation of analysis selections.

[1] It is based on the high energy physics GAUDI [52] framework first developed within the LHCb experiment.

[2] The grid consists of 13 Tier1 sites at the time of writing [54]

Processes are generated separately, so that different *samples* exist for each. There are several sequential production steps that go into the generation of a sample [55]:

1. Generation of the hard scatter event.
2. Simulation of initial and final state radiation, the underlying event, showering and hadronisation of coloured particles.
3. Simulation of particle interactions (hits) with a simulated detector.
4. Simulation of signal digitisation (digitised hits) to mimic detector read-out.
5. Simulation, digitisation and overlay of pile-up events.

An event generator takes as input the matrix element of the process of interest and a parton distribution function to generate the incoming and outgoing particles of the hard scatter event at tree-level. It additionally deals with the prompt decays of all unstable outgoing particles, where prompt is taken to mean particle lifetimes of $c\tau < 10$ mm. Simulations of additional interactions, step 2), is performed by the same or different generator.
ATLAS makes use of the GEANT4 [56] package, which simulates the propagation of particles through an accurately simulated ATLAS detector. In step 4), detector electronics are modelled as signals are converted from analogue to digital. The digitised output is of the same format as that of real data, which allows the running of the same data processing and reconstruction algorithms on both types of samples.
Pile-up simulation accounts for both in- (of the same bunch crossing) and out-of-time (neighbouring bunch crossings) pile-up. In-time pile-up is modelled by generating single, double and non-diffractive proton interactions using the Monte Carlo generator, Pythia [57], and subsequently passing them through the ATLAS detector simulation. The detector hits of numerous such interactions are overlaid with those of the generated event of interest to match the instantaneous luminosity in data. Out-of-time pile-up accounts for signals from previous or subsequent bunch crossings that affect the current bunch crossing. The signal integration time varies for each sub-detector thus such effects are sub-detector specific[3]. The overlay of out-of-time pile-up for the event of interest proceeds similarly to in-time-pile-up overlay, in addition taking into account the bunch crossing duration in which various sub-detector components remain sensitive to a signal.

5.3 Data object definitions

The following section define the reconstructed objects that are used in the analysis of data in subsequent chapters, namely, the definition of primary tracks and vertices (section 5.3.1) and jets (section 5.3.2). These objects are reconstructed in recorded data using full detector information. Objects that are reconstructed at the level of the trigger are described in their respective chapters. However, in most cases the reconstruction algorithms are the same.

[3]For the pixel detector signals affect only 2 neighbouring bunch crossings, whilst signals in the monitored drift tubes in the muon spectrometer span 32 bunch crossing in either direction.

5.3.1 Primary tracks and vertices

Primary tracks are the trajectory of charged primary particles. A primary particle is defined as a particle with a mean lifetime greater than 3×10^{-11} s that is either produced directly from the proton-proton interaction or from the decay of particles with a mean lifetime less than 3×10^{-11} s. Primary vertices are the position measurements of proton-proton interactions, reconstructed using primary tracks.

5.3.1.1 Track reconstruction

Track finding [58] begins in the silicon detector by clustering hits in the pixel and silicon strip sensors. The clusters represent 3 dimensional position measurements, also referred to as space-points. Sets of three space-points are used to seed the first track finding process. Track finding is an iterative procedure: remaining space-points in pixel and SCT layers that are compatible with the track trajectory are iteratively incorporated into the track measurement and the trajectory is remeasured. Ambigous cases in which clusters are found to be used for multiple track candidates, are resolved by computing a track score and giving preference to tracks that score more highly. The score is computed from the χ^2 of the track fit, the number of holes, the intrinsic resolution of the cluster depending on the detector region, and the logarithm of the track momentum where more weight is given to high momentum tracks. A hole is a hit that is predicted by the track trajectory but is not measured.
Track candidates are further required to have a track $p_T > 400$ MeV, ≤ 2 pixel and SCT holes, ≤ 1 pixel hole, $|d_0^{BL}| < 2.0$ mm and $|z_0^{BL} sin\theta| < 3.0$ mm, where d_0^{BL} and z_0^{BL} are the transverse and longitudinal impact parameters with respect to the beam spot[4], and θ is the track's polar angle to the beam line. Track candidates built from silicon detector hits are extrapolated to the TRT layers where TRT hits are associated to the track without modifications to the original track. Finally, a high-resolution track fit using all available information is performed to obtain the final track parameters and uncertainties. During the high-resolution fit, a neural network is employed to refine the measurement of cluster positions.

The average efficiency of primary track reconstruction is 80% for track p_T below 10 GeV, and 90% above [59]. Reconstruction efficiencies range from 85% for central tracks ($|\eta| < 1.0$) to 70% for very forward tracks ($2.0 < |\eta| < 2.4$).

5.3.1.2 Vertex reconstruction

Only good-quality tracks are used in the reconstruction of primary vertices [60], in which a good quality is defined based on the track impact parameters, their uncertainties and a minimum(maximum) number of required hits(holes) in the SCT or pixel layers.

The procedure in the reconstruction of vertices is seeding, vertex position determination and track compatibility checks.
The d-coordinate of the first seed position is taken from the beam spot centre and the z-coordinate as the mode of all z-coordinates of tracks at the point of closest approach to

[4]The beam spot refers to the transverse position of the LHC beams with respect to the centre of the detector.

the beam spot centre. Fits are applied to the seed and track hits in an iterative procedure: after each fit, the least compatible tracks are down-weighted and a new best vertex position computed. As a result, after some iterations, the least compatible tracks will have low weights and little influence over the fit, whilst highly compatible tracks have a large weight and so lead the fit. At the end of the iteration procedure, incompatible tracks are removed from the vertex and made available for the next vertex reconstruction in the event. The beam spot is determined from the spatial distribution of reconstructed primary vertices over many events, in which no beam spot constraints are imposed.

The event of interested is usually taken to be the process that emerged from the vertex with the highest $\Sigma_k(p_T^{trk})^2$. The vertex/event is referred to as the hard scatter.

5.3.2 Jets

5.3.2.1 Jet reconstruction

Two algorithms are used in the ATLAS jet reconstruction procedure: *topo-clustering* [61], based on the clustering of calorimeter cells, and *anti-kT jet reconstruction*, defined in [62] and implemented in [63], using topo-clusters as input.

Topo-clustering The topo-cluster algorithm clusters cells according to whether the significance of the cell energy is above a configured threshold, Γ:

$$\Gamma < \zeta_{cell} = |{}^{E_{cell}}/_{\sigma_{noise,cell}}|. \tag{5.2}$$

The significance of the cell energy, ζ_{cell}, is computed as the ratio of the cell energy and the electronic and pile-up noise $\sigma_{cell} = \sqrt{(\sigma^2_{electronic}) + \left(\sigma^2_{pile-up}\right)}$. A seed becomes the core of the cluster by requiring $\zeta_{cell} > \Gamma_{primary}$. Cells neighbouring the cluster in all three dimensions for which $\zeta^{EM}_{cell} > \Gamma_{secondary}$ are added to the growing cluster. Finally, any directly neighbouring cells for which $\zeta_{cell} > \Gamma_{tertiary}$ are added as well. The default configuration for ATLAS is $\Gamma_{primary} = 4$, $\Gamma_{secondary} = 2$ and $\Gamma_{tertiary} = 0$. In this way, a topo-cluster consists of a core of highly significant energy surrounded by cell energies ebbing away into the calorimeter noise, matching the expected signal of a particle within a hadronic shower.

Anti-k_T jet reconstruction The final jet is reconstructed out of topo-clusters. In the following, "particle" can refer to a topo-cluster or a proto-jet. The jet reconstruction algorithm relies on two distance measurements,

$$d_{ij} = \min(k^{2p}_{Ti}, k^{2p}_{Tj})\frac{\Delta^2_{ij}}{R^2}, \tag{5.3}$$

and

$$d_{iB} = k^{2p}_{Tj}, \tag{5.4}$$

where i and j are particles (proto-jet, topo-cluster), B is the beam, $\Delta_{ij} = \Delta y_{ij} + \Delta\phi_{ij}$ (distance measurement in the rapidity$-\phi$ plane), and k_t is the transverse momentum of the particle. When $p = -1$ in the equation above, the algorithm becomes the anti-k_T algorithm, which is commonly used in ATLAS. The algorithm identifies the smallest distance d_{ij} or d_{ib}. If $d_{ij} < d_{ib}$, meaning the smallest distance is between particles i and j,

these entities are combined to a new proto-jet; if $d_{ij} > d_{ib}$, meaning the smallest distance is between the beam and particle i, then particle i is defined as a jet and removed from the list of possible jet constituents in further jet reconstruction in the event. Since $p < 0$, the minimum distance is determined by the 'hardest' (highest transverse momentum) particle and the separation Δ_{ij}. Softer particles will in this way cluster to harder particles before clustering to each other. The radius parameter, R, determines the size of the area around a proto-jet within which particles will be viable to be clustered to the jet, since for any separation greater than R, d_{iB} becomes the minimum distance.

The anti-k_T algorithm carries two attributes that are important for jet reconstruction algorithms: it is *collinear* and *infrared safe*. The former means the final jet is unaffected in the case of a hard parton splitting in two, whilst the latter means the final jet is not drastically changed by soft particle radiation.
Jets are commonly reconstructed with a radius parameter $R = 0.4$ in ATLAS, although the usage of larger radius jets (known as large-R jets) of radius parameter $R = 1.0$ has also become common [64]. They are used in searches where Standard Model decay products have acquired very high transverse energy, either from an initial Lorentz boost or possibly from the large mass difference between decay products and a massive resonance. In this case, the decay angle relative to the momentum direction is small enough for the jets to appear merged as one large jet.

5.3.2.2 Jet track attributes

Primary tracks are used to define track-based properties of jets, such as the number or sum of momenta of tracks that point to a jet. The attributes are used in the calibration of jet energy and direction, as well as for the selection of jets from the hard scatter vertex. Jet track attributes are defined using only tracks that are associated to the same primary vertex. Therefore, the computation of jet track attributes requires tracks to be associated to vertices as well as jets.

Association of tracks to vertices The association of tracks to vertices is performed by requiring a small difference between the longitudinal coordinates, z_0, of the vertex and track and beam spot centre, as well as by requiring the track to have a small transverse impact parameter, d_0. Tracks that have been used in the reconstruction of the vertex are automatically associated to the vertex. For any remaining tracks, the requirements are

$$|(z_0^{trk} - z_0^{vtx} - z_0^{beamspot})\sin(\theta)| < 3\text{mm and} \quad (5.5)$$

$$|(d_0^{trk})| < 2\text{mm} \quad (5.6)$$

If multiple vertices are matched, the track is associated to the vertex with the smallest distance in z.

Ghost association of tracks to jets Tracks become a part of the jet *during* jet reconstruction: They are simply added as a second type of constituent in the anti-k_T algorithm. However, tracks are not allowed to contribute to the jet energy - this would be double-counting the energy, since tracks and topo-clusters measure energy of the same initial particle. For this reason, the track p_T is first scaled down to next-to-zero before they are added to the collection of constituents. They are thus referred to as ghost-associated tracks (ghost tracks).

5.3.2.3 Jet calibration

Jets are calibrated in order to scale them from the electromagnetic to hadronic level, and correct for energy dependencies on jet reconstruction algorithms, jet fragmentation, detector features and additional proton-proton interactions from the same and neighbouring bunch crossings [65].
The calibration chain consists of MC-based and in situ corrections. MC-based calibration correct energies to that of simulated stable particles found within a jet. Several MC generators are used to simulate dijet interactions with full detector simulation and the difference between the modelling outcomes is taken as a systematic uncertainty. The corrections are applied in MC and data.
In situ-based calibration further measures any differences in response between MC and data and corrects for this in data only.

The first calibration step is an *origin correction*, in which the jet four-momentum is recalculated based on the position of the primary vertex instead of the centre of the detector. The improvement on the η reoslution is from 0.06 to 0.045 for jet p_T of 20 GeV, and 0.03 to 0.006 for 200 GeV.
Jets are next corrected for pile-up effects based on factors of the following equation

$$p_T^{jet,corr} = p_T^{jet} - \rho A - \alpha \times (NPV - 1) - \beta \times (\mu) \tag{5.7}$$

The second term is a *jet area-based correction*, where ρ is the median of the event's jet energy density, calculated from the distribution of p_T^{jet}/A of all k_T jets[5] within $|\eta| < 2$. It provides a measure of the pile-up energy density. The applied correction is the density multiplied by the jet's area.
The jet-area based correction mainly adjusts for the central region. A residual dependence on pile-up remains particularly for the forward region which carries a much higher energy occupancy. The third and fourth terms are η-dependent *residual pile-up corrections*. They each separately correct for effects from in-time and out-of-time pile-up that are respectively correlated to the number of primary vertices and μ. The coefficients, α/β, are the slopes of the correlation between the jet p_T offset and NPV/μ.

The size of the jet area-, NPV- and μ-based corrections in equation 5.7 are shown in Figures 5.4a and 5.4b, where the right plot is averaged over μ and the left plot is averaged over NPV. The size of the corrections to p_T in the central region, $0 < |\eta| < 2.5$, are largely NPV-dependent. After the jet-area based calibration, the NPV-dependent residual offset is between $0.05 \times (NPV - 1)$ and $0.15 \times (NPV - 1)$. For an NPV range between 20 and 35 (typical for Run 2 conditions), the offset ranges from 1 GeV up to 5 GeV. The forward region, $|\eta| > 2.5$, shows both considerable NPV- and μ- dependent offsets of roughly $0.3 \times (NPV - 1)$ and $-0.3 \times (\mu)$. This results in partial cancellations of offsets but can result in adjustments of as large as 9 GeV for forward jets.

[5]The k_T algorithm corresponds to equation 5.3 where $p = 1$. The k_T algorithm is used in this case as it is sensitive to soft particles.

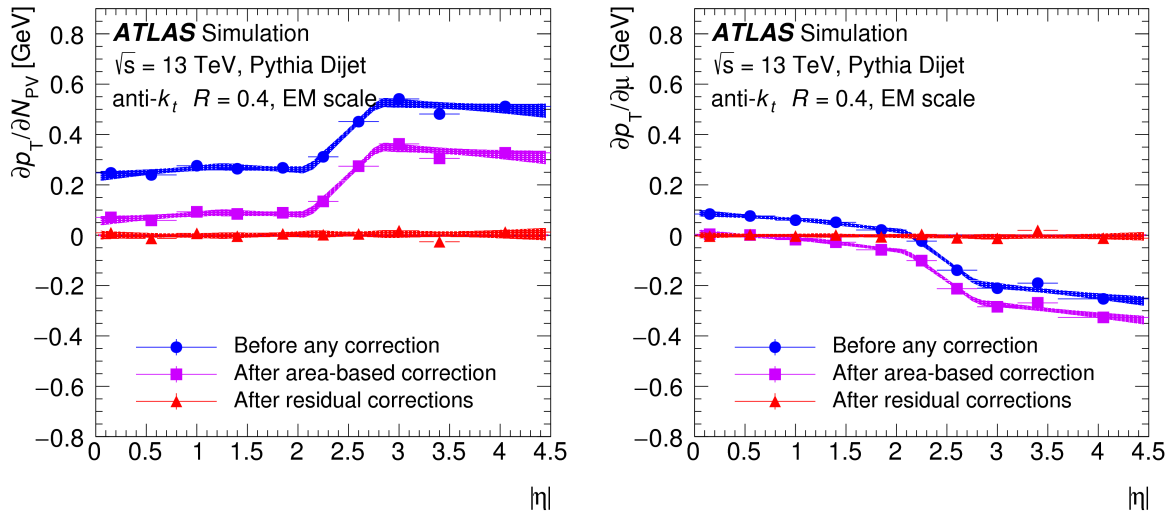

(a) NPV (b) μ

Figure 5.4: The dependence of EM-scale jet p_T on (a) NPV averaged over μ and (b) μ averaged over NPV as a function of $|\eta|$ for $p_T^{truth} = 25$ GeV is shown. The dependence on η is shown prior to pile-up corrections (blue circle), after the area-based correction (violet square), and after the residual correction (red triangle) are applied. The shaded bands represent the 68% confidence intervals of the linear fits in 4 regions of $|\eta|$. Taken from [65].

An *absolute MC-based calibration* correction scales the jet energy from the electromagnetic to particle level after parton fragmentation The average energy response is taken as the mean of a Gaussian fit applied to distributions of $\frac{E_{reco}}{E_{truth}}$ for different ranges of E_{truth} and η. The correction is derived by parameterising the average energy response as a function of E_{reco} and using the inverse of the average energy response. For the central region alone, the level of calibration varies from 55% at $E_{truth} = 30$ GeV to 20% at $E_{truth} = 1.2$ TeV.

A *global sequential calibration (GSC)* corrects for the fact that the calorimeter energy response varies depending on jet shower shape features and distribution of energy. The energy response depends on the jet p_T as well as whether the jet is quark- or gluon-initiated. Whilst a gluon-initiated jet emits a lot of softer particles and shower widely, a quark-initiated jet will have a narrow shape and contain few particles. The following jet attributes are used to reduce the dependence of the energy response on jet features:

- f_{Tile0}: the fraction of jet energy deposited in the first Tile calorimeter layer.
- f_{EM3}: the fraction of jet energy deposited in the last layer of the LAr calorimeter.
- n_{trk}: The number of tracks with $p_T > 1$ GeV ghost-associated to a jet.
- $\mathcal{W}_{trk} = \frac{\sum(\Delta R(jet,track)p_T^{trk})}{n_{trk}\sum p_T^{trk}}$: The average distance in $\eta - \phi$ between the jet axis and each track with $p_T > 1$ GeV, where each distance is weighted by the track p_T.
- $n_{segments}$: The number of muon track segments that are ghost-associated with the jet.

The first two variables, f_{Tile0} and f_{EM3}, correct for variations in the energy sampling depending on the jet's longitudinal shape. The variables, n_{trk} and $\mathcal{W}_{trk}$ are a measure of the jet constituent multiplicity and the jet's transverse shape, respectively, thus offering a good discrimination between gluon- and quark-initiated jets. The variable $n_{segments}$ accounts for leaked energy beyond the calorimeter detector in the case of highly energetic jets. Each correction is applied sequentially for ranges in jet p_T (in the case of $n_{segments}$, for ranges in total jet energy) and η. Whilst the average jet energy is left unchanged, the energy resolution is improved with each step. The dependence on jet variables is reduced to 2% after the GSC.

An in situ calibration is applied in two steps.
An *eta intercalibration* adjusts the energy scale of forward jets to that of well-measured central jets, ensuring a uniform energy response across $|\eta|$. A *residual in situ calibration* accounts for any residual effects arising from an imperfect detector by correcting for response differences between central jets and well-measured objects.
For the eta intercalibration, a dataset of dijet events is used to derive the energy response of jets in the forward region ($0.8 < |\eta| < 4.5$) relative to the energy response for central jets ($|\eta| < 0.8$) by measuring the energy in dijet systems as function of jet p_T and η. Jets in a dijet system are expected to be balanced. The jet response of the forward region is obtained by measuring the average asymmetry in p_T between the forward and central jet.

In the residual in situ calibration three different well-balanced topologies are employed, each suited for a different range in jet p_T. The topologies that are used are $Z(\rightarrow e^+e^-/\mu^+\mu^-) + jet$, $\gamma + jet$ and dijet production (where one jet is a well-measured high p_T jet). Corrections in overlapping ranges in p_T are combined using an interpolation of second-order polynomial splines[6].
The in situ calibration is at a level of 4% at 20 GeV and 2% at 2 TeV.

The final total systematic uncertainty on the jet energy scale varies from 1% for jets at 200 GeV to 4.5% for jets below 25 GeV.

5.3.3 Pile-up jets

QCD jets emerging from other proton interactions within the same event are a source of background and are suppressed by making use of track-based jet attributes that are a measure of the likely origin of a jet as pile-up discriminants.

5.3.3.1 Pile-up discriminants

One expects all ghost tracks in a jet that has emerged from the hard scatter event, to be associated to the hard scatter vertex. However, in busy events, a lot of soft tracks emerging from pile-up vertices will find their way into the hard scatter jet area. In order to measure the likelihood that a jet emerged from the hard scatter vertex, one can measure the *jet vertex fraction*, defined as the fraction of tracks within a jet associated to the hard scatter vertex:

$$\mathrm{JVF} = \frac{\sum_j p_T^{trk_j}(PV_0)}{\sum_N p_T^{trk_N}} \tag{5.8}$$

[6] piece-wise polynomial fits of the calibration factors as function of p_T

where tracks have a minimum p_T of 500 MeV, j runs over all hard scatter vertex-associated ghost tracks and N runs over all ghost tracks belonging to the jet.
However, the fraction is highly dependent on the amount of pile-up in an event, since the average scalar sum of pile-up track p_T grows linearly with the number of pile-up vertices. Consequently, the denominator becomes larger with respect to the numerator. For Run 2, a more useful quantity is therefore calculated, the corrected JVF:

$$\text{JVFCorr} = \frac{\sum_j p_T^{trk_j}(PV_0)}{\sum_j p_T^{trk_j}(PV_0) + \frac{\sum_{n\geq 1}\sum_l p_T^{trk_l}(PV_m)}{(k \cdot n_{trk}^{PU})}} \tag{5.9}$$

where l runs over ghost tracks associated to pile-up vertex m, $k = 0.01$ is the correction constant and n_{trk}^{PU} is the total number of tracks associated to a pile-up vertex and with $p_T < 30000$ MeV. The factor $k \cdot n_{trk}^{PU}$ is the correction factor. It serves to reduce the denominator in proportion to the pile-up in the event. As a result the corrected JVF (JVFCorr) is a stable measure of the jet vertex fraction.

In addition to JVFCorr, another variable that is useful for the identification of hard scatter jets is the ratio of the sum in p_T of the hard scatter-associated ghost tracks in a jet and the jet p_T:

$$R_{p_T} = \frac{\Sigma_j p_T^{trk_j}}{p_T^{jet}}. \tag{5.10}$$

Since it does not include pile-up tracks in the computation, it also has little dependence on the amount of pile-up.

5.3.3.2 The Jet Vertex Tagger

The values mentioned above are shown to have discriminatory power between hard scatter and pile-up jets. For ATLAS Run 2, the final pile-up jet rejection is performed by combining the pile-up independent variables, JVFCorr and $\mathrm{R_{p_T}}$, in a *jet-vertex-tagger* (JVT) [66]. The JVT is a discriminant that is constructed from a k-nearest neighbour (k-NN) algorithm based on the correlation between JVFCorr and $\mathrm{R_{p_T}}$. Training samples from a Monte Carlo dataset of $Z \rightarrow \mu^+\mu^- + jet$ events, containing the true origin information on jets, are used to fill the JVFCorr-$\mathrm{R_{p_T}}$ plane with data points from signal (hard scatter jets) and background (pile-up jets). The algorithm uses the concept of *nearest neighbour* signal and background points to compute the hard scatter likelihood for a query point - the jet's JVFCorr and $\mathrm{R_{p_T}}$ - in the two dimensional plane. In this case, the nearest neighbours are defined as the 100 nearest training points to the query point, using simply the Euclidean distance.
The likelihood is determined by computing the probability

$$P_{HS} = \frac{k_{HS}}{k_{HS} + k_{PU}} \tag{5.11}$$

where k_{HS} and k_{PU} are the number of hard scatter and pile-up training points of the first 100 nearest neighbours.

Figure 5.5 presents the resulting JVT likelihood as a finely-binned two-dimensional histogram. The jet JVT is obtained from a bilinear interpolation of the histogram bin

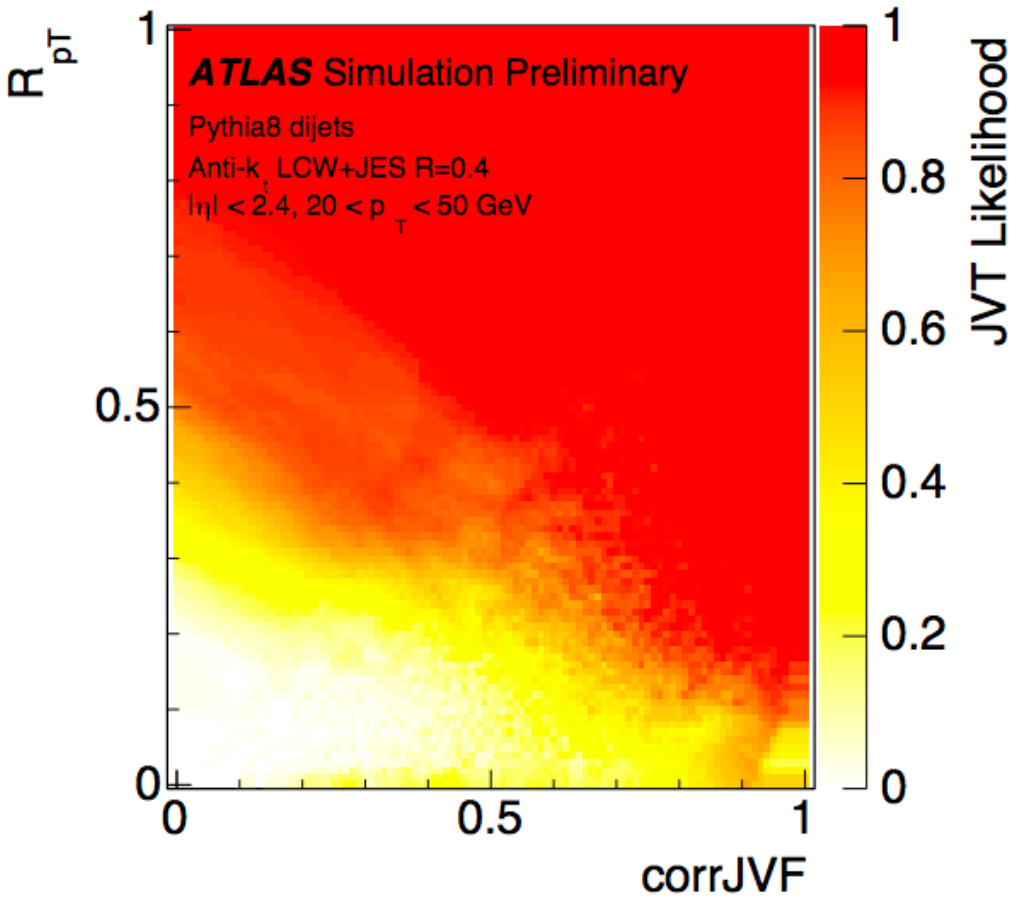

Figure 5.5: The JVT likelihood histogram is shown as a function of JVFCorr and R_{pT}. The likelihood is derived using jets with $20 < p_T < 50$ GeV and $|\eta| < 2.4$ from fully simulated events containing $Z \to \mu^+\mu^-$+ radiated jets. Further details are provided in the text. Taken from [66].

content.

The jet-vertex-tagger has been used to reject jets with a p_T below 60 GeV or 120 GeV, where the latter is the updated recommendation for remaining Run 2 analyses.
An average hard scatter jet acceptance efficiency working point of 92% - the nominal working point - with an accompanying fake rates of 3% is achieved for jets in reconstructed data [66]. The efficiency varies with jet p_T, increasing from 92% for a jet p_T of 20 to 30 GeV, to 96% for a jet p_T of 50 to 60 GeV, with a similar increase in fake rate.

Chapter 6

The ATLAS trigger system

In particle physics experiments, a trigger initiates the recording of data of a physics event and a data accqusition system serves to collect and manage the event data. In the ATLAS experiment, the trigger serves to select a subset of *interesting* events to record out of an initial $\mathcal{O}$(million) proton collisions that take place per second. The trigger-level data is a collection of various types of signals from different sub-detector components, which need to be integrated in order for the trigger to do a collective analysis of the event. This leads to a trigger and data acquisition system (TDAQ) that is highly complex.
Several factors limit the rate at which ATLAS is able to record data. One is storage limitations. The typical size of a recorded event at ATLAS is 2.5 MB. If all data were recorded for every filled bunch crossing, the volume of data would be $\mathcal{O}$(1000) PB per day for one experiment, which is an infeasible number. Another limitation is the available bandwidth that constrains the total amount of data that can be transferred off-site to Tier-0 and processed. A last limitation is the processing time of the TDAQ system, which is constrained by the size of buffers for temporary data storage during online processing. Limited by these constraints, the ATLAS experiment utilises a 2-level trigger system in which the initial 40 MHz collision rate is first reduced to a 100 kHZ rate by the Level-1 (L1) trigger, and then reduced to the final recording rate of 1.5 kHz by the High-Level Trigger (HLT). The L1 trigger relies on reduced granularity information from a subset of sub-detectors, which allows the system to process every collision that occurs, whilst the HLT can afford to make a more refined selection on the reduced rate. A schematic of the ATLAS trigger and data acquisition system is shown in Figure 6.1.

6.1 The Level-1 trigger

The L1 trigger system is required to process signals rapidly in order to trigger at a 40 MHz input rate. It is thus mainly hardware based and housed in a service cavern underground next to the experimental hall of the ATLAS detector, which minimises the transfer time of data to the trigger system.

The L1 trigger has two components: The Level-1 Calorimeter (L1Calo) trigger [68] and the Level-1 Muon (L1Muon) trigger [69]. As the names suggest, L1Calo processes data received from the calorimeter channels, and L1Muon processes data from the muon spectrometer. L1Calo and L1Muon reconstruct Level-1 *trigger objects* (TOBs). TOBs are data objects that are created online from energy or momentum measurements of detector components and identified as a type of particle with a measured momentum-energy four-

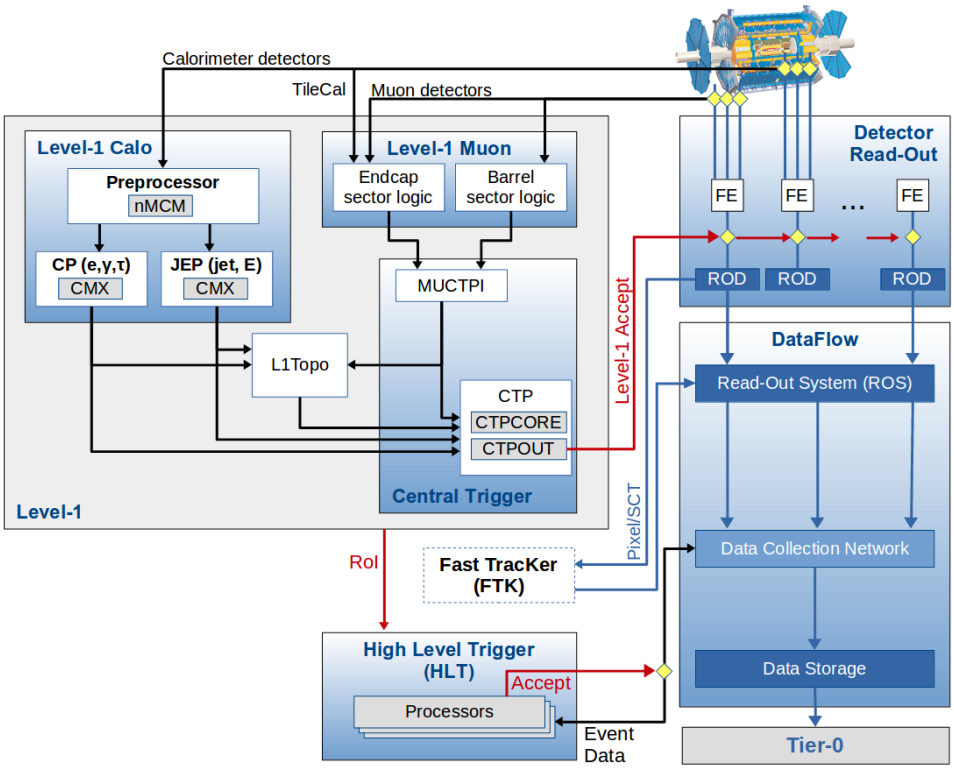

Figure 6.1: The components of the ATLAS trigger and data acquisition system are shown, and referred to in the text. Taken from [67]

vector. After reconstruction, the multiplicity of TOBs above predefined energy thresholds is sent to the Central Trigger Processor (CTP). The CTP compares the TOB multiplicity with items in a trigger menu (described in section 6.4) and issues an *L1-Accept* (L1A) in the case of a match.

An Level-1 topological trigger (L1Topo) receives input from L1Calo and L1Muon and runs algorithms based on topological information of TOBs. For example, it can compute the difference in η between the two most energetic L1Calo jets in the event. This gives the Level-1 trigger the ability to reject background events based on topological information. L1Topo was commissioned during Run 2.

During Level-1 processing, the complete event information from sub-detectors is buffered in the detector electronic front-end boards (FEBs). The FEB buffer size limits the Level-1 decision time to 2.5 μs. Once an L1A has been issued, the full event data is transferred from the FEBs to read-out driver (ROD) buffers. Event data is then transferred via read-out links to the data acquisition system's read-out system (ROS) where it is buffered and made accessible to the HLT. In addition, the HLT receives so-called *regions of interests* (RoIs) from the Level-1 system. RoIs are the $\eta - \phi$ coordinates, particle type and passed thresholds of TOBs identified by the Level-1 systems.

6.1.1 The Level-1 Muon Trigger

The Level-1 Muon system uses dedicated resistive plate chambers (covering the barrel region) and thin gap chambers (covering the endcap region) with a fast readout to identify muons. The schematic in 6.2 illustrates the triggering logic for the barrel. Coincident

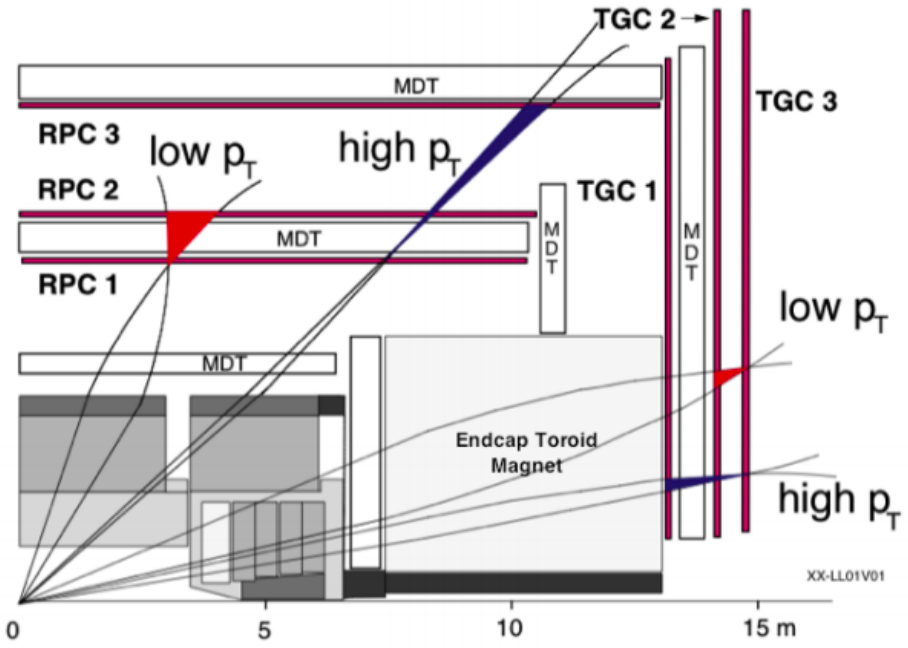

Figure 6.2: The Level-1 Muon system's triggering logic relies on three resistive plate chamber (RPC) layers in the central region and thin gap chambers in the endcap region. Hits in the first or third RPC/TPC layers coincident with hits in the pivot plane are required to lie within the triangular window of a settable width around the imaginary track of a "muon with infinite momentum". Taken from [70].

hits are identified as candidate tracks. An imaginary straight line, representing a muon of infinite momentum, is extrapolated from the collision point to the coincident hit in the pivot plane in the second layer. A triangular coincidence window extending either down to the first layer, for a low p_T regime, or up to the third layer, for a high p_T regime, represents a threshold on the maximum accepted deviation of hits in the respective layers from the straight line. Muon tracks at increasing p_T result in less curvature, therefore the window width defines the minimum p_T that a muon may have in order to pass through the window. There are six settable window width thresholds that define the level-1 muon p_T thresholds.

6.1.2 The Level-1 Calorimeter Trigger

The L1Calo trigger identifies electrons/photons, tau leptons and jets, as well as a significant amount of $E_{\mathrm{T}}^{\mathrm{miss}}$ and ΣE_T.
The input to L1Calo are *trigger tower* (TT) signals, which are the analogue signal sum of all calorimeter cells in an $\eta \times \phi$ window. The TT signals are summed within the calorimeter front-end boards for the electromagnetic and hadronic calorimeter layers separately. In the barrel region, trigger tower signals are the sum of an area of 0.1×0.1 in $\eta \times \phi$ across a calorimeter layer. In the forward region, ($|\eta| > 3.4$), the trigger tower area is defined more coarsely, 0.4×0.4 in $\eta \times \phi$. There are 7168 trigger tower channels in total.

The calculation of the transverse energy of each TT is performed by the L1Calo preprocessor modules (PPMs) [71]. The PPMs correct for the pedestal, enhance the signal-to-noise ratio, identify the peak of the pulse and finally compute the TT trans-

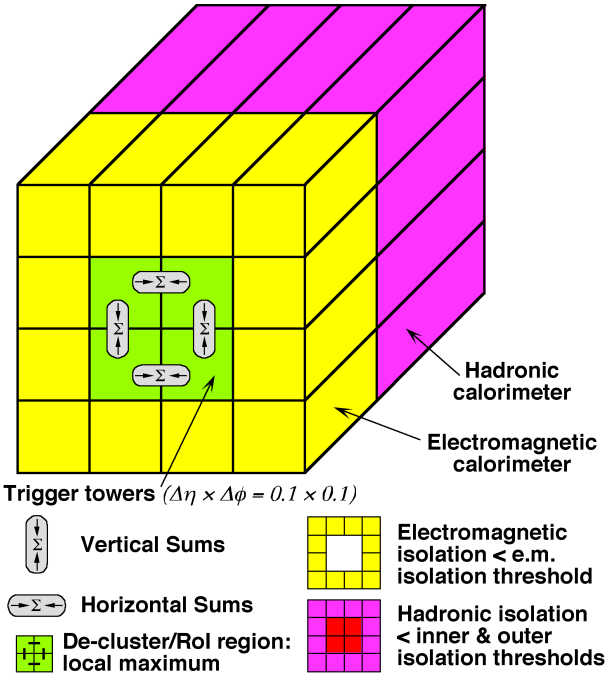

Figure 6.3: An illustration of the Level-1 clustering logic for the identification of electrons/photons and hadronic τs. Each block represents a trigger tower. Electrons/photons are identified by a minimum energy threshold requirement on 1x2 trigger tower elements in the electromagnetic core and maximum energy thresholds in the electromagnetic and hadronic isolation rings and hadronic core. For τ identification, the 2x2 trigger tower element summed energies in the hadronic core are added to the 1x2 trigger tower elements of the electromagnetic core.

verse energy. The tasks of the PPMs are extensively described in Chapter 7.

The preprocessors send the transverse energies of each TT to the Cluster Processor (CP) and the Jet/Energy-sum Processor (JEP), which are responsible for constructing L1Calo TOBs.

The CP reconstructs Level-1 electrons/photons[1] and hadronically decaying tau leptons from TTs within $|\eta| < 2.5$. Electrons/photons are expected to deposit most of their energy in the electromagnetic layer in a narrowed cone, whilst a hadronically decaying tau lepton is expected to extend also to the hadronic layer. The schematic in 6.3 demonstrates the geometry out of which TOBs are identified, where each square represents the area of a trigger tower. TOBs are identified with a *sliding window algorithm*, in which the summed energies of TTs are computed within a window that is incrementally moved across η and ϕ. An electron/photon TOB is identified if the sum of energy in a 1x2 TT window size in the electromagnetic inner core (green area) exceeds a programmable minimum EM energy threshold *and* if the sum of energy in the electromagnetic and hadronic isolation rings (yellow and pink area) do not exceed programmable maximum energy (isolation) thresholds. In addition, a veto on the transverse energy sum of the hadronic core (red area) can be required. A tau TOB is identified in a similar way, but the energy sums within a 2x2 TT window in the hadronic inner core are added to the 1x2 TT elements of the electromagnetic core.

[1]There is no way to distinguish electrons and photons at Level-1, thus they are treated as the same particle.

The JEP identifies hadronic jets, which are expected to deposit energy in the electromagnetic as well as hadronic layer into a larger cone compared to electromagnetic and hadronic tau objects. Jets are reconstructed from *Jet Elements*, which are the transverse energy sums of TTs in the EM or the HAD layer covering an area of 0.2x0.2 in $\eta - \phi$ for $|\eta| < 4.9$. A sliding window algorithm computes the energy sum for window sizes of either 2x2, 3x3 and 4x4 Jet Elements. A jet TOB is identified if the energy sum of Jet Elements within the window exceeds a programmable minimum jet energy threshold. The JEP additionally computes the total energy, ΣE_T and missing transverse energy, $E_{\mathrm{T}}^{\mathrm{miss}}$. The $\Sigma E_T$is computed as the scalar energy sum of all Jet Elements. The computation of $E_{\mathrm{T}}^{\mathrm{miss}}$ is the magnitude of the vector sum of all Jet Element energies:

$$\text{L1 } E_{\mathrm{T}}^{\mathrm{miss}} = \sqrt{\sum((E_T^{JE}\cos\phi^{JE})^2 + (E_T^{JE}\sin\phi^{JE})^2)}, \tag{6.1}$$

where E_T^{JE} is the energy measured for a Jet Element.

Finally, the TOBs determined by the CP and JEP are collected by the Cluster Merger Modules, which transmit the identified TOBs to L1Topo, and the TOB multiplicity to the CTP.

6.2 The High-Level Trigger

The High-Level Trigger (HLT) [72] is a computing farm located directly above ground from the detector hall. The HLT uses full-granularity measurements from the detector to reconstruct and identify electrons, taus, muons, jets, b-tagged jets, $E_{\mathrm{T}}^{\mathrm{miss}}$ and ΣE_T. The aim of the HLT is to reconstruct trigger objects that are as similar as possible to their offline counterparts. Offline-like algorithms are therefore made use of in the final identification as much as possible within the CPU constraints of the TDAQ.
HLT reconstruction generally relies on a fast reconstruction and a precision reconstruction stage. The former uses simplified algorithms to analyse information in the RoIs of the TOBs identified by the L1 trigger, and acts as seed to the latter stage, which uses offline-like algorithms for the final particle identification. Since HLT algorithms are rather intricate compared to the Level-1 algorithms, a description of each online particle identification method is spared. Instead focus is given on online tracking and jet reconstruction.

6.2.1 Online tracking

ID tracking information is necessary in order to identify electrons, muons, taus and b-jets. However, full-event track reconstruction is not possible due to the many inner detector read-out channels and the combinatoric nature of track finding algorithms, making track reconstruction too CPU-intensive. Instead, the HLT performs limited track reconstruction by employing two-stage reconstruction within RoIs. The two stages are: *Fast tracking*[2] and *precision tracking*. *Fast tracking* uses pattern-recognition algorithms designed solely for the trigger to supply fast but crudely reconstructed tracks within an RoI. The track hits and space points from the fast tracking algorithm are used as seeds to *precision tracking*, which runs offline-like track reconstruction.

[2]Not to be confused with tracks reconstruction by the Fast Tracker

For example, in the identification of electrons, fast tracking is used at first stage to identify track candidates that are successfully matched to electron clusters. Electron candidates may fail first stage requirements based on unsuccessful matches as well as the cluster shape. Precision tracks are used at second stage as an input to an offline-like multivariate likelihood discriminant.
Online b-tagging of jets uses 2-stage RoI tracking to reconstruct the hard scatter vertex and perform tracking for reconstructed jets of a minimum p_T. First, the fast track finder reconstructs > 5 GeV tracks within a narrow RoI of all jets above 35 GeV, to use in the reconstruction of the primary vertex. This is used to define an RoI for jets that is centred on the primary vertex position. Fast tracking followed by precision tracking is performed within the RoI for jets above a certain p_T to reconstruct 1 GeV tracks used in the identification of a secondary vertex.

Despite the use of limited tracking, still 40% of the HLT processing time is spent on inner detector track reconstruction, whilst 35% and 15% is spent on the muon spectrometer and calorimeter reconstruction respectively [72].

6.2.2 Online jet reconstruction

Jets, as well as $E_{\mathrm{T}}^{\mathrm{miss}}$ and ΣE_T as they use as input summed transverse energies of either jets or topo-cluster, are the only trigger objects that are reconstructed using the full detector calorimeter information without the use of first and second stage reconstruction.

The same offline algorithms are used in the reconstruction of online jets, namely the topo-clustering and the anti-k_T algorithms that have been described in section 5.3.2. Topo-clustering is most commonly performed for the central region only, $0 < \eta < 3.2$, or within the forward region, $\eta > 3.2$, for central and forward jet triggers, respectively. Online jet energies are calibrated prior to the trigger decision to bring them close to the same energy scale as offline jets. The only difference between offline and online jets prior to calibration is the noise term used in the topo-clustering algorithm. In the online case, it is retrieved from a database, whilst in the offline case, it is recalibrated depending on the running conditions during data taking.
No track reconstruction is performed for jets, due to the large number of jets in an event. As a result the online calibration does not include an origin correction, pile-up residual correction and the offline global sequential calibration which each rely on track or vertex information. The offline calibration factors for the jet-area pile-up correction, the JES correction, the GSC and the in-situ correction are used. The GSC calibration is only based on the first two variables, namely f_{LAr3} and f_{Tile0}.

6.3 Data transfer

Once the HLT has accepted an event, the full event information is stored on server nodes of the DAQ system onsite. The final storage location however is at the CERN storage facility (Tier-0). Data is transferred on a 1.5 GB/s line. It takes several hours for the data transfer to take place, and typically ends after an LHC proton fill has been depleted. Once data arrives at Tier-0, it is converted from bytestream to reconstructed analysable data by performing full-event reconstruction.

6.4 The trigger menu

The trigger menu essentially determines the physics that ATLAS records. It consists of *trigger chains*, which are a combination of Level-1 and HLT trigger elements. An example trigger chain is HLT_4j45_L1_3J15. This sets a trigger that records events in which at least 3 L1 jets with a transverse energy above 15 GeV were identified by the L1 system and a minimum of 4 HLT jets with transverse energies above 45 GeV were identified by the HLT system for the same event. The L1_3J15 trigger element is also termed the *seed* for the HLT_4j45 trigger, because it is only upon the Level-1 accept of a L1_3J15 that the requirements of the HLT_4j45 are tested.

The trigger menu is said to be dynamical because the rate of trigger chains can be enabled, disabled or changed on the fly during an LHC fill. It is possible to change the rate of a trigger by applying a 'prescale' to it. The prescale is a number, P_i, that dictates that only one of every P_i events accepted by trigger i is transferred to the next level. A trigger can be prescaled at Level-1 or HLT. For example, for a typical run in ATLAS in 2017, the HLT_4j45_L1_3J15 trigger chain had an L1 prescale of 170 and an HLT prescale of 13. This means that only for 1 out of every 170 L1_3J15 triggered events, the detector event information is sent on to the HLT; and similarly, 1 out of every 13 events triggered by HLT_4j45 and seeded by the prescaled L1_3J15, is recorded to offline.

6.5 Data recording streams

A recording stream is a way of separating data according to how it needs to be processed and what it is ultimately used for. The trigger menu defines the recording streams for each trigger. A graph of the trigger rates per stream is shown in Figure 6.4 during a typical LHC fill. The largest recording stream is the main physics stream. This records data that will be used for physics analyses. The triggers that feed this stream are generally unprescaled (a prescale of 1) so that physics analyses make full use of the LHC integrated luminosity. There is also a dedicated stream for B-physics triggers. The data recorded in this stream is stored on disk onsite and processed only when Tier-0 computing time is not in high demand. This has enabled the recording of low p_T muon events specific to B-physics but at the cost of a delayed analysis of the data, that can only occur after the end of Run 2.
The express stream syphons a small rate of physics events to Tier-0 where they are rapidly processed and validated for data quality checks during run-time. Streams classified as "other physics" are for example the *zero-bias* stream. The stream is filled with randomly selected events for filled bunch crossings. Such events are useful for the analysis of in-time and out-of-time pile-up.
There exists also streams unrelated to physics, such as the detector calibration and monitoring streams that record a subset of detector information used to monitor the detector state and update detector calibrations during run-time.
The stream labelled as "Trigger-Level Analysis" is a physics-dedicated light-weight stream for the recording of partial event information and closely relates to the work in this thesis. It is described in full in Chapter 9. The exponential decrease of the instantaneous luminosity during an LHC fill is apparent by the slope in rate. The occasional *increase* in rate is due to the changing of prescales to make full use of the recording bandwidth.

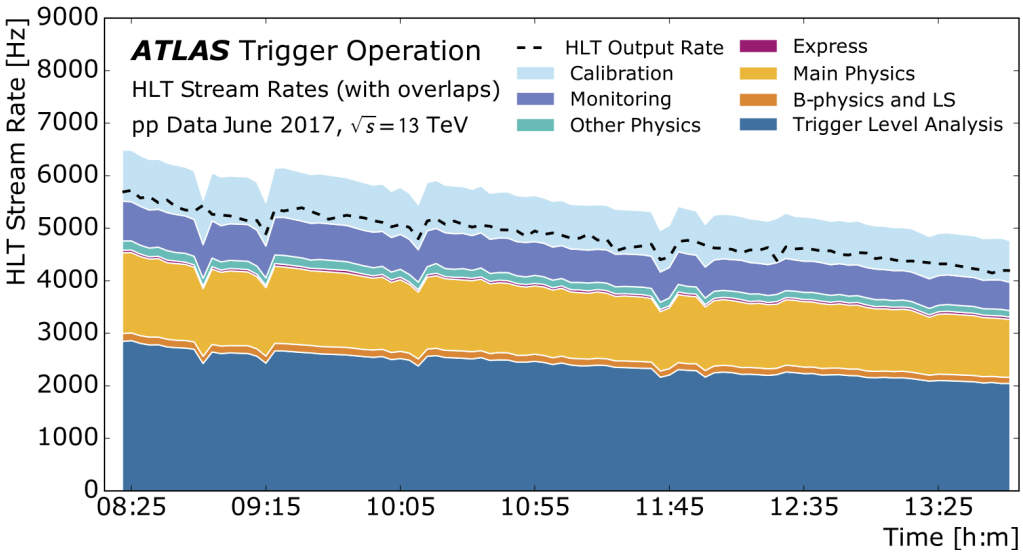

Figure 6.4: The HLT trigger rates of the various ATLAS recording streams is shown as a function of time during an LHC fill in 2017. The dashed black line is the total HLT output rate (excluding overlapping events recorded into different streams). The "Express" and "Calibration" streams record events for monitoring and calibration of the detector. The "Other Physics" stream is used for special physics-related purposes. The "B-Physics and Light States" stream is separate to the main physics stream as the events are stored onsite. The "Trigger-Level Analysis" stream is an analysis-dedicated stream that records trigger-objects. More information is provided in the text. Taken from [73].

6.6 Trigger rates

The LHC instantaneous luminosity has increased from $0.8 \times 10^{34}\,\mathrm{cm^2 s^{-1}}$ in Run 1 to $2 \times 10^{34}\,\mathrm{cm^2 s^{-1}}$ in Run 2. This increases the probability of high energy events occuring in a bunch crossing and thus increases the trigger rates.
Trigger rates of main physics triggers are regulated by increasing the energy threshold of triggers. This decreases the rate as the energy spectrum of particles created in collisions is an exponentially falling distribution. Prescales would be an alternative method of regulating rates, however the primary focus of LHC experiments is the probing of new high energy regions that have for the first time been opened up through the unprecedented colliding energies of the LHC. The sensitivity to the new high energy region is only limited by the integrated luminosity, which would be reduced by prescales.

The rising thresholds have affected types of analyses to different degrees. The thresholds of electron and muon triggers have been kept to approximately 25 GeV throughout Run 2, whilst the lowest threshold for single jet triggers has been gradually raised from 360 to 420 GeV. This is because the agenda of the collaboration has been designed to focus on precision measurements of electroweak processes such as leptonic Z, W, top and Higgs decay reconstruction [72]. The decision is motivated by the fact that the background rate for electroweak processes is much lower at a hadron collider compared to the high rate of jet production. This is illustrated in Figure 6.6, which presents the cross-sections of prominent processes at LHC energies (green vertical lines). The cross-sections for single W and Z processes are a magnitude less than inclusive jet production for jets above transverse energies of 20 GeV. Top and Higgs production cross-sections are another 3 to 7 magnitudes lower.

Whilst high-energy analyses are unaffected by the increasing trigger thresholds, sensitivity is lost to new rare processes at energies that fall below the trigger thresholds, despite the unprecedented amount of collisions.

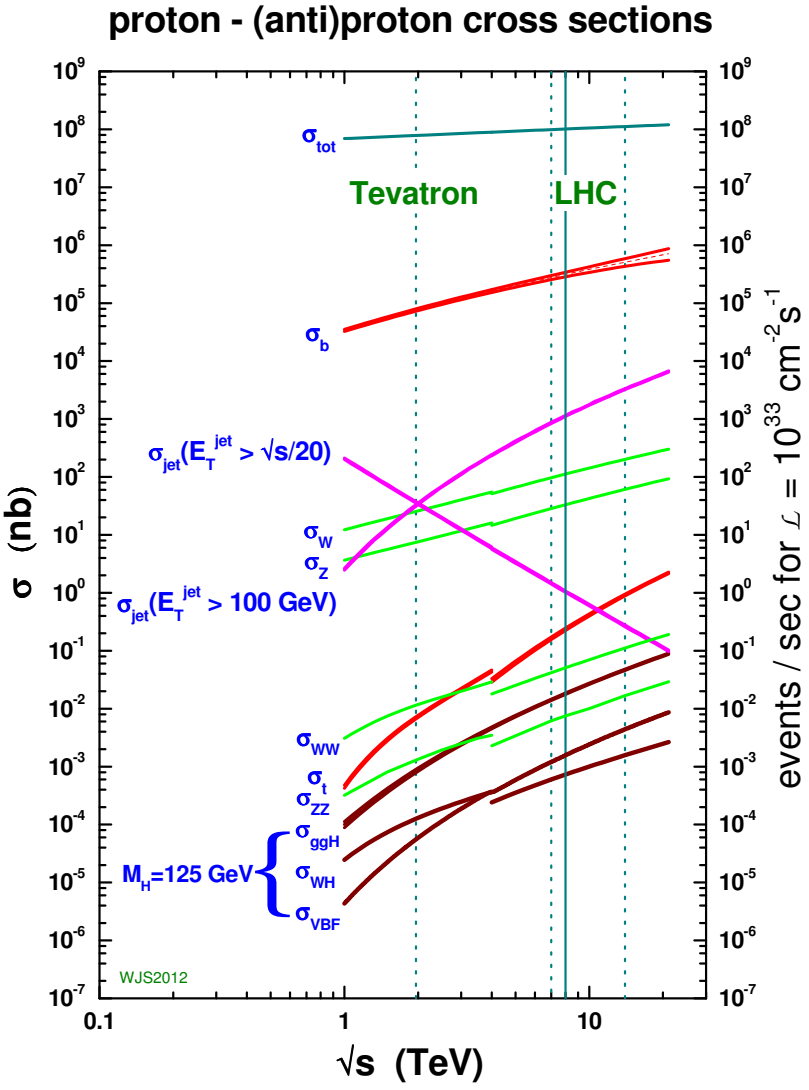

Figure 6.5: The cross-sections in nanobarns are shown as a function of $\sqrt{s}$ for various processes that are important at hadron colliders. The green vertical lines signify LHC colliding energies at 7, 8 and 14 TeV. Taken from [74]

Chapter 7

A new Level-1 calorimeter algorithm for enhanced bunch crossing identification

The Level-1 calorimeter trigger has essential tasks that subsequent recording of data heavily relies on. The first is the analysis of each collision in order to act as a first-stage filter as described in chapter 6. The other is the identification of the correct bunch crossing that a collision of interest originated in. If this decision is miscalculated, then the detector data from a different bunch crossing is recorded; the actual event of interest is irrevocably lost.
The Level-1 calorimeter hardware was upgraded before the start of Run 2 in preparation for more demanding running conditions. As part of the upgrade, the trigger tower preprocessors were made capable of analogue signal digitisation at a frequency of 80 MHz - this is double the previous frequency. One of the motivations for this was the implementation of a new algorithm that could perform the bunch crossing identification (BCID) for extremely saturated trigger tower pulses. The algorithm used during Run 1 and at the beginning of Run 2 had only been validated up to 8 TeV centre-of-mass energies [75], but new Run 2 energies of 6.5 TeV per beam meant that events in which a single tower receives a high energy deposit above the tested threshold could not be excluded.
Interestingly, the *Sat80* algorithm - the new BCID algorithm, so named because it operates on 80 MHz sampled saturated trigger tower pulses - turned out to become necessary for a different type of mistiming issue that emerged in Run 2, and made its commissioning a pressing issue.
The chapter starts with a detailed description of the Level-1 calorimeter trigger tower processing. This is to better understand the mistiming issue that is explained in section 7.2. The Sat80 algorithm logic is introduced in section 7.3. This is followed by the calibration of the algorithm parameters described in section 7.4 and finally the performance studies that validated the success of the algorithm once fully activated in physics data taking are presented in section 7.5.

7.1 Trigger tower pulse preprocessing

The Level-1 calorimeter trigger object reconstruction algorithms use as input the $\eta - \phi$ position and the calibrated transverse energies from the ADC of each trigger tower. Measuring the correct transverse energy is non-trivial and necessitates the preprocessing of

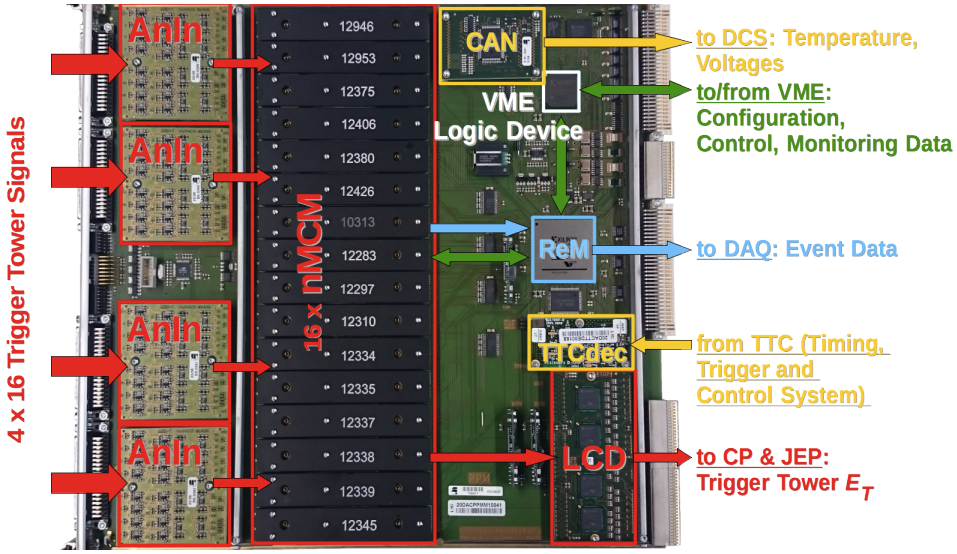

Figure 7.1: The various components of a Level-1 calorimeter preprocessor module are shown. One module holds 4 analogue input (AnIn) boards connected to 16 trigger tower channels each, a multi-chip module (MCM) per trigger tower channel, microcontroller for the communication with the Detector Control System (DCS) via CAN bus, the Readout Manager (ReM) for communication with the DAQ system, the Timing, Trigger and Control (TTC) decoder, and a Low Voltage Differential Signal Driver (LCD) for transmission to the JEP and CP systems.

the trigger tower ADC signal. Such tasks are performed by the Level-1 calorimeter trigger preprocessor modules (PPM) [71], the layout of which is shown in Figure 7.1 (acronyms are expanded in the caption). Each PPM holds 4 AnIn boards that each receive the analogue pulses for 16 TT channels. Multi-chip modules (MCMs) are used to perform the core tasks of the PPMs, one for every 4 trigger tower channel. In addition there is a microcontroller that communicates via CAN bus the module temperature and voltage states, the ReM for the sending of trigger tower preprocessing data to the DAQ system in the case of level-1 accepted events, the TTC decoder for the synchronisation with external clock cycles and the reception of Level-1 Accepts, and the LCD for the transmission of data to the CP and JEP systems.

Prior to Run 2, the MCMs of Run 1 were replaced by new MCMs (nMCMs) with enhanced capabilities as they:

- utilise new FPGAs[1] in replacement of the former ASICs[2]: The replacement has afforded programmable functionality and extended values such as 5 instead of 4-bit figures for the storing of pulse filter coefficients.
- process ADCs at 80 MHz - a factor 2 increase from the Run 1 sampling frequency.

The preprocessor nMCMs perform the following tasks:

- Trigger tower pulse analogue to digital conversion.
- Pedestal correction.
- Pulse shape filtering.

[1] Field-Programmable Gate Arrays
[2] Application Specific Integrated Circuit

- Bunch crossing identification.
- ADC to energy conversion.

Each operation is expanded upon in the following.

7.1.1 Analogue to digital conversion

The duration of a trigger tower digitised signal spans across 4-7 bunch crossings, depending on the calorimeter region. Different pulse shapes for various regions recorded during proton-proton collisions in 2016 are shown in Figure 7.2. Tile pulses are broad, whilst in contrast pulses from the forward calorimeters are very narrow. Pulses have a rise time of 50 ns, or 2 bunch crossings. In the case of the liquid argon calorimeter signals, pulses are shaped into bipolar analogue shapes in the front-end board electronics to achieve the 50 ns rise time.
Due to the trigger towers originating from different parts of the detector, signals travel along different cable lengths and therefore do not reach the receiver system at the same time. A coarse delay in 25 ns steps as well as a fine delay of ∼1 ns steps[3] is settable for each channel before digitisation occurs. Signals from proton-proton collisions are used to measure the timing for each individual channel by aligning trigger tower signals with respect to their peak. The assurance of a constant 50 ns rise-time for all pulses ensures that a peak alignment corresponds to an alignment of the pulse origins. The fine delay is tuned for each tower to ensure that the peak of the pulse is digitised. In this way the full height of the pulse is measured, else the pulse energy is underestimated.
The new MCMs are able to digitise the pulse every 12.5 ns, or in other words at a 80 MHz frequency. During nominal data taking however, only the 40 MHz samples corresponding to a bunch crossing are read out. Data with 80 MHz read-out, as is shown in Figure 7.2, was enabled upon special request only, as the extended read-out limited the trigger rate of the detector.

7.1.2 Pedestal correction and filtering

The digitised pulse is next convoluted with filter coefficients in order to enhance the signal-to-noise ratio. The logic is demonstrated in Figure 7.3. The ADC counts of every 5 consecutive digitised samples are multiplied by the autocorrelation filter coefficients, labelled a_1 to a_5, and summed to a number, f.
During Run 1, a matched filter scheme was used; the coefficients were derived from the pulse shape directly. The new MCMs enabled the move to a more sophisticated filter scheme by extending the number of bits available for the filter coefficients in the firmware design. The coefficients could now each be 4 bit long plus a sign, making negative coefficients possible. At the start of Run 2, the more flexible autocorrelation filter scheme was adopted, which took into account shape changes due to pile-up and other noise.

Autocorrelation filter coefficients are derived by calculating an autocorrelation matrix over many signals from *zero bias* data,

$$R_{ij} = \frac{n\sum S_i S_j - \sum S_i \sum S_j}{\sqrt{(n\sum S_i^2 - (\sum S_i)^2)(n\sum S_j^2 - (\sum S_j)^2)}} \tag{7.1}$$

[3]To be more precise, the step size is 1.04 ns as there are 24 settable steps within 25 ns.

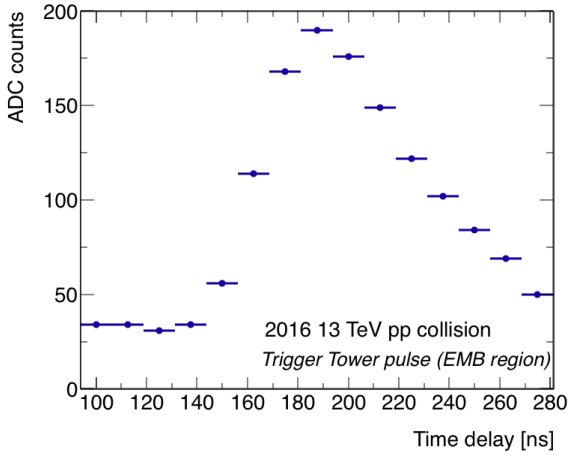

(a) EMB region

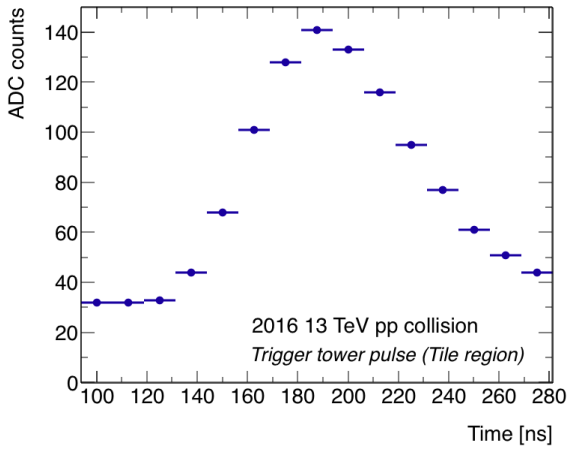

(b) Tile region

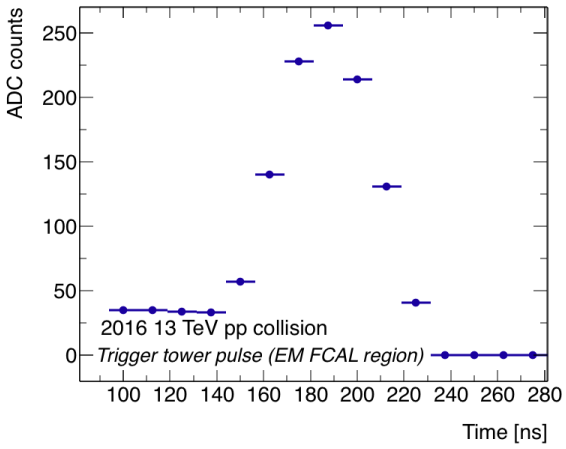

(c) EM FCal region

Figure 7.2: Examples of Trigger tower pulses in the electromagnetic barrel (EMB), Tile and electromagnetic forward calorimeter (EM FCAL) regions are shown, recorded at 80 MHz read-out during a physics run in 2016. A bunch crossing will correspond to every second sample, so that a full pulse is shown to extend across 4-7 bunch crossings. A rise-time extending over 2 bunch crossings for LAr pulses is guaranteed via pulse shaping in the front-end boards.

where S_i are numbered ADC samples that will include the ADC of the true pulse shape, g_i, convoluted with pile-up and electronic noise, and each sum runs over 5 adjacent samples. In this way, the correlation between ADCs in the signal window are taken into account. The optimal coefficients are computed for each signal sample as the inverted matrix times the known pulse shape, $a_i = R^{-1} \cdot g_i$, for i = 1,..,5. The programmable coefficients could be updated to better adapt to new running conditions.

After the filter coefficients are applied, a bunch crossing-dependent pedestal correction is subtracted from each filter sum. The pedestal correction is computed from averaging the pedestal - or ADC noise level - measured as a function of bunch crossing position over several thousand bunch orbits.

7.1.3 Bunch crossing identification

Two algorithms are employed to perform bunch crossing identification. The so-called *Peak Finder* (PF) algorithm is used to identify the correct bunch crossing (BC) for non-saturated and lowly saturated pulses, whilst a saturated BCID (SatBCID) algorithm is used for more highly saturated pulses. The BCID algorithms can be run in parallel and the decision that identifies the earliest sample is taken as the BCID.

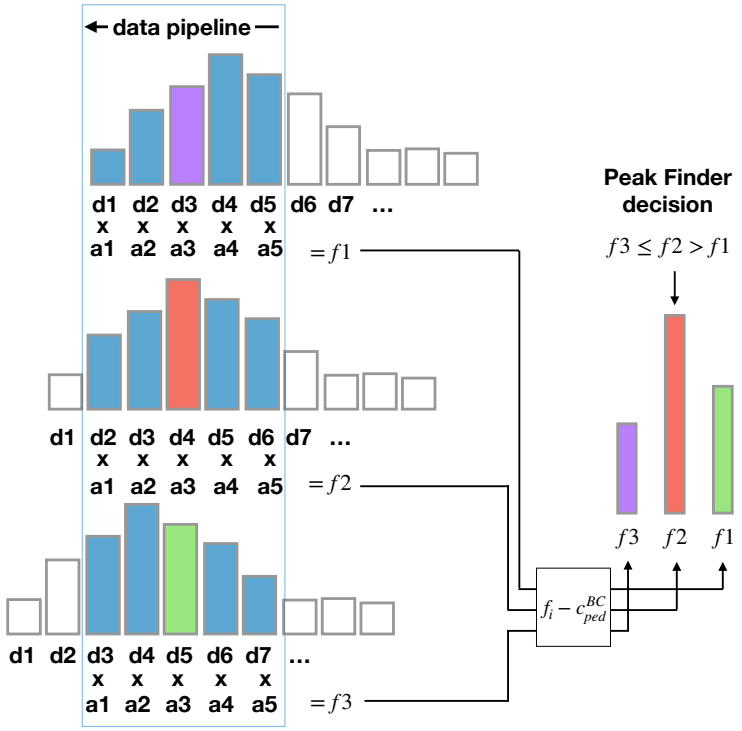

Figure 7.3: Pulse filtering and the Peak Finder algorithm logic: the numbers d_x represent the ADC of numbered samples in the data pipeline and a_{1-5} the autocorrelation filter coefficients. The sum is computed for every 5 filtered ADC samples. A bunch-crossing-dependent pedestal correction, c_{ped}^{BC}, is subtracted from each filter sum. The Peak Finder compares every 3 adjacent sums, f_{1-3}, and identifies f_2 as the triggered bunch crossing if $f_3 \leq f_2 > f_1$.

The *Peak Finder* logic is demonstrated in Figure 7.3. The PF compares every 3 adjacent sums, f_1-f_3, and identifies f_2 as the peak bunch crossing if $f_3 \leq f_2 > f_1$. Samples hit saturation at around 250 GeV energies. With the use of the Run 1 matched filters, the PF was able to reliably identify the BC for pulses with up to 2 to 3 saturated samples depending on the calorimeter region. For more highly-saturated pulses the SatBCID algorithm began to take over. During Run 1 and for the beginning of Run 2, a SatBCID algorithm was operated in a trivial configuration *that simply forced its decision onto the second saturated sample*. The interplay of the BCID algorithms on matched filters and their logic decisions is demonstrated in Figure 7.4. The PF logic results in a correct BC identification for non-saturated and lowly saturated pulses. At some point in rising saturation, the true pulse peak corresponds to the second saturated sample and the old SatBCID algorithm and PF decisions concur. Late PF decisions occur in the case of more than 3 saturated samples but due to the SatBCID algorithm decision, the correct BC is still identified. It is further shown that in the case of extremely saturated pulses there is simply no logic that allows the identification of the third saturated sample as the peak

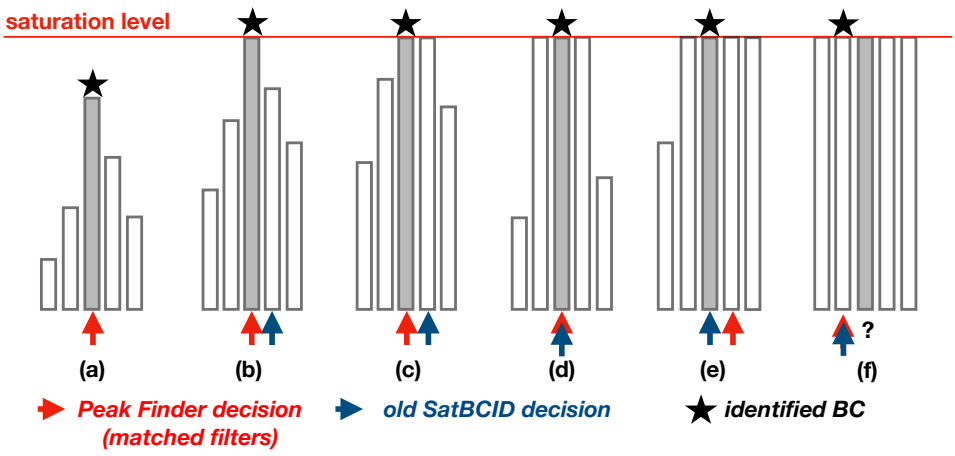

Figure 7.4: The interplay of the logic decision for the *Peak Finder* (with matched filters) and SatBCID algorithms during Run 1 is shown for pulses at various degrees of saturation. The SatBCID is only active when there is at least one saturated sample in the read-out window. The identified bunch crossing is the earliest sample identified by either algorithm.

(this was expected to never occur for Run 1 collision energies [75]). One of the reasons why the new MCMs were installed was to implement a new BCID algorithm that extends the decision logic to the third saturated sample.

7.1.4 ADC to energy conversion

Prior to being preprocessed in the PPM, the amplitudes of the analogue signals are adjusted using variable gain amplifiers, so that a voltage scale corresponding to 10 mV per 1 GeV of transverse energy is set for each tower. For trigger towers towards the forward region of the calorimeter, gain adjustments include a factor of $\sin\theta$ to convert raw energy to a measure of the transverse energy.
At the end of the preprocessing stage, a linear look-up table (LUT) is used to find the corresponding transverse energy for each trigger tower from the sum of filtered ADC samples, f, belonging to the identified bunch crossing. A saturated pulse is assigned the maximum 8-bit energy value of 255 GeV. Noise is suppressed by zeroing any sums that lie below a programmable noise threshold.

7.2 Run 2 mistiming problem

The adoption of the autocorrelation filter scheme at the start of Run 2 had a significant improvement on the efficiency of the bunch crossing identification. This is shown in Figure 7.5 for the electromagnetic endcap inner wheel (EMEC IW) region, which receives an increased amount of pile-up owing to its forward η coordinate and unshielded proximity

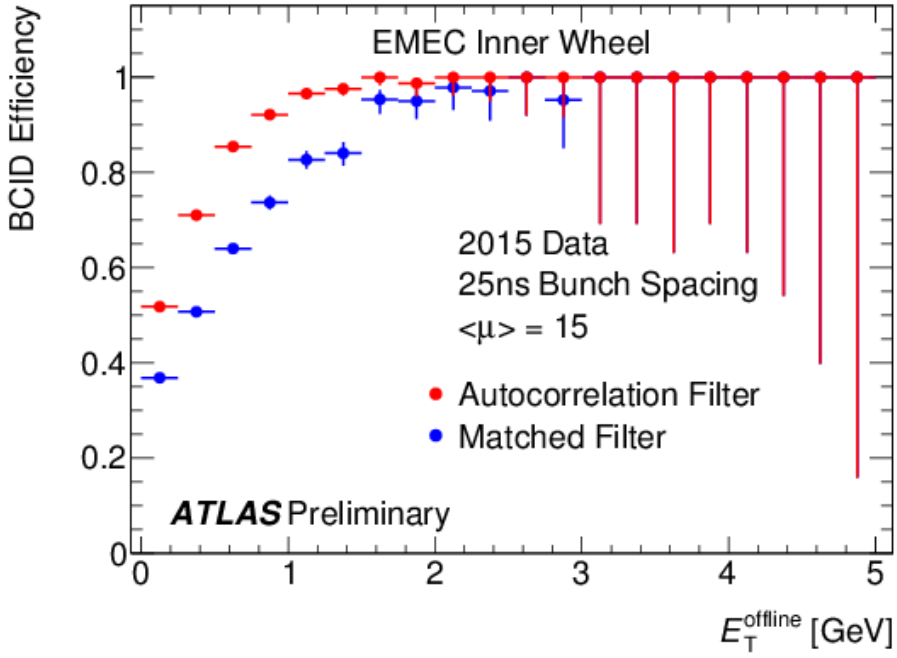

Figure 7.5: The performance of the autocorrelation filter scheme is compared to that of the matched filter scheme by comparing the efficiency for a trigger tower pulse to be identified in the correct bunch crossing by the *Peak Finder* logic as a function of the offline summed cell energy. The efficiency comparison is shown for the inner wheel of the electromagnetic endcap (EMEC IW) where there is a significant contribution of out-of-time pile-up. Taken from [76].

to the collision point. However, the new scheme was revealed to have an unfortunate side-effect. Due to the enabling of negative coefficients, it was possible for the *Peak Finder* to misidentify the bunch crossing of saturated pulses for certain wide pulse shapes. How this can arise is sketched out in the diagram in 7.6. The outer coefficients for the autocorrelation filter tend to be negative. For particularly wide pulses where the samples on the rising edge can shoot up once saturation hits, the negative coefficient may down-weight the peak sum too much, causing the peak finder decision to land one bunch crossing before the true peak. When the PF misidentifies a bunch crossing later, as was the case for matched filters, the consequences are not severe, as either the SatBCID for the same pulse or else a different trigger tower channel in the event generally identifies the correct bunch crossing first[4]. The issue becomes problematic when the PF is made to identify an early bunch crossing, in which case its decision is received first and the wrong event is recorded.

The initial rate of mistimed events was 4 events/fb^{-1} in early 2015. It affected data with TT energies above 700 GeV (2 TeV) in the hadronic (electromagnetic) layer. Due to the falling statistics at high energy, it was possible that a few missing events in a localised energy region would begin to affect p_T distributions in analyses. An nMCM firmware update was deployed in 2016 that disabled the *Peak Finder* decision once more than three samples have saturated - in other words, case (e) in Figure 7.7. Mistimed

[4]This is slightly more complicated than stated. The CP and JEP systems take as input the LUT energy of each tower assigned to that bunch crossing. An event with a saturated tower will generally have other towers containing high energy deposits that will satisfy a trigger. In this case the correct event is accepted and the following five bunch crossings (including the one that would have been incorrectly triggered by the saturated pulse) are vetoed due to the read-out time of the triggered event.

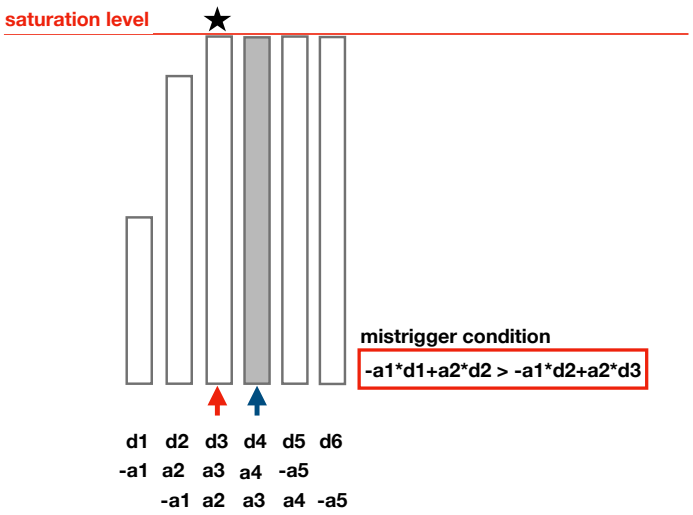

Figure 7.6: The condition for which a mistrigger can occur with the *Peak Finder* algorithm in combination with autocorrelation filters.

events still persisted however for a narrow band of saturation energies - corresponding to particle energies of around 1 TeV - now at a reduced rate of approximately 1 event per 1-2 fb^{-1}. An example of a mistimed TT pulse in the central liquid-argon calorimeter region is shown in Figure 7.8.

7.3 The Sat80 algorithm logic

Although the modification to the PF/SatBCID decision interplay served to mitigate the mistiming issue, a permanent solution was required to prevent the remaining occurrences of mistimed events and restore system robustness. The solution was the implementation of the Sat80 algorithm.

The logic of the Sat80 algorithm is based on comparisons of leading edge 80 MHz ADC samples of an ADC pulse to configurable threshold values in order to gauge the true position of the peak sample. By leading edge, it is meant the three 80 MHz samples before saturation. The samples directly before the onset of saturation will be large *if* they are a part of the main pulse shape - and thus close to the (saturated) pulse peak. They will be small if they lie off the pulse that is now fully saturated. The concept is illustrated in Figure 7.9. The blue region highlights the samples prior to saturation of which the height is an indication of the location of the true peak.

Two threshold values, *low* and *high*, can be stored as comparators. Taking n to be the peak sample (in other words the true BCID) and s to be the first saturated 40 MHz sample, the algorithm logic is as follows

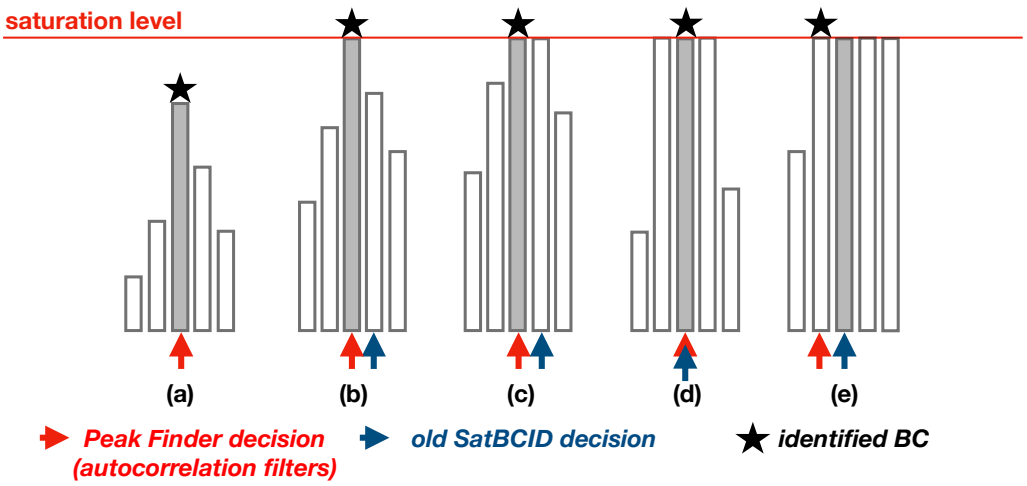

Figure 7.7: This time, the interplay of the logic decision for the *Peak Finder* using autocorrelations filters and SatBCID algorithms is shown for pulses at various degrees of saturation, as it was run at the beginning of Run 2. The autocorrelation scheme led to the PF firing a bunch crossing too early within a certain band of energy where the number of saturated samples was between 3 and 4.

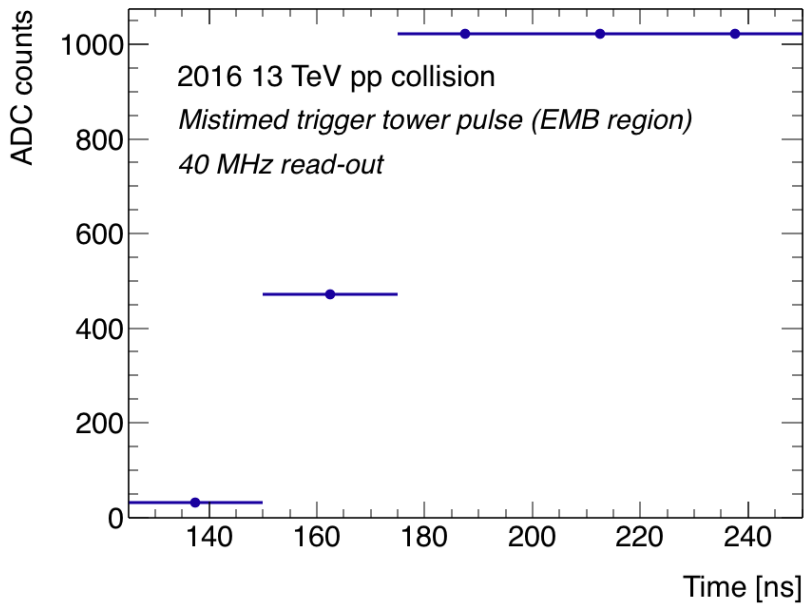

Figure 7.8: A real mistimed pulse in the electromagnetic barrel region during physics data taking is shown. The *Peak Finder* identified the first saturated sample as the BC - one bunch crossing too early - so that read-out was centred around the early bunch crossing. The true peak lay in the second saturated sample, which could be established by other trigger tower pulses in the event.

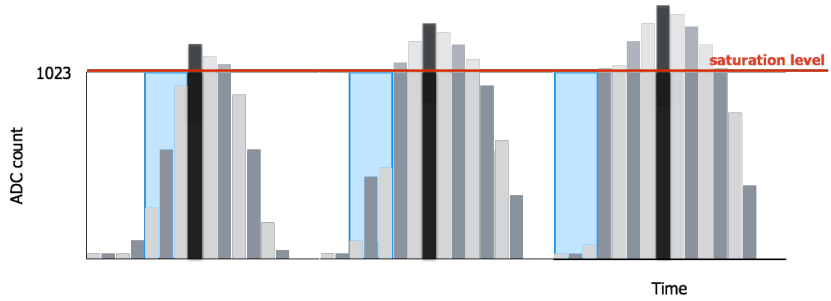

Figure 7.9: The Sat80 algorithm is based on the three 80 MHz samples before saturation. As more samples of the main pulse shape saturate, the first non-saturated samples will lie further from the pulse peak and thus closer to pedestal value.

$$\text{if } ADC[s-1] > high \text{ and } ADC[s-1.5] > low: \qquad n = s \tag{7.2}$$
$$\text{if } ADC[s-1] < high \text{ and } ADC[s-0.5] > high: \qquad n = s+1 \tag{7.3}$$
$$\text{if } ADC[s-1] > high \text{ and } ADC[s-1.5] < low: \qquad n = s+1 \tag{7.4}$$
$$\text{if } ADC[s-1] < low \text{ and } ADC[s-0.5] < high: \qquad n = s+2 \tag{7.5}$$

Integer values correspond to 40 MHz bunch crossings, whilst half integer values correspond to 80 MHz digitised samples in between bunch crossings. For instance, $s-1$ corresponds to the sample digitised at the bunch crossing immediately before the bunch crossing of the first saturated sample, s, spaced at 25 ns; $s-0.5$ corresponds to the sample in between these two bunch crossings, or 12.5 ns prior to s.
The determination of *low* and *high* requires knowledge of the ADC sample heights at various stages of saturation. Specifically, the thresholds are derived based on the following limit-setting logic

$$low1 < \textbf{low} < low2 \tag{7.6}$$

and

$$\textbf{high} > min[high1,\, high2], \tag{7.7}$$

where

$$low1 = ADC[n-2.5] \text{ at } E_{sat}[n-2] \tag{7.8}$$
$$low2 = ADC[n-1.5] \text{ at } E_{sat}[n] \tag{7.9}$$
$$high1 = ADC[n-1] \text{ at } E_{sat}[n] \tag{7.10}$$
$$high2 = ADC[n-1.5] \text{ at } E_{sat}[n-1], \tag{7.11}$$

where E_{sat} is the true transverse energy at which the sample reaches saturation; *low1* and *low2* are the lower and upper bounds on the *low* threshold; *high1* and *high2* are both upper bounds on the *high* threshold. In other words, the ADC heights of samples need to be established at various transverse energies at which following samples reach saturation.

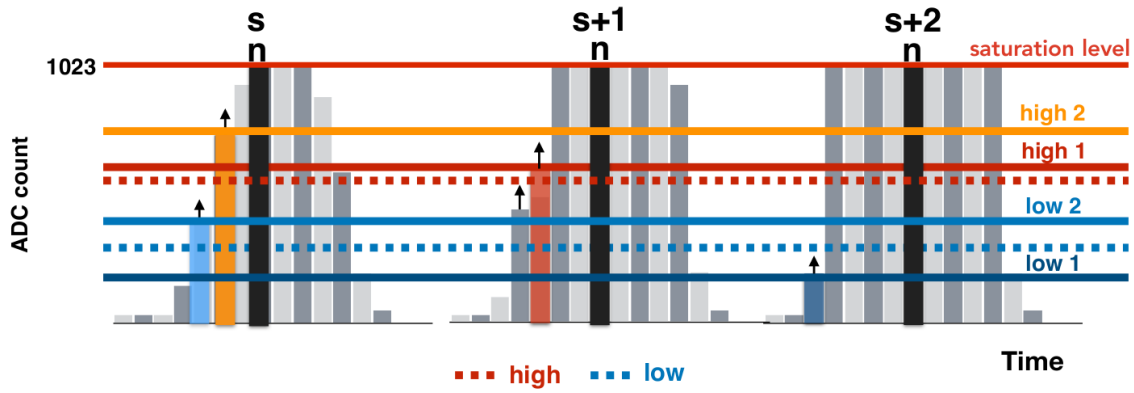

Figure 7.10: The placement of the threshold bounds at various stages of saturation are represented schematically for a template pulse shape. The arrows (black) point to the true peak sample that the algorithm logic should similarly point to. The bounds (*low1*, *low2*) on *low* are represented in blue; the bounds (*high1*, *high2*) on *high* are represented in red. The dotted lines roughly show the position of the final threshold values with respect to the bounds.

The way that this is done is shown schematically in Figure 7.10 and further explained in section 7.4. Referring to Figure 7.10, *low* is to be set anywhere between its two bounds (blue lines), whilst *high* is only constrained to lie below all of its bounds (red lines).

7.4 Calibration of algorithm thresholds

The algorithm relies on two thresholds, *low* and *high*. The *low* threshold is determined by the condition of *low1* and *low2* given by equation 7.6. The *high* threshold is determined by the condition of *high1* and *high2* given by equation 7.7. The thresholds are calibrated for each trigger tower based on real pulse shapes during proton collisions, which necessitates the identification and removal of background events and bad tower pulses. Good quality pulses are used to establish the leading edge ADC sample heights at saturation energies of peak samples by plotting the rise in ADC sample height with increasing transverse energy. The method is described in the following.

Event selection

During normal data taking, only the 5 40 MHz samples around the pulse peak are read out in the data stream. In order to derive the 80 MHz algorithm thresholds the full pulse digitized at 80 MHz was required. As this limits the trigger rate, the collection of data for the algorithm commissioning was done upon special request and opportunistically[5]. In the end, a total of 263 pb^{-1}were collected, which guaranteed sufficient statistics for all trigger tower channels.

[5]Opportunities arose in the case of two separate incidences that resulted in the shutdown of the ATLAS toroidal magnet. One of them was the infamous 'weasel' incident at the LHC[77] - a marten had gotten onto a 66 kV transformer, causing a short circuit, the sudden shut down of all accelerators, and the death of the marten. Without a toroidal magnetic field, usual data taking was not useful for physics. This made way for special data collection requests.

The algorithm parameters are derived based on good quality pulses that originate from real collisions. Event selections primarily aim to reject three types of backgrounds: Liquid-Argon noise bursts, beam background and cosmic rays. LAr noise bursts are sudden large bursts of electronic noise and so most easily identified. They will cause a concentrated area of trigger towers to saturate over several bunch crossings. Beam-induced background is a spray of secondary particles that are created when a proton beam scrapes one of the collimators upstream from the detector. The secondary particles - mostly muons - subsequently travel more or less parallel to the beam and hit the detector from one side. Beam background has distinct features: trigger tower signals will arrive approximately 10 ns earlier relative to collision signals as they did not travel from the centre of the detector, and signals will be concentrated around $\phi = 0, \pi$ - a line that aligns with the collimator slit. Cosmics are events that were triggered by a high-energy cosmic ray from the cosmic background that is constantly permeating our Earth. This type of background appears dull: a sparse number of trigger tower channels contain energy and trigger tower signals are randomly timed.
The following event selection criteria were applied in order to mitigate background events:

- A primary vertex with at least 5 associated tracks is required, to select events in which a good collision has appeared to have occurred.

- The difference between the average timing of lit-up calorimeter cells on either side of the detector is required to be within 10 ns, as is expected from the symmetry of collision events.

- At least two trigger towers above 90 ADC counts are required in each layer. This reduces LAr noise bursts as they are concentrated in the electromagnetic layer, and cosmic events that have low activity mostly in the outer hadronic layer.

At the level of per trigger tower, the following selections are made:

- The ADC of the peak sample has a minimum of 90 ADC counts (corresponding to $\sim$15 GeV). This ensures the pulse is sufficiently above pile-up noise.

- A minimum calorimeter pulse quality is required. The pulse quality measure is based on the summed χ^2 values of pulse shape fits to calorimeter cell pulses within the tower.

- A well-timed trigger tower. This is measured by fitting a Gauss-Landau curve to the digitised pulse and ensuring that the timing offset measured by the peak of the fit is within 3 ns. A Gauss-Landau curve is chosen as it most accurately describes the true shape of the underlying analogue pulse [78].

As an example, Figure 7.11 shows the timing offset for a trigger tower pulse during a single run, measured by the fitted peak of a Gauss-Landau fit. The trigger tower is located in the hadronic end cap at $\phi = 0$, a region that is strongly affected by beam-induced background. The second distribution of timing offsets around -10 ns is induced by the energy deposits of beam-induced secondary particles.

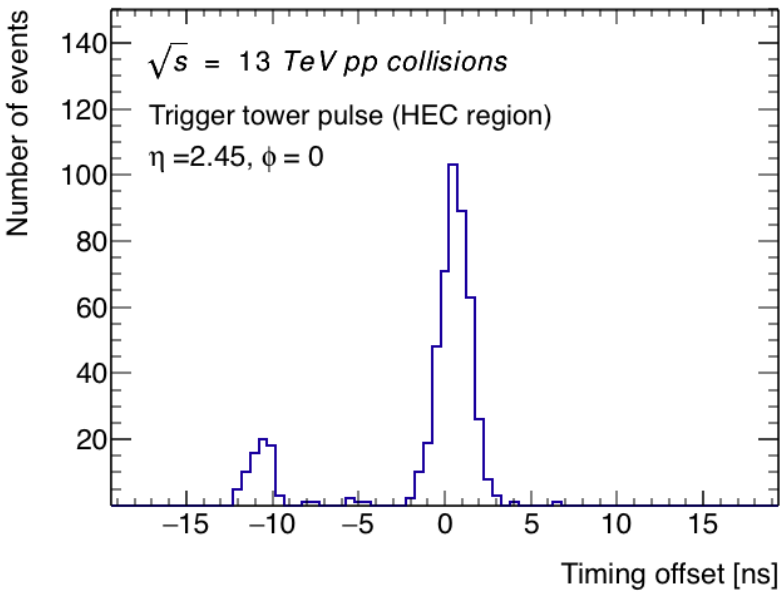

Figure 7.11: The timing offset distribution measured for a trigger tower in the hadronic end-cap (HEC) region. The timing offset is taken as the offset at the peak of a Gauss-Landau fit to the pulse. The events clustered around a timing offset of $\sim$ 10 ns originate from beam-induced background. The backgrund feature is especially prominent for trigger towers that lie along $\phi = 0, \pi$, as is the case for this tower. The selection of trigger tower pulses used in the derivation of the Sat80 thresholds includes only pulses with a minimum timing offset of 3 ns.

Threshold derivation

For the derivation of the threshold bounds, it is necessary to establish the dependency of the ADC of a sample on the true transverse energy. For example, the *low2* bound is the ADC of sample $n-1.5$ at the point that the true peak sample, n, has reached saturation (equation 7.9).

The height of each sample with respect to the saturation of samples at or close to the peak is investigated tower by tower via plots of the sample ADC counts as a function of the calorimeter transverse energy. The calorimeter transverse energy is the offline computed transverse energy of the sum of cell energies in each layer of the calorimeter region of the trigger tower, and provides an accurate measurement of the true energy of a trigger tower beyond saturation. The linear relationship between sample ADC counts and the calorimeter energy are shown in Figure 7.12 for a chosen tower in the EMB, Tile and EM FCal calorimeter region. Linear fits are applied so that the sample heights can be extrapolated. Further annotations in Figure 7.12a indicate where the *high1*, *high2* and *low2* threshold boundaries lie, following equations 7.9 – 7.11. The *low1* threshold boundary is not shown - it is the $n-2.5$ sample height at the point at which $n-2$ reaches saturation, which occurs at very high energies beyond the scale of the plot.
The three plots demonstrate how the slopes of the linear fits vary between representative towers because of the differing pulse shapes in each calorimeter region.

An $\eta-\phi$ map of the *low1* and *low2* and the minimum of *high1* and *high2* threshold bounds are shown in Figure 7.13 for the electromagnetic (left) and hadronic layer (right). The variation in η is distinct, however the variation in ϕ is uniform enough to derive a common threshold per absolute η bin, as long as the threshold is within the lowest or

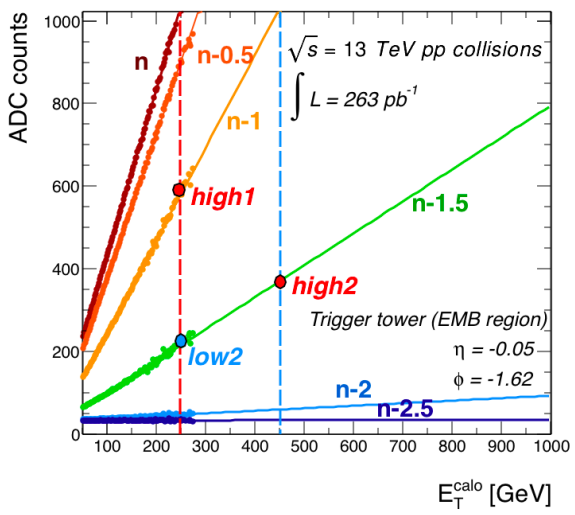

(a) EMB region

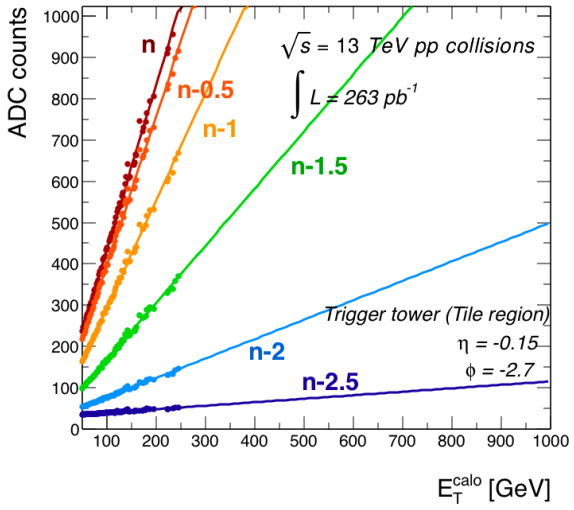

(b) Tile region

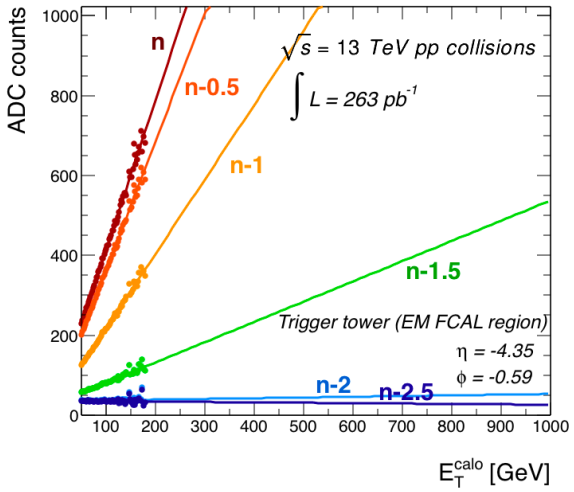

(c) EM FCal region

Figure 7.12: The ADC versus the summed calorimeter cell transverse energy is shown for the samples on the leading edge of trigger tower pulses for selected trigger towers in the EMB, Tile and FCal region. Each slope represents a pulse sample at and before the peak sample, n. The numbering of the samples goes as $n - i$, where i is an integer value for 40 MHz samples (corresponding to a bunch crossing), and a half-integer value for 80 MHz samples. In terms of nanoseconds, the samples from red to green are: samples digitised at t_{peak} − 0 ns, -12.5 ns, -25 ns, -37.5 ns, -50 ns and -62.5 ns. Additional annotations in Figure 7.12a indicate the position of three of the threshold boundaries.

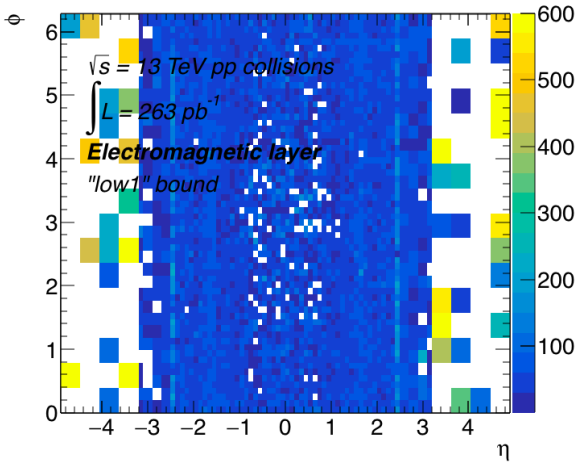

(a) EM *low1* threshold

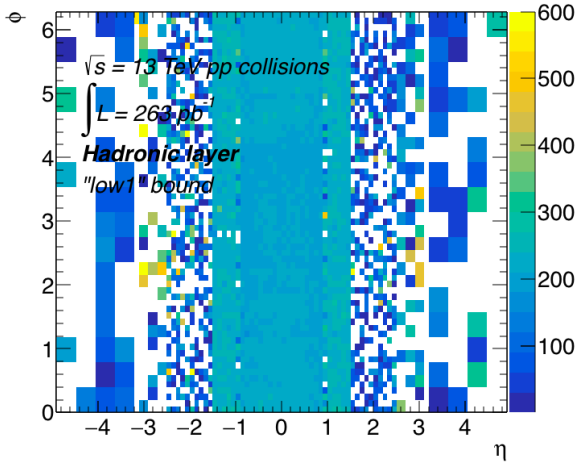

(b) HAD *low1* threshold

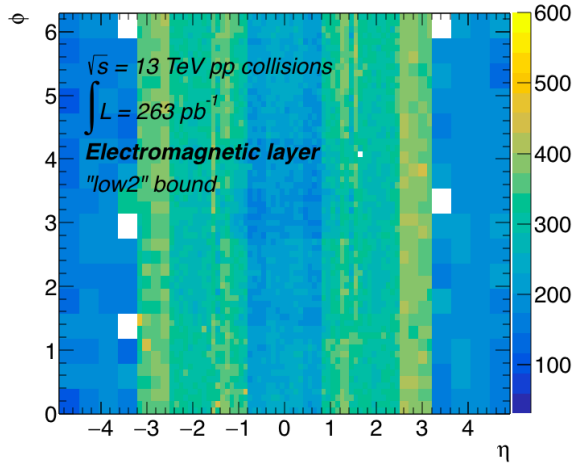

(c) EM *low2* threshold

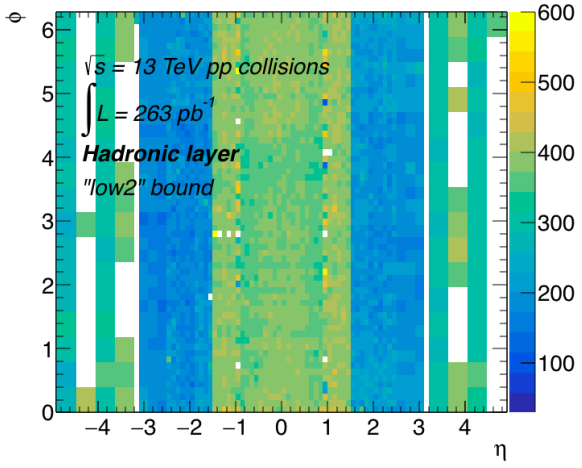

(d) HAD *low2* threshold

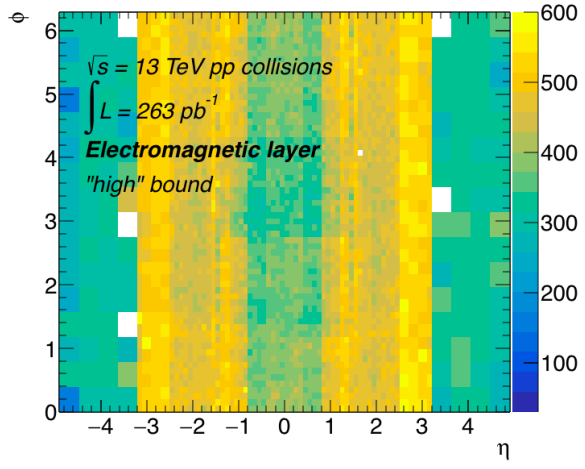

(e) EM min(*high1, high2*) threshold

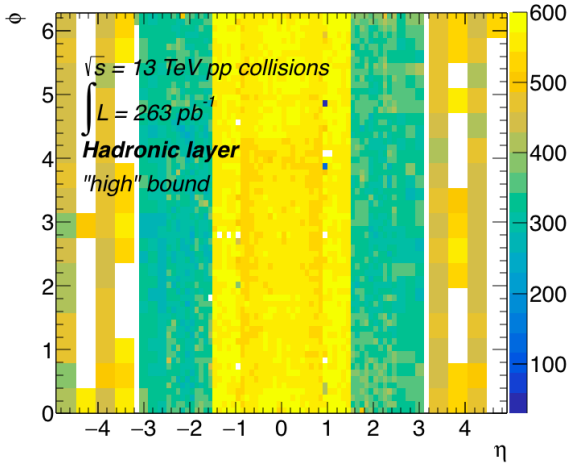

(f) HAD min(*high1, high2*) threshold

Figure 7.13: EM and HAD $\eta-\phi$ maps of Sat80 algorithm threshold bounds, *low1*, *low2* and the minimum value of *high1* and *high2* derived for each trigger tower.

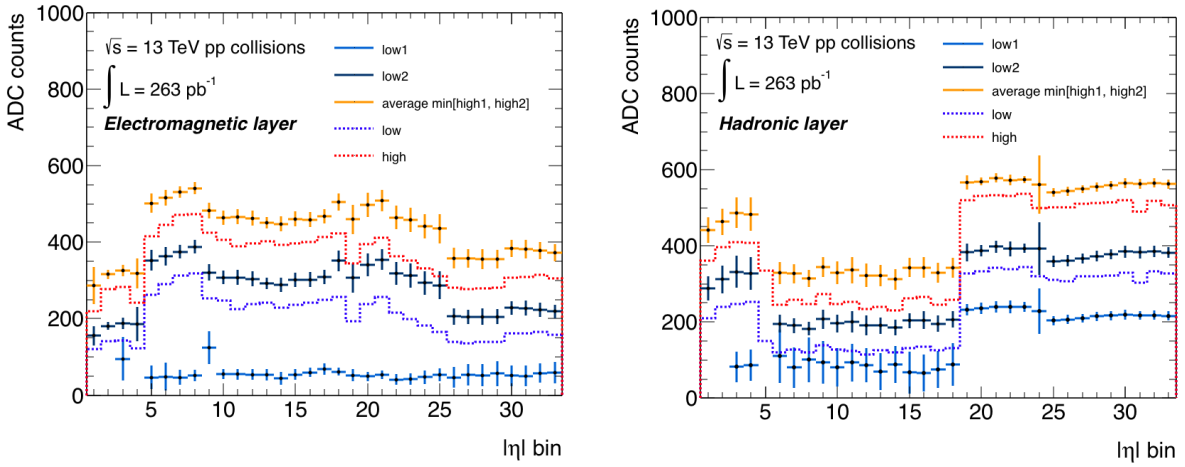

(a) Electromagnetic layer (b) Hadronic layer

Figure 7.14: The final *low* and *high* thresholds are presented as blue and red dashed lines, respectively. The $|\eta|$ bins are numbered starting from the central EM barrel or Tile region at $|\eta| = 0$ and ending in the FCal region. The averages are from the combined distributions along ϕ and having folded along $\eta = 0$, so that one threshold value is used for all towers with the same absolute η value. The *low* threshold was set 15 ADC counts below the lowest *low2* bound in that $|\eta|$ bin. It is ensured to be well above any *low1* bounds. The *high* threshold is set 15 ADC counts below the lowest *high* bounds for that $|\eta|$ bin.

highest bound of any given trigger tower for that $|\eta|$ range. For some bins, valid thresholds could not be found. This was particularly true in the case of the *low1* bound, where there was not always a measurable rise in the ADC samples. In other cases, thresholds could not be derived owing to low statistics - particularly in the forward region where the transverse energy is low.

The final thresholds are displayed in Figure 7.14, represented by the dashed lines. The numbering of the $|\eta|$ bins start from the central EMB or Tile region at $|\eta| = 0$ and end in the FCal region. The threshold boundaries shown are averaged over all towers with the same absolute η. The *high* threshold is set 15 ADC counts below the lowest *high1* or *high2* value for a given $|\eta|$ bin. The *low* threshold is set 15 ADC counts below the lowest *low2* value for a given η bin. Keeping the *low* threshold closer to *low2* as opposed to averaging *low1* and *low2* was deemed safer, as there was less chance of an early trigger caused by the first unsaturated sample in 7.10 case (c) fluctuating above the *low* threshold.

7.5 Validation and performance

In order to reduce the risk of affecting data taking, the new Sat80 algorithm was initially enabled in spy mode, which means its decision on the triggered bunch crossing was recorded without being activated. An offline analysis was performed in order to validate the Sat80 decision against the *Peak Finder* and the old SatBCID decision. Once validated in spy mode, it was officially activated in physics, followed by another analysis of events to identify any mistimed physics events.

7.5.1 Spy mode

A challenge presented itself in the validation of the Sat80 performance in spy mode in the case that the Sat80 decision was not found to be in agreement with the triggered bunch crossing: Since 80 MHz samples are not part of the read-out, the Sat80 algorithm's actual decision had to be inferred by other means. This was solved by reconfiguring a 3-bit word that was introduced in the preprocessor DAQ read-out as part of the nMCM upgrade. It was henceforth used as the Sat80 3-bit word to represent the six cases in Figure 7.15. The Sat80 word encodes all possible combinations of the comparison of

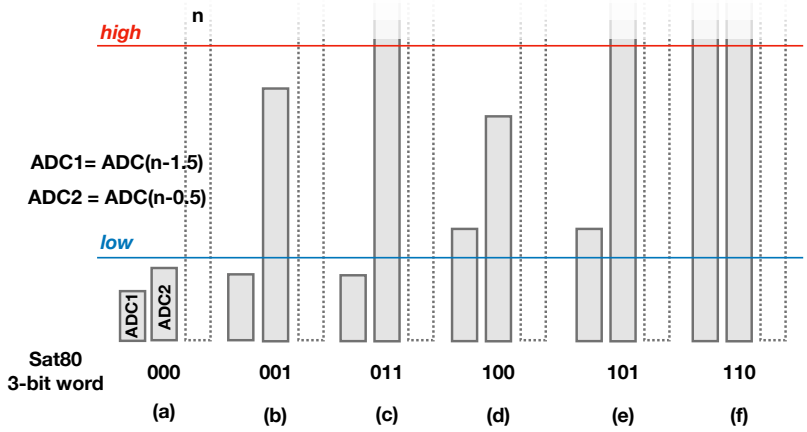

Figure 7.15: The Sat80 3-bit word is used to encode the six different configurations of the 80 MHz leading edge samples, "n-1.5" and "n-0.5", with respect to the Sat80 algorithm thresholds. Here, "n" is the sample triggered on by the active BCID algorithm.

the Sat80 algorithm thresholds to the leading edge 80 MHz samples,"n-1.5" and "n-0.5", where "n" is the sample that is identified as the peak bunch crossing and hence enables the evaluation of its decisions.

Confidence in the thresholds and firmware was gained by running the Sat80 in spy mode. The most interesting cases to consider were the events in which the *Peak Finder* had misidentified a bunch crossing too early. An example case is the mistimed pulse that was shown earlier in the chapter, Figure 7.8. This was recorded with Sat80 in spy mode. Figure 7.16 displays the same pulse along with the Sat80 thresholds and the Sat80 3-bit word, 001 in binary representation.

The Sat80 3-bit word indicates case (b) in Figure 7.15, or in other words,

- ADC[s-1] $>$ *high*
- ADC[s-1.5] $<$ *low* - where s = n, the central value triggered by the PF.

This corresponds to the condition in equation 7.4, $n = s + 1$, allowing one to deduce that the Sat80 would have correctly identified the bunch crossing for this event. There were 18 early mistimed events in total during the time that Sat80 was set in spy mode, and for each it was verified that the Sat80 decision had fallen on the correct bunch crossing. Furthermore, all other events for which the Sat80 decision disagreed with the active

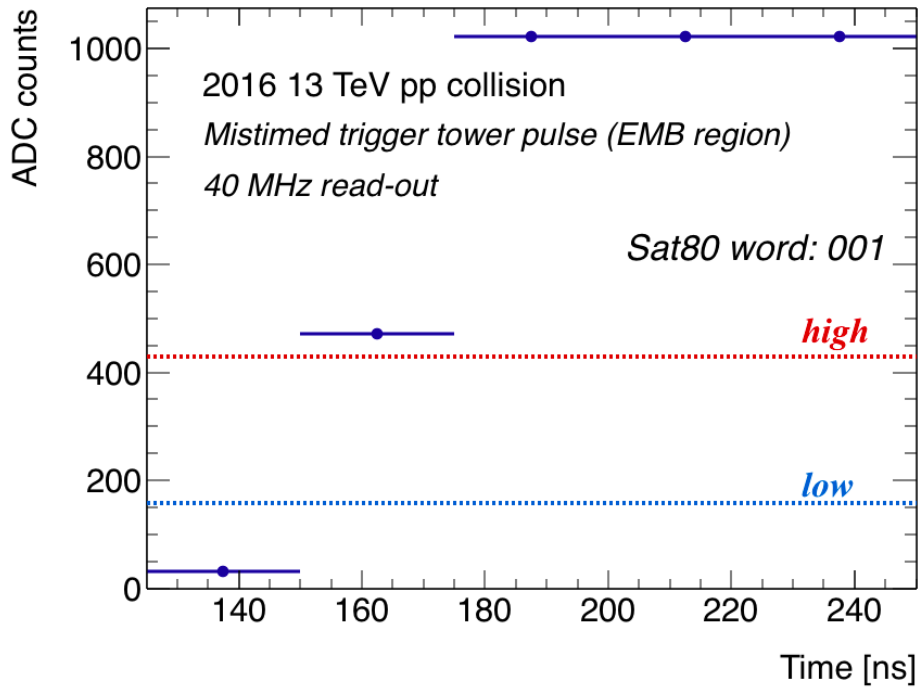

Figure 7.16: The same mistimed trigger tower pulse from Figure 7.8 is shown again, this time with the Sat80 algorithm thresholds set for that tower and the Sat80 3-bit word that indicates case (b) in Figure 7.15. It can be inferred that the Sat80 algorithm identified the correct bunh crossing.

PF/SatBCID algorithm were verified to be background events.

7.5.2 Activation

The Sat80 algorithm was officially activated in October 2016. Since the *Peak Finder* mistiming issue affected pulses with 3 or more saturated samples, it was decided to only activate(deactivate) the Sat80(PF) decision for pulses with ≥ 3 saturated samples.

Special attention and monitoring was performed following the first activation. Potential mistimed events were flagged by considering the timing of trigger towers that neighbour the saturated tower and computing the in-time fraction, $f_{in-time}$:

$$f_{in-time} = \frac{N_{in-time}^{R=0.5}}{N_{total}^{R=0.5}} \tag{7.12}$$

where $N_{total}^{R=0.5}$ is the total number of towers above 90 ADC in the peak slice and within a radius of 0.5 in $\eta - \phi$ and $N_{in-time}^{R=0.5}$ is the number of towers from the total number that are in-time. Towers are determined as in-time if they are centred and the PF has identified the centre sample as the BC. These events also had to be effectively distinguished from background events. The $\eta - \phi$ trigger tower channel maps in Figure 7.17 show the pulse activity of two real background events that had been triggered by the Sat80 algorithm. Figure 7.17a is a typical LAr noise burst event, and 7.17b is a typical cosmic event. The z-axis is the peak 40 MHz sample number, where samples are numbered from 1 to 5 and 3 corresponds to the sample of the identified bunch crossing. The centre of the circle

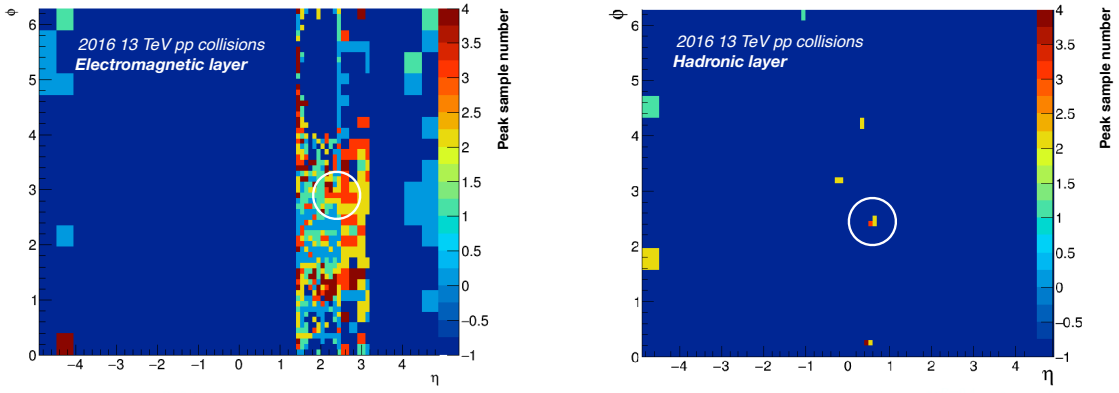

(a) Noise burst event

(b) Cosmic event

Figure 7.17: An $\eta-\phi$ map of trigger tower channels with pulse activity is shown for (a) a LAr noise burst event and (b) a cosmic ray event. The events were triggered by the Sat80. The peak sample number is shown on the z-axis. Samples are numbered from 1-5, where 3 is the centre sample corresponding to the identified bunch crossing. At the centre of the white circles are saturated trigger tower pulses for which the Sat80 was activated.The number and in-time fraction of trigger towers within the circle is calculated in order to flag possible real mistimed events, as explained in the text.

identifies the Sat80 triggered saturated tower. In addition, to $f_{in-time}$ and $N_{total}^{R=0.5}$, the total number of saturated pulses, N_{total}^{sat}, in the event was useful to identify noise burst events. Typical values for the in-time fraction, the total number of saturated towers, and the total number of towers within the radius for background events were

- Noise bursts: $f_{in-time} \lessapprox 0.25$, $N^{R=0.5} \gtrapprox 15$, and $N_{total}^{sat}5$.
- Cosmic background: $f_{in-time} \lessapprox 0.5$ and $N^{R=0.5} \lessapprox 2$.

Any events where, very conservatively, $f_{in-time} < 0.85$ and $2 < N_{total}^{R=0.5} < 20$ or $N_{total}^{sat} < 10$ were scrutinised one by one. In the scrutinisation of individual events, trigger tower pulse timing offsets were measured in order to match the offset to the beam-induced background timing, and trigger tower pulse shapes were matched to the expected shape of an in-time physics pulse.

A total of 7 fb^{-1}of proton collision data were analysed for mistimed events, which included events containing TT pulses up to a calorimeter energy of 3.5 TeV. The total sampled calorimeter energy distribution of saturated towers for which the bunch crossing was successfully identified by the combination of the PF and Sat80 algorithm decisions is shown in Figure 7.18. No non-background mistimed events were found.

An example of an in-time Sat80-identified dijet event is shown in Figure 7.19.

7.6 Final Run 2 performance

For a limited dataset, very high energy pulses and pulses in the end-caps and forward region are not well sampled in the analysis for mistimed events: Saturated pulses have a calorimeter energy that is an exponentially falling distribution and are mainly concentrated in the central EMB and Tile region. In order to continue monitoring for mistiming

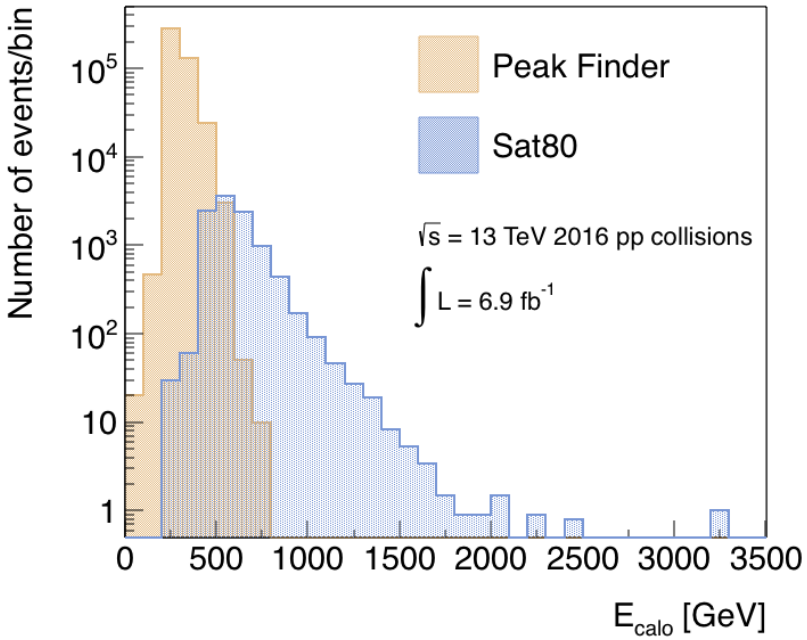

Figure 7.18: The calorimeter transverse energy distribution for saturated towers is shown for the first 7fb^{-1}of data that was collected with the Sat80 algorithm enabled. The *Peak Finder* algorithm performs bunch crossing identification for towers that have up to 2 saturated samples (yellow distribution). The Sat80 algorithm performs this for towers that have more than 2 saturated samples (blue distribution).

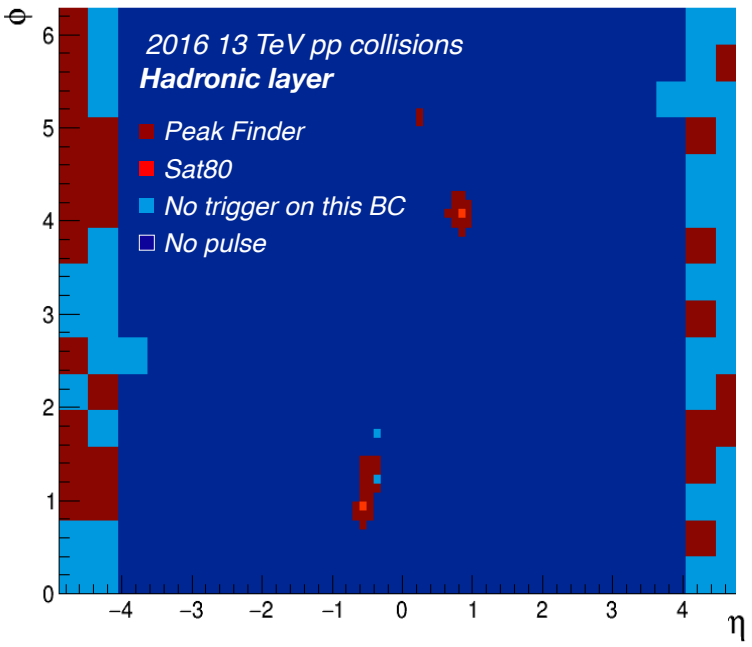

Figure 7.19: A dijet event that was correctly triggered by the Sat80 algorithm. Each jet contains a saturated pulse, the peak of which is identified by the Sat80. The correct timing of the saturated pulses are clearly verifiable by the surrounding towers for which the *Peak Finder* decision is in agreement.

issues for the remainder of Run 2, an automatic monitoring tool was created and implemented. The tool is designed to identify triggered events that contain significant energy in the bunch crossing after, as well as contain a certain number of mistimed towers of a good quality. Specifically, the tool selects L1_J100 triggered events for which an L1_J400 would have triggered in the following bunch crossing. Events are further filtered by requiring that they contain ≤ 4 bad quality trigger tower pulses, ≤ 3 good quality in-time pulses and ≥ 2 good-quality late pulses (offset by one bunch crossing later). The quality is based on the asymmetry of the pulse and the peak offset of a quadratic fit with respect to the peak ADC centre. Typically 0 to 2 events are filtered by the monitoring tool per run. Histograms similar to the $\eta - \phi$ maps of event activity in the previous section are automatically published online for mistimed candidate events so that they can be scrutinised manually.

In the entirety of Run 2, no mistimed collision event due to the Sat80 algorithm has been identified. The total integrated luminosity of physics data that has been collected with the Sat80 and *Peak Finder* combined decision amounts to 98 fb^{-1}.
The tool however successfully identified mistimed events in occasions of malfunction hardware. Moreover, it began to identify several genuine mistimed events in 2018 that had been identified by the *Peak Finder*. The total number amounted to 7 events in the Tile region, 3 in the central EM layer and 2 in a EM calorimeter transition region. The latter were likely due to the difficulty of calibrating pulses in the transition region, resulting in bad pulse shapes. The remainder were lowly saturated pulses. It is evident that undetermined changes in detector calibration or LHC running conditions in 2018 had once more revealed sensitive instabilities in the *Peak Finder* algorithm for saturated pulses. Notably, for each of the mistimed events containing saturated pulses the Sat80 would have identified the correct bunch crossing.

In Run 3 of the LHC, the Level-1 calorimeter trigger will be upgraded to exploit a finer calorimeter read-out granularity [79]. Whilst a part of the Level-1 calorimeter trigger preprocessor will gradually be replaced by a new digital processor designed to process finer granularity input from the LAr calorimeter, it will remain the preprocessor for the tile calorimeter inputs throughout. Therefore, the Sat80 algorithm will continue its role in Run 3. Based on the misidentified events by the PF in the final year of Run 2, it is foreseen to activate Sat80 for all saturated pulses.

The Sat80 was originally designed to extend the algorithm logic to be triggerable on the third saturated sample, $s + 2$.
One can deduce the minimum calorimeter energy at which the true peak lies at $s+2$ from an analysis of the energy slopes. For the forward region, this is only expected to occur at the impossible energies of > 50 TeV. For the Tile region, however, this is expected to occur at around 2.2 TeV.
During the analysis of individual events in the first 7 $\text{fb}^{-1}$of data with Sat80 enabled, there were no towers with energies above 2 TeV in the Tile region nor were there any $s+2$ cases found. Thus, the results of the automatic monitoring remains the only validation of the Sat80 performance at the high energy end. This offers an interesting case study to return to in the future.

Chapter 8

Dijet resonance searches: An overview

Any new mediator particle that can couple to Standard Model quarks, and thus be created directly from quark-quark interactions within a proton collision, can decay to quarks via the same coupling. The search for a resonance in events containing two central jets have been conducted since the earliest hadron colliders, namely the UA1 [80] and UA2 [81] experiments at the $Sp\bar{p}S$ and CDFI [82] and CDFII [43] at the Tevatron[1]. The attractive feature of a dijet resonance search is its inclusive nature: Searches can be based on a myriad of models. Some examples are axial vector gluons from a new heavy massive colour octet, alongside the Standard Model gluon octet, emerging from the spontaneous breaking of a chiral colour gauge group of SU(3)×SU(3) [83]; the decay of excited quarks in the scenario that quarks are composite particles [84]; quantum black holes [85, 86]; or heavy bosons from a new electroweak gauge groups such as a "left-right symmetric" $SU(2)_L \times SU(2)_R \times U(1)_Y$ extension of the Standard Model [87].

Dijet searches have generally used the same method over the years. The two leading pairs of jets are calibrated and selected, in which selection criteria are minimal: for ATLAS and CMS searches, the sole additional criteria following p_T^{jet} and η^{jet} selections, is a maximum allowable difference in jet rapidity of the jet pair, $y^* \equiv |y_{jet1} - y_{jet2}|$. The dijet mass spectrum is produced from the calibrated jets in data and a smooth functional fit is applied, based on the assumption that the dominant QCD background mass spectrum is smoothly falling. In this way, the data itself is used to derive the background estimate The spectrum is scanned for a localised deviation between the fit and the data. Limits are set on the expected event yield for a particular model if no significant deviation is found. Such has been the case for all dijet searches to date. By accounting for the signal acceptance - dependent on the detector geometry, detection efficiencies and kinematic selection - and the scaling of the cross-section with g_q^2, the coupling strength to Standard Model quarks as a function of the new particle mass can be constrained directly.

8.1 Dijet exclusion limits on Z' after LHC Run 1

The results shown in Figure 8.1 are dijet exclusion limits at 95% confidence, separated by collider experiment for an axial vector mediator based on the simplified dark matter

[1] A brief history of hadron colliders is provided in Appendix A.1.

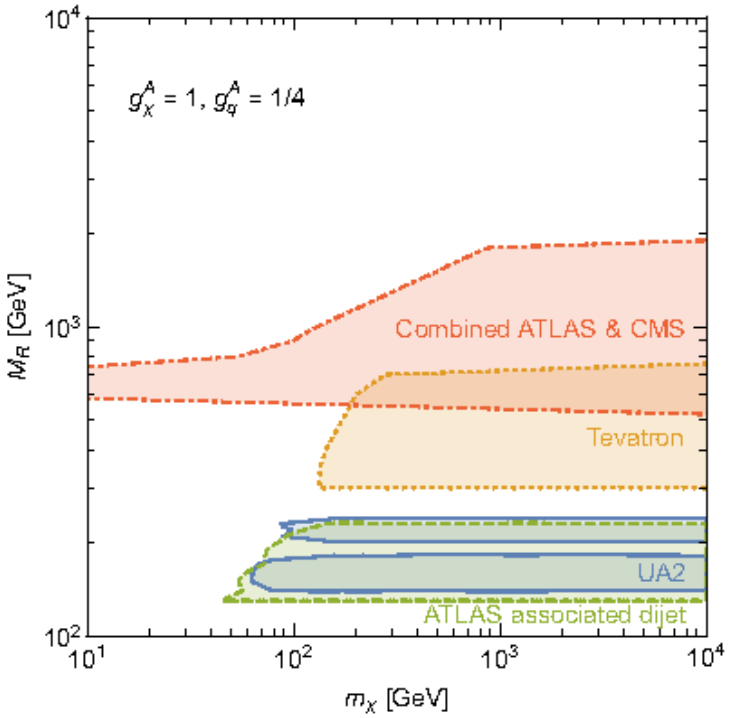

Figure 8.1: A combined plot of dijet search exclusion limits at 95% C.L. as recast in [33] from dijet searches at UA2 [], CDF [43] (labelled Tevatron), ATLAS [40, 88] and CMS [42]. Limits assume an axial vector mediator with a coupling to Dirac dark matter and a flavour universal coupling to quarks, for $g_\chi = 1$, $g_q = 0.25$.

model described in Section 3.2.4 (Figure 3.6 represents the same limits, combined). The results are a recast of dijet searches from UA2 [81] at $Sp\bar{p}S$, CDF [43] at the Tevatron and the Run 1 results from ATLAS [40, 88] and CMS [42]. The assumed couplings are $g_\chi = 1$ and $g_q = 0.25$.

After LHC Run 1, ATLAS and CMS set the first limits at mediator masses above 900 GeV. It is evident that below this mass point the leading dijet results from LHC had not improved on constraints from past colliders. Similarly, CDF had not gained sensitivity to the low mediator mass range at which the $Sp\bar{p}S$ experiments had previously set limits. The limitation is the trigger output for the single jet triggers and the total available bandwidth, as has been described in 6.6. Due to raised trigger thresholds, the output of lower p_T jets is throttled, and the result is gaps at low masses that are no longer being probed. The goal of future colliders will be to achieve higher energies and luminosities, in which case improving limits at low masses will become increasingly challenging. Leading limits from LHC experiments at low masses are from the "Atlas associated dijet" analysis [88]. It is a Run 1 search for dijet resonances with an associated $Z/W^\pm$ lepton decay, in which events were collected by lepton triggers. Low masses become probable as there is no trigger thresholds on the leading jet p_T, however the mass range is limited by the required production of a $Z/W^\pm$ boson. There is a gap between the bounds set by the "Atlas associated dijet" and the conventional ATLAS and CMS dijet combined bounds, that had not been covered by the LHC experiments during Run 1.

8.2 New dijet search strategies in LHC Run 2

In Run 2, two search strategies are conducted at ATLAS and CMS that are dedicated to covering the phase space left uncovered in Run 1: *(Boosted) Dijet+ISR* searches and *data scouting*.

The *dijet+ISR* search assumes a slightly different topology to the two-jet final state. It makes use of initial state radiation to trigger the event, where the radiated particle is either a photon or a gluon. The second and third jet, in case of the former, or the first two leading jets, in case of the latter, become the dijet pair. The dijet system incurs a transverse boost due to the recoil of the dijet system against the ISR. The boost leads to a stronger collimation of particles in the hadronisation process. The radius of collimation is roughly $2m_{Z'}/p_T^{Z'}$. At some point towards lower Z' masses and due to the boost from the energetic ISR, the shower radius is small enough for the dijets from the decay products to appear merged. Below this mass point a search for *boosted* dijet+ISR jet/photon is adopted. The boosted dijet pair is reconstructed as a large anti-k_T jet with a radius parameter of 1.
The advantage in a dijet+ISR search is the ability to reach lower masses as firstly the decay particles are boosted in energy by the recoil and secondly the jets in the signal selection are not directly limited by a trigger threshold. However, there remains a reduction in cross-section from requiring the radiation of an energetic photon or jet.

Data scouting is the implementation and collection of data via a dedicated *data scouting stream*, in which only partial event information is recorded, as opposed to the entire detector information. The reduced event size allows for a higher output rate and therefore lowered trigger thresholds. LHCb [89] and CMS [90] were the first to deploy the data scouting technique[2] during Run 1. In the case of CMS, it was used to record jets reconstructed at HLT and minimal additional information, in order to conduct a proof-of-concept dijet resonance search on a small dataset of 0.13 fb^{-1} [90]. ATLAS published its first use of the technique in Run 2, in ATLAS known as the *Trigger-object Level Analysis* (TLA), for the 2015 dataset [91]. It has seen greater development since then, as described fully in the following Chapter 9.
Whilst a trigger threshold still exists, the data scouting technique has the advantage that it retains full statistics as it collects every event with at least one jet above trigger threshold for an unprescaled trigger.

8.3 ATLAS dijet exclusion limits on Z in LHC Run 2

The current ATLAS upper limits at 95% confidence for datasets of Run 2 are shown in Figure 8.2 for an axial vector dark matter mediator coupling to quarks as function of mediator mass. The dark matter particle is assumed to have a very high mass of 10 TeV, so that dijet production and the signal width are unaffected by the dark matter-mediator coupling.
The most stringent limits are set by the TLA for masses between 400 and 1500 GeV with 29.7 fb^{-1}of data [92], reaching a lowest excluded coupling value, g_q, of 0.03. The

[2]In LHCb it is referred to as the Turbo Stream

(boosted) dijet+ISR results together probe a mass range between 100 GeV to 1 TeV. The boosted analysis excludes coupling values between 0.1 and 0.2 with 36.1 fb^{-1}of data [93]. The non-boosted analysis excludes couplings between 0.15 and 0.34 above masses of 200 GeV with an early Run 2 dataset of 15.5 fb^{-1} [94][3]. The conventional dijet analysis has excluded couplings of 0.25 at new high masses up to 3.5 TeV [95]. A further analysis sets limits in the search for b-tagged dijet resonances [96].
Resonance searches in top quarks pairs are similarly conducted, which is a relevant decay channel in the range where $m_{Z'} > 2m_t$. Run 2 results from ATLAS [97] set upper limits on quark couplings of 0.15-0.25 in the mediator mass range 500 GeV to 3 TeV. Here only the top leptonic decay channel ($t \to W^+b \to \ell^+\bar{\nu}b$, and the anti-particle equivalent) has been exploited: Although the top decays hadronically ($t \to W^+b \to q\bar{q}b$) 66% of the time, low lepton trigger thresholds and the low rate of electroweak background means the leptonic channel offers the same sensitivity.

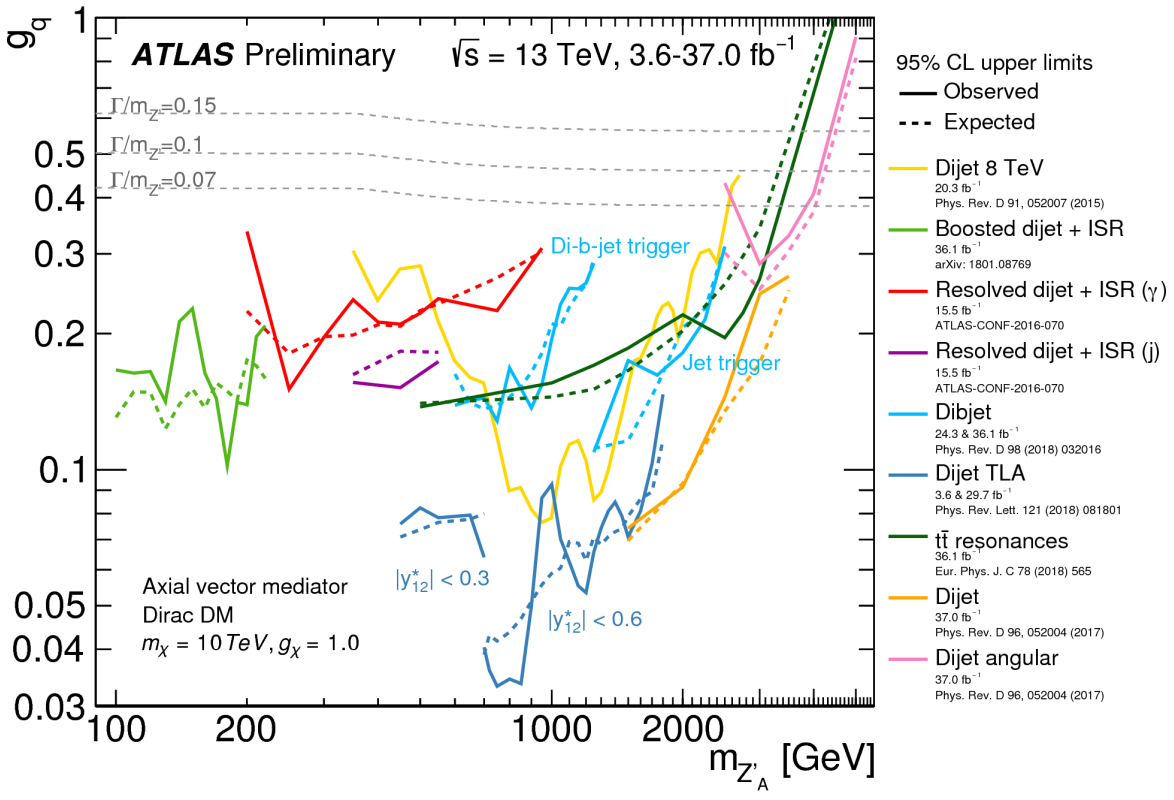

Figure 8.2: ATLAS combined upper limits on the coupling, g_q, as a function of mediator mass. The assumed model is an axial vector Z' with couplings to quarks and Dirac dark matter and zero coupling to leptons. Results are from dijet searches on 2015-2016 datasets imploying different search strategies that are described in the text. The dashed lines represent expected limits. The solid lines present the observed limits. Taken from [39].

[3]At the time of writing the latest results had not yet been published.

Chapter 9

The Trigger-object Level Analysis

9.1 Introduction

A major bottleneck for the recording of ATLAS data is the data transfer to Tier0. To regulate the output with increasing instantaneous luminosity, the lowest HLT single jet trigger threshold has been raised from 360 to 420 GeV during Run 2[1] - refer to Table 9.1. This similarly has shifted the starting low mass point in the dijet mass spectrum upwards, as this point roughly corresponds to twice that of the leading jet p_T.

year	L1 jet trigger	HLT jet trigger
2015	L1_J75	HLT_j360
2016	L1_J100	HLT_j380
2017	L1_J100	HLT_j420
2018	L1_J100	HLT_j420

Table 9.1: The lowest unprescaled Level-1 and HLT single jet triggers used during nominal running operations typical of that year are shown for the Run 2 period. Thresholds are given in GeV.

The development of the Trigger-object Level Analysis (TLA) technique within ATLAS is driven by the motivation to search for dijet resonances below the HLT trigger threshold, as described in the previous chapter. It uses a dedicated physics recording stream, the data scouting (DS) stream, which saves only the bare minimum information that is needed for a multi-jet search and relies on the fact that HLT reconstruction and offline algorithms are similar. This results in a 95.5% reduction in event size, casting the bandwidth of this recording stream negligible: There is no ill-effect of loosening the HLT single jet trigger threshold for this stream. In fact, the TLA does not rely on an HLT trigger at all, but records every event seeded by a Level-1 single jet trigger.

The plot in Figure 9.1 is the invariant dijet mass spectrum constructed from data recorded in the ATLAS main physics and DS stream. The blue line represents all data collected by single jet triggers in the physics main stream. This includes unprescaled triggers as well as prescaled low p_T triggers that record a fraction of events for calibration

[1]It is interesting to note that this is an age-old problem at hadron colliders. For example, a dijet analysis publication from the UA2 experiment at the $Sp\bar{p}S$ notes that their low-mass trigger threshold had to be raised from 66 GeV to 80 GeV between the years 1989 and 1990, and indeed "[i]n order for the UA2 trigger and data acquisition system to handle the high jet production rates with minimal dead time, data from tracking detectors were not read out for low mass two-jet candidates." []

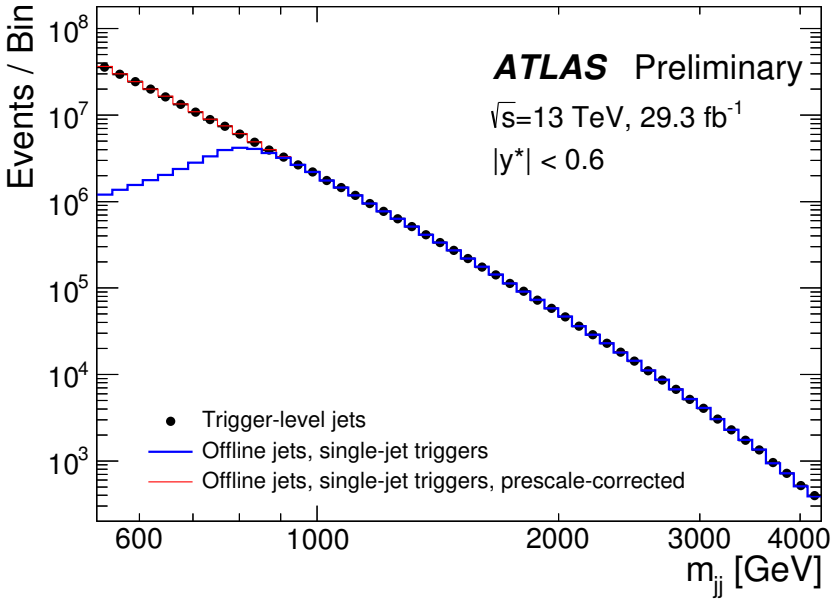

Figure 9.1: The dijet mass spectrum is shown for 3 different sets of data collected during the LHC 2016 physics running period: jets collected by all prescaled single jet triggers in the *main physics stream* (blue), the same jet events multiplied by the prescale factor (black) and so-called "trigger-level" jets (defined in text) collected by the *data scouting stream* (red). Several magnitudes of dijet data below 800 GeV dijet mass were recorded via the data scouting stream, which would otherwise not have been kept.

purposes. The black line is the same distribution but corrected for the prescale. Finally, the red line in Figure 9.1 represents the dijet event data that is recovered via the data scouting stream. The benefit is clear: the full statistical power of the LHC delivered data is kept and made use of down to mass ranges beyond HLT limitations. A mass limit at $\sim 440\,\text{GeV}$ remains, corresponding to the lowest unprescaled Level-1 jet trigger.

The challenging aspect of the TLA lies in the fact that it uses a different recording stream and a different data collection to any other search in ATLAS. It requires dedicated work towards a tailored calibration without the use of full detector information, in particular tracking information. The technicalities related to data recording and jet calibration are described in sections 9.2 and 9.3, in which final results show that despite the limited information, jets reconstructed at HLT can be measured with almost the same precision as offline jets. A particular challenge however remains in the mitigation of pile-up jets at low p_T, for which tracking information becomes essential. The current TLA does not use jets with a p_T below 85 GeV as a result. However, in section 9.4 this constraint is shown to have minimal impact on the Run 2 TLA dijet analysis.
This picture changes when considering the use of TLA data in other more complex jet topologies. These are explored in the second half of the chapter, section 9.5, dedicated to future developments for the TLA. It is studied to what extent alternative searches involving TLA jets are affected by pile-up jets. The studies lead up to the motivation of the benefits of a new ATLAS trigger upgrade, the Fast Tracker (FTK), which will serve to minimise the remaining difference between trigger-level and offline jets: the use of tracks. The upgrade will offer TLA a handle on pile-up for the first time, thereby enabling interesting developments for the use of the TLA technique.

9.2 The data scouting stream

The ATLAS data scouting (DS) stream has been recording data since 2015. The bare minimum information is written to the data scouting stream: The four-momenta of all jets above 20 GeV and several variables computed from detector information within the jet. The additional variables are calorimeter-based variables such as the ones that are used in a global sequential calibration of jets, and quality variables used to reject noisy jets. This is in contrast to the main physics stream where the full detector information (such as all calorimeter cells and tracking channels) is written out. The event size for a data scouted event is 30 kB, whilst a main physics event size is around 2.5 MB.
The fraction of the data scouting stream recording rate and bandwidth with respect to the total for the ATLAS recording system, is shown in the two pie charts in Figure 9.2. Despite the DS stream consuming almost half of the rate pie chart, the DS bandwidth occupies only 1% of the total ATLAS bandwidth, owing to the small event size.

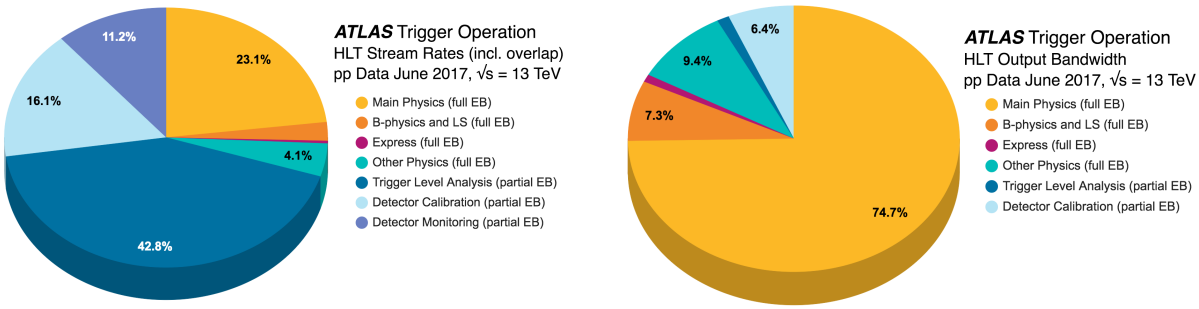

(a) The data scouting stream for TLA records at the highest rate. The physics stream for full-detector information events used by most physics analyses runs at almost a quarter of the total rate. Besides the dedicated B-Physics and Light States (LS) stream for B-physics and the 'other physics' stream (data collected by prescaled triggers for physics data calibration), the remaining streams are essential for the real-time calibration of the detector and prompt flagging of potential issues within the detector.

(b) Owing to the large event size of a main physics event, the main physics stream occupies almost 3/4 of the total bandwidth. The data scouting stream for TLA in contrast occupies only a percent.

Figure 9.2: Pie charts depicting the HLT recording rates (left) and HLT output bandwidth (right) for different recording streams in the ATLAS TDAQ system.

The main triggers for the collection of data in the DS are tabulated in 9.2, along with the amount of data that has been collected in total, and the corresponding jet p_T at 99% trigger efficiency.

The majority of data in the DS is collected by the lowest unprescaled Level-1 trigger, L1_J100, which is activated at all times. The data amounts to a total of 132.8 fb^{-1}(the 2016 dataset contains 29.7 fb^{-1}). The Level-1 J75 was activated during periods of low luminosity running conditions, such as during the commissioning year of 2015 and periods at the start of the year, which is why the total amount of data is only at 6.5 fb^{-1}. The L1_J150 trigger was previously activated towards the end of an LHC fill once the instantaneous luminosity has dropped below a certain threshold, with a prescale of 20. It was replaced by the L1_J150_DETA2 trigger that makes use of L1Topo to select

L1 jet trigger	$\mathcal{L}$	p_T at 99% trigger efficiency
L1_J100	29.0 fb^{-1}	220 GeV
L1_J75	6.5 fb^{-1}	185 GeV
L1_J50(_DETA2)	20.5 fb^{-1}	150 GeV
L1_J40	3.2 fb^{-1}	120 GeV

Table 9.2: The total amount of data in fb^{-1} collected by various triggers for TLA per year since the data scouting stream was activated. The corresponding lowest leading jet p_T at which the trigger is 99% efficient is also shown.

the most energetic Level-1 Jet pairs with an η difference less than 2, which compliments the y^* selection in the final analysis. The reduced rate after the topological requirement had allowed the trigger to run without prescale towards the end of a run. A total of 20.5 fb^{-1}had been collected with Level-1 J50 triggers. The Level-1 J40 was activated towards the end of 2018. It similarly was only activated at the end of a fill, with a prescale of 4. DS triggers introduced in the second half of Run 2 have extended the lower mass range to approximately 300 GeV for the next iteration of the TLA.

9.3 Trigger-level jet calibration

Jets recorded by the DS stream are referred to as *trigger-level jets*, to distinguish them from *offline jets* that have been reconstructed from the recorded data of the main physics stream.

The reconstruction of trigger-level jets has been described in the Atlas Trigger chapter, section 6.2, as this occurs during trigger processing. Unlike the calibration employed at HLT, which uses offline calibration factors directly, trigger-level jets are recalibrated after the recording of data in order to achieve a good precision of the jet energy for physics analysis. One of the main challenges for the TLA is to achieve this precision with reduced event information.

The trigger jet calibration chain is shown in Figure 9.3, where the *jet-area based pile-up correction* is the only calibration step that is retained from the HLT calibration sequence; subsequent calibration steps are applied after the recording of the event. A large part of the procedure is similar to that of offline jets where, following validation,

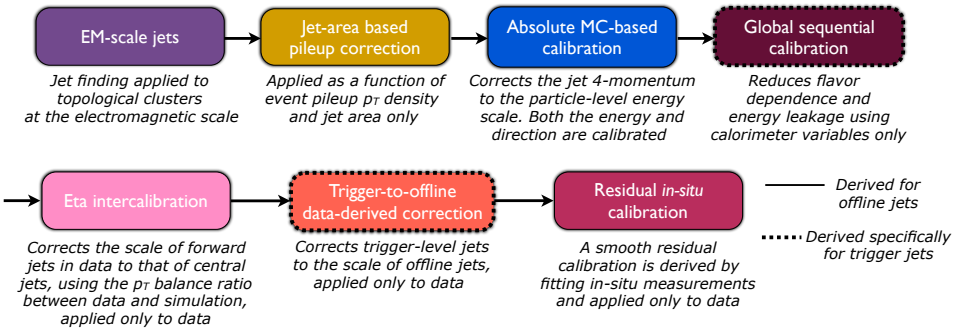

Figure 9.3: The TLA calibration chain.

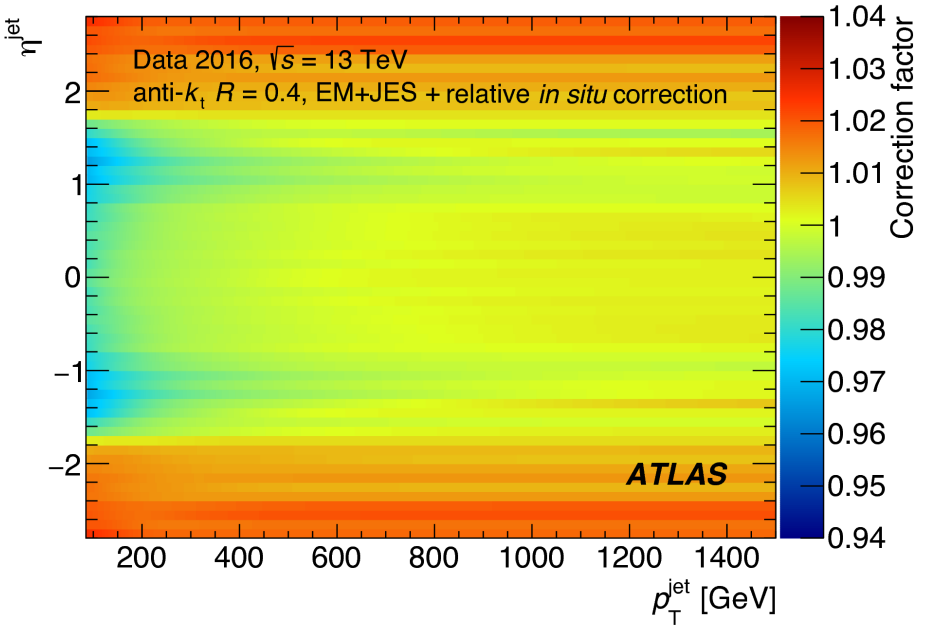

Figure 9.4: The correction factor that is applied to trigger-level jets after the relative in situ calibration, based on the p_T response between trigger-level and offline jets and derived from data in bins of jet η and p_T is shown. Taken from [92].

the same corrections could be applied to trigger-level jets. The calibration steps that are rederived or added for trigger jets on account of having only calorimeter information are outlined with dashed lines in the diagram and described in more detail in the following.

The *global sequential calibration (GSC)* necessarily differs from the offline corrections due to the lack of track-based jet attributes. Instead, a dedicated GSC is derived with the following calorimeter-based variables, which are computed online for each jet:

- f_{Tile0}: the fraction of jet energy deposited in the first Tile calorimeter layer.
- f_{EM3}: the fraction of jet energy deposited in the last layer of the LAr calorimeter.
- N_{90}: the minimum number of topo-cluster constituents in which 90% of the jet energy is contained.

The first two variables account for variations in the energy sampling depending on the jet's longitudinal shape, as in offline. The last variable is a measure of the jet constituent multiplicity and is thus a replacement for n_{trk} used in the offline calibration, accounting for the difference in energy response between gluon- and quark-initiated jets.
Unique to this calibration chain is the *trigger-to-offline data-derived correction*, applied after the eta intercalibration, in which trigger-level jet energies are scaled to match the energy of offline jets. A correction factor is derived as function of p_T and η by matching trigger to offline jets in data and computing the p_T ratio. The final factors are shown as function of p_T and η in Figure 9.4. The correction varies from less than 1% for jet $p_T^{jet} > 400$ GeV to 2% for $85 < p_T^{jet} < 100$ GeV and 3% for $|\eta^{jet}| > 2.0$.
This brings the trigger jets to the same scale as the offline jets prior to the final *residual in situ calibration* calibration step. This step has been slightly modified for trigger-level jets, after it was realised that the offline factors induced fluctuations in the

data. Specifically, the non-smoothness occurred from the splicing of the $Z + j$, $\gamma + j$ and *multi-jet* samples described in Section 5.3.2. The TLA-dedicated factors were sufficiently smoothened to better than the statistical precision of the TLA.

The total uncertainty for trigger jet energy scale that is achieved is on the 1-2% level in the kinematic range of TLA, which is overall within 1% of the respective offline uncertainties.

Offline calibration steps, described in section 5.3.2, that do not exist for trigger-level jets are

- The origin correction.
- The pile-up residual correction as a function of μ and number of primary vertices.
- A GSC correction based on the track width, the number of tracks and the number of muon segments.

There is additionally no jet-vertex-tagging for trigger-level jets.

Considering the difference in the calibration steps, the level of precision in energy measurement achieved for trigger-level jets with respect to offline jets within the relevant kinematic range has been highly successful.

9.4 Pile-up effects in dijets

Although the TLA applies a minimum 85 GeV jet p_T selection to avoid the effects of pile-up, it can be shown that this turns out to impose no limitations. The reason is that the low jet p_T asymmetry for the jet pair means that the second jet will be close to as energetic as the leading jet. The dijet mass spectrum for a minimum leading jet p_T of 120 GeV is shown in Figure 9.5, where the p_T threshold corresponds to a fully efficient TLA Level-1 J40 trigger - the lowest threshold TLA trigger activated in Run 2. In this case the fully calibrated offline jet collection in data is used, collected by a prescaled HLT trigger. In order to identify the pile-up jet contribution, the offline jet-vertex-tagger is used to suppress jets with an efficiency of 92%. The kinematic selection is $|\eta^{jet}| < 2.4$ and $y^* < 0.6$ for the jet pair. The mass spectrum is shown both for minimum jet p_T of 20 GeV and of 85 GeV, where in the case of the former, it is shown both for a jet selection in which pile-up jets have been suppressed and not suppressed. The lower panel of the plot depicts the ratio between the pile-up suppressed and non-suppressed spectrum. The mass spectrum rises and becomes smooth at a mass of around 300 GeV. It is evident that the 85 GeV p_T restraint only affects the spectrum below this point: lowering the minimum jet p_T does not increase statistics for the main spectrum. It is also evident that due to the energetic second leading jet, there is minimal pile-up contribution for a lowered jet p_T threshold of 20 GeV.

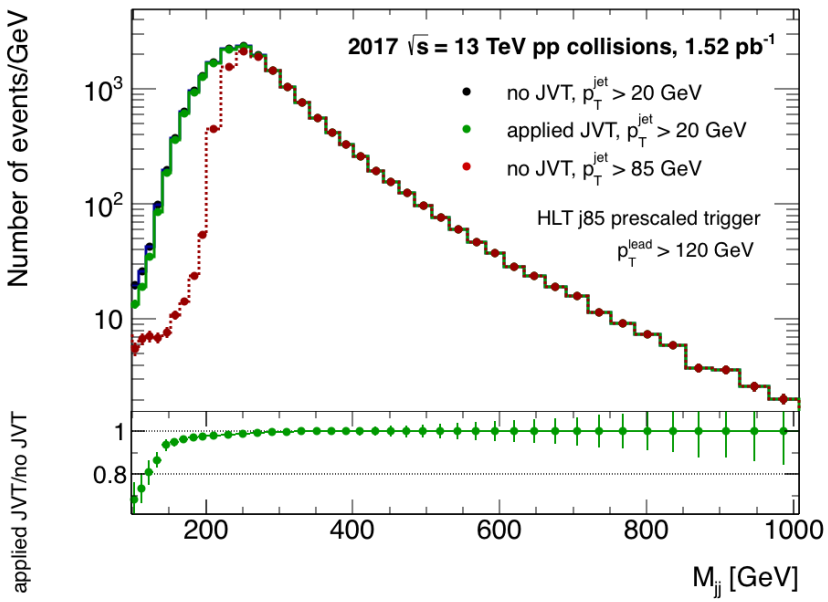

Figure 9.5: Invariant mass distributions in 2017 data for offline dijet pairs for a minimum leading jet p_T of 120 GeV, at which point a TLA Level-1 J40 trigger becomes fully efficient. Jets are paired after requiring $p_T^{jet} > 20$ GeV, $|\eta^{jet}| < 2.4$ and $y^* < 0.6$. The m_{jj} distribution after no further requirements is shown in dark blue ("no JVT"). The distribution for jet pairs that are not rejected by the jet-vertex-tagger (JVT) is shown in green ("applied JVT"). The distribution for jet pairs for which $p_T^{jet} > 85$ GeV is shown in red. The ratio between the histograms in which a JVT is applied/not applied, is shown in the lower panel.

9.5 Future developments for TLA

9.5.1 Future searches

The first successful use of trigger-level jets in a physics analysis has opened up many avenues that would benefit from lower trigger thresholds and that can be explored using the TLA technique.

One prospect is a TLA dijet+ISR search to extend the TLA dijet mass range. This is of interest as a TLA dijet+ISR search will have a larger amount of statistics compared to the offline equivalent owing to the lower trigger threshold requirement on the ISR, thereby offering the best sensitivity to dijet searches for the lowest mass range. It is planned to include a Level-1 photon trigger and the recording of reconstructed HLT photons in Run 3, which will enable a dijet+γ ISR search. The threshold limit for a Level-1 photon corresponds to approximately 50 GeV offline p_T.

Another avenue is the analysis of more complicated signature topologies of multijets. Multijet searches are to date mainly motivated by R-parity violating Supersymmetry [98–100] in which a small yet non-zero coupling to Standard Model quarks exist so that the decay of supersymmetric particles pair-produced in proton collisions results in a final state of multiple Standard Model jets, as depicted in 9.6a and 9.6b for stop and gluino pair

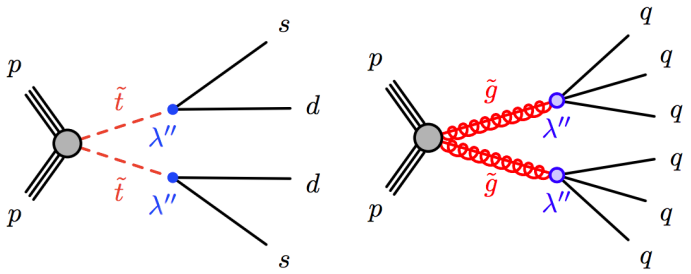

(a) stop pair production and direct decay to SM.

(b) gluino pair production and direct decay to SM.

Figure 9.6: The pair-production of top squarks (a) [98] or gluinos (b) [100] from the strong interaction, with direct decays into quarks through an R-parity-violating (RPV) coupling, denoted by λ". RPV Supersymmetry has so far been the main motivation for low mass resonance searches in high multiplicity of jets.

production[2]. Results from LHC experiments have increasingly disfavoured the simplest RPV supersymmetry models, excluding the existence of a stop particle in the mass range of 80 to 410 GeV [98, 99] and a gluino in the mass range of 200 to 1500 GeV [105], so that only very low and very high mass regions remain unexcluded.
Multijet signatures also emerge in a direct probe of the dark matter sector, such as in dark matter mediator decays to top quarks, which undergo hadronic decays. This signature was briefly mentioned in Chapter 8 in the context of an axial vector dark matter mediator. A dark matter mediator coupling to tops is also strongly motivated in "top-philic" models [106, 107], in which a new scalar mediator with Higgs-like Yukawa couplings to quarks is postulated, therefore coupling most strongly to the heaviest quark. Scalar dark matter mediator decay topologies are shown in Figures 9.7a and Figure 9.7b, for dark matter mediator production through loop-induced gluon fusion and with associated heavy flavour quarks, respectively. The decay to the next heaviest quark, the b quark, is also shown, which becomes a relevant signature in scenarios in which the decay to tops is not kinematically allowed.

The use of TLA jets is an opportunity to search for resonances in complex multijet topologies as motivated by the production of very low mass supersymmetric particles, dark matter mediators that result in top final states (although in this case online b-tagging information is required in addition), or model-agnostic multijet searches. The searches would benefit from the statistical gain provided by the lower jet thresholds in TLA as well as an extension to lower masses.

Finally, another prospect is to extend the technique to other objects entirely, such as a search in a resonance of two photons or b-tagged jets reconstructed at trigger-level.

[2]The allowable decay to SM particles in RPV Supersymmetry means that many supersymmetric models can no longer accommodate an LSP as a dark matter candidate. However, it is possible to reconcile supersymmetry with dark matter if either an axino [101, 102](the superpartner of the hypothetical QCD axion) or gravitino [103, 104] are postulated as the lightest supersymmetric particle, as they inherently have such a small coupling to the Standard Model that it is possible for their lifetime to exceed the age of the universe.

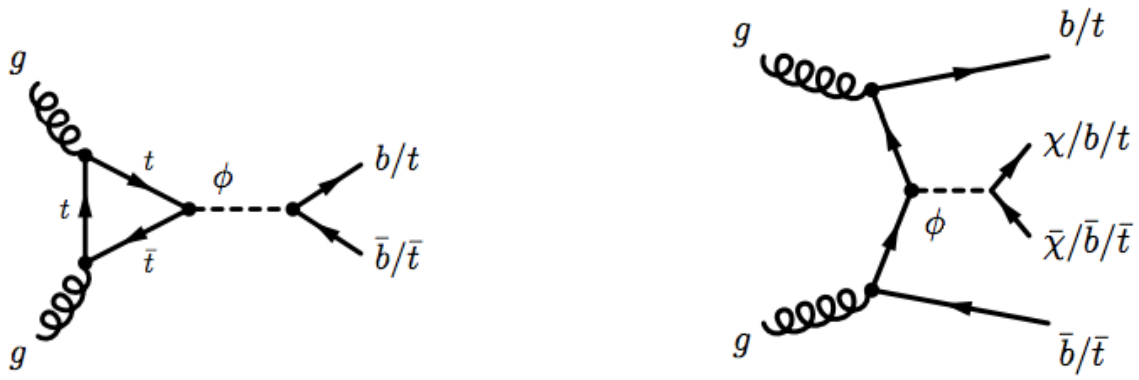

(a) Loop-induced gluon fusion production of a (pseudo)scalar dark matter mediator.

(b) Scalar dark matter mediator production with associated heavy flavour quarks.

Figure 9.7: Processes involving the production of a new scalar mediator with Higgs-like Yukawa couplings to fermions.

9.5.2 Search feasibilities in the presence of pile-up

The feasibility of searches introduced in the previous section within a TLA framework are explored in the following, in particular the extent to which pile-up effects play a role. Since the TLA is not able to separate hard scatter from pile-up jets, the technique is currently limited to jets with a p_T above the pile-up jet spectrum, resulting in a minimum p_T threshold of 85 GeV.
The following studies makes use of offline jets that have been fully calibrated down to 20 GeV. Pile-up jets are identified and removed using the offline jet-vertex-tagger (JVT) with a working point efficiency of 92%. Only jets with $p_T < 120$ GeV are considered by the JVT; more energetic jets are automatically identified as hard scatter jets.

Pile-up in a TLA dijet+ISR search Currently the lowest possible mass probed by the dijet TLA is approximately 300 GeV, using DS triggers activated in 2018. A TLA dijet+ISR search would be used to extend the mass range below this point. Whilst pile-up contributions remain minimal for masses at 300 GeV (Figure 9.5), effects become visible for lower masses. The pile-up jet contribution in a dijet+ISR search is demonstrated in Figure 9.8 where the invariant mass distribution following a dijet+ISR analysis selection is shown based on the same data as in Figure 9.5. The leading jet is taken to be the ISR and the second and third leading jets are paired. The distributions have the following common requirements: $p_T^{leading\ jet} > 150$ GeV (corresponding to the p_T at which a L1_J50 trigger is fully efficient), and $p_T^{jet} > 20$ GeV, $|\eta^{jet}| < 2.4$ and $y^* < 0.6$ for the second and third leading jets. The invariant mass distributions analogous to the plot in Figure 9.5 are again depicted. It is shown that the fraction of jets in the spectrum that contain pile-up is 2-10% for masses between 200 and 250 GeV, and 10-25% for masses below 200 GeV, as indicated by the ratio. It is additionally noted that the ratio exhibits a variable behaviour, caused by an increase in the pile-up contribution in the mass range of 100 to 150 GeV. It is thus evident that not only is the pile-up contribution to the dijet background a sizeable effect, but it also appears to induce structure in the invariant

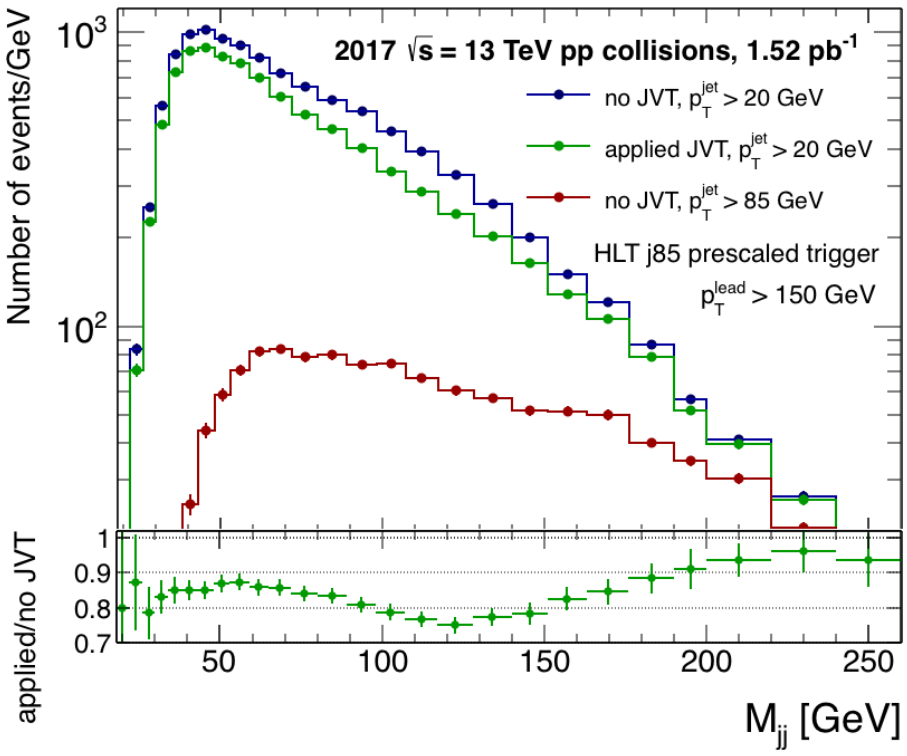

Figure 9.8: Invariant mass distributions for offline dijet pairs after a dijet+ISR selection. The leading jet, taken to be the ISR, is required to have a minimum p_T of 150 GeV. The second and third leading jets are paired after requiring $p_T^{jet} > 20$ GeV, $|\eta^{jet}| < 2.4$ and $y^* < 0.6$. The m_{jj} distribution after no further requirements is shown in dark blue ("no JVT"). The distribution for jet pairs that are not rejected by the jet-vertex-tagger (JVT) is shown in green ("applied JVT"). The distribution for jet pairs for which $p_T^{jet} > 85$ GeV is shown in red. The ratio between the histograms in which a JVT is applied/not applied, is shown in the lower panel.

mass distribution. This is in contradiction to the primary assumption in the derivation of a background estimate for dijet resonance searches, namely, that the dijet spectrum is smooth. It is further shown that the requirement of $p_T^{jet} > 85$ GeV reduces statistics by up to an order of magnitude, thereby reducing the statistical sensitivity of the TLA.

Pile-up in a TLA multijet search Pile-up effects become especially pronounced in the selection of a high multiplicity of jets. This is made evident in Figure 9.9, which simply depicts the jet multiplicity for events that contain at least six jets for which $p_T^{jet} > 20$ GeV and $|\eta^{jet}| < 2.4$, for two L1 triggers. The jet multiplicity is shown in the case of no pile-up rejection and with pile-up rejection for the same events. The fraction of events that still contain a minimum of six jets following the JVT selection is 0.42 and 0.26 for a minimum leading jet p_T of 220 and 120 GeV, respectively. That is to say, for a TLA L1_J100 (L1_J40) trigger, the multijet background for a six-jet selection is increased by ∼58 (74)% from the inclusion of pile-up jets.

The large background from pile-up reduces the significance of a signal, the extent to which is measured in the case of a top quark resonance and a Z' ditop resonance at a mass of 500 GeV. In each case, the tops decay hadronically, $t \to q\bar{q} + b$, giving rise to six-jet final states. The $t\bar{t}$ events have been generated in POWHEG [108], and the

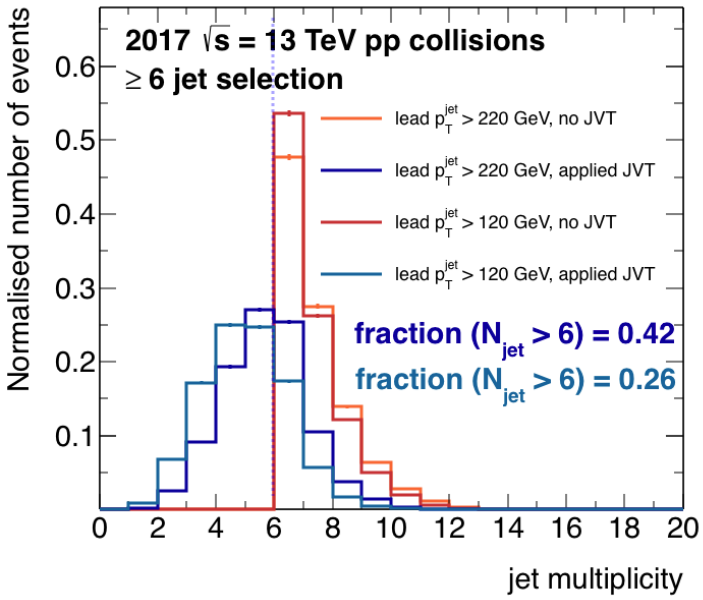

Figure 9.9: The jet multiplicity for a 2017 data run is shown for a minimum leading jet p_T of 220 GeV (red) and 120 GeV (orange) after requiring ≥ 6 jets for which p_T^{jet} and $|\eta^{jet}| < 2.4$. The jet multiplicity for the same events are shown after pile-up jets < 120 GeV are rejected by the jet-vertex-tagger.

showering process simulated in PYTHIA [57], whilst the Z' sample has been exclusively simulated in PYTHIA, with vector (axial vector) coupling stengths identical to those of the electroweak Z boson[3].
The multijet background is estimated using data, collected with a prescaled trigger. Owing to the limited statistics in data, there is no b-tag jet identification. Signals are therefore treated as three-jet decays of any quark flavour of an unknown particle.

A basic event selection is applied. A minimum leading jet p_T of 150 GeV is required, corresponding to a full trigger efficiency for a Level-1 J50 trigger[4]. Each event is required to have a minimum of six jets with $p_T^{jet} > 20$ GeV and $|\eta_{jet}| > 2.4$. The six leading jets are sorted into triplets by simply minimising $\sum(\Delta R)$, defined as

$$\sum(\Delta R) = (\Delta R_{i,j} + \Delta R_{i,k}) + (\Delta R_{l,m} + \Delta R_{l,n}), \tag{9.1}$$

computed for every combination of $\{i, j, k\}$ and $\{l, m, n\}$ for the six jet indices.
The mass asymmetry of the jet triplets, $t1$ and $t2$, is required to be less than 0.1,

$$A_{m_{t1},m_{t2}} = |\frac{m_{t1} - m_{t2}}{m_{t1} + m_{t2}}| < 0.1. \tag{9.2}$$

The reconstructed Z' is the sum of the $t1$ and $t2$ four-momenta. The same event selection is applied after the removal of jets identified as pile-up.

[3]The vector (axial vector) coupling strength is 0.18 (0.5) and 0.35 (0.5) for up-type and down-type quarks, respectively.

[4]Although the L1_J50 trigger was activated only at the end of an LHC fill in Run 2, it is a fair assumption that with an additional requirement of a high ($\geq$ 6) multiplicity of jets at HLT(for a future multijet-dedicated TLA trigger) may reduce rates sufficiently to allow a similar threshold to run unprescaled. Refer to Appendix A.2 for the minimum p_T thresholds already allowed for multijet triggers in the conventional physics recording stream.

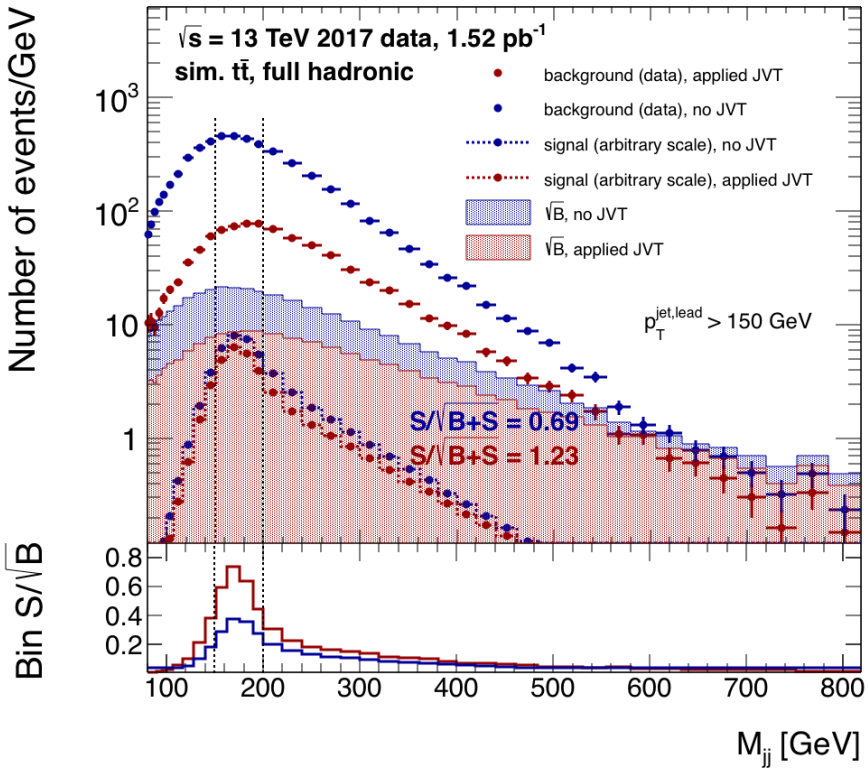

(a) Top reconstructed resonance

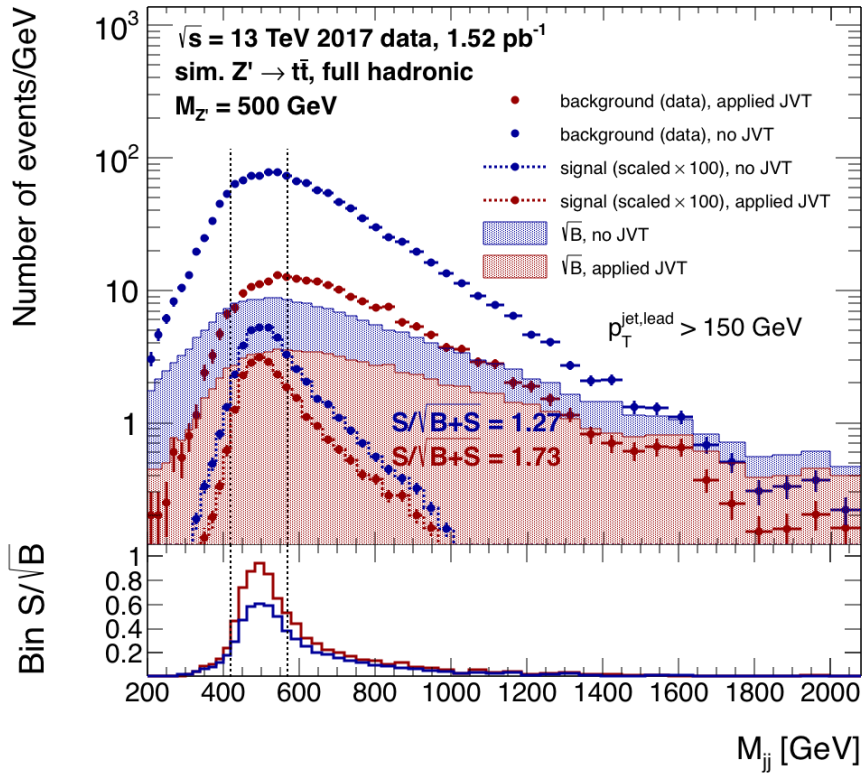

(b) ZPrime reconstructed resonance

Figure 9.10: Invariant mass distributions in signal and background are shown for (a) a top resonance and (b) an axial vector mediator resonance decaying to a $t\bar{t}$ final state. Distributions in blue have no pile-up rejection; Distributions in red include pile-up rejection. The background is derived from data collected by the prescaled HLT_j65 trigger. The top signal has been arbitrarily scaled, the Z' signal has been increased by a factor of 100. A minimum leading jet p_T of 150 GeV is required. The full event selection is described in the text.

The invariant mass distribution for a top (M_{jjj}) and Z' ($M_{t\bar{t}}$) are shown for both signal and background in Figures 9.10a and 9.10b, where the signal has been arbitrary scaled. The dashed line indicate the mass window for which $S/\sqrt{B+S}$ is calculated, whilst the bottom panel reflects the bin-by-bin signal significance. The pile-up contribution increases a multijet background by almost a magnitude. As a result, the significance of the top (Z') resonance is reduced by a factor of ∼2 (1.5).

In order to evade the pile-up contribution, it would be necessary to retain the minium p_T constraint of 85 GeV for all jets as in the TLA Run 2 dijet search. However, this severely limits the signal acceptance - in fact, it becomes worse than the signal acceptance gained in offline data, where lowered thresholds in multijet triggers are made use of. The signal acceptance of a six-jet signal for a $Z' \to t\bar{t}$ resonance at a mass of 500 GeV is compared in TLA-like jet thresholds and offline-like thresholds in Figure 9.11. The TLA-like jet thresholds are based on the L1_J50 trigger with a leading jet p_T 150 GeV, and the signal acceptance is shown both for the case of a minimum jet p_T requirement of 85 GeV and 20 GeV (the latter representing an ideal TLA, in which all recorded jets are calibrated and used). The offline jet thresholds are based on the lowest multijet trigger[5], HLT_5j65, which reaches full efficiency once the fifth leading jet $p_T > 75$ GeV. The current TLA imposes larger p_T constraints than what is necessary in an offline analysis. However, if the full p_T spectrum of recorded TLA data could be exploited, the signal acceptance would increase ten-fold.

9.5.3 Tracks in TLA

The lack of tracks is currently the main difference between a TLA and a conventional offline analysis and becomes limiting for extended TLA searches to lower dijet masses and higher jet multiplicity. This has made the new ATLAS trigger upgrade, the Fast Tracker (FTK), key to the expansion of the use of the TLA. FTK is designed to perform rapid track reconstruction at HLT for the full event, providing tracking information for every Level-1 accepted event and thus enabling the necessary developments for the TLA technique.

FTK tracks can be used to implement a jet-vertex-tagger for a TLA to mitigate the pile-up jet contributions outlined in the previous section. Moreover, track-based calibrations are expected to make a sizeable difference for the calibration of low p_T jets. For example, the usage of FTK vertices can be used for a pile-up NPV-based residual correction. The offline pile-up residual correction is shown to vary between 1 and 5 GeV for central jets. Whilst for 85 GeV jets this correction corresponds to an adjustment of 1% to 5%, for 20 GeV jets it corresponds to a sizeable adjustment of 5 to 25%.

Moreover, FTK will be pivotal in extending the TLA technique to new trigger-objects, such as b-tagged jets. Although HLT currently performs tracking for b-tagging jets, this is limited to HLT jets with $p_T > 225$ GeV in the case of a single b-jet trigger; or a leading HLT jet $p_T > 175$ GeV and a second leading jet $p_T > 60$ GeV in the case of a di-b-jet trigger (refer to Appendix A.2 for a full list of b-jet triggers used in 2017). In order to

[5]The trigger is employed by the ATLAS offline full-hadronic ditop resonance search on 2016 data that is not yet published.

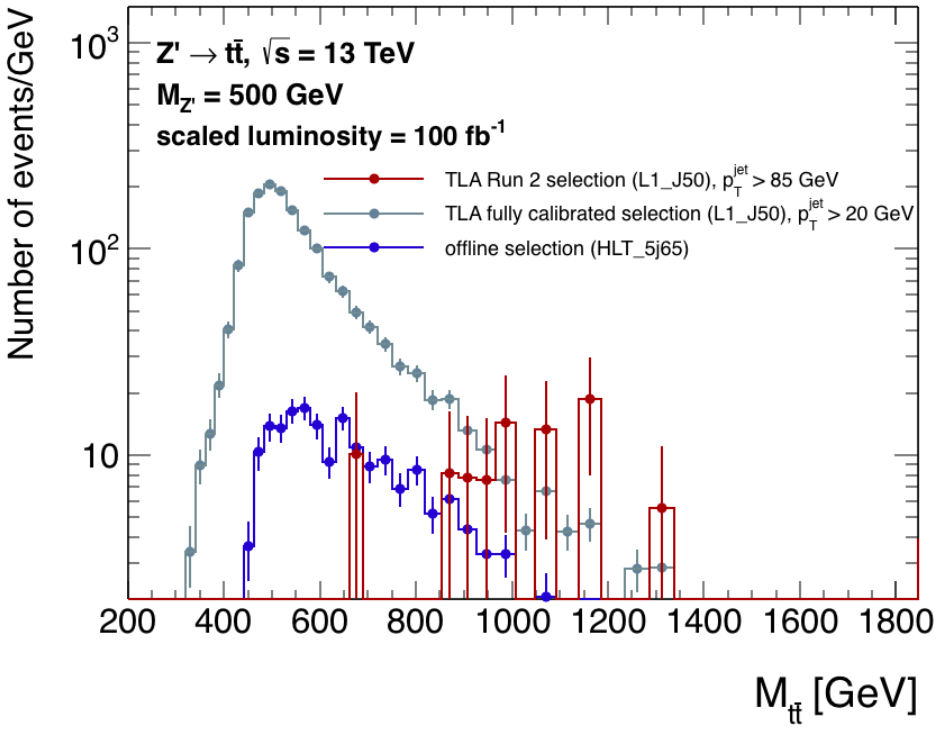

Figure 9.11: The reconstructed $t\bar{t}$ resonance for a simulated axial vector dark matter mediator with a mass of 500 GeV is shown in the case of a TLA-like selection with a minimum jet p_T constraint of 85 GeV (red) and 20 GeV (light blue), as well as an offline-like selection (dark blue). For the TLA case, an L1_J50 trigger and a minimum leading jet $p_T > 150$ GeV, are assumed. For the offline case, an HLT_5j65 trigger and a minimum jet $p_T > 75$ GeV for the fifth leading jet, are assumed.

achieve a greater sensitivity with respect to offline in the analysis of di-b-jet and ditop resonances, FTK becomes necessary to perform b-tagging of all jets recorded in the TLA.

Chapter 10

The new Fast-Tracker: online tracking

Due to the combinatoric nature of track finding algorithms, CPU time for track reconstruction scales quadratically with the number of track hits, which in turn scales linearly with luminosity [109]. In other words, tracking is a precious commodity in trigger processes. In Chapter 6 it has been described how current online tracking is used only sparingly by limiting the reconstruction to *Regions of Interest* and to trigger chains where it is crucial, such as b-tagged jet, electron, tau and muon triggers. It however remains one of the most CPU-intensive online algorithms [72]. The Fast Tracker (FTK) has been envisaged to provide full-event "fast tracks" for the High Level Trigger for every L1 accepted event, thereby relieving current track finding restraints at trigger level.

The first section of this chapter begins with an outline of the physics motivations of the FTK project. This is followed by a description of the Fast Tracker (FTK) hardware and FTK track reconstruction, section 10.2. Finally, as the primary focus within this work is the usage of FTK tracks in jets, a description of the integration of the FTK tracks in the jet trigger jet reconstruction is provided in section 10.3.

10.1 Physics Motivation

In addition to the physics motivations for FTK in a Trigger-object Level Analysis outlined in the previous chapter, FTK will benefit numerous signatures in offline analyses by improving the acceptance of physics signatures.

Tau lepton and b-jet triggers suffer from high trigger thresholds, owing to their extensive use of online tracking. The lowest threshold for a triggering on a single b-jet(tau) is 225 GeV(100 GeV) in Run 2. This has reduced the sensitivity to low p_T SM signatures such as the Higgs decay channels $H \to b\bar{b}$ and $H \to \tau\bar{\tau}$. Fast tracking at HLT will relieve the processing time that is currently needed for HLT tracking, allowing for lower thresholds for b-jet and tau triggers as they become less constrained in their usage of tracks. This increases the acceptance efficiency of the Higgs decay channels, and otherwise open up searches for beyond the Standard Model low-mass resonances of a similar signature.

Full-scan track and vertex reconstruction cannot currently be performed in the HLT. However, this would offer substantial benefits in the increasingly intense collision envi-

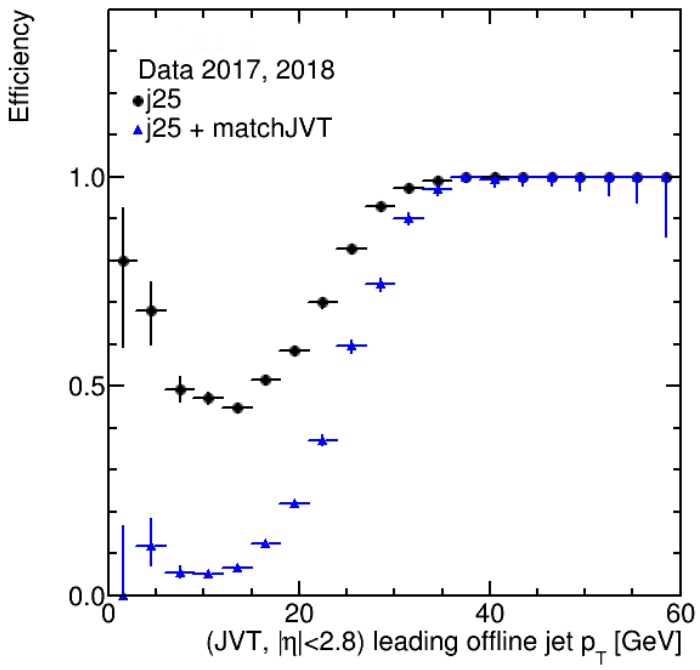

Figure 10.1: The trigger efficiency curve is shown for the HLT_j25 trigger in data with respect to the leading offline jet p_T before and after the removal of pile-up jets identified by the JVT. The black curve represents a trigger selection on all HLT jets, the blue curve represents a trigger selection after HLT jets identified as pile-up jets are removed - representing an online JVT selection. HLT jets are identified as pile-up by matching them to offline jets and using the offline computed JVT variable [110].

ronment at the LHC. It offers a way to distinguish in-time pile-up jets from hard scatter signals, thereby reducing the trigger rate for triggers that rely on jets.
A large fraction of events pass a low p_T jet trigger selection because of pile-up jets, as illustrated in the trigger efficiency curve of Figure 10.1 for the prescaled HLT_j25 trigger. The event rate can be reduced by 50% with the use of early pile-up jet rejection - this is the difference between the black and blue curve. In this case, the rate is reduced by 4 Hz, which is 12% of the lowest unprescaled HLT single jet trigger. More significant rate reductions are expected for multijet triggers. Moreover, pile-up jet rejection would concurrently reduce the rate of $E_{\mathrm{T}}^{\mathrm{miss}}$ and ΣE_T triggers, which rely on the sum of jet transverse energies. The rates for these triggers are especially sensitive to pile-up, increasing non-linear with μ.

Finally, tracks can be used to improve online jet calibration, which in turn increases the trigger efficiency. Currently, a track-based GSC *is* applied to the limited jets at the HLT that have been processed in the b-jet trigger. The improvements in the trigger efficiency with the application of a track-based GSC can therefore already be demonstrated in the current trigger. Figure 10.2 is the trigger efficiency for the HLT_j450 trigger as function of the offline jet p_T. For a calibration based on track and calorimeter information, the offline jet p_T at which the single jet trigger reaches full efficiency is around 5 GeV lower compared to a calorimeter-only based calibration.

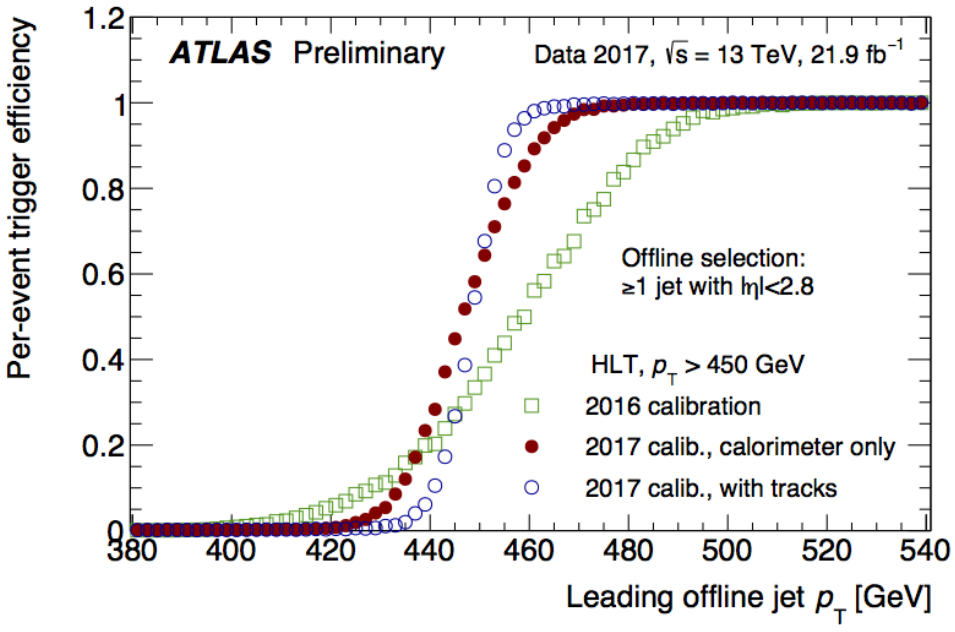

Figure 10.2: The trigger efficiency for jets with a p_T above 450 GeV at HLT is shown as a function of offline jet p_T. The green curve is the efficiency in which no global sequential calibration is used, whilst the red and the blue curves show the improvements when a calorimeter-only and calorimeter and track-based GSC, respectively, is used. Each additional calibration step is shown to extend the plateau of 100% trigger efficiency to lower p_T. Taken from [111].

10.2 Fast tracker system and track reconstruction

The Fast Tracker [112] is a parallel processing hardware-based system located in the same cavern as the Level-1 trigger system and is designed to reconstruct tracks at the Level-1 accept rate of 100 kHz. The design performance is 1 fit per nanosecond. This is firstly achieved by segmenting the detector region into 64 $\eta - \phi$ towers, each processed by separate hardware in parallel. Secondly, FTK performs tracking in two stages, the first of which makes use of a large bank of track templates (the pattern bank) and *associative memory* to match track hits to each template. In both stages, a track fit is obtained by performing a linear calculation of the hit coordinates and pre-calculated constants.

The FTK functionality is schematically presented in Figure 10.2. It consists of a Data Formatter (DF), Associative Memory (AM) boards, the Data Organizer (DO), the Track Fitter (TF) and the Hit Warrior (HW) unit, Second Stage Boards (SBB), the FTK-to-Level2 Interface Card (FLIC), and finally the FTK Read-Out Buffers (ROBs).

The FTK hit processing and track reconstruction can be divided into the following steps:

1. *Hit clustering and formation of "super-strips"*
2. *First-stage track finding*
3. *Second-stage track finding*

The steps are expanded upon in the following.

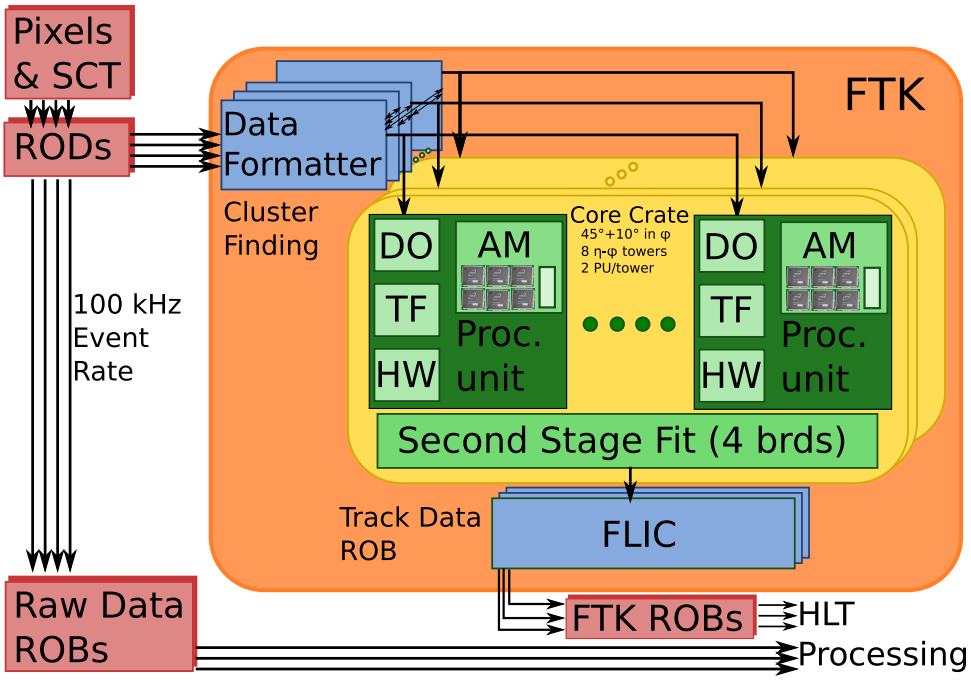

Figure 10.3: A schematic of the FTK electronics system is shown. The Data Formatter (DF) performs hit clustering and forming of super-strips and distributes the data to the processing units. One processing unit contains the Associate Memory (AM), Data Organiser (DO), Track Fitter (TF) and Hit Warrior. These complete the first-stage tracking on super-strips from 8 tracking layers: Namely, pattern matching, organisation of strips and identified track patterns, track fitting and removal of duplicate hits. The Second-Stage Boards (SSB) extrapolate and perform precision track fitting on hits from all 12 tracking layers. The FTK-to-Level2 Interface Card (FLIC) organises, fomats and sends tracks to the ATLAS Read-Out System. Taken from [112].

1) Hit clustering and formation of "super-strips": Hits are clustered and clusters are then formed into "super-strips" in order to reduce the amount of data processed during first stage tracking.
Data from the 4 inner pixel layers and the 8 silicon strip detector layers are transferred from the detector read-out drivers to the Data Formatter. Pixel hits are clustered by connecting hits side-by-side or diagonally in two dimensions and the cluster centroids are computed. SCT hits are already clustered in SCT front-end chips so that only minimal clustering is required to extend clusters across read-out channel boundaries. The maximum programmable cluster size is 7 by 9 pixels.
Henceforth hits refer to cluster centroids. The DF organises and sends the cluster centroids to the corresponding $\eta - \phi$ tower core crate (with some overlap to account for crate boundaries). Here, clusters from three pixel layers (including the IBL) and five SCT layers are combined into coarser resolution "super strips" (SS), which are then used in the pattern-recognition stage in the AM. The "super strip" resolution is set to be variable and can be optimised to achieve the best pattern finding efficiency however with a manageable data size and processing time. Hits are also pre-emptively stored in the Data Organiser, a database built on the fly, in which hits are addressed by the SS ID. This allows them to be easily retrieved in case of a successful match.

2) First-stage Track Finding: FTK stores a large pattern bank on its Associative Memory boards. The pattern bank is a stack of track pattern templates of super strips in the first 8 layers, derived in simulated ATLAS events. On the order of 1 billion patterns

are generated per tower [113].
As soon as super strips are created they are sent to the Associate Memory board. The AM achieves rapid track identification via large parallelism: as hits pass through they are compared to the corresponding layer in each loaded pattern simultaneously. The moment super strips hits in the last layer have been matched, successful pattern matches have been identified. A minimum of 7 successful hit matches is deemed a successful match. The track or tracks in the matched template are identified as "roads". The road ID is sent to the DO where full-resolution hits can now be retrieved via the road's associated SS IDs.
The Track Fitter accesses a unique set of constants for each silicon module which it uses to approximate a helical track fit to the hits via a linear calculation. Track fits require a minimum χ^2 in order for the track IDs to be passed on for second-stage fitting.
The Hit Warrior takes care of duplicate tracks: if two tracks overlap by a certain number of hits, the higher quality track is kept, where quality is measured by the χ^2 and the number of layers with a hit.

3) Second-stage Track Finding: The second stage aids in reducing the high fake rate of the first stage and improves the helix parameter resolution. Tracks that survive the first-stage χ^2 requirement are passed onto the SSB, where they are extrapolated to a further 4 layers across the Pixel and SCT detector. Nearby hits to the extrapolated curve are found and a full 12-layer fit is performed via linear calculation, in which the helix parameters are obtained. Again, a χ^2 requirement rejects any bad fits. Finally, the complete information such as the track hits, χ^2 values and helix parameters are passed on to the High-Level Trigger Read-Out System via the FLIC. The minimum p_T of reconstructed tracks sent to the HLT is 1 GeV.

The reconstruction of FTK vertices is performed in the HLT. The same procedure as has been described for the reconstruction of offline vertices, section 5.3.1, is used.

The efficiency for FTK track reconstruction relative to offline tracks are shown as a function of p_T and η in Figure 10.4a and 10.4b, respectively. The efficiencies were derived based on a simulated dataset containing hadronically decaying $t\bar{t}$ events. For an average pile-up of 46, the track reconstruction efficiency with respect to offline is 85% for 1 GeV tracks, rising to just below 95% for 10 GeV tracks. Along η the efficiency fluctuates around 88% and drops to 79% at $\eta > 2.4$. For an average pile-up of 69, the efficiency drops by 2% overall.

The fake rates for the same simulated dataset are shown as function of track p_T and η in Figures 10.4c and 10.4d, respectively. The fake reconstruction rate is around 5% for tracks below 5 GeV and can rise to 10% at higher momenta. The fake rate is strongly η dependent: for $|\eta| < 1$ it remains at a low 3% and reaches a 8% fake rate above $|\eta| > 2$. The same samples were used to establish the primary vertex reconstruction efficiency. The efficiency is around 42% with respect to offline [112].

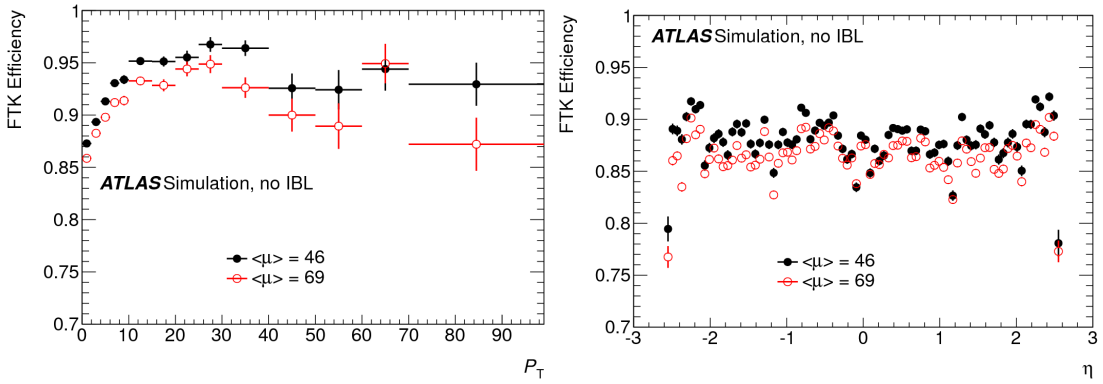

(a) Efficiency versus track p_T (b) Efficiency versus track η

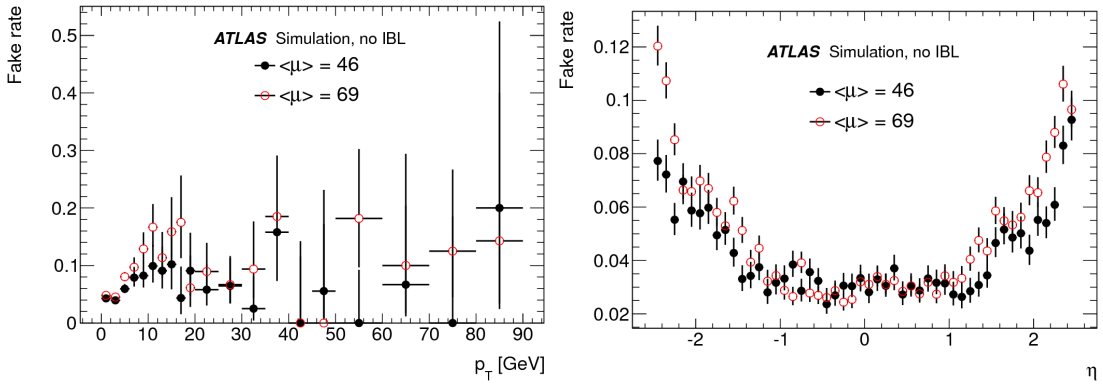

(c) Efficiency versus track p_T (d) Fake rate versus track η

Figure 10.4: The FTK track reconstruction efficiency and fake rates are shown as functions of p_T and η, based on simulated $t\bar{t}$ events. Efficiencies are measured with respect to offline tracks. Fake rates count tracks that cannot be matched to truth tracks. Black(red) points are derived from a simulated dataset with an average μ of 46(69). Taken from [112].

10.3 FTK-HLT jet trigger integration

The integration of FTK tracks in the HLT jet trigger occurs in the ATLAS Athena software. A detailed description of the HLT jet trigger software with integrated usage of FTK can be found in Appendix A.3.

FTK tracks in the jet trigger are used to define jet track attributes for each reconstructed FTK vertex. These are defined by first associating tracks to vertices and secondly ghost-associating tracks to jets that lie within the inner detector acceptance region, $|\eta| < 2.5$. The track-to-vertex association and the ghost-association of tracks is performed in the same way as in offline reconstruction that has been described in sections 5.3.2.2 and 5.3.2.2. The jet track attributes, defined in section 5.3.2.2, are n_{trk}, $\mathcal{W}_{trk}$, Σp_T^{trk}, JVF and JVFCorr.

The first two variables are to be used for the commissioning of an offline-like GSC for online jets. Σp_T^{trk} is used to calculate R_{p_T}, from equation 5.10. It is to be used together with JVFCorr to commission an online jet vertex tagger, to reject pile-up jets online. A TLA analysis will be able to use the same jet track attributes since, like the calorimeter based attributes, they are recorded along with the jet in the Data Scouting stream. Jets with recorded FTK track attributes are referred to as FTK jets.

The successful integration of the FTK system in the jet trigger is demonstrated in a comparison of the jet track attributes, n_{trk}, Σp_T^{trk} and $\mathcal{W}_{trk}$, between offline jets and FTK jets that have been matched within a radius of $\Delta R = 0.3$, in Figures 10.5 and 10.6. Comparisons in Figure 10.5 are based on a dataset of fully simulated $t\bar{t}$ events including simulation of the FTK system, whilst comparisons in Figure 10.6 are based on a 2017 dataset in which digitised data has been reprocessed with a simulated FTK system. FTK jets are reconstructed in the HLT jet trigger.
The attributes are shown to loosely agree, verifying that the jet track attributes are computed correctly. Furthermore, the mostly linear agreement is a positive indication that jet track attributes computed with FTK tracks are comparable to attributes computed with offline tracks, lending themselves to a similar effectiveness in their usage. An exception is a notable discrepancy at high sums in track momenta and large track widths, which may be explained by the decline in efficiency for FTK track momenta above 30 GeV.

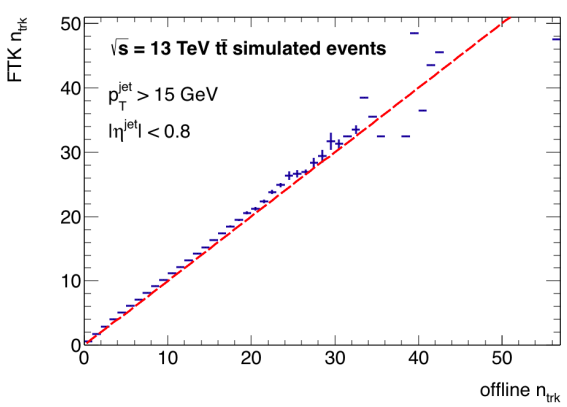

(a) n_{trk} (simulated $t\bar{t}$ dataset)

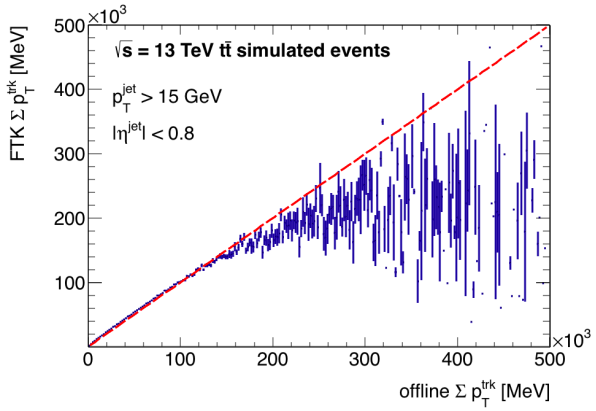

(b) Σp_T^{trk} (simulated $t\bar{t}$ dataset)

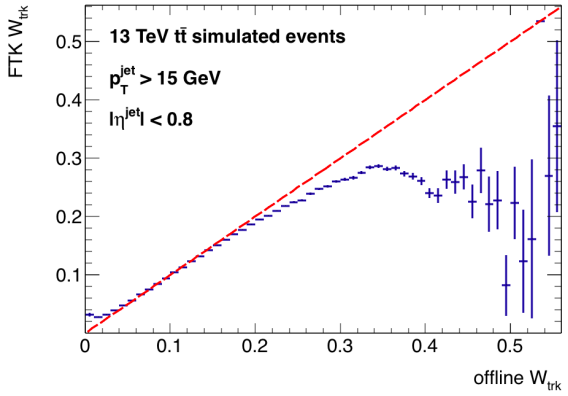

(c) $\mathcal{W}_{trk}$ (simulated $t\bar{t}$ dataset)

Figure 10.5: A comparison between FTK and offline jets is shown for three jet track attributes: n_{trk}, Σp_T^{trk} and $\mathcal{W}_{trk}$, for jets with $p_T > 15$ GeV and $|\eta| < 0.8$ and tracks with $p_T > 1$ GeV. The dataset contains generated $t\bar{t}$ events that have been passed through a full ATLAS simulation that includes a simulation of the FTK system. FTK jets are reconstructed in the HLT jet trigger.

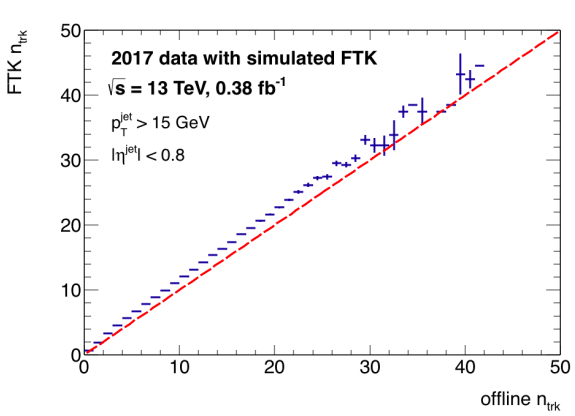

(a) n_{trk} (data with simulated FTK)

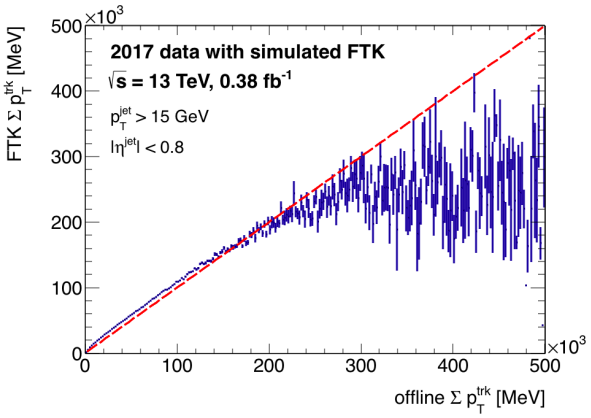

(b) Σp_T^{trk} (data with simulated FTK)

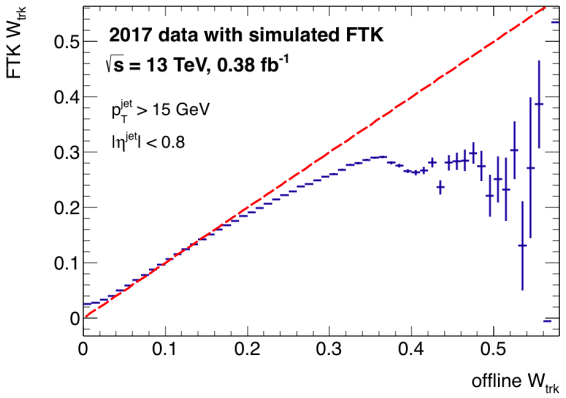

(c) $\mathcal{W}_{trk}$ (data with simulated FTK)

Figure 10.6: A comparison between FTK and offline jets is shown for three jet track attributes: n_{trk}, Σp_T^{trk} and $\mathcal{W}_{trk}$, for jets with $p_T > 15$ GeV and $|\eta| < 0.8$ and tracks with $p_T > 1$ GeV. 2017 data is reprocessed from digitised data with a simulated FTK system. FTK jets are reconstructed in the HLT jet trigger.

Chapter 11

FTK jet pile-up rejection studies

The usage of FTK tracks in trigger jets are studied, with the goal of measuring the performance of pile-up jet rejection. The studies are based on a set of simulated dijet samples that include the simulation of the FTK system. The "truth" information in the samples are used to determine the "true" jet origin: either originating from the hard-scatter or a pile-up interaction, independent of any tracking information.

The four pile-up discriminating variables, JVF, JVFCorr, R_{p_T}, and JVT have been introduced in section 5.3.3, where JVT is the official variable used in offline pile-up jet rejection.
The simulated samples are used to study each variable computed from FTK tracks. The pile-up discrimination performance is tested for different amount of pile-up and in the case of JVT, different ranges in η and jet p_T. The FTK-based JVT performance is subsequently compared to the offline JVT performance.
Finally, two analysis searches are used in a further comparison of the FTK and offline pile-up rejection performance in simulation. The first is a dijet+ISR jet analysis using a TLA trigger selection. The second is the reconstruction of a W and top resonance based on a dataset of simulated $t\bar{t}$ events.

11.1 Event selection and object definition

The simulated dataset contains the production of dijet events that have been generated using the Monte Carlo generator, PYTHIA [57]. The generation includes the hadronisation and showering of incoming and outgoing quarks. The events are passed through the full ATLAS detector simulation and pile-up events have been overlaid with a μ value ranging from 40 to 70 interactions per bunch crossing (refer to chapter 5 for more details on ATLAS simulation).

The reconstructed hard scatter vertex, also referred to as PV0, is defined as the vertex with the highest $\Sigma(p_T^{trk})^2$ in the event.

For the events included in the analysis it is required that $|\Delta z| < 0.2$ mm, where Δz is the difference between z coordinates of the reconstructed and truth vertex. This ensures that the hard scatter event originates from the "true" hard scatter vertex, as it may happen that the overlaid pile-up event is more energetic than the "true" event.

A jet is labelled as a true hard-scatter (HS) jet by requiring at least one truth jet of

$p_T > 10$ GeV within a distance $\Delta R < 0.3$. A jet is labelled as a true pile-up (PU) jet if no truth jets above 4 GeV are found to match it within $\Delta R < 0.6$.

11.2 Vertex reconstruction efficiency

In addition to the track reconstruction efficiency, which has already been discussed in Chapter 10, the reconstruction of the hard scatter vertex is important for the identification of tracks emerging from the hard scatter vertex in pile-up rejection techniques. The FTK vertex reconstruction is expected to differ from offline not only because of the lower FTK track reconstruction efficiency but also because the minimum p_T of FTK tracks is 1 GeV, whilst in offline, the minimum track p_T is 500 MeV. This affects the vertex reconstruction efficiency as well as lead to jet track attributes that are less sensitive to "softer" tracks.

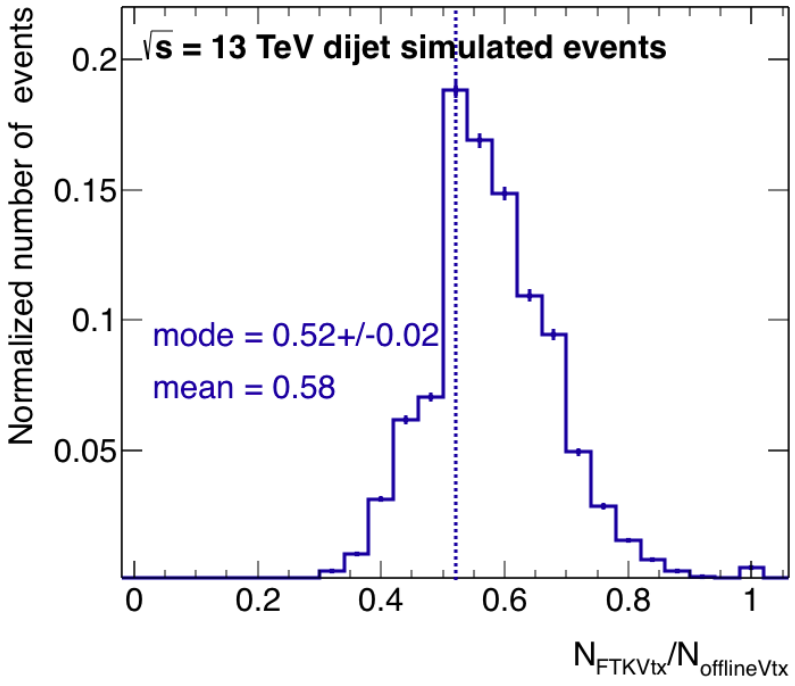

Figure 11.1: The ratio between the number of reconstructed FTK vertices and the number of reconstructed offline vertices is shown. The mean and mode of the distribution are 0.58 and 0.52 respectively. The almost 50% reduced number of FTK vertices is at least partly due to the higher minimum FTK track p_T: 1 GeV versus 500 MeV in offline.

The ratio of the number of FTK vertices and offline vertices per event is shown in Figure 11.1. Almost 50% less FTK vertices are reconstructed. However, the FTK vertex reconstruction efficiency is shown to be dependent on the vertex $\sum p_T^{trk}$ in Figure 11.2. The efficiency with respect to offline reaches 98%(100%) at a vertex $\sum p_T^{trk^2}$ of 80(150) GeV. As a result the efficiency of the reconstruction of the hard vertex is better than 50%: Only in 8% of events does it appear that the FTK hard scatter vertex failed to be reconstructed. This is estimated by the number of events in which the difference between the z parameters of the primary FTK and offline vertex is greater than 0.2 mm.

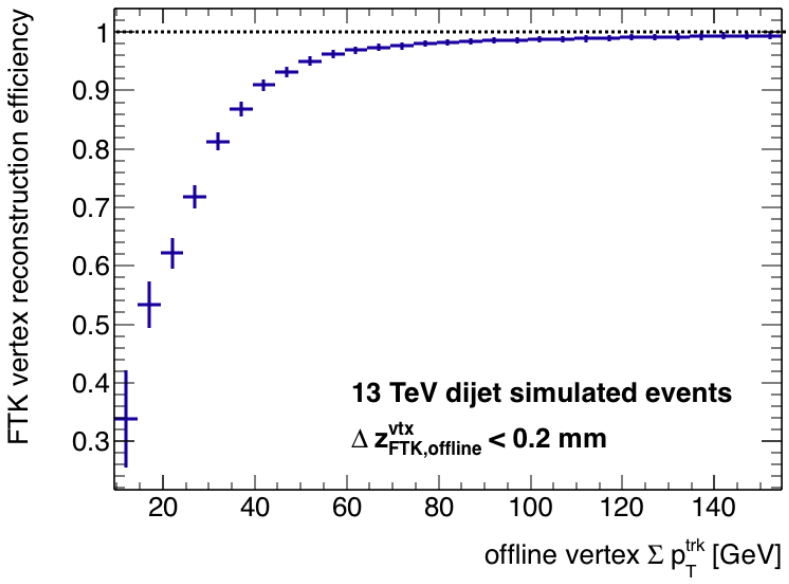

Figure 11.2: The FTK vertex reconstruction efficiency is shown as the ratio between the number of offline vertices matched to an FTK vertex and the total number of offline vertices as a function of the offline vertex $\sum {p_T^{trk}}^2$. Offline vertices are counted as matched if the difference in z between FTK and offline is within 0.2 mm.

11.3 Computation of JVT

For the initial studies shown here, the offline-derived likelihood histogram [66], shown in Figure 5.5 and described in section 5.3.3, is used to interpolate the FTK JVT. The graphs in Figure 11.3 show the JVFCorr versus R_{p_T} correlation for hard scatter and pile-up labelled FTK jets separately. As a reminder, it is this correlation that is exploited in the Jet Vertex Tagger.

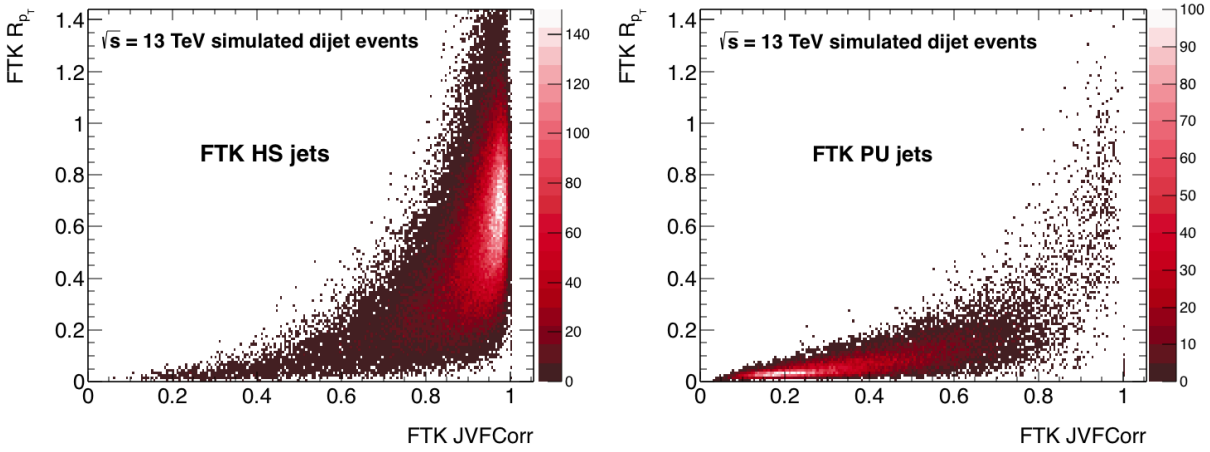

(a) FTK JVFCorr versus R_{p_T} for HS jets.

(b) FTK JVFCorr versus R_{p_T} for PU jets.

Figure 11.3: The correlation between JVFCorr and R_{p_T} are shown for FTK hard scatter (left) and pile-up jets (right). The *Jet Vertex Tagger* algorithm returns the likelihood that the jet has originated from the hard scatter vertex based on this correlation.

11.4 Rejection variable performance

The distributions for each of the four variables, JVF, JVFCorr, R_{p_T} and JVT, for hard scatter and pile-up jets are set in contrast in Figure 11.4. The pile-up rejection power is dependent on how well separated the rejection variable distributions are for hard scatter jets from pile-up jets.

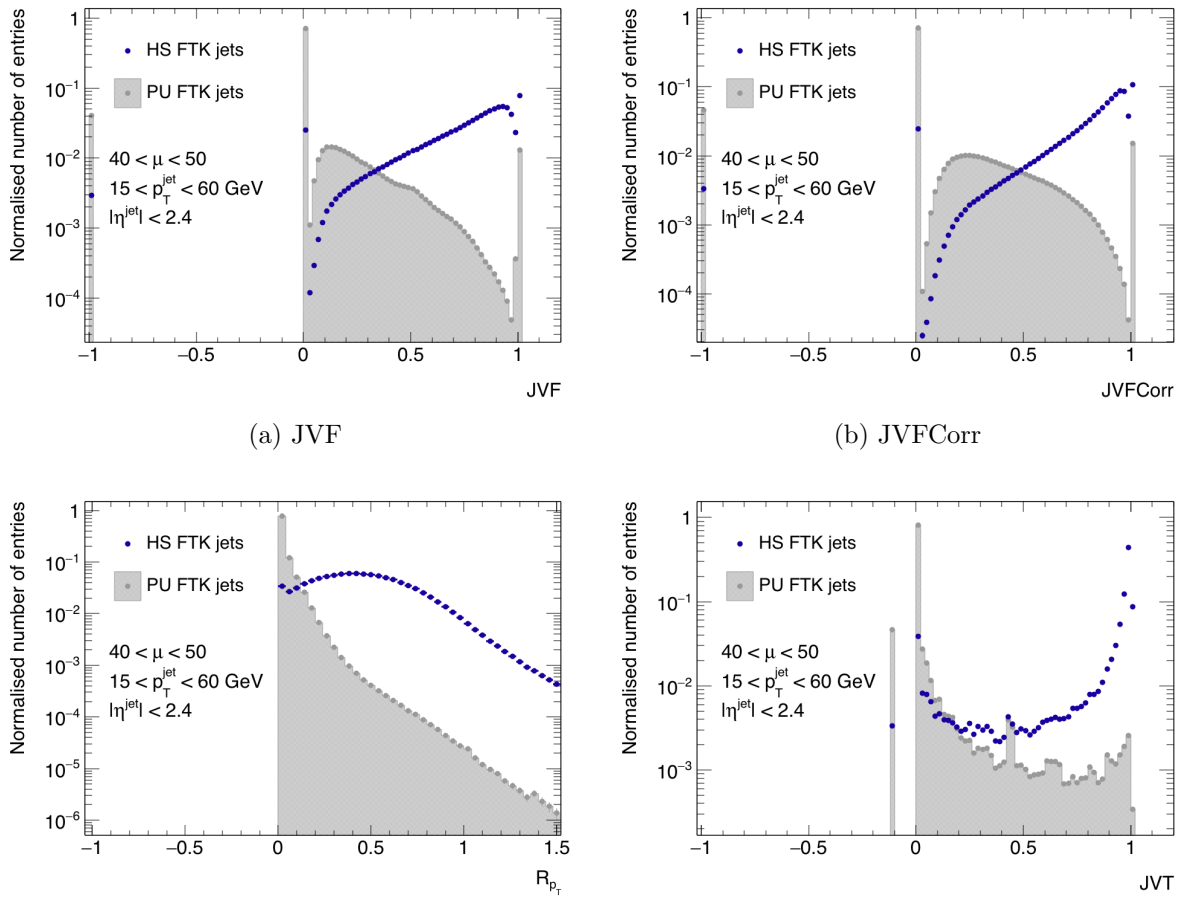

(a) JVF (b) JVFCorr

(c) R_{p_T} (d) JVT

Figure 11.4: Variable distributions for hard scatter jets (blue) are contrasted against those for pile-up jets (grey), for $40 < \mu < 50$ and jets with $15 <$ jet $p_T < 60$ GeV, jet $|\eta| < 2.4$. The separation in the distributions offers a way of discriminating between hard scatter and pile-up jets. More distinct distributions will lead to a higher hard scatter jet acceptance rate with an accompanying lower pile-up jet acceptance rate.

The acceptance efficiency of hard scatter jets versus the acceptance efficiency of pile-up jets using one of the rejection variable as a discriminant is shown in Figure 11.5 for each variable separately. The performance for $R_{p_T}$and JVT appear very similar.
On average, at a true rate efficiency of 92%, the accompanying fake rate is 8% and 7% for JVF and JVFCorr/R_{p_T} respectively. For JVT it is 6%. The JVT discriminant thus appears to perform only slightly better.

11.4.1 Changes with pile-up

JVF was formerly used in Run 1 for the rejection of offline pile-up jets. It is however sensitive to pile-up conditions and therefore has been replaced by JVFCorr and R_{p_T}, which

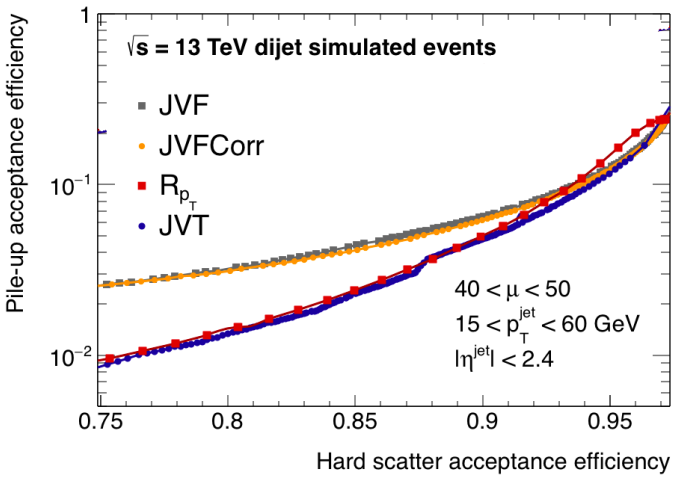

Figure 11.5: The acceptance efficiency of hard scatter jets versus pile-up jets is shown for JVF, JVFCorr, R_{p_T} and JVT for $40 < \mu < 50$.

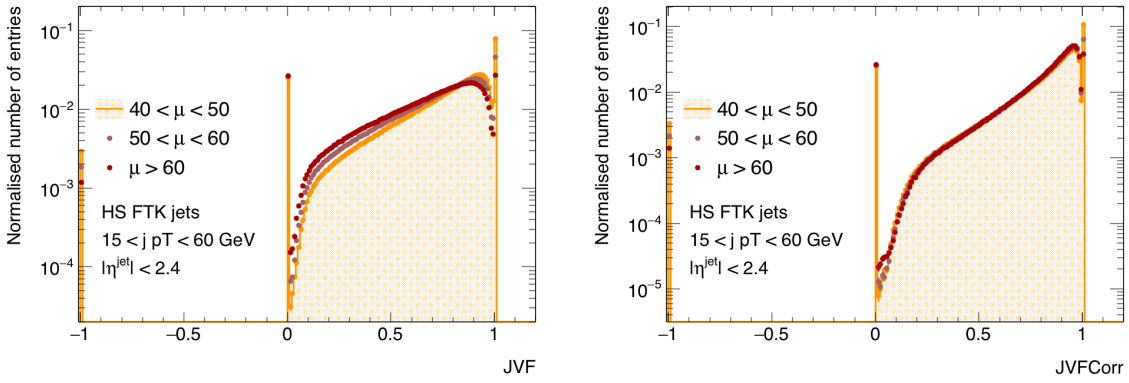

(a) JVF

(b) JVFCorr

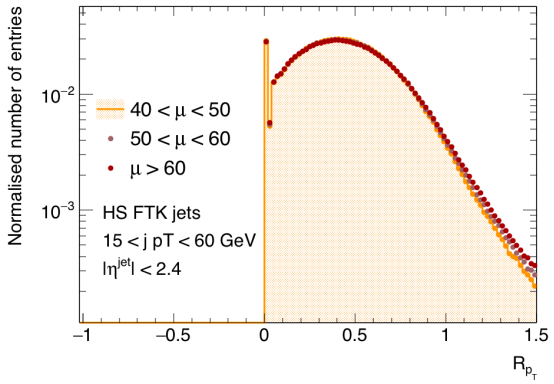

(c) R_{p_T}

Figure 11.6: Variable distributions for hard scatter jets are shown for different ranges in μ. JVF exhibits a dependence on the amount of in-time pile-up; JVFCorr and R_{p_T} exhibit no dependence.

are robust against increasing amounts of pile-up (see section 5.3.3). JVFCorr contains a correction factor in the denominator, equation 5.9, that corrects for this effect. Therefore it is expected that the FTK JVFCorr and R_{p_T} appear stable with changing pile-up.

The effects of pile-up in JVF is illustrated in Figure 11.6a, where the JVF distribution for hard scatter jets is shown to change for different ranges in μ.
The equivalent distributions for JVFCorr are shown in Figure 11.6b, where difference between different ranges in μ appear much reduced. Similarly, R_{p_T} shows little change for different μ ranges, Figure 11.6c.

Choosing a variable working point that results in an average HS acceptance efficiency of 92% for $40 < \mu < 50$, the efficiency is computed for each variable for several ranges in μ and presented in Table 11.1. The efficiency drops by 4% for the FTK JVF between a minimum μ of 40 and maximum μ of 70. On the other hand, the efficiencies for the FTK JVFCorr and R_{p_T} vary by less than 1%. Since the JVT depends directly on JVFCorr and R_{p_T}, it will similarly have no dependence on μ.

μ	JVF	JVFCorr	R_{p_T}
$40 < \mu < 50$	91.78 ± 0.01 %	91.62 ± 0.02 %	92.16 ± 0.02 %
$50 < \mu < 60$	90.00 ± 0.02 %	91.85 ± 0.01 %	92.60 ± 0.01 %
$60 < \mu < 70$	87.96 ± 0.02 %	92.03 ± 0.02 %	92.59 ± 0.02 %

Table 11.1: The efficiencies for different μ ranges are shown for variable cuts at 92% average efficiency for JVF, JVFCorr and R_{p_T}. The errors given are statistical.

11.4.2 Changes with jet kinematics

The dependence of the pile-up rejection efficiency on jet p_T and η is studied focusing on the JVT discriminant only. Figure 11.7a shows the hard scatter distributions for the FTK JVT for different p_T ranges, in which the shape of the distributions are shown to clearly change for each bin. In a similar depiction, the η variation is shown in Figure 11.7b. In comparison, the η-binned distributions do not vary as widely.

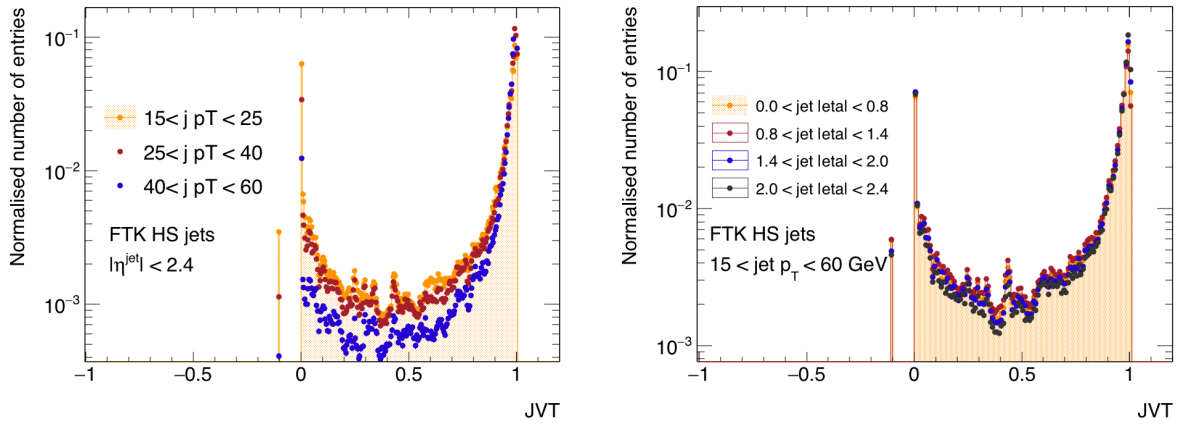

(a) p_T binned JVT HS (b) η binned JVT HS

Figure 11.7: Distributions of JVT for hard scatter jets is shown for different ranges of FTK jet p_T (left) and jet $|\eta|$(right). The distributions are shown to vary with jet p_T resulting in efficiencies that vary around the average acceptance efficiencies.

The hard scatter acceptance efficiency and pile-up fake rate for each range in p_T and η are summarised in Tables 11.2 and 11.3, respectively, assuming an average acceptance working point of 92% as before.

p_T	15-25 GeV	25-45 GeV	45-60 GeV
$\|\eta\| < 0.8$	85.15 ± 0.03%	92.27 ± 0.02%	96.03 ± 0.02%
$0.8 < \|\eta\| > 1.4$	83.70 ± 0.04%	92.75 ± 0.03%	95.42 ± 0.02%
$1.4 < \|\eta\| > 2.0$	84.73 ± 0.04%	90.28 ± 0.04%	95.92 ± 0.03%
$2.0 < \|\eta\| > 2.4$	85.77 ± 0.05%	90.02 ± 0.05%	96.10 ± 0.04%

Table 11.2: The FTK hard scatter jet acceptance efficiency for different p_T and η ranges are shown for a JVT cut at 92% average efficiency. The errors given are statistical.

p_T	15-25 GeV	25-45 GeV	45-60 GeV
$\|\eta\| < 0.8$	6.62 ± 0.01%	4.71 ± 0.02%	5.83 ± 0.05%
$0.8 < \|\eta\| > 1.4$	6.51 ± 0.01%	4.96 ± 0.01%	5.39 ± 0.05%
$1.4 < \|\eta\| > 2.0$	6.52 ± 0.01%	5.14 ± 0.02%	5.64 ± 0.08%
$2.0 < \|\eta\| > 2.4$	6.39 ± 0.02%	4.89 ± 0.05%	5.82 ± 0.15%

Table 11.3: The FTK pile-up jet acceptance efficiency (fake rate) for different p_T and η ranges are shown for a JVT cut at 92% average efficiency. The errors given are statistical.

A rather large variation in efficiency is shown across p_T. The hard scatter acceptance varies between 84-96%. The accompanying variation in fake rate sits more stably between 5 and 6%.
Only a small η-dependence is measured, varying around 1-2%.

11.5 Comparison to offline performance

Finally, the pile-up jet rejection performance for FTK jets is compared to that of offline jets.

Figure 11.8 is a comparison of the JVT distribution for FTK and offline hard scatter and pile-up jets, where the dashed lines indicate the JVT of 92% average acceptance efficiency. It is evident that 92% efficiency is reached at relatively low values of JVT in the case of FTK. This can be partially attributed to the fact that around 3% of FTK hard scatter jets are trackless (in this case, JVT takes on the value of -0.1) whilst for offline this fraction is close to zero. The greater number of trackless FTK jets can be expected from the higher threshold on the track p_T and the lower track reconstruction efficiency with respect to offline. At the same time the lower minimum p_T in offline tracks appears to make offline jets more sensitive to soft effects, resulting in a wider JVT distribution for offline pile-up jets.
Figure 11.9 compares the resulting efficiency curve for the FTK and offline JVT for jets with a p_T between 15 and 60 GeV and $|\eta| < 2.4$. For offline jets, the accompanying fake rate at an efficiency of 92% is 3% which is in agreement with official ATLAS results [66]. The results show that the FTK performance compares well. For a hard scatter acceptance efficiency of 92%, the fake rate for FTK jets, of 6%, is 3% higher than the fake rate for offline jets. The difference in fake rate decreases towards lower efficiencies: For a hard scatter efficiency of 85%, the offline fake rate is 1.5% and the FTK fake rate is only slightly higher, at 2%.

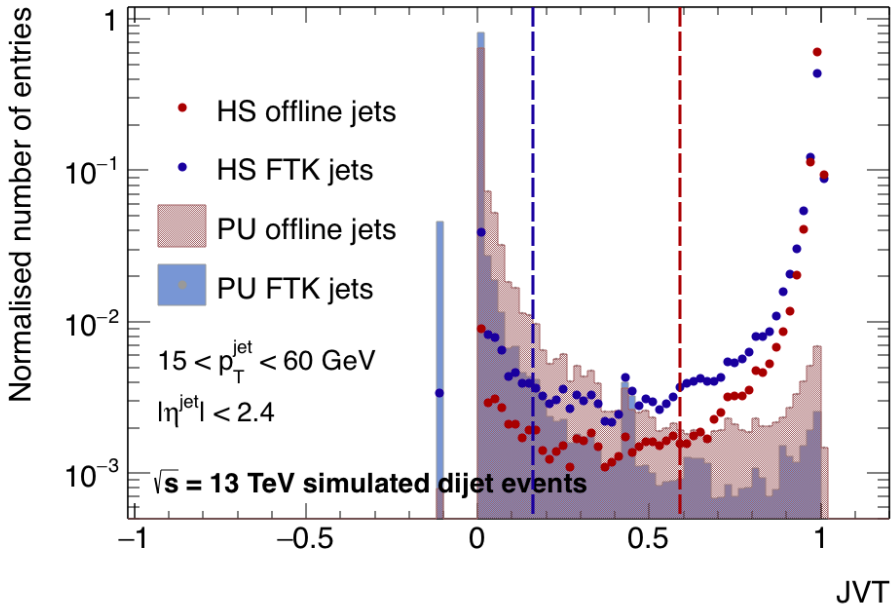

Figure 11.8: The JVT distributions for hard scatter (circles) and pile-up jets (solid distributions) are shown for FTK (blue) and offline jets (red). The accompanying blue and red dashed lines indicate the JVT values at which the average acceptance efficiency is 92%.

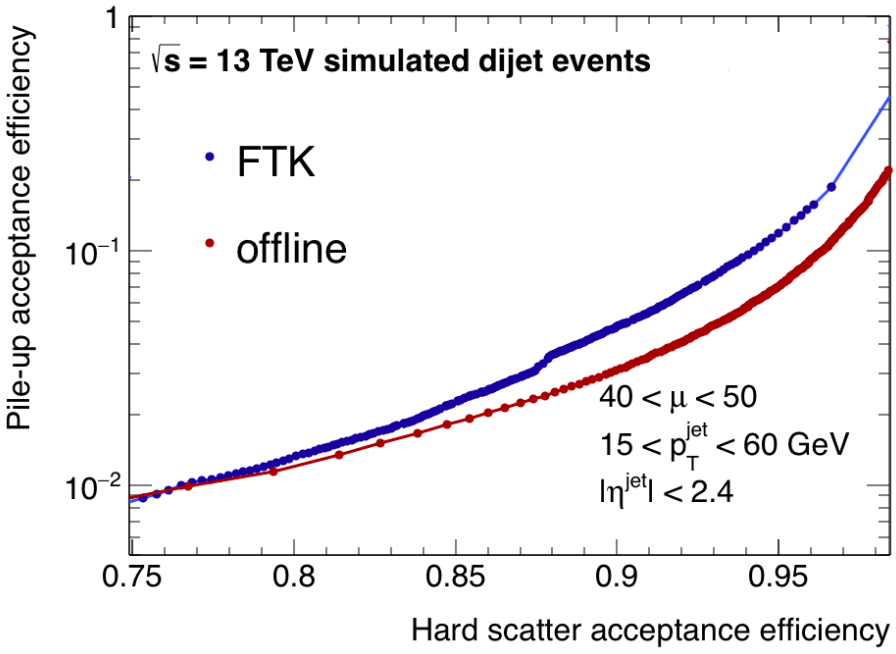

Figure 11.9: The acceptance efficiency of hard scatter jets versus pile-up jets is shown for (a) JVFCorr and (b) R_{pT} for FTK (blue) and offline jets (red). Ony jets with $15 <$ jet $p_T < 60$ GeV and jet $|\eta| < 2.4$ are included. At equal true positive efficiencies of 92%, the accompanying fake rate for JVT is 3% higher for FTK jets compared to offline jets.

11.6 Pile-up rejection for a dijet + ISR jet signal

In chapter 9, Figure 9.8, it was shown that the pile-up background in a TLA dijet+ISR analysis selection in data comprised between 10 and 25% of the low end dijet mass spec-

trum. In the following it is assessed how well the dijet invariant mass distribution is found to agree with the "true" hard scatter jet distribution following the removal of jets rejected by the JVT for both FTK and offline jets.

Event selection An event selection identical to the dijet+ISR selection in Chapter 9 is applied. The leading jet is required to have a minimum p_T of 150 GeV, corresponding to the p_T at which a L1_J50 trigger is fully efficient. The second and third leading jets are taken as the jet pair, requiring that $p_T^{jet} > 20$ GeV and $|\eta^{jet}| < 2.4$ and $y^* < 0.6$.

Results The dijet mass distribution is shown in 11.10 for three different selections. The dark blue distribution represents a jet selection with no applied JVT whilst the red (light blue) distribution represents the offline (FTK) jet selection with an applied JVT at 92% average efficiency. The solid orange distributions represents the jet selection in which jets have been matched to a truth jet, thus representing the "true" hard scatter distribution. The agreement between the truth matched spectrum and the pile-up rejected spectrum is reflected in the lower panel of the respective plots.
It is shown that the pile-up jet background is eliminated by applying a JVT. The agreement between the "true" distribution and the pile-up suppressed distribution is within 2-3% for offline jets, and within 2-4% for FTK jets. The largest disagreement for both cases is in an excess of pile-up jets between 100 and 150 GeV, where the largest contribution from the pile-up spectrum lies.

11.7 Pile-up rejection for a $t\bar{t}$ signal

In order to assess the FTK performance of pile-up jet suppression in a multijet signal, a simple analysis is performed on a dataset of fully simulated $t\bar{t}$ events, including the FTK system, for which tops decay hadronically: $t \to W + b$, where $W \to q\bar{q}$. The events were generated in POWHEG [108], and the showering process was simulated in PYTHIA.
Pile-up can affect a resonance in two ways. It can firstly lead to a larger multijet background rate for events that are not a signal event. Secondly, pile-up can diminish a resonance in a signal event itself, by replacing signal jets in the jet selection. The latter effect is expected to broaden a signal. In the following, the width of a W and top resonance are measured with and without pile-up rejection both in the case of FTK and offline jets, for comparison.

Event selection Events passing the L1_J20 trigger are selected, which is the lowest possible Level-1 jet trigger threshold. A minimum leading jet p_T of 85 GeV is required for full trigger efficiency. Each event is required to have a minimum of six jets with $p_T^{jet} > 20$ GeV and $|\eta_{jet}| > 2.4$. At least two jets are required to have been identified as originating from a bottom-flavoured quark (a b-tagged jet) by a multivariate ATLAS b-tagging algorithm [114]. A working point is chosen so that the b-tag efficiency is 77% with a 1/137 light-flavoured quark fake rate. FTK jets are identified as b-tagged by matching them to offline b-tagged jets. For the reconstruction of the W, the four leading

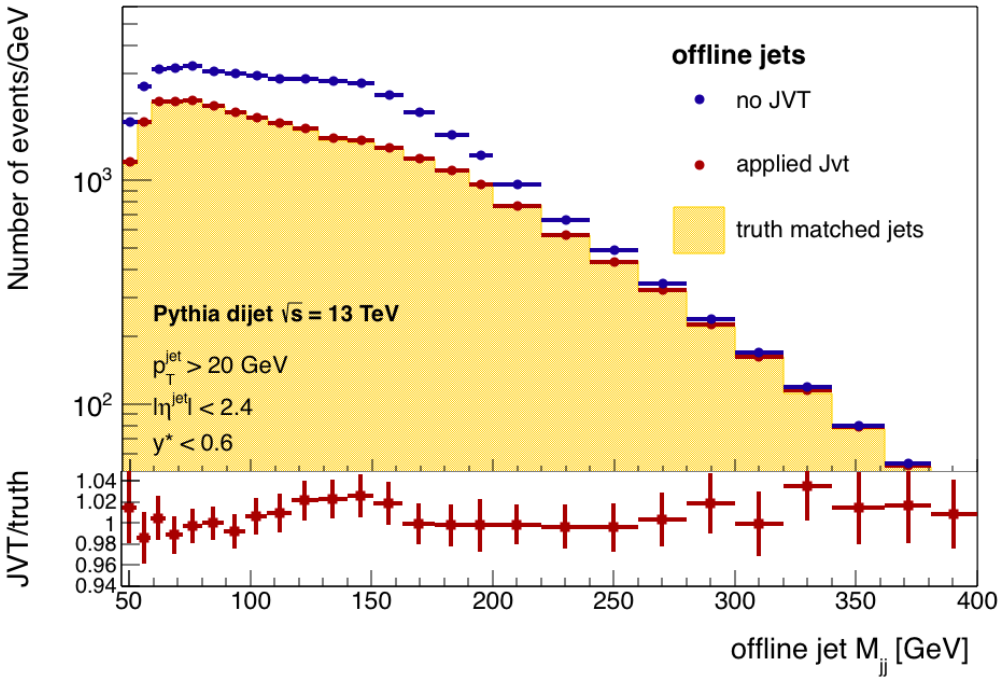

(a) offline jets

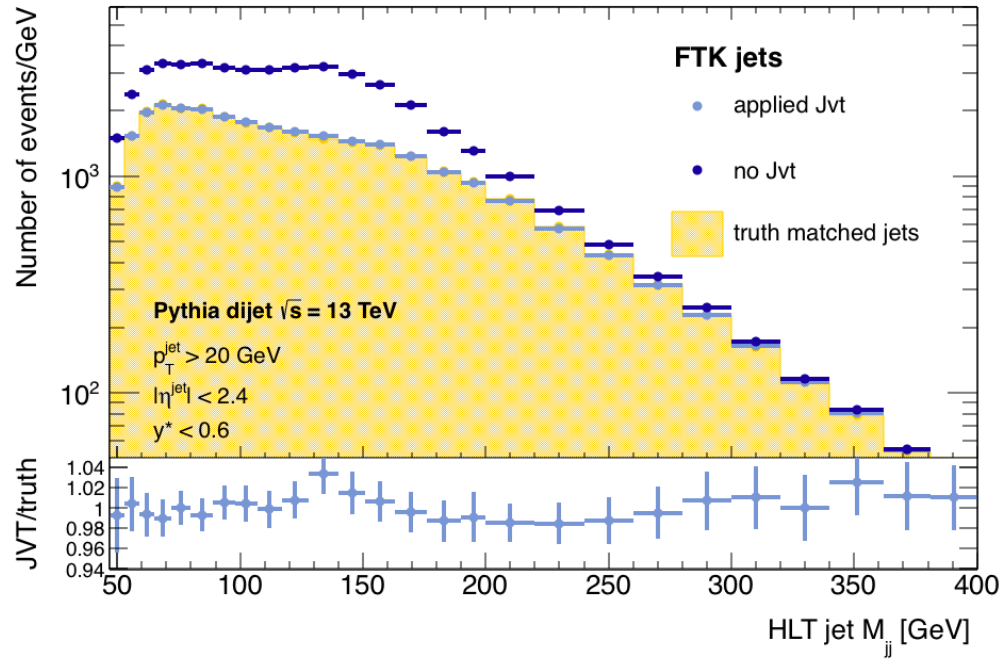

(b) FTK jets

Figure 11.10: The dijet mass distribution of offline (top) and FTK jets (bottom) following a dijet+ISR signal selection is shown for: no pile-up rejection (no JVT, dark blue); jets matched to a truth jet (solid orange), representing the true hard scatter event; with pile-up rejection (applied JVT, red/light blue). The ratio between the applied JVT and truth matched distributions is shown in the lower panel.

non-b-tagged jets are paired by *minimizing* $\Sigma(1 - \Delta R)$, defined as

$$\Sigma(1 - \Delta R) = |(1 - \Delta R_{i,j})| + |(1 - \Delta R_{k,l})|, \tag{11.1}$$

computed for every combination of i, j, k and l representing the indices of the first four light-flavoured jets. The minimisation with respect to 1 reduces cases in which a jet is paired to one of its radiated gluons. Additionally it is required that

$$0.5 < |(1 - \Delta R_{i,j})| < 2., \tag{11.2}$$

for both jet pairs.
The mass asymmetry of the resulting jet pairs is required to be less than 0.1,

$$A_{m_{W1},m_{W2}} = |\frac{m_{W1} - m_{W2}}{m_{W1} + m_{W2}}| < 0.1. \tag{11.3}$$

Finally, the W four-momentum of each jet pair is paired to the closest b-jet to reconstruct each top, and again a maximum mass asymmetry of 0.1 is required for the reconstructed top pair.
The event selection is purposefully agnostic to the top and W boson masses. The same selection is performed after the removal of jets identified as pile-up by their JVT.
The cutflows and variable distributions for the $t\bar{t}$ analysis are provided in Appendix A.5.

Results The JVT pile-up suppression reduces the final number of events by around 33%. The purity of the signal selection after selecting all jets in the event where $p_T^{jet} > 20$ GeV and $|\eta_{jet}| > 2.4$ is presented in Figure 11.11, in which the number of truth-matched jets in the first six leading jets is depicted. After a JVT selection, the fraction of events that contain a purely hard scatter selection increases from 45 to 78% (by 33%), in the case of offline jets, and from 40 to 68% (by 28%) in the case of FTK jets (the effective efficiency is the product of the selection efficiency of each jet and thus lower than 92%).

The widths of the reconstructed W and top resonance bumps are measured by applying a fit using a crystal ball function that describes a combined Gaussian core and a power-law low-end tail. The function is provided in Appendix A.5.

The σ parameter of the fitted function is used to compare the resolution of the resonance. The results for the W resonance are shown in Figures 11.12a and 11.12b for offline and FTK jets, respectively, after normalising the peaks to the total number of events. The equivalent results for the top resonance are shown in Figures 11.13a and 11.13b. The same colour code is used as for the previous plots. In the offline case, the W resonance fit σ are 13.1 and 12.4 for no JVT and applied JVT respectively. In the FTK case, the respective fit σ are 14.1 and 13.3. The broader widths in the case of HLT jets is expected as the energy resolution is lower than for the fully-calibrated offline jets. In both cases, the result is a 5-6% reduction in width. For the top resonance, the same fit σ are 22.0 and 21.0 in the offline case, and 23.2 and 22.2 in the FTK case. This similarly is a reduction in width of $\sim$5%.

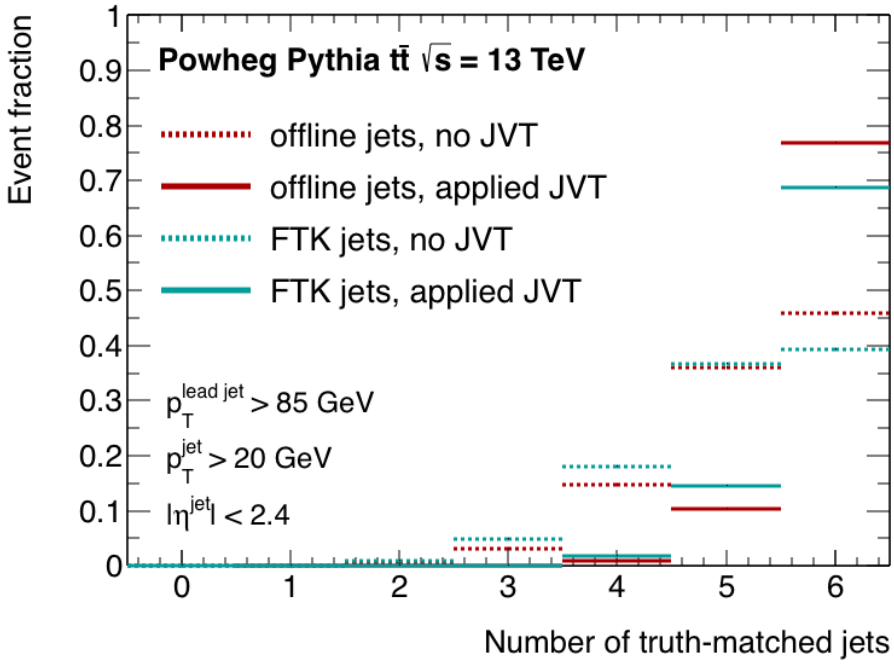

Figure 11.11: The number of offline (red) and FTK (light blue) jets that are matched to a truth jet of the first six leading jets per event are shown. The dashed and solid lines represent the selection without and with an applied JVT, respectively.

11.8 Summary and final remarks

The studies shown here have demonstrated the ability of using FTK tracks to reject pile-up jets.

The use of R_{p_T} and JVFCorr in FTK jets are shown to be robust under changing pile-up conditions. This was tested for μ ranging from 40 to 70.

It is shown that a comparable pile-up rejection performance in FTK jets can be achieved relative to an offline performance. The studies show that the same efficiency for the acceptance of hard scatter jets can be achieved with an FTK JVT, however with an accompanying fake rate that is 3% higher with respect to the offline JVT.
In the case of FTK, the efficiency appears highly dependent on the jet p_T, however, decreasing from 95% for jet p_T between 40 and 60 GeV to 85% for jet p_T below 25 GeV. The decrease in efficiency at low p_T is likely because of the minimum FTK track p_T threshold of 1 GeV, which results in lost sensitivity to soft tracks. In offline the amount of variation with p_T is measured to be only $\pm 3\%$ for the same samples (additional plots are provided in Appendix A.4).

The impact of pile-up jet rejection for the reduction of a multijet background was demonstrated in the case of the mass distribution for a dijet+ISR jet selection. Pile-up rejection can concurrently enhance a resonance for a signal of multiple jets. This was demonstrated for a top and W resonance in a simulated $t\bar{t}$ selection, where the effect was, albeit slight, a reduction of the gaussian width of the resonances of approximately 5% after an applied JVT. In both measurements, the results for the FTK JVT proved to be generally within 2% to that of offline.

The initial studies have left a lot of room for future improvement: A better performance can be expected for an FTK-dedicated jet-vertex-tagger, in which a likelihood discriminant is derived from the correlation of the FTK JVFCorr and R_{p_T}. Furthermore, the measure of R_{p_T} is expected to improve for jet energies that are more precisely measured. A full FTK jet calibration developed within the framework of the TLA analysis may therefore result in a significantly better measurement of $R_{p_T}$and consequently an improved measurement of the JVT. Finally, it is possible to use the track hits identified by FTK as a seed to HLT precision tracking, thereby improving the quality of tracks. The performance of "refitted" tracks and the accompanying CPU costs is a subject for future study.

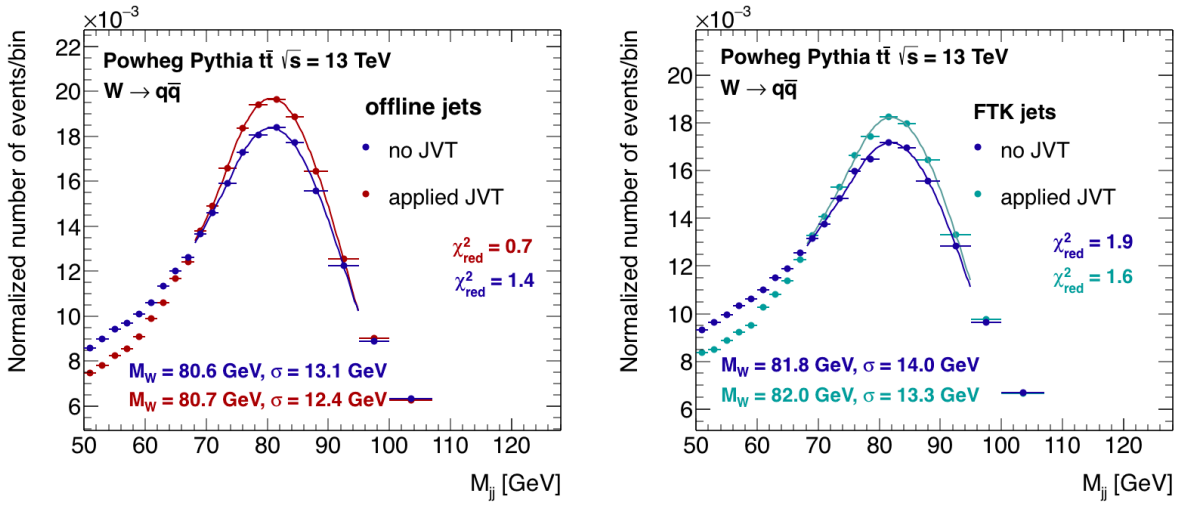

(a) offline jets (b) FTK jets

Figure 11.12: A crystal ball function fit is applied to the reconstructed W mass resonance for a selection with no JVT (dark blue) and a selection with JVT (red/light blue) for offline jets (left) and FTK jets (right). The width of the Gaussian core of the fitted function, σ, and the fit mean, or peak mass, M, are given.

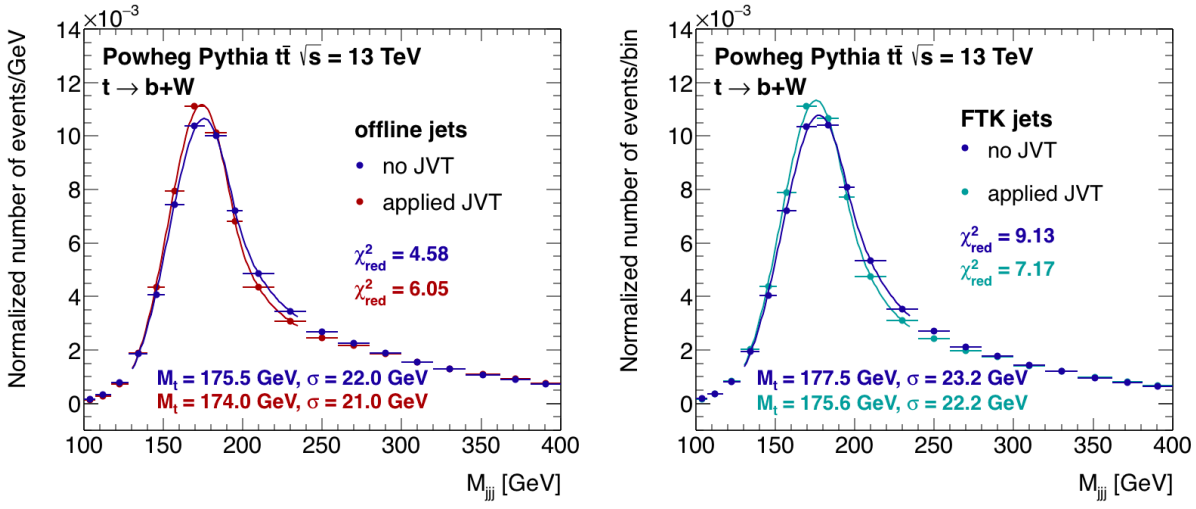

(a) offline jets (b) FTK jets

Figure 11.13: A crystal ball function fit is applied to the reconstructed top mass resonance for a selection with no JVT (dark blue) and a selection with JVT (red/light blue) for offline jets (left) and FTK jets (right). The width of the Gaussian core of the fitted function, σ, and the fit mean, or peak mass, M, are given.

Chapter 12

Conclusion

Discovering new physics beyond the Standard Model is one of the major goals of the Large Hadron Collider. One reason to expect new discoveries at the LHC is the theory of weakly-interacting dark matter particles (WIMPS), which are predicted to lie in the range of the colliding energies. However, no new particles have yet been discovered.

The physics that is searchable at the LHC is largely determined by the experiment's trigger system. Unprobed search regions lie not only in novel ideas that call for new trigger implementations but may also lie below current trigger thresholds.
The work herein resolved two trigger-level challenges that lead to improvements in the ATLAS trigger benefitting all physics analyses, albeit with the latter focusing on the improvement of low mass dark matter resonances.

A new firmware-based algorithm that identifies the bunch crossing of triggered events was commissioned for the ATLAS first-level trigger. It extended the triggerable range to the new high energies produced in proton collisions at centre-of-mass energies of 13 TeV. At the same time the algorithm resolved a mistiming issue that formerly resulted in the corruption of data within a certain energy band, affecting all physics analyses. Following its commissioning, the algorithm was permanently activated for Run 2. It has had a 100 percent success rate over a total of 98 $\text{fb}^{-1}$of integrated luminosity.

The output of a new trigger electronics component, the Fast Tracker (FTK), was successfully integrated into the software-based jet trigger of the ATLAS High Level Trigger (HLT). The Fast Tracker provides reconstructed tracks to the HLT for every event accepted at first level. It replaces and expands the function of current HLT track finding algorithms that are used restrictively due to their high CPU consumption. In the case of the jet trigger, tracks are made available for the first time, where they are used to reconstruct *FTK jets* that have defined jet track attributes. These aid in jet calibration and background jet suppression. The use of FTK jets will in particular enhance physics searches performed by the ATLAS Trigger-Object-Level Analysis (TLA), which relies on "light-weight" data reconstructed at trigger-level, instead of offline reconstruction from the entire detector read-out. The analysis technique has so far been used to set the strongest upper limits on the quark coupling to a new dark matter mediator particle decaying to two jets for low mediator masses between 400 GeV and 1.5 TeV. However, extending the TLA technique to more complex multijet topologies is severely limited by the contamination of jets from background proton collisions (pile-up), increasing background rates by as much as an order of magnitude.

The first analysis of FTK jets was conducted, in which the ability of using FTK tracks to reject pile-up jets in simulation was demonstrated. Initial results showed that despite the system's elementary form of track reconstruction, using FTK tracks is comparably effective to using offline tracks, for which sophisticated and CPU-intensive track finding algorithms are made use of. It was shown that the same hard scatter jet identification efficiency of 92% can be achieved with a fake rate of 6%, which is 3% higher than in offline. It was demonstrated that this could eliminate a ∼20% pile-up background in a TLA dijet+ISR jet analysis search for dijet mass resonances below 200 GeV. Using the reconstructed W boson and top quark resonance in a dataset of simulated $t\bar{t}$ events, it was shown that offline and FTK tracks are similarly effective in enhancing a resonance bump in multijet signals by reducing the contamination of spurious jets in a true signal event itself: In both cases, the gaussian widths of the W resonance and top resonance were reduced by 5%.
The comparable performance between the usage of offline and FTK tracks proclaim the significant role that FTK will play in enhancing the sensitivity of the Trigger-Object Analysis to new physics in Run 3 by improving online particle identification and trigger-level jet calibration, as well as extending search regions to lower resonance masses unencumbered by pile-up jets.

In August of 2018 the FTK system successfully produced its first 12-layer tracks in ATLAS in proton collisions. The event display is shown in Figure 12.1.

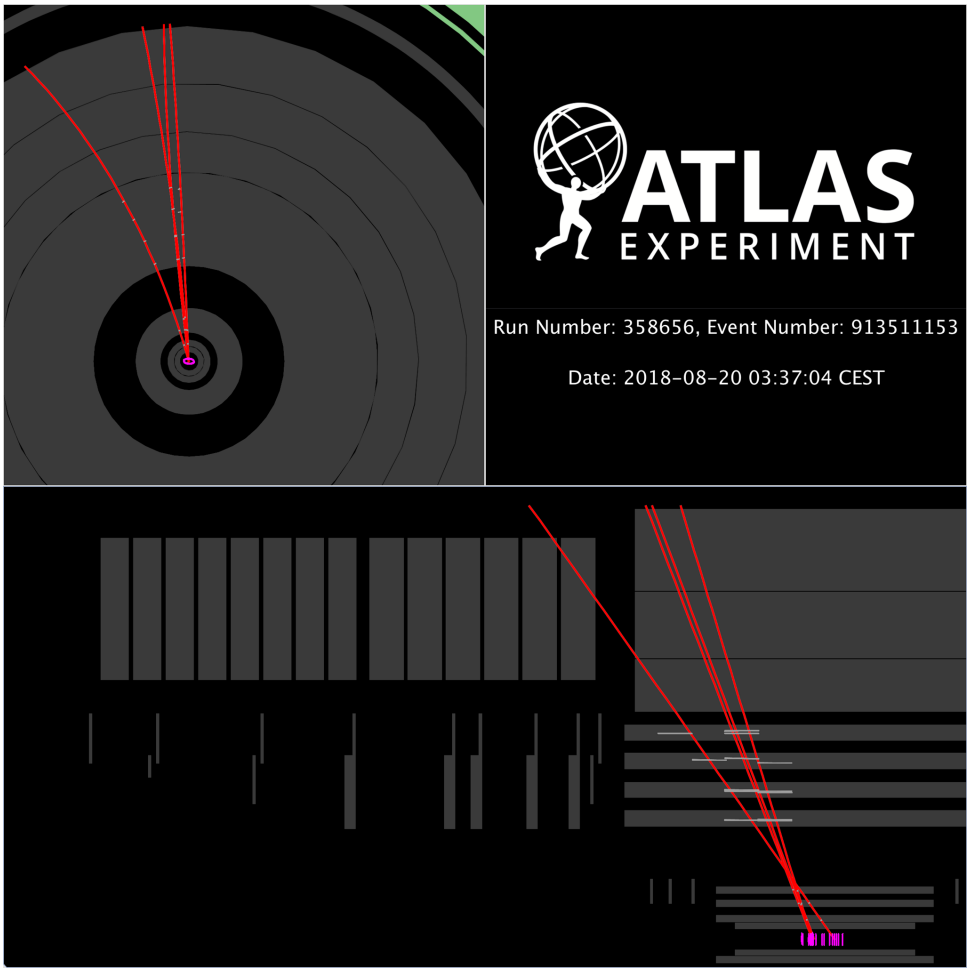

Figure 12.1: Event display of a proton-proton collision event including FTK information for a partially commissioned system. The event was recorded on 20th August 2018. The top panel is a x-y (transverse) projection of the ATLAS inner detector. The bottom panel is a r-z (lateral) projection. One FTK tower covering 1/64 of the Inner Detector geometrical coverage, is enabled. The FTK cluster positions are shown as white points and SCT strips are shown as white lines. The red lines show trajectories corresponding to track parameters obtained from an offline fit to the cluster positions determined by FTK. The primary vertices determined from tracks reconstructed offline are shown in purple. Taken from [113].

Appendix A

Appendix

A.1 The history of hadron colliders

New discoveries in particle physics have benefited greatly from circular accelerators colliding two beams as the use of circular colliders extends the energy scale and amount of data on fundamental physics. This is because the resulting energy in a circular collider is twice that of each beam[1] and furthermore, beams can be circulated and made to collide repeatedly until the beam particles have been depleted.
Beam energies are given as the nominal particle energies within the beam, i.e. at nominal velocity, γmc^2 where m is the particle mass and γ the Lorentz factor. The proton mass is 5 magnitudes larger than the electron mass, meaning proton beams circulated to the same speed will have a far greater energy. Moreover, lepton beams are severely limited by the loss in energy to synchrotron radiation, which scales with γ^4 [115]. For this reason, hadron colliders are the preferential choice when it comes to pushing the energy frontier in circular colliders.

The first hadron accelerator was the ISR (intersecting storage rings) [116] at CERN. Operated from 1971 to 1984, it served to prove the usefulness of hadron colliders. Research at the collider was dedicated to developing and improving accelerator techniques. The ISR paved the way for the earliest hadron collider dedicated to physics, the *Super proton anti-proton Synchrotron*, $Sp\bar{p}S$, at CERN [117]. At the time there was mounting pressure to discover the Z and W bosons, following the first observation of their evidence through neutral currents in 1973. The *Super Proton Synchrotron* already existed at the time as a supplier of particles to fixed target experiments. This was converted into the $Sp\bar{p}S$, a collider that could circulate and collide protons and anti-protons. The collider ran from 1981 to 1991.
During this period, the hermetic detector concept was growing in favour. A hermetic detector is designed to measure particle decays with as much of the 4π full coverage around the interaction point as possible. A trait of a hermetic detector is its 'onion-layer' configuration of *sub-detector components*. A sub-detector component makes use of a particular technology to measure particle properties. Sub-detectors form concentric layers around the interaction point and are each dedicated to the sampling of a different particle type. Such a detector is also referred to as a general-purpose detector.
Two general-purpose detectors were built for the $Sp\bar{p}S$, UA1 and UA2 (UA stands for

[1] In contrast, when a single beam is made to collide with a fixed target, the energy made available to the system increases with the square root of the beam energy

Undergroud Area), successfully measuring the Z and W bosons for the first time. The $Sp\bar{p}S$ operated at a maximum centre of mass energy ($\sqrt{s}$) of 650 GeV.
The presently second largest hadron collider ever built was the Tevatron [118], based at the Fermi National Accelerator Laboratory in USA. It operated between 1987 and 2011 at centre of mass energies up to 1.8 TeV. The two general-purpose detectors were CDF (Collider Detector and Fermilab) and D0, which were used to jointly discover the Top quark in 1995.
The Tevatron was decommissioned around the same time that the Large Hadron Collider, presently the largest collider ever built, began colliding at energies of 7 TeV. The LHC has had two data taking runs: Run 1 from 2010-2012 at up to 8 TeV, and Run 2 from 2015-2018 at 13 TeV. ATLAS and CMS shared success in discovering the Higgs Bosons during Run 1.

For the hadron colliders mentioned above, an undiscovered yet predicted particle in the Standard Model was a major motivation and successfully discovered. Experiments however also made use of the general-purpose detectors to search for particles beyond the Standard Model via a myriad of decay signatures, including searches for dark matter candidates.

A.2 ATLAS 2017 Trigger Menu

The ATLAS trigger menu [73] of main triggers used for data taking with luminosity up to $1.7 \times 10^{34}\,\mathrm{cm}^{-2}\mathrm{s}^{-1}$. Tabulated alongside each trigger is complimentary information on the offline kinematic selection for a minimum 99% trigger efficiency, Level-1 and HLT p_T and trigger-object multiplicity threshold, and Level-1 and HLT trigger rates. Data scouting triggers are not included.

Trigger	**Typical offline selection**	**Trigger Selection**		**Level-1 Peak Rate (kHz)**	**HLT Peak Rate (Hz)**
		Level-1 (GeV)	HLT (GeV)	$L = 1.7 \times 10^{34}\,\mathrm{cm}^{-2}\mathrm{s}^{-1}$	
Single leptons	Single isolated μ, $p_T > 27$ GeV	20	26 (i)	16	187
	Single isolated tight e, $p_T > 27$ GeV	22 (i)	26 (i)	26	178
	Single μ, $p_T > 52$ GeV	20	50	16	65
	Single e, $p_T > 61$ GeV	22 (i)	60	26	17
	Single τ, $p_T > 170$ GeV	100	160	1.2	49
Two leptons	Two μ's, each $p_T > 15$ GeV	2×10	2×14	2.0	30
	Two μ's, $p_T > 23, 9$ GeV	20	22, 8	16	42
	Two very loose e's, each $p_T > 18$ GeV	2×15 (i)	2×17	1.6	11
	One e & one μ, $p_T > 8, 25$ GeV	20 (μ)	7, 24	16	5
	One e & one μ, $p_T > 18, 15$ GeV	15, 10	17, 14	2.0	4
	One e & one μ, $p_T > 27, 9$ GeV	22 (e, i)	26, 8	26	2
	Two τ's, $p_T > 40, 30$ GeV	20 (i), 12 (i) (+jets, topo)	35, 25	5.1	59
	One τ & one isolated μ, $p_T > 30, 15$ GeV	12 (i), 10 (+jets)	25, 14 (i)	2.1	9
	One τ & one isolated e, $p_T > 30, 18$ GeV	12 (i), 15 (i) (+jets)	25, 17 (i)	3.9	16
Three leptons	Three loose e's, $p_T > 25, 13, 13$ GeV	20, 2×10	24, 2×12	1.2	< 0.1
	Three μ's, each $p_T > 7$ GeV	3×6	3×6	0.2	8
	Three μ's, $p_T > 21, 2 \times 5$ GeV	20	20, 2×4	16	8
	Two μ's & one loose e, $p_T > 2 \times 11, 13$ GeV	2×10 (μ's)	$2 \times 10, 12$	2.0	0.3
	Two loose e's & one μ, $p_T > 2 \times 13, 11$ GeV	$2 \times 8, 10$	$2 \times 12, 10$	1.6	0.2
One photon	One loose γ, $p_T > 145$ GeV	22 (i)	140	26	46
Two photons	Two loose γ's, $p_T > 55, 55$ GeV	2×20	50, 50	2.4	6
	Two medium γ's, $p_T > 40, 30$ GeV	2×20	35, 25	2.4	18
	Two tight γ's, $p_T > 25, 25$ GeV	2×15 (i)	2×20 (i)	2.4	15
Single jet	Jet ($R = 0.4$), $p_T > 435$ GeV	100	420	3.4	33
	Jet ($R = 1.0$), $p_T > 480$ GeV	100	460	3.4	24
E_T^{miss}	$E_T^{miss} > 200$ GeV	50	110	4.4	100
Multi-jets	Four jets, each $p_T > 125$ GeV	3×50	4×115	0.5	16
	Five jets, each $p_T > 95$ GeV	4×15	5×85	4.9	10
	Six jets, each $p_T > 80$ GeV	4×15	6×70	4.9	4
	Six jets, each $p_T > 60$ GeV, $\lvert\eta\rvert < 2.0$	4×15	6×55, $\lvert\eta\rvert < 2.4$	4.9	15
b–jets	One b ($\epsilon = 40\%$), $p_T > 235$ GeV	100	225	3.4	15
	Two b's ($\epsilon = 60\%$), $p_T > 185, 70$ GeV	100	175, 60	3.4	12
	One b ($\epsilon = 40\%$) & three jets, each $p_T > 85$ GeV	4×15	4×75	4.9	15
	Two b's ($\epsilon = 70\%$) & one jet, $p_T > 65, 65, 160$ GeV	$2 \times 30, 85$	$2 \times 55, 150$	2.7	15
	Two b's ($\epsilon = 60\%$) & two jets, each $p_T > 45$ GeV	4×15	4×35	4.9	13
B-Physics	Two μ's, $p_T > 11, 6$ GeV	11, 6	11, 6 (di-μ)	3.1	50
	Two μ's, $p_T > 6, 6$ GeV, $2.5 < m(\mu, \mu) < 4.0$ GeV	2×6 (J/ψ, topo)	2×6 (J/ψ)	1.8	59
	Two μ's, $p_T > 6, 6$ GeV, $4.7 < m(\mu, \mu) < 5.9$ GeV	2×6 (B, topo)	2×6 (B)	1.8	7
	Two μ's, $p_T > 6, 6$ GeV, $7 < m(\mu, \mu) < 12$ GeV	2×6 (Υ, topo)	2×6 (Υ)	1.5	10
Total Rate				85	1550

Figure A.1: The ATLAS 2017 trigger menu of main triggers. Taken from [73].

A.3 HLT Jet Trigger with integrated FTK tracks

The flowchart of the jet trigger execution of the trigger chain HLT_j420_J100_ftk is shown in Figure A.2. Trigger chains are made of trigger elements that are decoded into algorithm sequences. Each sequence defines the order in which the algorithms are executed.
An FTK service provider is responsible for executing the reconstruction of tracks and vertices. The track to vertex association is performed within the jet trigger. Topo-clustering is executed in parallel. After tracks are ghost-scaled, topo-clusters and ghost tracks are formatted and fed as input into a jet builder that is identical to offline[2]. The jet builder is responsible for computing the calorimeter- and track-based jet attributes. Currently, online jet calibration only makes use of the calorimeter-based attributes. The final stage is the testing of the trigger chain "hypothesis". A counter is used to count the number of calibrated jets with transverse momenta above the p_T threshold in the "hypothesis".

[2]It makes use of FastJet[63], a jet reconstruction tool that is external to ATLAS.

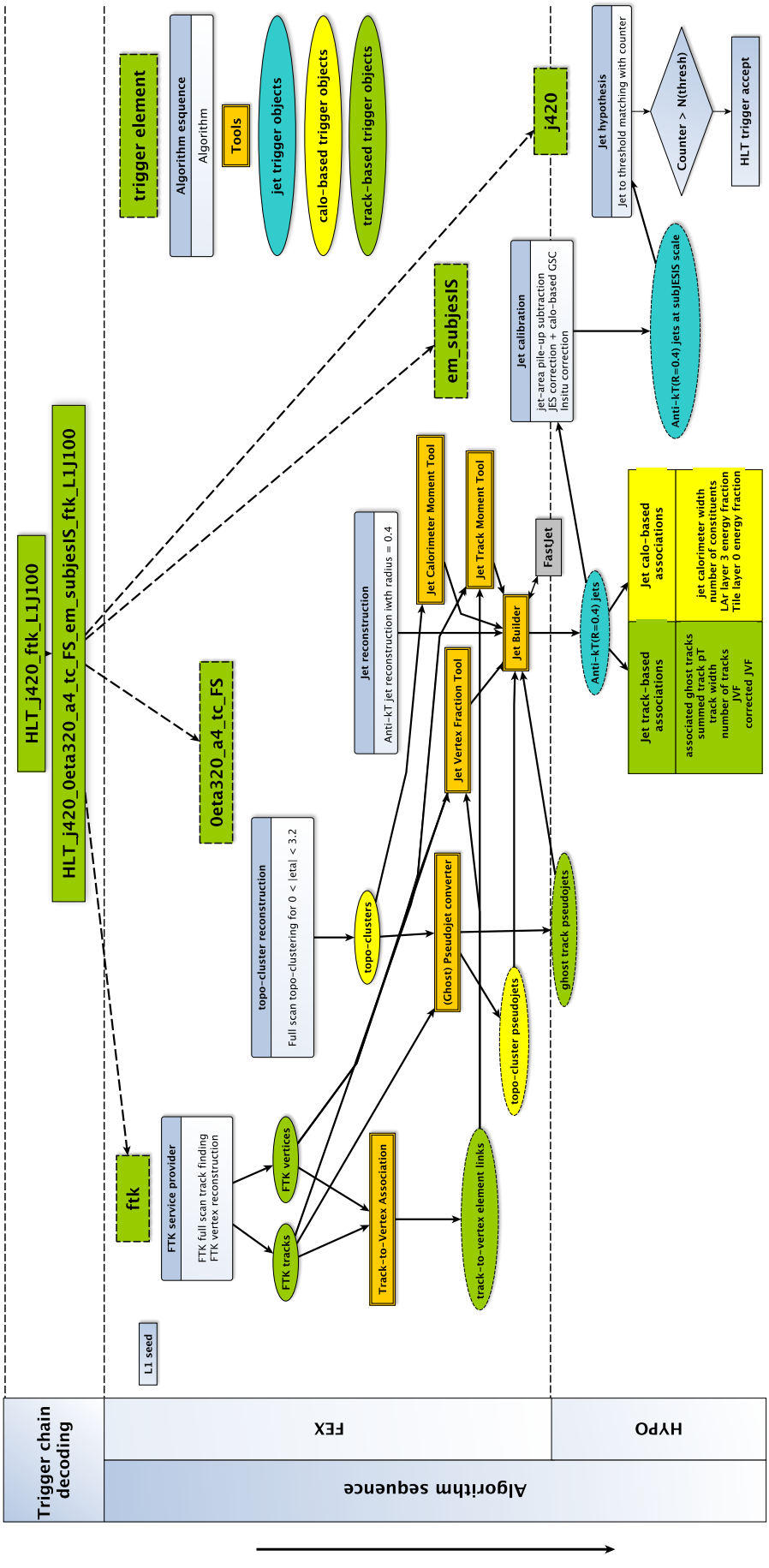

Figure A.2: Flowchart of the jet trigger slice within the trigger menu.

A.4 JVT p_T and η-binned acceptance efficiency

The JVT hard scatter acceptance efficiency at 92% average efficiency is shown for different jet p_T ranges as a function of $|\eta^{jet}|$ for offline and FTK jets in Figure A.3a and A.3b, respectively.

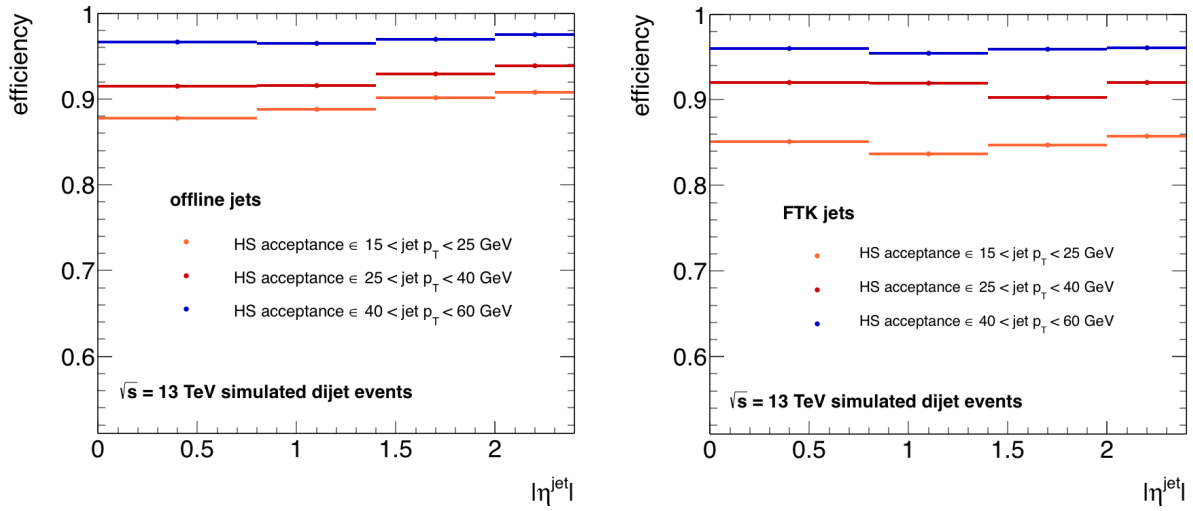

(a) offline JVT (b) FTK JVT

Figure A.3: JVT acceptance efficiency at average 92% efficiency as function of $|\eta^{jet}|$ for different ranges in p_T.

A.5 Pile-up rejection in $t\bar{t}$ signal

A.5.1 The crystal ball function

The crystall ball function is given as

$$f(x;\alpha;n;\bar{x};\sigma) = N \cdot \begin{cases} exp(-\frac{(x-\bar{x})^2}{2\sigma^2}), & \text{if } \frac{x-\bar{x}}{\sigma} > -\alpha. \\ A \cdot (B - \frac{x-\bar{x}}{\sigma})^{-n}, & \text{if } \frac{x-\bar{x}}{\sigma} \leqslant \alpha. \end{cases} \tag{A.1}$$

where

$$A = (\frac{n}{|\alpha|})^n \cdot exp(-\frac{|\alpha|^2}{2}), \tag{A.2}$$

$$B = \frac{n}{|\alpha|} - |\alpha|, \tag{A.3}$$

$$N = \frac{1}{\sigma(C+D)}, \tag{A.4}$$

$$C = \frac{n}{|\alpha|} \cdot \frac{1}{n-1} \cdot exp(-\frac{|\alpha|^2}{2}), \tag{A.5}$$

$$D = \sqrt{\pi}2(1 + erf(\frac{|\alpha|}{\sqrt{2}})). \tag{A.6}$$

Here, erf is the error function,

$$erf(x) = \frac{1}{\sqrt{x}} \int_{-x}^{x} e^{-t^2} dt. \tag{A.7}$$

A.5.2 Variable distributions

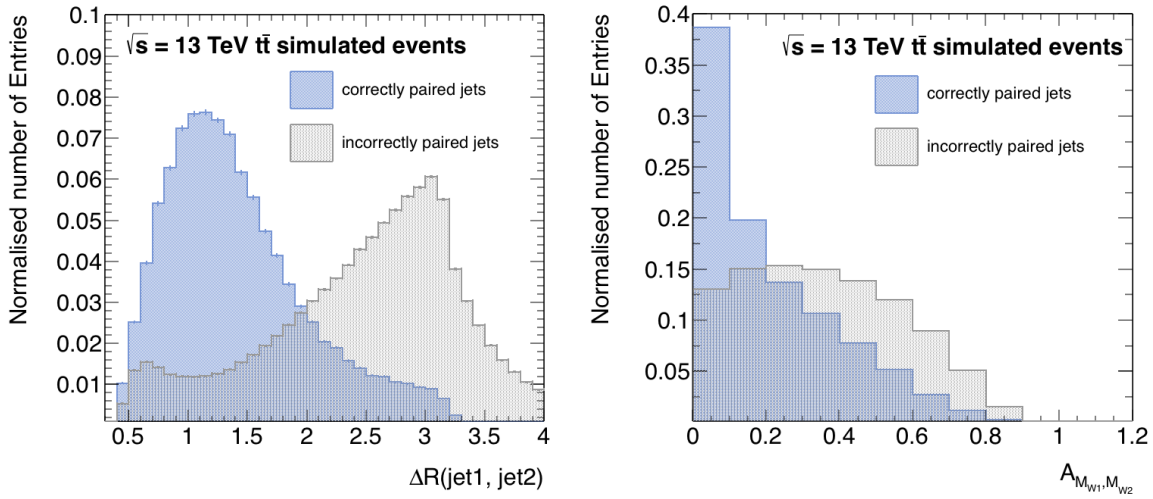

(a) ΔR (b) Mass asymmetry

Figure A.4: The distribution for ΔR (left) and $A_W = (|M_{W1} - M_{W2}|)/(M_{W1} + M_{W2})$ (right) are shown for jet pairs that are correctly and incorrectly matched.

A.5.3 Cutflows

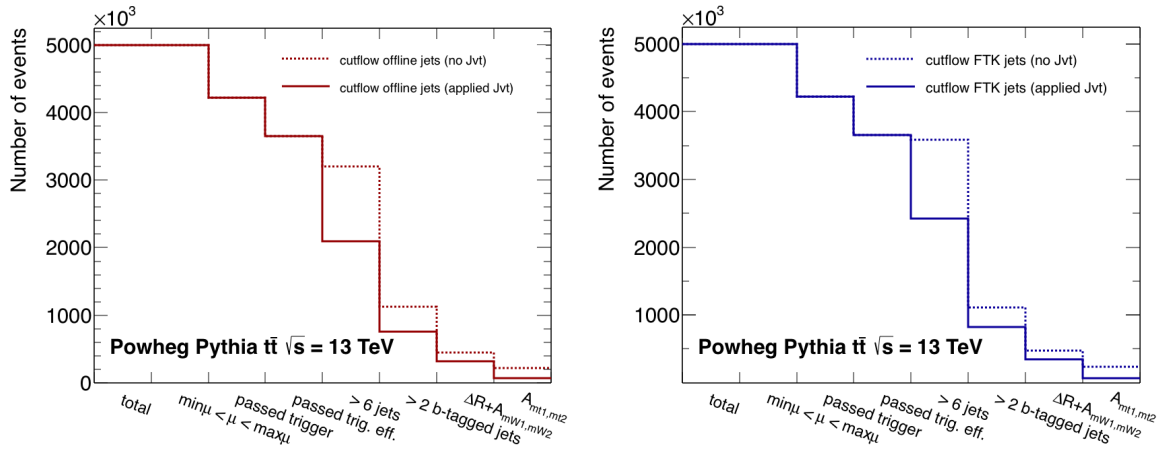

(a) offline jets (b) FTK jets

Figure A.5: The cutflow for selection of events in the reconstruction of the W and top mass is shown for no applied JVT (dashed line) and for applied JVT (solid line). Events are required to pass the HLT_j75_L1_J20 trigger. For full trigger efficiency, a minimum leading jet p_T of 85 GeV is required. Only jets with $p_T^{jet} > 20$ GeV and $|\eta| < 2.4$ are selected.

A.5.4 Non-normalised W and top mass distributions

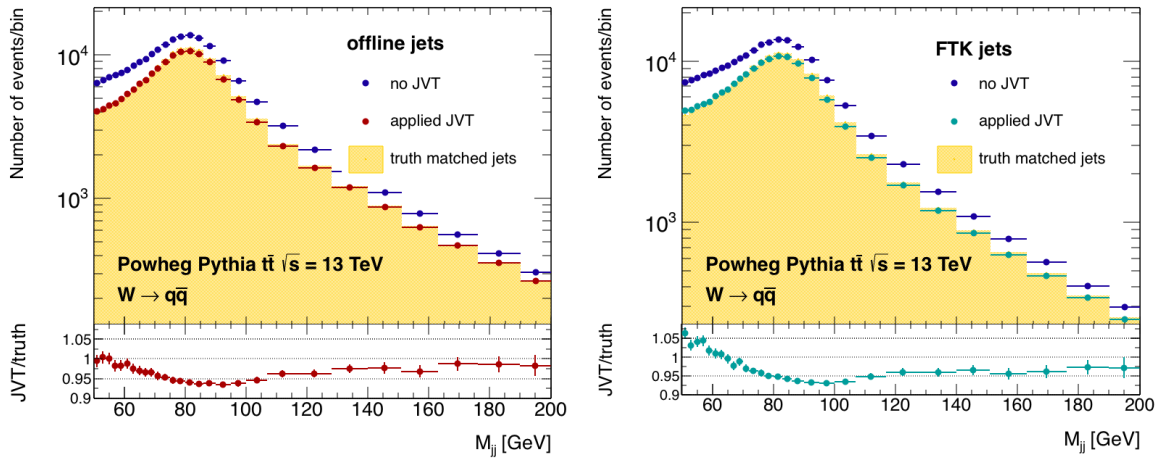

(a) offline jets (b) FTK jets

Figure A.6: The dijet mass spectrum containing a W mass resonance is shown for a simulated $t\bar{t}$ dataset following a signal selection that has been described in Chapter 11, for offline (left) and FTK (right) jets, separately. The reconstructed dijet mass with no applied JVT (dark blue), applied JVT (red in the case of offline, light blue in the case of FTK jets), and for truth-matched jets (solid orange) are shown. The ratio between the applied JVT and truth-matched spectrum is shown in the lower panel.

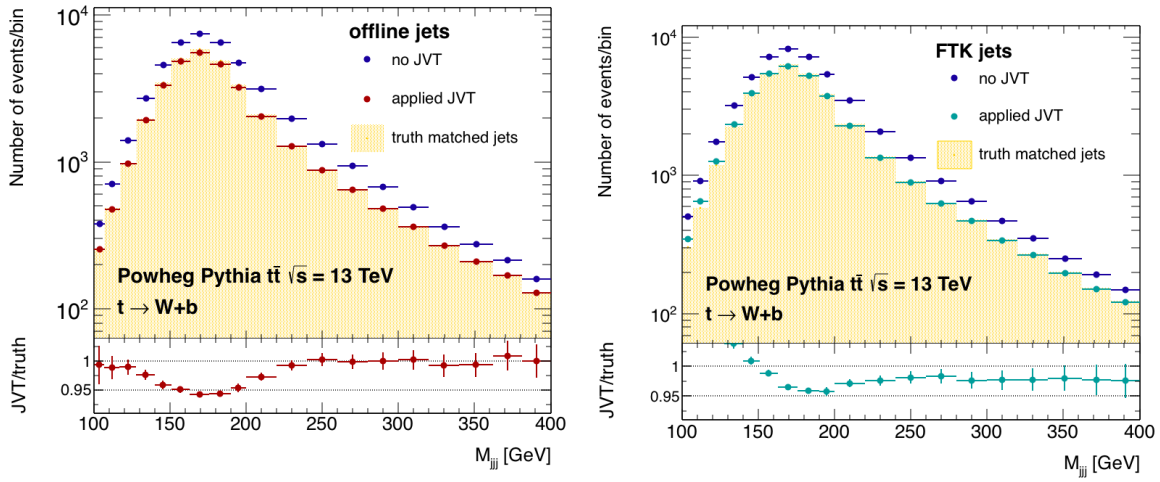

(a) offline jets (b) FTK jets

Figure A.7: The trijet mass spectrum containing a top mass resonance is shown for a simulated $t\bar{t}$ dataset following a signal selection that has been described in Chapter 11, for offline (left) and FTK (right) jets, separately. The reconstructed mass with no applied JVT (dark blue), applied JVT (red in the case of offline, light blue in the case of FTK jets), and for truth-matched jets (solid orange) are shown. The ratio between the applied JVT and truth-matched spectrum is shown in the lower panel.

Bibliography

[1] M. Tanabashi et al., *Review of Particle Physics*, Phys. Rev. **D98** (2018) p. 030001.

[2] M. Thomson, *Modern particle physics*, Cambridge University Press, 2013, ISBN: 9781107034266, URL: http://www-spires.fnal.gov/spires/find/books/www?cl=QC793.2.T46::2013.

[3] D. Griffiths, *Introduction to elementary particles*, 2008, ISBN: 9783527406012.

[4] C. P. Burgess and G. D. Moore, *The standard model: A primer*, Cambridge University Press, 2006, ISBN: 9780511254857, 9781107404267, 9780521860369.

[5] "Elementary particles included in the Standard Model", https://commons.wikimedia.org/w/index.php?curid=4286964, By MissMJ - Own work by uploader, PBS NOVA, Fermilab, Office of Science, United States Department of Energy, Particle Data Group, Public Domain. Accessed: 2018-08-01.

[6] T. Rothman and S. Boughn, *Can gravitons be detected?*, Found. Phys. **36** (2006) pp. 1801–1825, arXiv: gr-qc/0601043 [gr-qc].

[7] R. U. Abbasi et al., *Indications of Intermediate-Scale Anisotropy of Cosmic Rays with Energy Greater Than 57 EeV in the Northern Sky Measured with the Surface Detector of the Telescope Array Experiment*, Astrophys. J. **790** (2014) p. L21, arXiv: 1404.5890 [astro-ph.HE].

[8] P. Fayet, *Supersymmetry and Weak, Electromagnetic and Strong Interactions*, Phys. Lett. **64B** (1976) p. 159.

[9] J.-L. Gervais and B. Sakita, *Field Theory Interpretation of Supergauges in Dual Models*, Nucl. Phys. **B34** (1971) pp. 632–639, [,154(1971)].

[10] "ATLAS Supersymmetry Searches Public Results", https://twiki.cern.ch/twiki/bin/view/AtlasPublic/SupersymmetryPublicResults, Accessed: 2018-11-15.

[11] "CMS Supersymmetry Searches Public Results", https://twiki.cern.ch/twiki/bin/view/CMSPublic/PhysicsResultsSUS, Accessed: 2018-11-15.

[12] C. L. Bennett et al., *Nine-year Wilkinson Microwave Anisotropy Probe (WMAP) Observations: Final Maps and Results*, The Astrophysical Journal Supplement Series **208** (2013) p. 20, URL: http://stacks.iop.org/0067-0049/208/i=2/a=20.

[13] J. C. Kapteyn, *First Attempt at a Theory of the Arrangement and Motion of the Sidereal System*, **55** (1922) p. 302.

[14] V. C. Rubin, N. Thonnard, and W. K. Ford Jr., *Rotational properties of 21 SC galaxies with a large range of luminosities and radii, from NGC 4605 /R = 4kpc/ to UGC 2885 /R = 122 kpc/*, Astrophys. J. **238** (1980) p. 471.

[15] M. Kowalski et al., *Improved Cosmological Constraints from New, Old, and Combined Supernova Data Sets*, The Astrophysical Journal **686** (2008) p. 749, URL: http://stacks.iop.org/0004-637X/686/i=2/a=749.

[16] N. Aghanim et al., *Planck 2018 results. VI. Cosmological parameters*, (2018), arXiv: 1807.06209 [astro-ph.CO].

[17] M. Viel, J. S. Bolton, and M. G. Haehnelt, *Cosmological and astrophysical constraints from the Lyman α forest flux probability distribution function*, **399** (2009) pp. L39–L43, arXiv: 0907.2927.

[18] N. A. Bahcall, L. M. Lubin, and V. Dorman, *Where is the Dark Matter?*, **447** (1995) p. L81.

[19] X.-P. Wu and L.-Z. Fang, *A Statistical Comparison of Cluster Mass Estimates from Optical/X-Ray Observations and Gravitational Lensing*, **483** (1997) pp. 62–67.

[20] V. Springel et al., *Simulations of the formation, evolution and clustering of galaxies and quasars*, **435** (2005) pp. 629–636.

[21] D. Clowe, A. Gonzalez, and M. Markevitch, *Weak lensing mass reconstruction of the interacting cluster 1E0657-558: Direct evidence for the existence of dark matter*, Astrophys. J. **604** (2004) pp. 596–603, arXiv: astro-ph/0312273 [astro-ph].

[22] J. Bowman, A. Rogers, R. Monsalve, T. Mozdzen, and N. Mahesh, *An absorption profile centred at 78 megahertz in the sky-averaged spectrum*, English (US), Nature **555** (2018) pp. 67–70, ISSN: 0028-0836.

[23] S. Dodelson, E. I. Gates, and M. S. Turner, *Cold dark matter models*, Science **274** (1996) pp. 69–75, arXiv: astro-ph/9603081 [astro-ph].

[24] R. Barkana, *Possible interaction between baryons and dark-matter particles revealed by the first stars*, **555** (2018) pp. 71–74, arXiv: 1803.06698.

[25] A. Boyarsky, M. Drewes, T. Lasserre, S. Mertens, and O. Ruchayskiy, *Sterile Neutrino Dark Matter*, (2018), arXiv: 1807.07938 [hep-ph].

[26] R. D. Peccei, *The Strong CP problem and axions*, Lect. Notes Phys. **741** (2008) pp. 3–17, [,3(2006)], arXiv: hep-ph/0607268 [hep-ph].

[27] N. Du et al., *Search for Invisible Axion Dark Matter with the Axion Dark Matter Experiment*, Phys. Rev. Lett. **120** (15 2018) p. 151301, URL: https://link.aps.org/doi/10.1103/PhysRevLett.120.151301.

[28] G. Jungman, M. Kamionkowski, and K. Griest, *Supersymmetric dark matter*, Phys. Rept. **267** (1996) pp. 195–373, arXiv: hep-ph/9506380 [hep-ph].

[29] S. P. Martin, *A Supersymmetry primer*, (1997) pp. 1–98, [Adv. Ser. Direct. High Energy Phys.18,1(1998)], arXiv: hep-ph/9709356 [hep-ph].

[30] T. Han, Z. Liu, and S. Su, *Light Neutralino Dark Matter: Direct/Indirect Detection and Collider Searches*, JHEP **08** (2014) p. 093, arXiv: 1406.1181 [hep-ph].

[31] A. De Simone and T. Jacques, *Simplified models vs. effective field theory approaches in dark matter searches*, Eur. Phys. J. **C76** (2016) p. 367, arXiv: 1603.08002 [hep-ph].

[32] D. Abercrombie et al., *Dark Matter Benchmark Models for Early LHC Run-2 Searches: Report of the ATLAS/CMS Dark Matter Forum*, (2015), ed. by A. Boveia, C. Doglioni, S. Lowette, S. Malik, and S. Mrenna, arXiv: 1507.00966 [hep-ex].

[33] M. Chala, F. Kahlhoefer, M. McCullough, G. Nardini, and K. Schmidt-Hoberg, *Constraining Dark Sectors with Monojets and Dijets*, JHEP **07** (2015) p. 089, arXiv: 1503.05916 [hep-ph].

[34] E. Aprile et al., *Dark Matter Search Results from a One Tonne× Year Exposure of XENON1T*, (2018), arXiv: 1805.12562 [astro-ph.CO].

[35] D. S. Akerib et al., *First results from the LUX dark matter experiment at the Sanford Underground Research Facility*, Phys. Rev. Lett. **112** (2014) p. 091303, arXiv: 1310.8214 [astro-ph.CO].

[36] A. e. a. Tan, *Dark Matter Results from First 98.7 Days of Data from the PandaX-II Experiment*, Phys. Rev. Lett. **117** (12 2016) p. 121303, URL: https://link.aps.org/doi/10.1103/PhysRevLett.117.121303.

[37] F. Petricca et al., "First results on low-mass dark matter from the CRESST-III experiment", *15th International Conference on Topics in Astroparticle and Underground Physics (TAUP 2017) Sudbury, Ontario, Canada, July 24-28, 2017*, 2017, arXiv: 1711.07692 [astro-ph.CO].

[38] P. Agnes et al., *Low-Mass Dark Matter Search with the DarkSide-50 Experiment*, Phys. Rev. Lett. **121** (2018) p. 081307, arXiv: 1802.06994 [astro-ph.HE].

[39] "Summary plots from the ATLAS Exotic physics group", https://atlas.web.cern.ch/Atlas/GROUPS/PHYSICS/CombinedSummaryPlots/EXOTICS/, Accessed: 2018-09-08.

[40] G. Aad et al., *Search for new phenomena in the dijet mass distribution using $p-p$ collision data at $\sqrt{s}=8$ TeV with the ATLAS detector*, Phys. Rev. **D91** (2015) p. 052007, arXiv: 1407.1376 [hep-ex].

[41] V. Khachatryan et al., *Search for dark matter, extra dimensions, and unparticles in monojet events in protonproton collisions at $\sqrt{s}=8$ TeV*, Eur. Phys. J. **C75** (2015) p. 235, arXiv: 1408.3583 [hep-ex].

[42] V. Khachatryan et al., *Search for resonances and quantum black holes using dijet mass spectra in proton-proton collisions at $\sqrt{s}=8$ TeV*, Phys. Rev. **D91** (2015) p. 052009, arXiv: 1501.04198 [hep-ex].

[43] T. e. a. Aaltonen, *Search for new particles decaying into dijets in proton-antiproton collisions at* $\sqrt{s} = 1.96$ TeV, Phys. Rev. D **79** (11 2009) p. 112002, URL: https://link.aps.org/doi/10.1103/PhysRevD.79.112002.

[44] L. Evans and P. Bryant, *LHC Machine*, Journal of Instrumentation **3** (2008) S08001, URL: http://stacks.iop.org/1748-0221/3/i=08/a=S08001.

[45] "Summary plots from the ATLAS Luminosity Group", https://twiki.cern.ch/twiki/bin/view/AtlasPublic/LuminosityPublicResultsRun2, Accessed: 2018-10-13.

[46] M. Benedikt, P. Collier, V Mertens, J. Poole, and K. Schindl, *LHC Design Report*, CERN Yellow Reports: Monographs, CERN, 2004, URL: https://cds.cern.ch/record/823808.

[47] S Fartoukh et al., *The Achromatic Telescopic Squeezing Scheme: Basic Principles and First Demonstration at the LHC*, (2012).

[48] "The HL-LHC project", http://hilumilhc.web.cern.ch/about/hl-lhc-project, Accessed: 2018-08-08.

[49] T. A. Collaboration, *The ATLAS Experiment at the CERN Large Hadron Collider*, Journal of Instrumentation **3** (2008) S08003, URL: http://stacks.iop.org/1748-0221/3/i=08/a=S08003.

[50] "The ATLAS Collaboration", https://atlas.cern/discover/collaboration, Accessed: 2018-08-19.

[51] P. Calafiura, W. Lavrijsen, C. Leggett, M. Marino, and D. Quarrie, "The Athena control framework in production, new developments and lessons learned", *Computing in high energy physics and nuclear physics. Proceedings, Conference, CHEP'04, Interlaken, Switzerland, September 27-October 1, 2004*, 2005 pp. 456–458.

[52] G. Barrand et al., "GAUDI - The software architecture and framework for building LHCb data processing applications", *Proceedings, 11th International Conference on Computing in High-Energy and Nuclear Physics (CHEP 2000): Padua, Italy, February 7-11, 2000*, 2000 pp. 92–95, URL: http://chep2000.pd.infn.it/abst/abs_a152.htm.

[53] N. Geddes, *The Large Hadron Collider and Grid computing*, Phil. Trans. Roy. Soc. Lond. **A370** (2012) pp. 965–977.

[54] "The Grid: A system of tiers", https://home.cern/about/computing/grid-system-tiers, Accessed: 2018-10-13.

[55] G. Aad et al., *The ATLAS Simulation Infrastructure*, Eur. Phys. J. **C70** (2010) pp. 823–874, arXiv: 1005.4568 [physics.ins-det].

[56] S. Agostinelli et al., *GEANT4: A Simulation toolkit*, Nucl. Instrum. Meth. **A506** (2003) pp. 250–303.

[57] T. Sjöstrand, S. Mrenna, and P. Z. Skands,
A Brief Introduction to PYTHIA 8.1,
Comput. Phys. Commun. **178** (2008) p. 852, arXiv: 0710.3820 [hep-ph].

[58] The ATLAS collaboration, *Performance of the ATLAS Track Reconstruction Algorithms in Dense Environments in LHC Run 2*,
Eur. Phys. J. **C77** (2017) p. 673, arXiv: 1704.07983 [hep-ex].

[59] *Performance of the ATLAS Inner Detector Track and Vertex Reconstruction in the High Pile-Up LHC Environment*, (2012).

[60] K. Grimm et al., "Primary vertex reconstruction at the ATLAS experiment",
tech. rep. ATL-SOFT-PROC-2017-051. 4, CERN, 2017,
URL: http://cds.cern.ch/record/2253428.

[61] ATLAS Collaboration, *Topological cell clustering in the ATLAS calorimeters and its performance in LHC Run 1*, Eur. Phys. J. C **77** (2017) p. 490,
arXiv: 1603.02934 [hep-ex].

[62] M. Cacciari, G. P. Salam, and G. Soyez, *The anti-k_t jet clustering algorithm*,
JHEP **04** (2008) p. 063, arXiv: 0802.1189 [hep-ph].

[63] M. Cacciari, G. P. Salam, and G. Soyez, *FastJet User Manual*,
Eur. Phys. J. C **72** (2012) p. 1896, arXiv: 1111.6097 [hep-ph].

[64] G. Aad et al., *Performance of jet substructure techniques for large-R jets in proton-proton collisions at $\sqrt{s}$ = 7 TeV using the ATLAS detector*,
JHEP **09** (2013) p. 076, arXiv: 1306.4945 [hep-ex].

[65] The ATLAS collaboration,
Jet energy scale measurements and their systematic uncertainties in proton-proton collisions at $\sqrt{s} = 13$ TeV with the ATLAS detector,
Phys. Rev. **D96** (2017) p. 072002, arXiv: 1703.09665 [hep-ex].

[66] "Tagging and suppression of pileup jets with the ATLAS detector",
tech. rep. ATLAS-CONF-2014-018, CERN, 2014,
URL: https://cds.cern.ch/record/1700870.

[67] "ATLAS DAQ approved plots",
https://twiki.cern.ch/twiki/bin/view/AtlasPublic/ApprovedPlotsDAQ,
Accessed: 2018-10-13.

[68] R. Achenbach et al., *The ATLAS level-1 calorimeter trigger*,
JINST **3** (2008) P03001.

[69] G. Aad et al.,
Performance of the ATLAS muon trigger in pp collisions at $\sqrt{s} = 8$ TeV,
Eur. Phys. J. **C75** (2015) p. 120, arXiv: 1408.3179 [hep-ex].

[70] W Buttinger, "The ATLAS Level-1 Trigger System",
tech. rep. ATL-DAQ-PROC-2012-024, CERN, 2012,
URL: https://cds.cern.ch/record/1456546.

[71] B. Asman et al., *The ATLAS Level-1 Calorimeter Trigger: PreProcessor implementation and performance*, JINST **7** (2012) P12008.

[72] The ATLAS collaboration, *Performance of the ATLAS trigger system in 2015*,
European Physical Journal. C, Particles and Fields **77** (2017),
URL: http://www.osti.gov/pages/servlets/purl/1379836.

[73] "ATLAS Trigger Operation Public Results", https://twiki.cern.ch/twiki/bin/view/AtlasPublic/TriggerOperationPublicResults, Accessed: 2018-09-25.

[74] "W.J. Stirling, private communication.", http://www.hep.ph.ic.ac.uk/~wstirlin/plots/plots.html, Accessed: 2018-19-09.

[75] H Martinez, N Besson, and N Morange, "Update on the study and validation of the BCID of the L1Calo at very high transverse energies", tech. rep. ATL-COM-LARG-2012-025, CERN, 2012, URL: https://cds.cern.ch/record/1476908.

[76] "ATLAS Level-1 Calorimeter Trigger Public Results", https://twiki.cern.ch/twiki/bin/view/AtlasPublic/L1CaloTriggerPublicResults, Accessed: 2018-09-25.

[77] "Large Hadron Collider: Weasel causes shutdown", https://www.bbc.com/news/world-europe-36173247, Accessed: 2018-10-26.

[78] V Lang and R Stamen, "Precision Synchronization of the ATLAS Level-1 Calorimeter Trigger with Collision Data in 2010 and 2011", tech. rep. ATL-DAQ-PUB-2012-001, CERN, 2012, URL: https://cds.cern.ch/record/1454684.

[79] M. Wessels, "Upgrade of the ATLAS Level-1 Calorimeter Trigger", *Proceedings, 19th Real Time Conference (RT2014): Nara, Japan, May 26-30, 2014*, 2014.

[80] C. Albajar et al., *Two-jet mass distributions at the CERN proton-antiproton collider*, Physics Letters B **209** (1988) pp. 127 –134, ISSN: 0370-2693, URL: http://www.sciencedirect.com/science/article/pii/0370269388918436.

[81] J. Alitti et al., *A Measurement of two jet decays of the W and Z bosons at the CERN $\bar{p}p$ collider*, Z. Phys. **C49** (1991) pp. 17–28.

[82] F. Abe et al., *Search for new particles decaying to dijets at CDF*, Phys. Rev. D **55** (9 1997) R5263–R5268, URL: https://link.aps.org/doi/10.1103/PhysRevD.55.R5263.

[83] P. H. Frampton and S. L. Glashow, "Chiral color: an alternative to the standard model", tech. rep. BU-HEP-87-4. HUTP-87-A-007. IFP-283-UNC, Boston Univ., 1987, URL: http://cds.cern.ch/record/175797.

[84] U. Baur, I. Hinchliffe, and D. Zeppenfeld, *Excited Quark Production at Hadron Colliders*, Int. J. Mod. Phys. **A2** (1987) p. 1285.

[85] X. Calmet, W. Gong, and S. D. H. Hsu, *Colorful quantum black holes at the LHC*, Phys. Lett. **B668** (2008) pp. 20–23, arXiv: 0806.4605 [hep-ph].

[86] D. M. Gingrich, *Quantum black holes with charge, colour, and spin at the LHC*, J. Phys. **G37** (2010) p. 105008, arXiv: 0912.0826 [hep-ph].

[87] E. Eichten, I. Hinchliffe, K. Lane, and C. Quigg, *Supercollider physics*, Reviews of Modern Physics **56** (1984) pp. 579–707.

[88] The ATLAS collaboration,
Search for a dijet resonance produced in association with a leptonically decaying W or Z boson with the ATLAS detector at $\sqrt{s} = 8$ *TeV*, (2013).

[89] R. Aaij et al., *Measurement of forward* J/ψ *production cross-sections in pp collisions at* $\sqrt{s} = 13$ *TeV*,
JHEP **10** (2015) p. 172, [Erratum: JHEP05,063(2017)],
arXiv: 1509.00771 [hep-ex].

[90] V. Khachatryan et al., *Search for narrow resonances in dijet final states at* $\sqrt{(s)} = 8$ *TeV with the novel CMS technique of data scouting*,
Phys. Rev. Lett. **117** (2016) p. 031802, arXiv: 1604.08907 [hep-ex].

[91] The ATLAS collaboration, *Search for low-mass dijet resonances using trigger-level jets with the ATLAS detector in pp collisions at* $\sqrt{s} = 13$ *TeV*, (2018), arXiv: 1804.03496 [hep-ex].

[92] The ATLAS collaboration, *Search for low-mass dijet resonances using trigger-level jets with the ATLAS detector in pp collisions at* $\sqrt{s} = 13$ *TeV*,
Phys. Rev. Lett. **121** (2018) p. 081801, arXiv: 1804.03496 [hep-ex].

[93] The ATLAS collaboration, *Search for light resonances decaying to boosted quark pairs and produced in association with a photon or a jet in proton-proton collisions at* $\sqrt{s} = 13$ *TeV with the ATLAS detector*, (2018),
arXiv: 1801.08769 [hep-ex].

[94] "Search for new light resonances decaying to jet pairs and produced in association with a photon or a jet in proton-proton collisions at $\sqrt{s} = 13$ TeV with the ATLAS detector", tech. rep. ATLAS-CONF-2016-070, CERN, 2016,
URL: https://cds.cern.ch/record/2206221.

[95] The ATLAS collaboration, *Search for new phenomena in dijet events using* 37 fb^{-1} *of pp collision data collected at* $\sqrt{s} = 13$ TeV *with the ATLAS detector*,
Phys. Rev. D **96** (5 2017) p. 052004,
URL: https://link.aps.org/doi/10.1103/PhysRevD.96.052004.

[96] The ATLAS collaboration, *Search for resonances in the mass distribution of jet pairs with one or two jets identified as b-jets in proton-proton collisions at* $\sqrt{s} = 13$ *TeV with the ATLAS detector*, Phys. Rev. **D98** (2018) p. 032016,
arXiv: 1805.09299 [hep-ex].

[97] The ATLAS collaboration,
Search for heavy particles decaying into top-quark pairs using lepton-plus-jets events in protonproton collisions at $\sqrt{s} = 13$ *TeV with the ATLAS detector*,
Eur. Phys. J. **C78** (2018) p. 565, arXiv: 1804.10823 [hep-ex].

[98] The ATLAS collaboration, *A search for pair-produced resonances in four-jet final states at* $\sqrt{s} = 13$ *TeV with the ATLAS detector*,
Eur. Phys. J. **C78** (2018) p. 250, arXiv: 1710.07171 [hep-ex].

[99] C. Collaboration, *Search for low-mass pair-produced dijet resonances using jet substructure techniques in proton-proton collisions at a center-of-mass energy of* $\sqrt{s} = 13$ TeV, (2016).

[100] G. Aad et al., *Search for massive supersymmetric particles decaying to many jets using the ATLAS detector in pp collisions at $\sqrt{s} = 8$ TeV*, Phys. Rev. **D91** (2015) p. 112016, [Erratum: Phys. Rev.D93,no.3,039901(2016)], arXiv: 1502.05686 [hep-ex].

[101] E. J. Chun and H. B. Kim, *Axino Light Dark Matter and Neutrino Masses with R-parity Violation*, JHEP **10** (2006) p. 082, arXiv: hep-ph/0607076 [hep-ph].

[102] M. Endo, K. Hamaguchi, S. P. Liew, K. Mukaida, and K. Nakayama, *Axino dark matter with R-parity violation and 130 GeV gamma-ray line*, Phys. Lett. **B721** (2013) pp. 111–117, arXiv: 1301.7536 [hep-ph].

[103] M. Hirsch, *Collider signals of gravitino dark matter in bilinearly broken R-parity*, PoS **HEP2005** (2006) p. 343.

[104] F. Takayama and M. Yamaguchi, *Gravitino dark matter without R-parity*, Phys. Lett. **B485** (2000) pp. 388–392, arXiv: hep-ph/0005214 [hep-ph].

[105] A. M. Sirunyan et al., *Search for pair-produced three-jet resonances in proton-proton collisions at $\sqrt{s} = 13$ TeV*, Submitted to: Phys. Rev. (2018), arXiv: 1810.10092 [hep-ex].

[106] C. Arina et al., *A comprehensive approach to dark matter studies: exploration of simplified top-philic models*, JHEP **11** (2016) p. 111, arXiv: 1605.09242 [hep-ph].

[107] T. Plehn, J. Thompson, and S. Westhoff, *Dark Matter from Electroweak Single Top Production*, Phys. Rev. **D98** (2018) p. 015012, arXiv: 1712.08065 [hep-ph].

[108] P. Nason, *A New method for combining NLO QCD with shower Monte Carlo algorithms*, JHEP **11** (2004) p. 040, arXiv: hep-ph/0409146.

[109] A. Salzburger, *Optimisation of the ATLAS Track Reconstruction Software for Run-2*, J. Phys. Conf. Ser. **664** (2015) p. 072042.

[110] "Emanuel Demetrio Mendes Gouveia, private communication.", Accessed: 2018-03-11.

[111] "ATLAS Trigger Operation Public Results", https://twiki.cern.ch/twiki/pub/AtlasPublic/JetTriggerPublicResults, Accessed: 2018-09-25.

[112] M Shochet et al., "Fast TracKer (FTK) Technical Design Report", tech. rep. CERN-LHCC-2013-007. ATLAS-TDR-021, ATLAS Fast Tracker Technical Design Report, 2013, URL: https://cds.cern.ch/record/1552953.

[113] "ATLAS FTK Public Results", https://twiki.cern.ch/twiki/bin/view/AtlasPublic/FTKPublicResults, Accessed: 2018-10-28.

[114] "Optimisation and performance studies of the ATLAS *b*-tagging algorithms for the 2017-18 LHC run", tech. rep. ATL-PHYS-PUB-2017-013, CERN, 2017, URL: http://cds.cern.ch/record/2273281.

[115] H. Wiedemann,
Particle Accelerator Physics: Basic Principles and Linear Beam Dynamics,
Springer Berlin Heidelberg, 2013, ISBN: 9783662029039,
URL: https://books.google.de/books?id=Oo_uCAAAQBAJ.

[116] K. Johnsen, *CERN Intersecting Storage Rings (ISR)*,
Proc. Natl. Acad. Sci. U. S. A. **70** (1973) 619–626. 8 p, National Academy of Sciences Autumn Meeting (October 1972): Symposium: New Accelerators,
URL: https://cds.cern.ch/record/2318386.

[117] *First Proton Anti-proton Collisions in the CERN SPS Collider*,
Phys. Lett. **B107** (1981) pp. 306–309, [,7.27(1981)].

[118] R. R. Wilson, *The Tevatron*, Phys. Today **30N10** (1977) pp. 23–30.